

A MOLECULAR APPROACH TO NANOSCALE MAGNETIC MATERIALS:  
NEW IRON AND MANGANESE CLUSTERS FROM THE USE OF PYRIDYL ALCOHOLS

By

TAKETO TAGUCHI

A DISSERTATION PRESENTED TO THE GRADUATE SCHOOL  
OF THE UNIVERSITY OF FLORIDA IN PARTIAL FULFILLMENT  
OF THE REQUIREMENTS FOR THE DEGREE OF  
DOCTOR OF PHILOSOPHY

UNIVERSITY OF FLORIDA

2009

© 2009 Taketo Taguchi

To my family

## ACKNOWLEDGMENTS

First and foremost, I would like to thank my research advisor, Professor George Christou, for the opportunity to pursue my goal of earning a doctoral degree in chemistry in his research group. His guidance, insightful advice, and constant encouragement have been invaluable in attaining my goal. He was always available for me to ask questions and seek advice. He was always open to the bizarre ideas I often came up with and brought to him. He always encouraged me to do whatever I was interested in trying. His comments on my research projects or chemistry in general were always eye-opening, and I have said the phrase “Oh, I’ve never thought of that!” a million times in the 5 years of my PhD. studies. Additionally, his advice on writing scientific papers and making effective presentations has been truly enlightening, and I sincerely appreciate it. I learned from him to look at data from different perspectives, to speculate deeply about them, and to organize given information with comprehensive views. Furthermore, he often spent hours with me in person in the lab to teach me chemistry and techniques. After 5 years of his guidance, I finally feel that I started to understand chemistry, slowly but surely. The fun I have now seems to be increasing exponentially. Thus it is indeed sad that it is time to graduate and leave his group, but what he taught me here, what he helped me to accomplish here, and all what we talked about here are definitely my treasures in my future endeavors.

I would also like to express my gratitude to the other members of my committee, Professor Daniel. R Talham, Professor Nicolo Omenetto, Professor Adam S. Veige, and Professor Mark W. Meisel. I often asked Professor Veige about organic synthesis and techniques. He also gave me invaluable advice about applications for postdoctoral fellow positions. I truly appreciate his time and thoughtful advice for me. I would also like to thank Dr. Khalil A. Abboud and his staff at University of Florida Center for X-Ray Crystallography for solving my crystal structures. I would like to acknowledge Dr. Wolfgang Wernsdorfer for providing essential single crystal

measurements on the  $Mn_{12}$  compound below 1.8 K using his micro-SQUID apparatus, and Professor Stephen Hill and Changyun Koo at the UF Physics Department for the HFEPR measurements. Special gratitude goes to Dr. Ted A. O'Brien for performing semiempirical calculations on my Fe compounds. I would also like to thank Dr. Ogawa who taught me organic synthesis. Thanks to his assistance in the early stage of my Ph.D. study, I became able to carry out multistep organic reactions without much hesitation. I also express my sincerest gratitude to Dr. Mukaibo for her constant encouragement and insightful discussions. Thanks to her encouragement and support, I very much enjoyed my study at UF and my life in Gainesville.

I had a really good time in Christou group thanks to all of its members, past and present. I thank all secretaries, Sondra, Melinda, and Alice, who greatly assisted my research. I thank all post-docs, past and present, Dr. Murugesu, Dr. King, Dr. Stamatatos, Dr. Liu, Dr. Papatriantafyllopoulou, Dr. Ethymiou, Dr. Maayan, and Dr. Singh for their great assistance and advice. Special appreciation is given to Dr. Stamatatos. When I was trying to get initial results, he guided me and assisted me greatly. When I was preparing presentations and writing scientific reports, he spent a tremendous amount of time and energy to help me. Thanks to his great assistance in the early stage of my Ph.D. study, I was able to get my study on track. I would also like to thank the graduate students in Christou group, past and present, John, Nicole, Abhu, Dolos, Alina, Rashmi, Chris, Antonio, Arpita, Shreya, Jennifer, Dina, Jenn, Andy, Emir, Katye, and Xun-Gao. My appreciation also goes to the high school and undergraduate students with whom I worked, Garrett, Mike, Matt, Alex, and Radhika. When they were struggling with their chemistry, I found myself struggling far harder for their success than my own. When they got their first crystals, it was more pleasing to me than getting results for myself. I was really fortunate to work with these wonderful people throughout my study here. In this regard, I would

also like to thank Professor Christou for giving me such wonderful opportunities. I learned really a lot from all Christou group members, not only about chemistry but also about life in general. Everyone is in my treasured memory, and every minute I spent with them consists of my entire life.

Finally, I would like to express my sincerest gratitude to my family, my father, mother, sister, grandfather, and grandmother for being always understanding and supportive. Their faith in me has been invaluable in every aspect of my life. I really appreciate that they raised me in a warm and loving family. Thanks to the same hearty and relaxing atmosphere, I always felt happy and greatly energized when I came back to Japan during holidays. Because of my family's support, I was able to come this far. I am forever grateful for their love and support.

## TABLE OF CONTENTS

	<u>page</u>
ACKNOWLEDGMENTS.....	4
LIST OF TABLES.....	10
LIST OF FIGURES .....	12
LIST OF ABBREVIATIONS.....	19
ABSTRACT.....	20
CHAPTER	
1 GENERAL INTRODUCTION .....	23
2 NEW TETRA AND HEXANUCLEAR IRON CLUSTERS FROM THE USE OF 2-(HYDROXYMETHYL)PYRIDINE.....	32
2.1 Introduction .....	32
2.2 Experimental Section .....	34
2.2.1 Syntheses.....	34
2.2.2 X-Ray Crystallography.....	35
2.2.3 Other Studies.....	37
2.2.4 Theoretical Calculations.....	37
2.3 Results and Discussion .....	38
2.3.1 Syntheses.....	38
2.3.2 Description of Structures.....	40
2.3.3 Magnetochemistry .....	43
2.3.3.1 Direct current magnetic susceptibility studies .....	43
2.3.3.2 Alternating current magnetic susceptibility studies.....	46
2.3.3.3 Rationalization of the $S = 3$ ground state of Complex 2-1 .....	48
2.4 Conclusions .....	51
3 UNUSUAL FE8, FE9, AND FE18 STRUCTURAL TYPES FROM THE USE OF 2,6-PYRIDINEDIMETHANOL.....	67
3.1 Introduction .....	67
3.2 Experimental Section .....	69
3.2.1 Syntheses.....	69
3.2.2 X-ray Crystallography .....	71
3.2.3 Other Studies.....	72
3.3 Results and Discussion .....	73
3.3.1 Syntheses.....	73
3.3.2 Description of Structures.....	76
3.3.3 Magnetochemistry .....	79

3.3.3.1	Direct current magnetic susceptibility studies .....	79
3.3.3.2	Alternating current magnetic susceptibility studies.....	81
3.3.3.3	Rationalization of the $S = 5/2$ Ground State of Complex 3-4.....	82
3.3.3.4	Single-Crystal, High Frequency EPR (HF-EPR) Spectroscopy.....	84
3.4	Conclusions .....	87
4	MN CLUSTERS FROM THE USE OF BULKY PYRIDYLALCOHOLS: STRUCTURAL AND MAGNETIC STUDIES .....	105
4.1	Introduction .....	105
4.2	Experimental Section .....	107
4.2.1	Syntheses.....	107
4.2.2	X-ray Crystallography.....	111
4.2.3	Other Studies.....	113
4.3	Results and Discussion .....	114
4.3.1	Syntheses.....	114
4.3.1.1	Reactions with dphmpH .....	114
4.3.1.2	Reactions with dmhmpH .....	116
4.3.2	Description of Structures.....	117
4.3.3	Magnetochemistry .....	124
4.3.3.1	Direct current magnetic susceptibility studies .....	124
4.3.3.2	Alternating current magnetic susceptibility studies.....	131
4.3.3.3	Hysteresis Studies below 1.8 K.....	134
4.3.4	Structural Comparison of hmp <sup>-</sup> , dmhmp <sup>-</sup> , and dphmp <sup>-</sup> Mn <sub>x</sub> Products.....	135
4.4	Conclusions .....	137
5	NEW MN4 AND MN7 CLUSTERS FROM THE USE OF PHENYLDIPYRIDIN-2- YLMETHANOL .....	168
5.1	Introduction .....	168
5.2	Experimental Section .....	170
5.2.1	Syntheses.....	170
5.2.2	X-Ray Crystallography.....	172
5.2.3	Other Studies.....	173
5.3	Results and Discussion .....	174
5.3.1	Syntheses.....	174
5.3.2	Description of Structures.....	176
5.3.3	Electrochemistry .....	178
5.3.4	Magnetochemistry .....	179
5.3.4.1	Direct Current Magnetic susceptibility studies.....	179
5.3.4.2	Alternating Current Magnetic susceptibility studies .....	181
5.4	Conclusions .....	182
APPENDIX		
A	BOND DISTANCES AND ANGLES.....	196

B	LIST OF COMPOUNDS.....	212
C	VAN VLECK EQUATIONS .....	213
	LIST OF REFERENCES .....	225
	BIOGRAPHICAL SKETCH .....	245

## LIST OF TABLES

<u>Table</u>	<u>page</u>
2-1 Crystallographic Data for <b>2-1</b> ·8MeCN, <b>2-2</b> ·6MeCN and <b>2-3</b> ·2MeOH. ....	53
2-2 Calculated ground states ST of complex <b>2-1</b> with various $J_{23}$ values. ....	54
3-1 Crystallographic Data for <b>3-1</b> ·7MeOH, <b>3-3</b> ·7MeCN·H <sub>2</sub> O and <b>3-4</b> ·7CH <sub>2</sub> Cl <sub>2</sub> . ....	89
3-2 Bond Valence Sums for Selected O Atoms in Complex <b>3-3</b> . ....	90
3-3 Bond Valence Sums for Selected O Atoms in Complex <b>3-4</b> . ....	90
4-1 Crystallographic Data for <b>4-1</b> ·2MeCN, <b>4-2</b> ·3MeCN and <b>4-3</b> ·4MeCN. ....	138
4-2 Crystallographic Data for <b>4-4</b> ·7MeCN, <b>4-5</b> ·3CH <sub>2</sub> Cl <sub>2</sub> and <b>4-6</b> ·Et <sub>2</sub> O. ....	139
4-3 Bond Valence Sums for the Mn Atoms in Complex <b>4-1</b> . ....	140
4-4 Bond Valence Sums for the Mn Atoms in Complex <b>4-2</b> . ....	140
4-5 Bond Valence Sums for the Mn Atoms in Complex <b>4-3</b> . ....	140
4-6 Bond Valence Sums for the Mn Atoms in Complex <b>4-4</b> . ....	141
4-7 Bond Valence Sums for the Inorganic Oxygen Atoms in Complex <b>4-4</b> . ....	141
4-8 Bond Valence Sums for the Mn Atoms in Complex <b>4-5</b> . ....	142
4-9 Bond Valence Sums for the Inorganic Oxygen Atoms in Complex <b>4-5</b> . ....	142
4-10 Complexes with hmp <sup>-</sup> , dmhmp <sup>-</sup> , or dphmp <sup>-</sup> , and the Alkoxide O Atom Binding Mode. ....	143
5-1 Crystallographic Data for <b>5-1</b> ·0.5MeCN and <b>5-2</b> ·2MeCN. ....	184
5-2 Bond Valence Sums for the Mn Atoms in Complex <b>5-1</b> . ....	185
5-3 BVS for Selected O Atoms in <b>5-1</b> . ....	185
A-1 Selected interatomic distances (Å) and angles (°) for [Fe <sub>6</sub> O <sub>2</sub> (hmp) <sub>10</sub> (H <sub>2</sub> O) <sub>2</sub> ](NO <sub>3</sub> ) <sub>4</sub> ·8MeCN ( <b>2-1</b> ·8MeCN) ....	196
A-2 Selected interatomic distances (Å) and angles (°) for [Fe <sub>6</sub> O <sub>2</sub> (hmp) <sub>8</sub> (NO <sub>3</sub> ) <sub>4</sub> (H <sub>2</sub> O) <sub>2</sub> ](NO <sub>3</sub> ) <sub>2</sub> ·6MeCN ( <b>2-2</b> ·6MeCN) ....	197
A-3 Selected interatomic distances (Å) and angles (°) for [Fe <sub>4</sub> (N <sub>3</sub> ) <sub>6</sub> (hmp) <sub>6</sub> ]·2MeOH ( <b>2-3</b> ·2MeOH) ....	198

A-4	Selected interatomic distances (Å) and angles (°) for [Fe <sub>8</sub> O <sub>3</sub> (OMe)(pdm) <sub>4</sub> (pdmH) <sub>4</sub> (MeOH) <sub>2</sub> ](ClO <sub>4</sub> ) <sub>5</sub> ·7MeOH ( <b>3-1</b> ·7MeOH).....	199
A-5	Selected interatomic distances (Å) and angles (°) for [Fe <sub>18</sub> O <sub>6</sub> (OH) <sub>8</sub> (pdm) <sub>10</sub> (pdmH) <sub>4</sub> (H <sub>2</sub> O) <sub>4</sub> ](ClO <sub>4</sub> ) <sub>10</sub> ·7MeCN·3H <sub>2</sub> O ( <b>3-3</b> ·7MeCN·3H <sub>2</sub> O) .....	200
A-6	Selected interatomic distances (Å) and angles (°) for [Fe <sub>9</sub> O <sub>4</sub> (OH) <sub>2</sub> (O <sub>2</sub> CMe) <sub>10</sub> (pdm)(pdmH) <sub>4</sub> ](NO <sub>3</sub> ) <sub>7</sub> ·7CH <sub>2</sub> Cl <sub>2</sub> ( <b>3-4</b> ·7CH <sub>2</sub> Cl <sub>2</sub> ) .....	202
A-7	Selected interatomic distances (Å) and angles (°) for [Mn <sub>4</sub> O <sub>2</sub> (O <sub>2</sub> CBu <sup>t</sup> ) <sub>5</sub> (dphmp) <sub>3</sub> ]·2MeCN ( <b>4-1</b> ·2MeCN).....	203
A-8	Selected interatomic distances (Å) and angles (°) for [Mn <sub>6</sub> O <sub>4</sub> (OMe) <sub>2</sub> (O <sub>2</sub> CPh) <sub>4</sub> (dphmp) <sub>4</sub> ]·3MeCN ( <b>4-2</b> ·3MeCN). .....	204
A-9	Selected interatomic distances (Å) and angles (°) for [Mn <sub>11</sub> O <sub>7</sub> (OMe) <sub>7</sub> (O <sub>2</sub> CPh) <sub>7</sub> (dphmp) <sub>4</sub> (MeOH) <sub>2</sub> ]·4MeCN ( <b>4-3</b> ·4MeCN). .....	205
A-10	Selected interatomic distances (Å) and angles (°) for [Mn <sub>7</sub> O <sub>3</sub> (OH) <sub>3</sub> (O <sub>2</sub> CBu <sup>t</sup> ) <sub>7</sub> (dmhmp) <sub>4</sub> ]·7MeCN ( <b>4-4</b> ·7MeCN) .....	206
A-11	Selected interatomic distances (Å) and angles (°) for [Mn <sub>12</sub> O <sub>7</sub> (OH)(OMe) <sub>2</sub> (O <sub>2</sub> CPh) <sub>12</sub> (dmhmp) <sub>4</sub> (H <sub>2</sub> O)]·3CH <sub>2</sub> Cl <sub>2</sub> ( <b>4-5</b> ·3CH <sub>2</sub> Cl <sub>2</sub> ) .....	207
A-12	Selected interatomic distances (Å) and angles (°) for (HNEt <sub>3</sub> )[NaMn <sub>6</sub> O <sub>4</sub> (dmhmp) <sub>4</sub> (N <sub>3</sub> ) <sub>4</sub> ](ClO <sub>4</sub> ) <sub>2</sub> ·Et <sub>2</sub> O ( <b>4-6</b> ·Et <sub>2</sub> O). .....	209
A-13	Selected interatomic distances (Å) and angles (°) for [Mn <sub>4</sub> O <sub>4</sub> (O <sub>2</sub> CMe) <sub>3</sub> (pdpm) <sub>3</sub> ]·0.5MeCN ( <b>5-1</b> ·0.5MeCN).....	210
A-14	Selected interatomic distances (Å) and angles (°) for [Mn <sub>7</sub> O <sub>4</sub> (pdpm) <sub>6</sub> (N <sub>3</sub> ) <sub>4</sub> ](ClO <sub>4</sub> ) <sub>2</sub> ·2MeCN ( <b>5-2</b> ·2MeCN).....	211

## LIST OF FIGURES

<u>Figure</u>	<u>page</u>
1-1	Representations of magnetic dipole arrangements in (i) paramagnetic, (ii) ferromagnetic, (iii) antiferromagnetic, and (iv) ferrimagnetic materials..... 29
1-2	Typical hysteresis loop of a magnet, where M is magnetization, H is the applied magnetic field and Ms is the saturation value of the magnetization. .... 29
1-3	Representation of (a) the $[\text{Mn}_{12}\text{O}_{12}]^{16+}$ core and (b) the $[\text{Mn}_{12}\text{O}_{12}(\text{O}_2\text{CMe})_{16}(\text{H}_2\text{O})_4]$ complex with peripheral ligation. $\text{Mn}^{\text{IV}}$ orange; $\text{Mn}^{\text{III}}$ green; O red; C gray. .... 29
1-4	Representative plots of the potential energy versus (a) the orientation of the ms vector ( $\theta$ ) along the z axis and (b) the ms sublevel for an $\text{Mn}_{12}$ complex with an S = 10 ground state, experiencing zero-field splitting. .... 30
1-5	In-phase (as $\chi_M''$ ) and out-of-phase (as $\chi_M'$ ) AC susceptibility signals for a dried, microcrystalline sample of $[\text{Mn}_{12}\text{O}_{12}(\text{O}_2\text{CR})_{16}(\text{H}_2\text{O})_4]$ at the indicated oscillation frequencies. .... 30
1-6	Magnetization hysteresis loops for a typical $[\text{Mn}_{12}\text{O}_{12}(\text{O}_2\text{CR})_{16}(\text{H}_2\text{O})_4]$ complex in the 1.3-3.6 K temperature range at a 4 mT/s field sweep rate. M is normalized to its saturation value, Ms. .... 31
1-7	Representation of the change in energy of ms sublevels as the magnetic field is swept from zero to a non-zero value. Resonant magnetization tunneling occurs when the ms sublevels are aligned between the two halves of the diagram. .... 31
2-1	The structure of 2-(hydroxymethyl)pyridine (hmpH)..... 54
2-2	The structure of complex <b>2-1</b> (top) and a stereopair (bottom). Hydrogen atoms have been omitted for clarity. Color code: $\text{Fe}^{\text{III}}$ green; O red; N, blue; C grey. .... 55
2-3	The fully labeled core of complex <b>2-1</b> . Color code: $\text{Fe}^{\text{III}}$ green; O red. .... 56
2-4	The structure of complex <b>2-2</b> (top) and a stereopair (bottom). Hydrogen atoms have been omitted for clarity. Color code: $\text{Fe}^{\text{III}}$ green; O red; N, blue; C grey. .... 57
2-5	The structure of complex <b>2-3</b> (top), a stereopair (bottom), and the labeled core. Hydrogen atoms have been omitted for clarity. Color code: $\text{Fe}^{\text{III}}$ green; O red; N, blue; C grey. .... 58
2-6	Plot of $\chi_M T$ vs T for complex <b>2-1</b> . .... 59
2-7	Plot of $\chi_M T$ vs T for complex <b>2-2</b> . .... 59

2-8	Plot of $\chi_M T$ vs T for complex <b>2-3</b> . The solid line is the fit of the data; see the text for the fit parameters. ....	60
2-9	Reduced magnetization ( $M/N\mu_B$ ) vs H/T plot for complex <b>2-1</b> . The solid lines are the fit of the data; see the text for the fit parameters. ....	61
2-10	Two-dimensional contour plot of the root-mean-square error surface for the $D$ vs $g$ fit for complex <b>2-1</b> . ....	61
2-11	Reduced magnetization ( $M/N\mu_B$ ) vs H/T plot for complex <b>2-2</b> . The solid lines are the fit of the data; see the text for the fit parameters. ....	62
2-12	Two-dimensional contour plot of the root-mean-square error surface for the $D$ vs $g$ fit for complex <b>2-2</b> . ....	62
2-13	In-phase ac susceptibility ( $\chi_M'$ , plotted as $\chi_M' T$ vs T) of complex <b>2-1</b> in a 3.5 Oe ac field oscillating at the indicated frequencies. ....	63
2-14	In-phase ac susceptibility ( $\chi_M'$ , plotted as $\chi_M' T$ vs T) of complex <b>2-2</b> in a 3.5 Oe ac field oscillating at the indicated frequencies. ....	63
2-15	Scheme presenting a continuum of spin coupling values and spin alignments between completely satisfied situation and completely frustrated situation for an antiferromagnetically coupled pathway: see the text for details. ....	64
2-16	Diagrammatic scheme of the core structures of complex <b>2-1</b> , presenting the ZILSH exchange constants $J$ and the spin coupling $\hat{S}_A \cdot \hat{S}_B$ for each Fe-Fe pathway and rationalizing the $S = 3$ ground state of <b>2-1</b> : see the text for details. ....	65
2-17	Mapping of the possible $S_T$ values of <b>2-1</b> with various $J_{13}$ and $J_{23}$ values, presenting the influence of lowering of the symmetry of the triangular unit on the spin of the ground state. ....	66
3-1	Structure of ligand: 2,6-pyridinedimethanol (pdmH <sub>2</sub> ). ....	90
3-2	Summary of the reactions concerning <b>3-1</b> , <b>3-2</b> and <b>3-3</b> . ....	91
3-3	The structure of complex <b>3-1</b> (top), a stereopair (middle), and the labeled core. Hydrogen atoms have been omitted for clarity. Color code: Fe <sup>III</sup> green; O red; N blue; C gray. ....	92
3-4	The structure of complex <b>3-3</b> (top), a stereopair (middle), and the labeled core. Hydrogen atoms have been omitted for clarity. Color code: Fe <sup>III</sup> green; O red; N blue; C gray. ....	93
3-5	The structure of complex <b>3-4</b> (top), and a stereopair (bottom), viewed along the ab-plane. Hydrogen atoms have been omitted for clarity. Color code: Fe <sup>III</sup> green; O red; N blue; C grey. ....	94

3-6	The structure of complex <b>3-4</b> (top), and its labeled core (bottom), viewed along the b-axis. Hydrogen atoms have been omitted for clarity. Color code: Fe <sup>III</sup> green; O red; N blue; C grey. ....	95
3-7	Plot of $\chi_M T$ vs T for complex <b>3-1</b> . ....	96
3-8	Plot of $\chi_M T$ vs T for complex <b>3-3</b> . ....	96
3-9	Plot of $\chi_M T$ vs T for complex <b>3-4</b> . ....	97
3-10	Reduced magnetization ( $M/N\mu_B$ ) vs H/T plot for complex <b>3-3</b> . The solid lines are the fit of the data; see the text for the fit parameters. ....	97
3-11	Two-dimensional contour plot of the root-mean-square error surface for the $D$ vs $g$ fit for complex <b>3-3</b> . ....	98
3-12	Reduced magnetization ( $M/N\mu_B$ ) vs H/T plot for complex <b>3-4</b> . The solid lines are the fit of the data; see the text for the fit parameters. ....	98
3-13	Two-dimensional contour plot of the root-mean-square error surface for the $D$ vs $g$ fit for complex <b>3-4</b> . ....	99
3-14	In-phase ac susceptibility ( $\chi_M'$ , plotted as $\chi_M' T$ vs T) of complex <b>3-3</b> in a 3.5 Oe ac field oscillating at the indicated frequencies. ....	99
3-15	In-phase ac susceptibility ( $\chi_M'$ , plotted as $\chi_M' T$ vs T) of complex <b>3-4</b> in a 3.5 Oe ac field oscillating at the indicated frequencies. ....	100
3-16	Rationalization of the $S = 5/2$ ground state of <b>3-4</b> , on the basis of the predicted magnitudes of the various pairwise $J_{ij}$ exchange constants and the resulting spin frustration effects; frustrated interactions are shown in blue. The viewpoint and atom labels are those of Figure 3-6 (bottom). ....	101
3-17	(a) Angle-dependent HFEPN spectra ( $2^\circ$ steps) for complex <b>3-4</b> obtained at 8 K and 91.3 GHz. The red traces correspond to the hard planes of two crystals in the twinned sample (see main text). (b) Plot of the peak positions associated with the highest field doublet observed in (a); see main text for explanation. ....	102
3-18	91.3 GHz temperature dependent HFEPN spectra for complex <b>3-4</b> with the applied field aligned closer to the easy-axes of the two crystals in comparison to the data in Figure 3-17. The labels $\alpha$ and $\beta$ differentiate resonances originating from the two crystals in the twinned sample; for some of the peaks, subscripts are included with the label indicating the approximate magnitude of ms associated with the level from which the transition is excited. ....	103
3-19	Frequency dependence of the HFEPN peak positions for complex <b>3-4</b> corresponding to the same field orientation as the spectra displayed in Figure 3-17. The red and blue squares correspond the $\alpha$ and $\beta$ resonances, respectively. Meanwhile, the red and	

	blue curves represent the corresponding best simulations of the frequency dependence; see text for further explanation. ....	104
4-1	Structure of ligands: 2-(hydroxymethyl)pyridine (hmpH), 2-(pyridine-2-yl)propan-2-ol (dmhmpH), and diphenyl (pyridine-2-yl)methanol (dphmpH).....	143
4-2	A picture of crystals of <b>4-1</b> .....	144
4-3	A picture of crystals of <b>4-2</b> .....	144
4-4	A picture of crystals of <b>4-3</b> .....	144
4-5	A picture of crystals of <b>4-4</b> .....	145
4-6	A picture of crystals of <b>4-5</b> .....	145
4-7	A picture of crystals of <b>4-6</b> .....	145
4-8	The structure of complex <b>4-1</b> , with core Mn–O bonds shown in purple. Hydrogen atoms and methyl groups on pivalates have been omitted for clarity. Color code: Mn <sup>III</sup> green; O red; N blue; C gray.....	146
4-9	The structure of complex <b>4-8</b> , with core Mn–O bonds shown in purple. Hydrogen atoms and methyl groups on pivalates have been omitted for clarity. Color code: Mn <sup>III</sup> green; O red; N blue; C gray.....	146
4-10	The structure of complex <b>4-2</b> with the Mn <sup>III</sup> Jahn–Teller elongation axes shown as yellow bonds (top), and a stereopair (bottom). Hydrogen atoms have been omitted for clarity. Color code: Mn <sup>III</sup> green; O red; N blue; C gray.....	147
4-11	The structure of complex <b>4-3</b> with intramolecular hydrogen-bonds shown as dashed lines (top), and a stereopair (bottom). Hydrogen atoms and benzoate phenyl rings (except for the ipso carbon atoms) have been omitted for clarity. Color code: Mn <sup>II</sup> yellow; Mn <sup>III</sup> green; O red; N blue; C gray. ....	148
4-12	The fully labeled core of complex <b>4-3</b> . Color code: Mn <sup>II</sup> yellow; Mn <sup>III</sup> green; O red; C gray.....	149
4-13	The structure of complex <b>4-4</b> with intramolecular hydrogen-bonds shown as dashed lines (top), and a stereopair The thicker orange bonds indicate the positions of the Mn <sup>III</sup> Jahn–Teller elongation axes. Hydrogen atoms and methyl groups on pivalate groups have been omitted for clarity. Color code: Mn <sup>II</sup> yellow; Mn <sup>III</sup> green; O red; N blue; C grey. ....	150
4-14	The fully labeled core of complex <b>4-4</b> . Color code: Mn <sup>II</sup> yellow; Mn <sup>III</sup> green; O red.....	151
4-15	The structure of complex <b>4-5</b> with intramolecular hydrogen-bonds shown as dashed lines (top), and a stereopair (bottom). Hydrogen atoms and phenyl rings (except for	

	the ipso carbon atoms) on benzoate groups have been omitted for clarity. Color code: Mn <sup>II</sup> yellow; Mn <sup>III</sup> green; O red; C gray; N blue.....	152
4-16	The fully labeled core of complex <b>4-5</b> . Color code: Mn <sup>II</sup> yellow; Mn <sup>III</sup> green; O red; C gray.....	153
4-17	The structure of complex <b>4-6</b> (top), a stereopair (middle), and the labeled core (bottom). The thicker orange bonds indicate the positions of the Mn <sup>III</sup> Jahn–Teller elongation axes. Hydrogen atoms have been omitted for clarity. Color code: Mn <sup>III</sup> green; O red; C gray; N blue; Na Purple. ....	154
4-18	1 D chain of complex <b>4-6</b> viewed perpendicular (top) and parallel (bottom) to c-axis. Hydrogen atoms have been omitted for clarity. Mn <sup>III</sup> green; O red; C gray; N blue; Na Purple .....	155
4-19	Plots of $\chi_{MT}$ vs. T for complexes <b>4-1</b> .....	156
4-20	Plots of $\chi_{MT}$ vs. T for complexes <b>4-2</b> .....	156
4-21	Plots of $\chi_{MT}$ vs. T for complexes <b>4-3</b> .....	157
4-22	Plots of $\chi_{MT}$ vs. T for complexes <b>4-4</b> .....	157
4-23	Plots of $\chi_{MT}$ vs. T for complexes <b>4-5</b> .....	158
4-24	Plots of $\chi_{MT}$ vs. T for complexes <b>4-6</b> . The solid line is the fit of the data; see the text for the fit parameters .....	158
4-25	Mn labeling scheme employed in eq.4-7.....	159
4-26	Plots of reduced magnetization ( $M/N\mu_B$ ) vs H/T for complex <b>4-5</b> . The solid lines are the fit of the data; see the text for the fit parameters.....	160
4-27	Two-dimensional contour plot of the root-mean-square error surface for the D vs g fit for complex <b>4-5</b> . ....	160
4-28	Plots of reduced magnetization ( $M/N\mu_B$ ) vs H/T for complex <b>4-6</b> . The solid lines are the fit of the data; see the text for the fit parameters.....	161
4-29	Two-dimensional contour plot of the root-mean-square error surface for the D vs g fit for complex <b>4-6</b> . ....	161
4-30	AC susceptibility of complex <b>4-2</b> in a 3.5 G field oscillating at the indicated frequencies: (top) in-phase signal ( $\chi_M'$ ) plotted as $\chi_M'T$ vs T; and (bottom) out-of-phase signal $\chi_M''$ vs T. ....	162

4-31	AC susceptibility of complex <b>4-3</b> in a 3.5 G field oscillating at the indicated frequencies: (top) in-phase signal ( $\chi_M'$ ) plotted as $\chi_M' T$ vs T; and (bottom) out-of-phase signal $\chi_M''$ vs T. ....	163
4-32	In-phase ac susceptibility ( $\chi_M'$ , plotted as $\chi_M' T$ vs T) of complex <b>4-4</b> in a 3.5 G ac field oscillating at the indicated frequencies. ....	164
4-33	AC susceptibility of complex <b>4-5</b> in a 3.5 G field oscillating at the indicated frequencies: (top) in-phase signal ( $\chi_M'$ ) plotted as $\chi_M' T$ vs T; and (bottom) out-of-phase signal $\chi_M''$ vs T. ....	165
4-34	In-phase ac susceptibility ( $\chi_M'$ , plotted as $\chi_M' T$ vs T) of complex <b>4-6</b> in a 3.5 G ac field oscillating at the indicated frequencies. ....	166
4-35	Single-crystal magnetization (M) vs dc field (H) hysteresis loops for a single crystal of <b>4-5</b> ·3CH <sub>2</sub> Cl <sub>2</sub> at different scan rates (top) and temperatures (bottom). ....	167
5-1	Structure of ligands: 2-(hydroxymethyl)pyridine (hmpH) and phenyldipyridin-2-ylmethanol (pdpmH). ....	185
5-2	The structure of complex <b>5-1</b> (top), and a stereopair (bottom). The thicker yellow bonds indicate the positions of the Mn <sup>III</sup> Jahn–Teller elongation axes. Hydrogen atoms have been omitted for clarity. Color code: Mn <sup>III</sup> green; Mn <sup>IV</sup> orange; O red; N blue; C grey. ....	186
5-3	Space-filling diagram of <b>5-1</b> ; sideview (top), topview (middle), and a stereoview (bottom), emphasizing the sterically hindered positioning of the unbound pyridine groups. Color code: Mn <sup>III</sup> green; Mn <sup>IV</sup> orange; O red; N blue; C grey. ....	187
5-4	The structure of complex <b>5-2</b> (top), and a stereopair (bottom). Hydrogen atoms have been omitted for clarity. Color code: Mn <sup>II</sup> yellow; Mn <sup>III</sup> green; O red; N blue; C grey..	188
5-5	The labeled core of complex <b>5-2</b> . Color code: Mn <sup>II</sup> yellow; Mn <sup>III</sup> green; O red; C grey.....	189
5-6	Cyclic voltammogram at glassy carbon electrode of complex <b>5-1</b> in CH <sub>2</sub> Cl <sub>2</sub> containing 0.1M NBu <sup>n</sup> <sub>4</sub> PF <sub>6</sub> and ferrocene as an internal standard.....	190
5-7	Cyclic voltammogram of <b>5-1</b> at different scan rates. ....	191
5-8	Plot of the square root of the scan rate, $v^{1/2}$ vs the anodic peak current, $i_a$ for the oxidation process in Figure <b>5-7</b> . ....	191
5-9	Plot of $\chi_M T$ vs T for complex <b>5-1</b> . The solid line is the fit of the data; see the text for the fit parameters.....	192
5-10	Plot of $\chi_M T$ vs T for complex <b>5-2</b> . ....	192

5-11	Plots of reduced magnetization ( $M/N\mu_B$ ) vs $H/T$ for complex <b>5-2</b> . The solid lines are the fit of the data; see the text for the fit parameters.....	193
5-12	Two-dimensional contour plot of the root-mean-square error surface for the $D$ vs $g$ fit for complex <b>5-2</b> . .....	194
5-13	In-phase ac susceptibility ( $\chi_M'$ , plotted as $\chi_M'T$ vs $T$ ) of complex <b>5-2</b> in a 3.5 Oe ac field oscillating at the indicated frequencies. ....	195

## LIST OF ABBREVIATIONS

Bu <sup>t</sup>	tertiary butyl
BVS	bond valence sum
CV	cyclic voltammogram
dphmpH	diphenyl (pyridine-2-yl)methanol
dmpH	2-(pyridine-2-yl)propan-2-ol
hmpH	2-hydroxymethyl pyridine
HFEPR	high Frequency electron paramagnetic resonance
pdmH <sub>2</sub>	2,6-pyridine dimethanol
pdpmH	phenyldipyridin-2-ylmethanol
Py	pyridine
TIP	temperature independent paramagnetism
ZFS	zero-field splitting

Abstract of Dissertation Presented to the Graduate School  
of the University of Florida in Partial Fulfillment of the  
Requirements for the Degree of Doctor of Philosophy

A MOLECULAR APPROACH TO NANOSCALE MAGNETIC MATERIALS:  
NEW IRON AND MANGANESE CLUSTERS FROM THE USE OF PYRIDYL ALCOHOLS

By

Taketo Taguchi

December 2009

Chair: George Christou  
Major: Chemistry

Polynuclear transition metal clusters have been of great interest primarily due to their relevance in molecular magnetism and bioinorganic chemistry, as well as their aesthetically pleasing structures. A particularly appealing area in molecular magnetism is the study of single-molecule magnets (SMMs) which possess a significant energy barrier to relaxation of their magnetization vector and thus function as monodisperse, nanoscale magnetic particles below their blocking temperature. This work focuses on the preparation and characterization of polynuclear iron and manganese clusters as new nanoscale magnetic materials.

Non-carboxylate Fe<sup>III</sup> cluster chemistry has been explored in the presence of the bidentate N,O ligand, the anion of 2-hydroxymethylpyridine (hmp<sup>-</sup>), and it has proven to be a useful route to new Fe<sup>III</sup> clusters spanning Fe<sub>4</sub> and Fe<sub>6</sub> nuclearities and topologies that are both very rare. Of these, the Fe<sub>6</sub> complex displayed a counterintuitive  $S = 3$  ground state spin value, and it was rationalized by semiempirical theoretical calculations using ZILSH methods.

A non-carboxylate approach for Fe<sup>III</sup> cluster synthesis was further explored in the presence of the tridentate O,N,O group, 2,6-pyridinedimethanol (pdmH<sub>2</sub>), and it has led to the isolation of new Fe<sub>8</sub> non-carboxylate cluster products with an unprecedented topology, and with an  $S = 0$  ground state spin. The reactivity of these Fe<sub>8</sub> clusters was explored, and this revealed that they

transform to an Fe<sub>18</sub> product under mild hydrolysis. The Fe<sub>18</sub> product shows an unprecedented metal topology and an  $S = 4$  ground state spin, and is the highest nuclearity non-carboxylate Fe<sup>III</sup> cluster discovered to date. Apart from the non-carboxylate Fe<sup>III</sup> chemistry, the reactions of pdmH<sub>2</sub> in the presence of carboxylate were also explored, and led to the isolation of a new Fe<sub>9</sub> product with a prototypical structure, and with a ground state spin of 5/2. The latter was rationalized on the basis of the exchange interactions predicted from magnetostructural correlations. The combined results demonstrate the versatility of pdmH<sub>2</sub> to give new high nuclearity products, and show that the presence and absence of carboxylates can have a marked effect on the obtained products.

In the development of new synthetic routes to polynuclear metal clusters, the choice of the ligands has always been a key issue. In order to provide a new ligand design strategy for the isolation of novel clusters, the introduction of two bulky phenyl or methyl groups onto the CH<sub>2</sub> group of hmpH was investigated. The use of diphenyl-hmpH (dphmpH) has led to the isolation of Mn<sub>4</sub>, Mn<sub>6</sub>, and Mn<sub>11</sub> products with very rare or prototypical structures, and with  $S = 0, 3,$  and  $5/2$  ground state spin values, respectively. These clusters are distinctly different from those obtained previously with hmpH itself, and it is also seen that dphmp<sup>-</sup> prefers to bind as a bidentate chelate, disfavoring the bridging modes favored by hmp<sup>-</sup>. It was concluded that the two phenyl groups had almost completely removed the ability of the alkoxide O atom to bridge, and thus dphmp<sup>-</sup> primarily functions as a bidentate chelate. This was rationalized as a combination of the steric bulk of the two phenyl groups, as well as their electron-withdrawing effect on the O atom. The less-bulky dimethyl-hmpH (dmhmpH) was then employed in order to switch back on the bridging modes as a result of both the smaller size of methyl groups and their electron-donating rather than electron-withdrawing character, while still hopefully providing sufficient

steric differences with  $\text{hmp}^-$  to lead to new products. This hope was fulfilled, with  $\text{dmhmp}^-$  acting as a perturbed  $\text{hmp}^-$ ; that is, it functioned as a chelating and bridging ligand, as does  $\text{hmp}^-$ , but it yielded products that are structurally distinct from any seen previously in  $\text{Mn}/\text{hmp}^-$  chemistry. The resulting  $\text{Mn}/\text{dmhmp}^-$  products,  $\text{NaMn}_6$ ,  $\text{Mn}_7$ , and  $\text{Mn}_{12}$ , show very rare or prototypical structures and significant ground state spin values of  $S = 12$ ,  $7/2$ , and  $13/2$ , respectively. In addition, the  $\text{Mn}_{12}$  proved to be a new SMM, as confirmed by single-crystal micro-SQUID studies.

As an expansion of this ligand design strategy, a potentially tridentate ligand phenyldipyridine-2-ylmethanol ( $\text{pdpmH}$ ), in which one phenyl and one pyridyl groups were added onto the  $\text{CH}_2$  unit of  $\text{hmpH}$ , was employed and successfully led to novel  $\text{Mn}_4$  and  $\text{Mn}_7$  clusters. Interestingly, the potentially tridentate ligand  $\text{pdpmH}$  mainly acts as a bidentate ligand. The reluctance of  $\text{pdpm}^-$  to serve as a tridentate ligand is found to be due to the nearby steric bulk of the phenyl and pyridyl groups. Magnetochemical characterization revealed that the  $\text{Mn}_4$  and  $\text{Mn}_7$  have ground state spin values of  $S = 0$  and  $29/2$ , respectively. The combined results demonstrate the usefulness and potential of a ligand design strategy in the synthesis of a variety of new metal clusters.

## CHAPTER 1 GENERAL INTRODUCTION

Coordination chemistry is of interest from a variety of disciplines, including bioinorganic chemistry, supramolecular chemistry, and material sciences. This thesis work focuses on the preparation and characterization of new iron and manganese complexes especially with respect to their relevance in magnetic materials research.

Magnetism is one of the fundamental properties of matter, and the utilization of magnetic materials has been central to technological development.<sup>1</sup> The magnetic field associated with a magnetic substance is the result of an electrical charge in motion, specifically, the spin and orbital angular momenta of electrons within atoms of a material. While all matter is composed of atoms containing one or more electrons, only a small handful of materials behave as magnets. In most substances, atoms have closed electron shells; i.e., electrons with magnetic fields aligned in opposite directions are paired with each other. Such materials with no magnetic moment are called diamagnets.<sup>2,3</sup> Hence, the crucial element that distinguishes a magnetic substance, or a paramagnet, from a diamagnet is the existence of a magnetic moment that arises from at least one unpaired electron.

The various types of magnetic materials are grouped according to their response or susceptibility,  $\chi$ , to an applied magnetic field. The electron pairs of a diamagnet interact with an applied field, generating a repulsive field that weakly repels the diamagnet from the applied field; the sign of  $\chi$  is negative. In contrast, a paramagnet is attracted to an applied magnetic field; the sign of  $\chi$  is positive. The strength of the attraction is governed both by the number of unpaired electrons in the material as well as the nature of the interactions of its electron spins.<sup>1,4</sup> Both the temperature dependence as well as the absolute magnitude of  $\chi$  are distinguishing measures of the various types of paramagnetism.<sup>6</sup> Simple paramagnetic behavior is observed in

substances in which the magnetic moments of unpaired electrons are independent of each other. In the absence of a magnetic field, individual magnetic moments are randomly oriented. As a field is applied, the moments align parallel, albeit weakly, to the field; this alignment is opposed by the randomizing effect of thermal energy (Figure 1-1). The susceptibility of these materials is inversely proportional to temperature as defined by the Curie Law ( $\chi = C/T$ ), where  $C$  is the Curie constant.<sup>2-7</sup> There are other paramagnetic materials, however, that display a temperature dependence unlike that of a simple paramagnet. In these substances, the individual magnetic moments interact so that all the unpaired electrons align in the same direction: such species are called ferromagnets. In contrast, some materials contain unpaired electrons interacting in such a way that the spins align in an antiparallel fashion (i.e., pointing in opposite directions): these materials are called antiferromagnets, if the individual spins all have the same magnitude and there is no net magnetic moment, or ferrimagnets, if the interacting spins have different magnitudes and thus there is a net magnetic moment.<sup>1-7</sup> Examples of ferromagnets include iron, cobalt, nickel, and several rare earth metals and their alloys, while magnetite,  $\text{Fe}_3\text{O}_4$ , is a ferrimagnet.

Ferro-, antiferro-, and ferrimagnetic ordering occurs below a critical temperature,  $T_c$ . Below  $T_c$ , the magnetic moments for ferro- and ferrimagnets align in small domains. In the absence of an applied magnetic field, despite the nature of interactions, a net zero magnetization is thermodynamically favored, as different domains have their net magnetizations randomly oriented. The application of a strong magnetic field induces the alignment of all of the domains with the field and hence, with each other, imparting a net magnetization to the material. As alignment occurs, the interaction of spins becomes sufficiently strong to overcome dipole interactions and entropy considerations that maintain the random alignment of the domains.<sup>5, 7</sup>

When a magnetic field is applied and then removed at a temperature below  $T_c$ , the magnetization induced by the field does not entirely disappear and in some cases can remain equal to the field-induced magnetization. This is in contrast to the behavior observed for paramagnetic systems, in which the spins immediately randomly reorient following removal of the field. Because an additional field is required to reverse the direction of the magnetization, magnetic storage of information is possible in particles of ferromagnetic or ferrimagnetic materials. This behavior is observed in the classical hysteresis behavior of magnets (Figure 1-2).<sup>4, 6, 7</sup>

In order to achieve the storage of greater quantities of digital information on smaller surface areas, the development of magnetic particles of nanoscale dimensions is necessary. One approach towards this end involves the fragmentation of bulk ferromagnets or ferrimagnets such as ferro-spinels. For example, crystals of magnetite can be broken down such that each fragment is smaller in size than a single domain (20-200 nm); these nanoscale magnetic particles are known as superparamagnets. The magnetic moments within one superparamagnetic particle are ferrimagnetically aligned due to short-range order. Alignment of the superparamagnets is induced by the application of a magnetic field, resulting in remnant magnetization. The reversal of the magnetization direction of a single domain requires energy to overcome the crystal field anisotropy. Hence, slow magnetization relaxation is not related to domain formation as with a traditional ferromagnet but rather involves an energy barrier that arises in part from the magnetic anisotropy associated with the shape of the particles. Providing no control in size versus properties and a non-uniform response to an applied field, the major drawback of this approach is the wide distribution of particle sizes that results from fragmentation.

Another approach toward the preparation of nanoscale magnetic materials is called bottom-up approach, which is based on the syntheses of molecule-based magnets. In 1967, it was

discovered that the compound  $[\text{Fe}^{\text{III}}(\text{S}_2\text{CNEt}_2)\text{Cl}]$  behaves as a ferromagnet at 2.46 K due to intermolecular interactions.<sup>7-9</sup> Since then, chemists have been synthesizing a wide variety of such molecule-based magnets using paramagnetic molecular units. They are 1-, 2-, or 3-D lattices of interacting molecular units, which are synthesized from single molecules and selected bridging groups. Advantages of this approach include low density, low temperature processability, solubility, and others.<sup>10-11</sup>

A very specific case within the area of molecule-based magnets is the zero-dimensional nanoscale magnets, called single-molecule magnets (SMMs), which are individual molecules capable of functioning as nanoscale magnetic particles.<sup>12, 13</sup> Such molecules behave as magnets below their blocking temperature ( $T_B$ ), exhibiting hysteresis in magnetization versus dc field scans. The first molecule proven to show such behavior was  $[\text{Mn}_{12}\text{O}_{12}(\text{O}_2\text{CMe})_{16}(\text{H}_2\text{O})_4]$  (**1-1**) with a ground state spin value ( $S_T$ ) equal to 10 (Figure 1-3).<sup>14-17</sup> While the properties of common molecule-based magnets are due to long-range interaction between individual units, the behavior of an SMM is intrinsic to the molecule. To be a single-molecule magnet, a molecule must have a large ground-state spin ( $S_T$ ) and a significant anisotropy of the easy axis (Ising) type, which is reflected in a large and negative zero-field splitting parameter ( $D$ ). In the dodecanuclear complex **1-1**, the large ground state spin arises from exchange interactions between the  $S = 3/2$  spins of the  $\text{Mn}^{\text{IV}}$  ions and the  $S = 2$  spins of the  $\text{Mn}^{\text{III}}$  ions. The anisotropy of a cluster is primarily a consequence of the single-ion anisotropies of the constituent ions within the cluster and of the relative orientations of the magnetic axes of these ions with respect to each other. The significant anisotropy of the complex **1-1** is resulted from the approximately parallel alignment of the Jahn-Teller elongation axes of the eight  $\text{Mn}^{\text{III}}$  ions.

The combination of a negative easy-axis type magnetic anisotropy along with a large ground-state spin results in the splitting of the ground state spin into  $2S_T+1$  sublevels. Since  $D$  is negative, the larger  $|m_s|$  states lie lower in energy (Figure 1-4). To reverse the spin of the molecule from along the  $-z$  (spin up) to the  $+z$  (spin down) axis of the molecule, a potential energy barrier must be overcome. The height of the energy barrier ( $\Delta E$ ) for the reversal of magnetization direction is given by  $S^2 |D|$  for integer spins and  $(S^2-1/4) |D|$  for half-integer spins. Experimental evidence for this behavior is supported by the appearance of frequency-dependent signals ( $\chi_M''$  signals) in out-of-phase AC magnetic susceptibility measurements, as shown in Figure 1-5, and of hysteresis loops in magnetization versus DC field scans (Figure 1-6).

One of the unique magnetic behaviors of SMMs is seen in the appearances of steps in the hysteresis loops. Instead of the the above-mentioned thermal activation over the energy barrier (classical mechanism), the spin reversal can also occur by tunneling through the energy barrier. Such tunneling, called quantum tunneling of the magnetization (QTM), was first reported in 1996 for molecules of **1-1**.<sup>18</sup> The observed steps correspond to an increase in the relaxation rate of magnetization that occurs when there is an energy coincidence of  $m_s$  sublevels on the opposite sides of the potential energy barrier (Figure 1-7). For these critical field values,  $H = nD/g\mu_B$ , at which steps occur, QTM is allowed, resulting in an increase in the relaxation rate of the molecule.<sup>18-21</sup>

For the continuing interest in understanding this new magnetic phenomenon of single-molecule magnetism, and in finding other compounds that exhibit similar properties, numerous synthetic strategies aimed at the improvement of these materials have been considered. However, in contrast to the relative ease with which synthetic routes are developed in other fields of chemistry, the preparation of polynuclear metal complexes presents a considerable challenge.

One of the primary goals of this research is the development of new synthetic methods aimed at the preparation of new polynuclear metal complexes. In the following chapters, several new synthetic strategies to prepare polynuclear transition metal clusters, as well as a new concept in the ligand design, are described. These preparative methodologies have led to the isolation of novel complexes that exhibit very rare or unprecedented metal topologies and interesting magnetic properties. The synthesis, structure, and characterization of these compounds will be discussed.

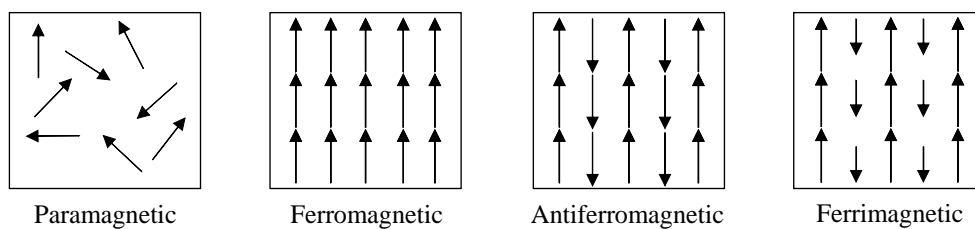


Figure1-1. Representations of magnetic dipole arrangements in (i) paramagnetic, (ii) ferromagnetic, (iii) antiferromagnetic, and (iv) ferrimagnetic materials.

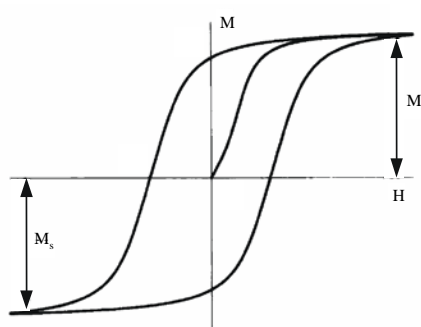


Figure 1-2. Typical hysteresis loop of a magnet, where  $M$  is magnetization,  $H$  is the applied magnetic field and  $M_s$  is the saturation value of the magnetization.

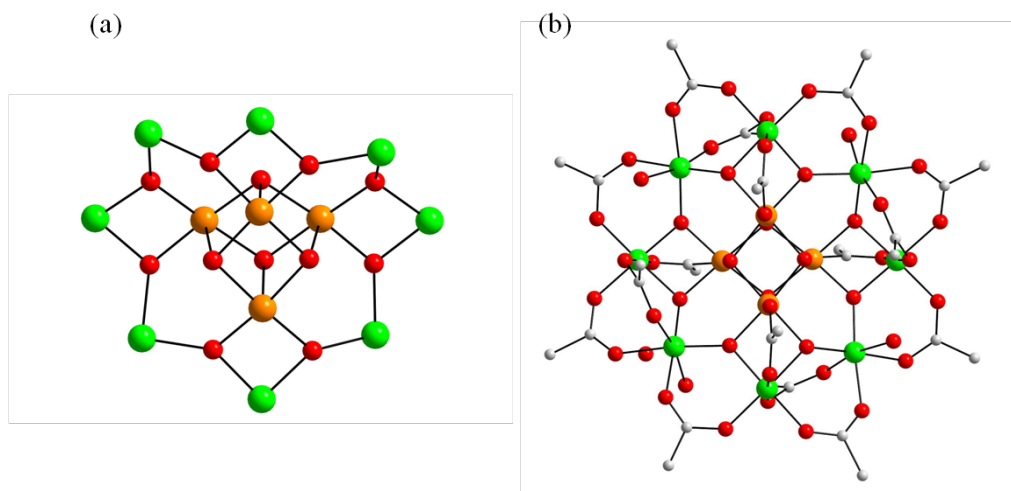


Figure 1-3. Representation of (a) the  $[\text{Mn}_{12}\text{O}_{12}]^{16+}$  core and (b) the  $[\text{Mn}_{12}\text{O}_{12}(\text{O}_2\text{CMe})_{16}(\text{H}_2\text{O})_4]$  complex with peripheral ligation.  $\text{Mn}^{\text{IV}}$  orange;  $\text{Mn}^{\text{III}}$  green; O red; C gray.

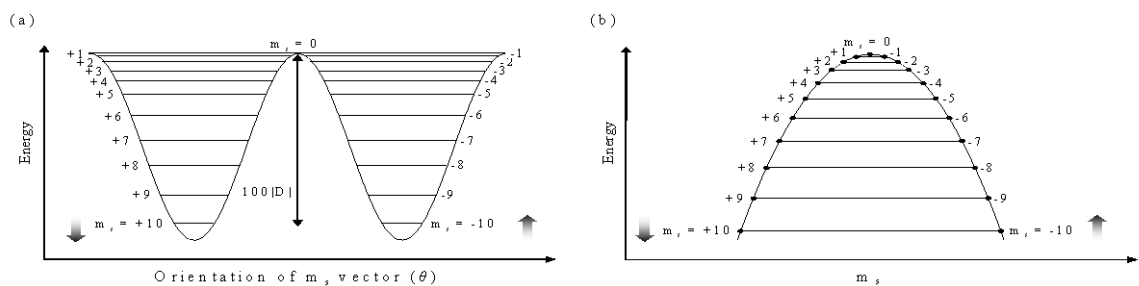


Figure 1-4. Representative plots of the potential energy versus (a) the orientation of the  $m_s$  vector ( $\theta$ ) along the  $z$  axis and (b) the  $m_s$  sublevel for an  $Mn_{12}$  complex with an  $S = 10$  ground state, experiencing zero-field splitting.

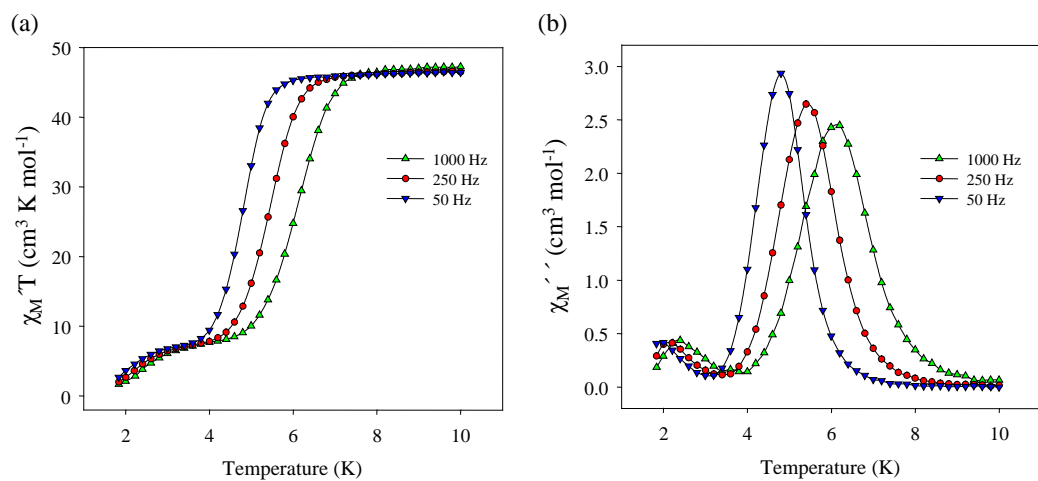


Figure 1-5. In-phase (as  $\chi_M''$ ) and out-of-phase (as  $\chi_M'''$ ) AC susceptibility signals for a dried, microcrystalline sample of  $[Mn_{12}O_{12}(O_2CR)_{16}(H_2O)_4]$  at the indicated oscillation frequencies.

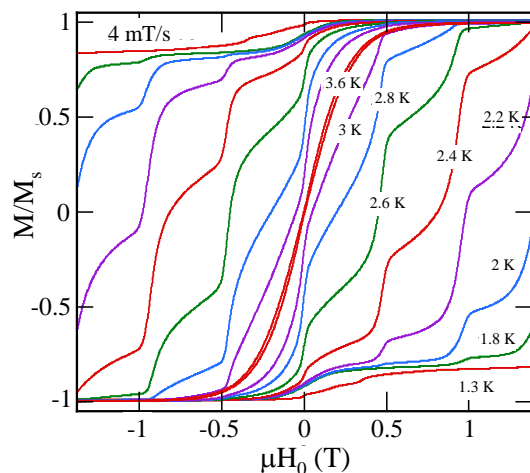


Figure 1-6. Magnetization hysteresis loops for a typical  $[\text{Mn}_{12}\text{O}_{12}(\text{O}_2\text{CR})_{16}(\text{H}_2\text{O})_4]$  complex in the 1.3-3.6 K temperature range at a 4 mT/s field sweep rate.  $M$  is normalized to its saturation value,  $M_s$ .

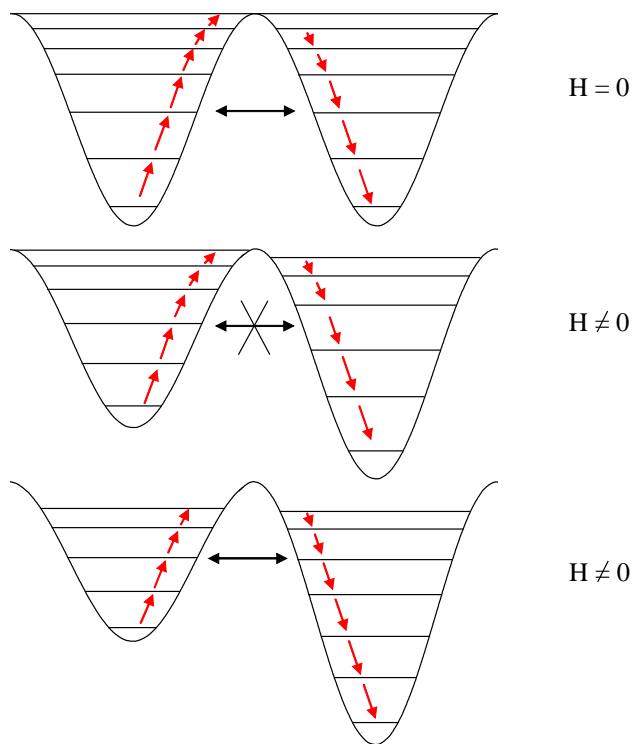


Figure 1-7. Representation of the change in energy of  $m_s$  sublevels as the magnetic field is swept from zero to a non-zero value. Resonant magnetization tunneling occurs when the  $m_s$  sublevels are aligned between the two halves of the diagram.

CHAPTER 2  
NEW TETRA AND HEXANUCLEAR IRON CLUSTERS FROM THE USE OF 2-  
(HYDROXYMETHYL)PYRIDINE

**2.1 Introduction**

The last two decades have witnessed an explosive growth in the interest in polynuclear iron<sup>III</sup> compounds with primarily oxygen-based ligation. This has been mainly due to their relevance to two fields, bioinorganic chemistry and molecular magnetism, as well as the intrinsic architectural beauty and aesthetically pleasing structures they possess. Iron-oxo centers are found in several non-heme metalloproteins. Hemerythrin, ribonucleotide reductase, and methane monooxygenase are examples of enzymes with diiron metallosites,<sup>22-24</sup> whereas the protein ferritin, which is responsible for iron storage, can accommodate up to ~4500 iron ions in an iron/oxide/hydroxide core.<sup>25-29</sup> A number of polynuclear iron complexes have thus been synthesized and studied as possible models for ferritin to gain insights into the biomineralization process involved in the formation of its metal core.<sup>30-32</sup> In the area of magnetism, high-spin iron<sup>III</sup> ions have a relatively large number of unpaired electrons ( $d^5$ ,  $S = 5/2$ ) and normally undergo strong, antiferromagnetic exchange interactions. With high enough  $Fe_x$  nuclearities and the appropriate topologies, these compounds can sometimes possess large ground-state spin ( $S$ ) values and can even occasionally function as single-molecule magnets (SMMs).<sup>13, 33, 34</sup> The latter are molecules that display slow magnetization relaxation rates and which, below a certain (blocking) temperature ( $T_B$ ), can function as single-domain magnetic particles of nanoscale dimensions.<sup>35, 36</sup> Such SMMs thus represent a molecular, “bottom-up” approach to nanomagnetism.<sup>35</sup> Although exchange interactions between  $Fe^{III}$  centers are essentially always antiferromagnetic, certain  $Fe_x$  topologies can nevertheless result in large spin ground states because of spin frustration effects. Spin frustration is defined here in its general sense as the occurrence of competing exchange interactions of comparable magnitude that prevent (frustrate)

the preferred spin alignments.<sup>37-39</sup> For example, in certain topologies the spins of two antiferromagnetically coupled metal ions (or other spin carriers) may be forced into a parallel alignment by other, stronger interactions; thus, the intrinsic preference of the spins to align antiparallel is frustrated. A sufficient quantity and distribution of frustrated exchange pathways in some  $\text{Fe}_x$  topologies can lead to the significantly large values of the total molecular spin mentioned above, even when all the pairwise  $\text{Fe}_2$  exchange interactions are antiferromagnetic. Thus, we continue to have a great interest in rationalizing and understanding the exchange interactions and the resulting ground state  $S$  of polynuclear  $\text{Fe}^{\text{III}}$  molecules.

For the above reasons, we continue to seek synthetic methods to new  $\text{Fe}_x$  complexes. One approach that has proven successful is the use of alcohol-containing chelates. On deprotonation, these will provide alkoxide groups, which are excellent bridging units that can foster formation of high nuclearity products.<sup>40-43</sup> We have a particular fondness for pyridyl alcohols, especially 2-(hydroxymethyl)pyridine (hmpH, Figure 2-1), which have proven to be versatile chelating and bridging groups that have yielded several polynuclear  $3d$  metal clusters with large  $S$  values<sup>44, 45</sup> and SMM behavior.<sup>46-53</sup> However, in  $\text{Fe}^{\text{III}}$  chemistry there has been only very limited use of hmpH.<sup>54, 55</sup> Even for the previously reported  $\text{Fe}^{\text{III}}$  clusters with pyridyl-alkoxide groups, the majority also contain carboxylate groups as a result of the use of triangular  $[\text{Fe}_3\text{O}(\text{O}_2\text{CR})_6(\text{L})_3]^+$  compounds as reagents, a common strategy in both  $\text{Fe}^{\text{III}}$  and  $\text{Mn}^{\text{III}}$  chemistry.<sup>56-62</sup> While carboxylates ( $\text{RCO}_2^-$ ) are excellent bridging groups in  $\text{Fe}^{\text{III}}$  chemistry,<sup>63</sup> in the present chapter we report some results from a recent investigation of non-carboxylate  $\text{Fe}^{\text{III}}$  cluster chemistry, which have led to new  $\text{Fe}_4$  and  $\text{Fe}_6$  products. We describe the syntheses, structures, and magnetochemical characterization of these complexes, as well as theoretical rationalization of the experimental observations.

## 2.2 Experimental Section

### 2.2.1 Syntheses

All manipulations were performed under aerobic conditions using chemicals and solvents as received unless otherwise stated. *Safety note: Azide salts are potentially explosive; such compounds should be synthesized and used in small quantities and treated with utmost care at all times.*

**[Fe<sub>6</sub>O<sub>2</sub>(hmp)<sub>10</sub>(H<sub>2</sub>O)<sub>2</sub>](NO<sub>3</sub>)<sub>4</sub> (2-1).** To a stirred solution of hmpH (0.48 mL, 5.0 mmol) and NEt<sub>3</sub> (0.14 mL, 1.0 mmol) in MeCN (30 mL) was added solid Fe(NO<sub>3</sub>)<sub>3</sub>·9H<sub>2</sub>O (0.40 g, 1.0 mmol). The resulting brown solution was stirred for 1 h and filtered, and the filtrate was layered with Et<sub>2</sub>O/ hexanes (1:1, v/v). After 2 days, large brown crystals of **2-1**·8MeCN were collected by filtration, washed with cold MeCN (2 × 5 mL) and Et<sub>2</sub>O (2 × 5 mL), and dried under vacuum; the yield was ~55%. Anal. Calcd (Found) for **2-1**·1MeCN: C, 41.99 (41.63); H, 3.81 (3.73); N, 11.85 (12.11). Selected IR data (KBr, cm<sup>-1</sup>): 1608(m), 1570(w) 1483(w), 1483(m), 1439(m), 1383(s), 1355(s), 1285(m), 1221(w), 1156(w), 1079(m), 1050(m), 1019(w), 828(w), 764(m), 718(m), 675(m), 646(m), 528(m), 444(w), 410(w).

**[Fe<sub>6</sub>O<sub>2</sub>(hmp)<sub>8</sub>(NO<sub>3</sub>)<sub>4</sub>(H<sub>2</sub>O)<sub>2</sub>](NO<sub>3</sub>)<sub>2</sub> (2-2).** To a stirred solution of hmpH (0.29 mL, 3.0 mmol) and NEt<sub>3</sub> (0.14 mL, 1.0 mmol) in MeCN (30 mL) was added solid Fe(NO<sub>3</sub>)<sub>3</sub>·9H<sub>2</sub>O (0.40 g, 1.0 mmol). The resulting brown solution was stirred for 1 h and filtered, and the filtrate was layered with Et<sub>2</sub>O (30 mL). After 2 days, large brown crystals of **2-2**·6MeCN were collected by filtration, washed with cold MeCN (2 × 5 mL) and Et<sub>2</sub>O (2 × 5 mL), and dried under vacuum; the yield was ~60%. Anal. Calcd (Found) for **2-2** (solvent-free): C, 35.15 (35.03); H, 3.20 (3.05); N, 11.96 (11.68). Selected IR data (cm<sup>-1</sup>): 3418 (mb), 1608 (m), 1570 (w), 1483 (w), 1439 (m), 1383 (s), 1285 (m), 1221 (w), 1156 (w), 1075 (m), 1049 (m), 1022 (w), 826 (w), 763 (m), 719 (m), 677 (m), 647 (m), 530 (m), 459 (w), 412 (w).

**[Fe<sub>4</sub>(N<sub>3</sub>)<sub>6</sub>(hmp)<sub>6</sub>] (2-3)**. To a stirred solution of hmpH (0.29 mL, 3.0 mmol) and NEt<sub>3</sub> (0.14 mL, 1.0 mmol) in a solvent mixture comprised of MeCN/MeOH (30 mL, 5:1 v/v) was added solid Fe(NO<sub>3</sub>)<sub>3</sub>·9H<sub>2</sub>O (0.40 g, 1.0 mmol). The resulting brown solution was stirred for 1 h, during which time solid NaN<sub>3</sub> (0.20 g, 3.0 mmol) was added in small portions. The resulting dark red solution was stirred for a further 3 h and filtered, and the filtrate was layered with Et<sub>2</sub>O (30 mL). After 6 days, dark red crystals of **2-3**·2MeOH were collected by filtration, washed with cold MeCN (2 × 5 mL) and Et<sub>2</sub>O (2 × 5 mL), and dried under vacuum; the yield was ~50%. Anal. Calcd (Found) for **2-3** (solvent-free): C, 38.46 (38.73); H, 3.23 (3.07); N, 29.90 (29.49). Selected IR data (cm<sup>-1</sup>): 3419 (mb), 2077 (s), 2052 (s), 1607 (m), 1568 (w), 1482 (m), 1433 (m), 1355 (m), 1287 (m), 1220 (w), 1154 (w), 1085 (m), 1060 (m), 1047 (m), 821 (w), 764 (m), 721 (m), 667 (m), 647 (m), 513 (m), 474 (w), 420 (m).

### 2.2.2 X-Ray Crystallography

Data were collected on a Siemens SMART PLATFORM equipped with a CCD area detector and a graphite monochromator utilizing Mo K $\alpha$  radiation ( $\lambda = 0.71073 \text{ \AA}$ ). Suitable crystals of **2-1**·8MeCN, **2-2**·6MeCN, and **2-3**·2MeOH were attached to glass fibers using silicone grease and transferred to a goniostat where they were cooled to 173 K for data collection. An initial search of reciprocal space revealed a monoclinic cell for **2-1**·8MeCN and **2-3**·2MeOH, and a triclinic cell for **2-2**·6MeCN; the choices of space groups  $C2/c$  (for **2-1**·8MeCN),  $P\bar{1}$  (for **2-2**·6MeCN), and  $P2_1/c$  (for **2-3**·2MeOH) were confirmed by the subsequent solution and refinement of the structures. Cell parameters were refined using up to 8192 reflections. A full sphere of data (1850 frames) was collected using the  $\omega$ -scan method (0.3° frame width). The first 50 frames were remeasured at the end of data collection to monitor instrument and crystal stability (maximum correction on I was <1%). Absorption corrections by integration were

applied based on measured indexed crystal faces. The structures were solved by direct methods in SHELXTL6,<sup>64</sup> and refined on  $F^2$  using full-matrix least-squares. The non-H atoms were treated anisotropically, whereas the H atoms were placed in calculated, ideal positions and refined as riding on their respective C atoms. Unit cell parameters and structure solution and refinement data are listed in Table 2-1.

For **2-1**·8MeCN, the asymmetric unit consists of a half  $\text{Fe}_3$  cluster, two  $\text{NO}_3^-$  anions, four MeCN molecules one of which is disordered over two positions. The pyridyl group is disordered and was refined in two parts with their site occupation factors dependently refined. The coordinated protons were obtained from a difference Fourier map and refined freely but with their thermal parameters fixed at 1.5 that of the oxygen atom. Atom O3 did not refine properly anisotropically thus its anisotropic parameters were constrained to be equivalent to O1. A total of 611 parameters were refined in the final cycle of refinement using 19774 reflections with  $I > 2\sigma(I)$  to yield  $R_1$  and  $wR_2$  of 7.33 and 17.75%, respectively.

For **2-2**·6MeCN, the asymmetric unit consists of half of the  $\text{Fe}_6$  cation, one  $\text{NO}_3^-$  anion, and three disordered MeCN molecules of crystallization. The latter could not be modeled properly; thus the program SQUEEZE,<sup>65</sup> a part of the PLATON package of crystallographic software, was used to calculate the solvent disorder area and remove its contribution to the overall intensity data. One coordinated  $\text{NO}_3^-$  (monodentate) has all three O atoms disordered while the second (also monodentate) has only two O atoms disordered, with the third O being common to both parts. A total of 447 parameters were included in the structure refinement using 8212 reflections with  $I > 2\sigma(I)$  to yield  $R_1$  and  $wR_2$  of 4.11 and 10.05%, respectively.

For **2-3**·2MeOH, the asymmetric unit consists of half of the  $\text{Fe}_4$  cluster and a MeOH molecule of crystallization disordered near an inversion center. The azide ligand consisting of

atoms N10-N11-N12 is disordered, and the N11-N12 segment was refined in two parts with their site occupation factors dependently refined. A total of 332 parameters were included in the structure refinement using 5769 reflections with  $I > 2\sigma(I)$  to yield  $R_1$  and  $wR_2$  of 4.82 and 11.56%, respectively.

### 2.2.3 Other Studies

Infrared spectra were recorded in the solid state (KBr pellets) on a Nicolet Nexus 670 FTIR spectrometer in the 400–4000  $\text{cm}^{-1}$  range. Elemental analyses (C, H, and N) were performed by the in-house facilities of the University of Florida Chemistry Department. Variable-temperature dc and ac magnetic susceptibility data were collected at the University of Florida using a Quantum Design MPMS-XL SQUID susceptometer equipped with a 7 T magnet and operating in the 1.8–300 K range. Samples were embedded in solid eicosane to prevent torquing. Magnetization versus field and temperature data were fit using the program MAGNET.<sup>66</sup> Pascal's constants were used to estimate the diamagnetic corrections, which were subtracted from the experimental susceptibilities to give the molar paramagnetic susceptibilities ( $\chi_M$ ). The exchange interactions in **2-3** were calculated by Dr. Ted A. O'Brien at Department of Chemistry and Chemical Biology, Indiana University-Purdue University Indianapolis (IUPUI), using matrix diagonalization methods described elsewhere.<sup>67</sup>

### 2.2.4 Theoretical Calculations

Semiempirical calculations were performed at IUPUI using the ZILSH method<sup>67, 68</sup> to analyze the exchange interactions underlying the magnetic properties observed for complex **2-1**. These calculations take place in several stages. First, energies and spin couplings are computed for a set of spin component wavefunctions using the intermediate neglect of differential overlap spectroscopic (INDO/S) model of Zerner<sup>69, 70</sup> and the local spin operator of Davidson.<sup>71, 72</sup>

Estimates of the exchange constants  $J_{AB}$  that appear in the Heisenberg spin Hamiltonian (HSH) of eq.2-1, where  $\hat{H}_0$  contains all spin-independent terms,

$$\hat{H} = \hat{H}_0 - 2 \sum_{A<B} J_{AB} \hat{S}_A \cdot \hat{S}_B \quad (2-1)$$

are then obtained from these quantities by simultaneous solution of eq.2-2,

$$E_i = E_0 - 2 \sum_{A<B} J_{AB} \langle \hat{S}_A \cdot \hat{S}_B \rangle^i \quad (2-2)$$

which to a good approximation, give the energies of the spin components and the actual spin states of the complex.<sup>73</sup> In the second stage, the exchange constants are adjusted using a genetic algorithm fitting method<sup>68</sup> to more closely reproduce the experimentally measured variable temperature magnetic susceptibility of the complex. In the third and final stage, the exchange constants found in the second stage are substituted into the Heisenberg spin Hamiltonian, which is diagonalized in a basis of spin component to yield the final energies and wavefunctions of the spin states.

One important quantity that can be calculated from the wavefunctions is the spin coupling  $\langle \hat{S}_A \cdot \hat{S}_B \rangle$  for each pair of metal ions. These values are useful for identifying exchange pathways that are spin frustrated.<sup>73, 74</sup> The spin coupling indicates the actual alignment of  $z$  components  $S_{z,A}$  and  $S_{z,B}$  in the state, while the exchange constant  $J_{AB}$  indicates the preferred alignment. Any pathway with  $\langle \hat{S}_A \cdot \hat{S}_B \rangle$  and  $J_{AB}$  of different signs is thus frustrated under the  $-2J$  convention. This is used to describe the spin interactions in the ground state of **2-1** (vide infra).

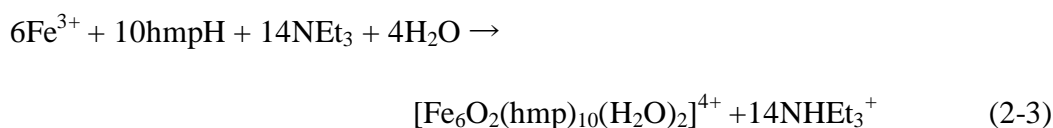
## 2.3 Results and Discussion

### 2.3.1 Syntheses

As stated earlier, the present study arose as part of our investigation of the reactions of hmpH with Fe<sup>III</sup> sources in the absence of carboxylate groups. We have in some cases also added

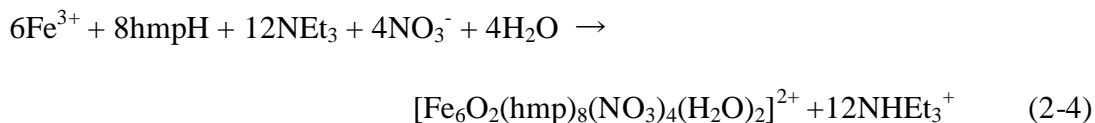
a source of azides, which are also excellent bridging ligands and can foster the formation of high nuclearity products.<sup>75</sup>

Various reactions have been systematically explored by differing reagent ratios, reaction solvents, and other conditions before the following successful procedures were identified. The reaction of  $\text{Fe}(\text{NO}_3)_3 \cdot 9\text{H}_2\text{O}$  with hmpH and  $\text{NEt}_3$  in a 1:5:1 molar ratio in MeCN gave a brown solution and the subsequent isolation of well-formed brown crystals of  $[\text{Fe}_6\text{O}_2(\text{hmp})_{10}(\text{H}_2\text{O})_2](\text{NO}_3)_4 \cdot 8\text{MeCN}$  (**2-1**·8MeCN) in high yields (~55%). The formation of **2-1** is summarized in eq 2-3. Note that the  $\text{NEt}_3$  has the role of proton acceptor to facilitate both the



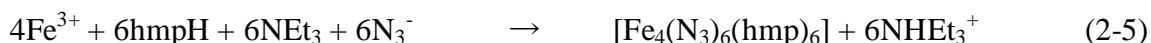
deprotonation of the hmpH groups and  $\text{H}_2\text{O}$  molecules as a source of the bridging  $\text{O}_2^-$  ions; although the excess of hmpH employed could in principle also carry out these roles, the yield of complex **2-1** was only ~5% in the absence of  $\text{NEt}_3$ . However, when more than 1 equiv of  $\text{NEt}_3$  was used, insoluble amorphous precipitates that were probably polymeric were rapidly formed.

In contrast, a decrease in the amount of hmpH from 5 to 3 equiv (or less) did not give **2-1**, but the similar product  $[\text{Fe}_6\text{O}_2(\text{hmp})_8(\text{NO}_3)_4(\text{H}_2\text{O})_2](\text{NO}_3)_2$  (**2-2**·6MeCN) in high yields (~60%). The formation of **2-2** is summarized in eq. 2-4.



Complexes **2-1** and **2-2** were also obtained using other reaction solvents (i.e., MeOH,  $\text{CH}_2\text{Cl}_2$ ), but the yields were appreciably lower and the crystalline precipitate was found to be contaminated with some other solid products.

The addition of 3 equiv of NaN<sub>3</sub> to the reaction mixture that yields **2-2**, but in a MeCN/MeOH solvent mixture to aid solubility, gave a deep red solution and subsequent isolation of [Fe<sub>4</sub>(N<sub>3</sub>)<sub>6</sub>(hmp)<sub>6</sub>] $\cdot$ 2MeOH (**2-3 $\cdot$ 2MeOH) in yields of ~50%. The formation of **2-3** is summarized in eq. 2-5. Increasing the amount of sodium azide still gave complex **2-3**, but the**



reaction was not so clean and the yield was appreciably lower. With the identity of **2-3** established, we also tried several other Fe<sup>3+</sup>/hmpH/NEt<sub>3</sub>/N<sub>3</sub><sup>-</sup> ratios, and particularly with a large excess of FeX<sub>3</sub> (X = Cl<sup>-</sup>, NO<sub>3</sub><sup>-</sup>, ClO<sub>4</sub><sup>-</sup>), to see if higher nuclearity azide-containing products might be obtained, but in all cases complex **2-3** was the isolated product, in varying yields. As for **2-1** and **2-2**, the NEt<sub>3</sub> was again essential to obtain **2-3** in good yields and too much NEt<sub>3</sub> also again gave insoluble powders, which formed rapidly from the reaction solution.

### 2.3.2 Description of Structures

The partially labeled structure and a stereoview of the cation of [Fe<sub>6</sub>O<sub>2</sub>(hmp)<sub>10</sub>(H<sub>2</sub>O)<sub>2</sub>](NO<sub>3</sub>)<sub>4</sub> (**2-1**) are shown in Figure 2-2, and its labeled core in Figure 2-3; selected interatomic distances and angles are listed in Table A-1.

Complex **2-1** crystallizes in monoclinic space group *C2/c* and displays crystallographic *C*<sub>2</sub> symmetry; the asymmetric unit therefore contains only half of the Fe<sub>6</sub> cation, two NO<sub>3</sub><sup>-</sup> anions, and four lattice MeCN molecules. The structure comprises six Fe atoms in a chair conformation. This can be described as a central Fe<sub>4</sub> rectangle (Fe1, Fe1', Fe2, Fe2') with two additional Fe atoms Fe3 and Fe3' at two opposite ends and 1.398(2) Å above and below the central Fe<sub>4</sub> plane. However, a better description of the structure is as two triangular [Fe<sub>3</sub>(μ<sub>3</sub>-O<sup>2-</sup>)] units joined together at two of their apices; each connection Fe1/Fe2' and Fe1'/Fe2 is by two bridging hmp<sup>-</sup> alkoxo groups. Each [Fe<sub>3</sub>(μ<sub>3</sub>-O<sup>2-</sup>)] triangular unit is essentially isosceles (Fe1...Fe3 = 3.064(2) Å,

Fe2...Fe3 = 3.030(2) Å, Fe1...Fe2 = 3.671(2) Å) and essentially planar (the oxide is only 0.004 Å from the Fe3 plane), and the  $\mu_3$ -oxide has Y-shaped geometry with the largest angle Fe1-O3-Fe2 being 153.7(3)°. The two equivalent sides of each isosceles triangle are bridged by an alkoxide O atom of an hmp<sup>-</sup> group that chelates to a basal Fe atom. The ligation is completed by a chelating hmp<sup>-</sup> group on each apical Fe atom Fe3 and Fe3', each of the latter also possessing a terminal H<sub>2</sub>O ligand. All the Fe atoms are six-coordinate with distorted octahedral geometries. The distortions at the four central Fe atoms are particularly pronounced, with angles at *cis* and *trans* ligands ranging from 73.2(2) to 111.6(2)°, and 148.7(2) to 167.6(2)°, respectively. The NO<sub>3</sub><sup>-</sup> counterions are hydrogen-bonded to the terminal water groups on Fe3 and Fe3' (O7...O63 = 2.668(8) Å, O7...O73 = 2.685(8) Å).

The partially labeled structure and a stereoview of the cation of [Fe<sub>6</sub>O<sub>2</sub>(hmp)<sub>8</sub>(NO<sub>3</sub>)<sub>4</sub>-(H<sub>2</sub>O)<sub>2</sub>](NO<sub>3</sub>)<sub>2</sub> (**2-2**) are shown in Figure 2-4; selected interatomic distances and angles are listed in Table A-2. The structure of **2-2** is very similar to **2-1**, with the difference being the two chelating hmp<sup>-</sup> groups in **2-1** have been replaced by four terminal NO<sub>3</sub><sup>-</sup> groups in **2-2**. Complex **2-2** crystallizes in triclinic space group  $P\bar{1}$  and displays crystallographic *C<sub>i</sub>* symmetry. The core of the molecule again comprises two triangular [Fe<sub>3</sub>( $\mu_3$ -O<sup>2-</sup>)] units joined together at two of their apices; each connection Fe1/Fe2' and Fe1'/Fe2 by two bridging hmp<sup>-</sup> alkoxo groups. Each [Fe<sub>3</sub>( $\mu_3$ -O<sup>2-</sup>)] triangular unit is essentially isosceles (Fe1...Fe3 = 3.127(5) Å, Fe2...Fe3 = 3.095(3) Å, Fe1...Fe2 = 3.648(3) Å) and essentially planar (the oxide is only 0.004 Å from the Fe<sub>3</sub> plane), and the  $\mu_3$ -oxide has Y-shaped geometry with the largest angle Fe1-O3-Fe2 being 149.1(1)°. The two equivalent sides of each isosceles triangle are bridged by an alkoxide O atom of an hmp<sup>-</sup> group that chelates to a basal Fe atom. The ligation is completed by two monodentate NO<sub>3</sub><sup>-</sup> groups on each apical Fe atom Fe3 and Fe3', each of the latter also possessing a terminal H<sub>2</sub>O

ligand. All the Fe atoms are six-coordinate with distorted octahedral geometries. The distortions at the four central Fe atoms are particularly pronounced, with angles at *cis* and *trans* ligands ranging from 72.6(8) to 114.9(8)° and 147.5(8) to 173.3(8)°, respectively. The NO<sub>3</sub><sup>-</sup> counterions are hydrogen-bonded to the terminal water groups on Fe3 and Fe3' (O6...O15 = 2.689(2) Å, O6...O14 = 2.672(2) Å) and serve to bridge separate Fe<sub>6</sub> molecules in the crystal.

There are several structural types of Fe<sup>III</sup><sub>6</sub> clusters previously reported in the literature, differing in the Fe<sub>6</sub> topology. These have been conveniently referred to as (a) planar,<sup>55, 67, 76-79</sup> (b) twisted-boat,<sup>57, 80-84</sup> (c) chair-like,<sup>55</sup> (d) parallel triangles,<sup>85-88</sup> (e) octahedral,<sup>89-92</sup> (f) fused or extended butterflies,<sup>60, 61, 73, 93-100</sup> (g) cyclic,<sup>101-106</sup> and (h) linked-triangles.<sup>107-109</sup> As can be anticipated, these different Fe<sub>6</sub> topologies have led to a variety of ground-state spin *S* values among these complexes, spanning *S* = 0, 1, 3, and 5. There is only one known example of an Fe<sup>III</sup><sub>6</sub> complex of class (c), i.e. possessing a chair-like Fe<sub>6</sub> topology; [Fe<sub>6</sub>O<sub>2</sub>Cl<sub>4</sub>(hmp)<sub>8</sub>](ClO<sub>4</sub>)<sub>2</sub> (**2-4**).<sup>55</sup> The structure of complex **2-4** is very similar to that of **2-1**, except that the end Fe atoms Fe3 and Fe3' of **2-1** each possess a chelating hmp<sup>-</sup> and a terminal H<sub>2</sub>O, whereas these atoms in **2-4** each possess only two terminal Cl<sup>-</sup> ions and are thus five-coordinate.

The partially labeled structure, a stereoview, and the labeled core of [Fe<sub>4</sub>(N<sub>3</sub>)<sub>6</sub>(hmp)<sub>6</sub>] (**2-3**) are shown in Figure 2-5; selected interatomic distances and angles are given in Table A-3. Complex **2-3**·2MeOH crystallizes in the monoclinic space group *P2<sub>1</sub>/c* with the Fe<sub>4</sub> molecule lying on an inversion center. The molecule comprises a nonlinear array of four Fe<sup>III</sup> atoms (Fe2-Fe1-Fe1' = 129.73°) with each Fe<sub>2</sub> pair bridged by the alkoxide arms of two chelating hmp<sup>-</sup> groups. There is thus a total of six η<sup>1</sup>:η<sup>2</sup>:μ hmp<sup>-</sup> groups, and peripheral ligation is completed by six terminal azide groups, three each on the two end Fe atoms Fe2 and Fe2'. The central Fe1-O2-Fe1'-O2' rhombus is strictly planar as a result of the inversion center, and the other two rhombi

are nearly so, with the Fe1-O1-Fe2-O3 torsion angle being 5.2°. The Fe<sup>III</sup> atoms are both six-coordinate with distorted octahedral geometry, with Fe1 having the greater distortion from ideal geometry. The Fe-N and Fe-O bond lengths are as expected for high-spin iron<sup>III</sup>.<sup>98, 110, 111</sup>

There have been a large number of Fe<sub>4</sub> complexes reported in the literature, and these possess a wide variety of metal topologies such as rectangles, rhombs, butterflies, etc.<sup>112, 113</sup> However, the only previous Fe<sub>4</sub> compounds with a similar kind of extended, chain-like topology as in **2-3** and an [Fe<sub>4</sub>(μ-OR)<sub>6</sub>]<sup>6+</sup> core are [Fe<sub>4</sub>{(py)<sub>2</sub>C(OMe)O}<sub>2</sub>{(Hpy)(py)C(OMe)O}<sub>2</sub>(dbcat)<sub>4</sub>]<sup>2+</sup> (**2-5**)<sup>114</sup> (dbcat<sup>2-</sup> is 3,5-di-*t*-butylcatecholate) and [Fe<sub>4</sub>(OH)<sub>2</sub>(rac-arabitol)<sub>4</sub>]<sup>6-</sup>.<sup>115</sup>

### 2.3.3 Magnetochemistry

#### 2.3.3.1 Direct current magnetic susceptibility studies

Variable-temperature magnetic susceptibility measurements were performed on dried polycrystalline samples of complex **2-1**·MeCN, **2-2**, and **2-3**, restrained in eicosane to prevent torquing, in a 1 kG (0.1 T) field and in the 5.0-300 K range. For **2-1**,  $\chi_M T$  steadily decreases from 9.16 cm<sup>3</sup>mol<sup>-1</sup>K at 300 K to a near-plateau value of ~6.10 cm<sup>3</sup>mol<sup>-1</sup>K at 45-20 K and then further decreases to 5.64 cm<sup>3</sup>mol<sup>-1</sup>K at 5.0 K (Figure 2-6). The 300 K value is much less than the spin-only ( $g = 2$ ) value of 26.25 cm<sup>3</sup>mol<sup>-1</sup>K for six non-interacting Fe<sup>III</sup> ions, indicating the presence of strong antiferromagnetic interactions, as expected for oxo-bridged Fe<sup>III</sup> systems. The  $\chi_M T$  near-plateau value in the 20-45 K range appears to be heading for a final value of ~6 cm<sup>3</sup>mol<sup>-1</sup>K, the spin-only ( $g = 2$ ) value of a species with an  $S = 3$  ground state, before exhibiting the final decrease at temperatures below 10 K. The latter decrease is likely due to a combination of Zeeman effects from the applied dc field, zero-field splitting (ZFS), and any weak intermolecular antiferromagnetic exchange interactions.

For **2-2**,  $\chi_M T$  steadily decreases from 9.79 cm<sup>3</sup>mol<sup>-1</sup>K at 300 K to a near-plateau value of ~6.80 cm<sup>3</sup>mol<sup>-1</sup>K at 50-15 K and then slightly decreases to 6.43 cm<sup>3</sup>mol<sup>-1</sup>K at 5.0 K (Figure 2-7).

The 300 K value is again much less than the spin-only ( $g = 2$ ) value of  $26.25 \text{ cm}^3\text{mol}^{-1}\text{K}$  for six non-interacting  $\text{Fe}^{\text{III}}$  ions. The 5.0 K value is close to the spin-only ( $g = 2$ ) value of a complex with an  $S = 3$  ground state.

For **2-3**,  $\chi_M T$  steadily decreases from  $12.56 \text{ cm}^3\text{Kmol}^{-1}$  at 300 K to  $0.56 \text{ cm}^3\text{Kmol}^{-1}$  at 5.0 K (Figure 2-8). Again, the 300 K value is much less than the spin-only ( $g = 2$ ) value of  $17.50 \text{ cm}^3\text{Kmol}^{-1}$  for four non-interacting  $\text{Fe}^{\text{III}}$  ions, indicating the presence of strong antiferromagnetic exchange interactions, and the 5.0 K value indicates an  $S = 0$  ground state.

To confirm the indicated  $S_T = 3$  ground state of complex **2-1** and **2-2**, and to estimate the magnitude of the zero-field splitting parameter  $D$ , magnetization vs dc field measurements were made on restrained samples at applied magnetic fields and temperatures in the 1–70 kG and 1.8–10.0 K ranges, respectively. The resulting data for **2-1** are shown in Figure 2-9 as a reduced magnetization ( $M/N\mu_B$ ) vs  $H/T$  plot, where  $M$  is the magnetization,  $N$  is Avogadro's number,  $\mu_B$  is the Bohr magneton, and  $H$  is the magnetic field. The data were fit using the program MAGNET,<sup>66</sup> by diagonalization of the spin Hamiltonian matrix assuming only the ground state is populated, incorporating axial anisotropy ( $D\hat{S}_z^2$ ) and Zeeman terms, and employing a full powder average. The corresponding spin Hamiltonian is given by eq. 2-6, where  $\hat{S}_z$  is the easy-axis spin operator,  $g$  is the Landé  $g$  factor and  $\mu_0$  is the vacuum permeability.

$$\mathcal{H} = D\hat{S}_z^2 + g\mu_B\mu_0\hat{S}\cdot H \quad (2-6)$$

The best fit for **2-1**·MeCN is shown as the solid lines in Figure 2-9 and was obtained with  $S = 3$  and either of the two sets of parameters:  $g = 1.94$  and  $D = +0.78 \text{ cm}^{-1}$ , or  $g = 1.96$  and  $D = -0.62 \text{ cm}^{-1}$ . Alternative fits with  $S = 2$  or 4 were rejected because they gave unreasonable values of  $g$ . It is common to obtain two acceptable fits of magnetization data for a given  $S$  value, one with  $D > 0$  and the other with  $D < 0$ , since magnetization fits are not very sensitive to the sign of

*D*. In order to assess which is the superior fit and also to ensure that the true global minimum had been located, we calculated the root-mean-square *D* vs *g* error surface for the fits using the program GRID,<sup>116</sup> which calculates the relative difference between the experimental  $M/N\mu_B$  data and those calculated for various combinations of *D* and *g*. The error surface is shown as a two-dimensional contour plot in Figure 2-10 and it clearly shows only two minima, with positive and negative *D* values, with the latter being superior quality and thus suggesting the true sign of *D* for **2-1**·MeCN is negative, but a more reliable and accurate determination of the sign and magnitude of *D* requires use of a more sensitive technique such as EPR spectroscopy.

The best fit for **2-2** is shown as the solid lines in Figure 2-11 and was obtained with  $S = 3$  and either of the two sets of parameters:  $g = 2.07, D = 0.57 \text{ cm}^{-1}$  and  $g = 2.08, D = -0.44 \text{ cm}^{-1}$ . Alternative fits with  $S = 2$  or  $4$  were rejected because they gave unreasonable values of *g*. The error surface for **2-2** is shown as a two-dimensional contour plot in Figure 2-12, and it shows only the two minima with positive and negative *D* values, with the latter being of superior quality and thus suggesting the true sign of *D* is negative.

Given the small size of complex **2-3**, the susceptibility data to 300 K were fit by a matrix diagonalization method described elsewhere<sup>67</sup> to obtain the individual pairwise exchange constants  $J_{ij}$  between Fe atoms  $\text{Fe}_i$  and  $\text{Fe}_j$ . The isotropic Heisenberg spin Hamiltonian that is appropriate for centrosymmetric complex **2-3** is given in eq. 2-7. Three parameters were employed in the fit: exchange constants  $J_1$  and  $J_2$  for the two outer (Fe1-Fe2 and Fe1'-Fe2') and

$$\mathcal{H} = -2J_1(\hat{S}_1 \cdot \hat{S}_2 + \hat{S}_1 \cdot \hat{S}_2') - 2J_2(\hat{S}_1 \cdot \hat{S}_1') - 2J_3(\hat{S}_1 \cdot \hat{S}_1' + \hat{S}_2 \cdot \hat{S}_2') \quad (2-7)$$

one central (Fe1-Fe1') interactions and the *g* factor. The next-nearest neighbor interactions  $J_3$  were assumed to be zero. A temperature-independent paramagnetism (TIP) term was kept

constant at  $800 \times 10^{-6} \text{ cm}^3 \text{ K mol}^{-1}$ . The fit (solid line in Figure 2-8) gave  $J_1 = -9.2 \text{ cm}^{-1}$ ,  $J_2 = -12.5 \text{ cm}^{-1}$ , and  $g = 2.079$ . Similar values of  $J_1 = -4.8 \text{ cm}^{-1}$  and  $J_2 = -13.0 \text{ cm}^{-1}$  were reported for **2-5**.<sup>114</sup>

As expected, the interactions between the  $\text{Fe}^{\text{III}}$  centers in **2-3** are strongly anti-ferromagnetic, resulting in a ground-state spin of  $S = 0$ . The latter is again as expected for a “linear” array of four  $\text{Fe}^{\text{III}}$  atoms, since the constituent exchange interactions  $J_1$  and  $J_2$  are not competing, and  $J_3 \approx 0$ ; thus there are no spin frustration effects in this complex.

### 2.3.3.2 Alternating current magnetic susceptibility studies

As an additional, independent assessment of the ground state  $S$  value, we collected ac susceptibility data on **2-1**·MeCN and **2-2** in the 1.8-10 K range using a 3.5 G ac field oscillating at frequencies in the 50-1000 Hz range. If the magnetization vector can relax fast enough to keep up with the oscillating field, then there is no imaginary (out-of-phase) susceptibility signal ( $\chi''_{\text{M}}$ ), and the real (in-phase) susceptibility ( $\chi'_{\text{M}}$ ) is equal to the dc susceptibility. However, if the barrier to magnetization relaxation is significant compared to thermal energy ( $kT$ ), then there is a non-zero  $\chi''_{\text{M}}$  signal and the in-phase signal decreases. In addition, the  $\chi'_{\text{M}}$  and  $\chi''_{\text{M}}$  signals will be frequency-dependent. The main advantage of ac studies in the present case is that no dc field is used. This precludes problems arising from a dc field, such as the stabilization of  $M_S$  levels of low-lying excited spin  $S$  states with an  $S$  greater than that of the ground state, and thus their approach (and even crossing) in energy with ground state  $M_S$  levels. Since our fits of dc magnetization data assumed that only the ground state  $M_S$  levels are populated, this Zeeman effect involving excited states could give erroneous estimates of the ground state. The obtained in-phase  $\chi'_{\text{M}}$  signal for **2-1**·MeCN is plotted as  $\chi'_{\text{M}}T$  in Figure 2-13, and can be seen to be almost temperature-independent, decreasing only slightly with temperature below 10 K, before decreasing a bit more rapidly below  $\sim 4$  K. Extrapolating to 0 K the data from above 4 K (to avoid lower temperature effects from the slight anisotropy and weak intermolecular interactions)

gives a value of 5.8-5.9 cm<sup>3</sup>Kmol<sup>-1</sup> range, which is consistent with an  $S = 3$  ground state and  $g < 2$ , in excellent agreement with the dc magnetization fits. We conclude that complex **2-1** does indeed have an  $S = 3$  ground state. There is no out-of-phase ac susceptibility signal down to 1.8 K, the operating limit of our SQUID magnetometer.

For complex **2-2**, the in-phase  $\chi'_{MT}$  signal below 10 K is almost temperature independent (Figure 2-14), and extrapolation of the plot to 0 K from above 4 K gives a value of ~6.4 cm<sup>3</sup>Kmol<sup>-1</sup> range. This indicates an  $S = 3$  ground state and  $g \sim 2.07$ , in excellent agreement with the dc magnetization fit. There is no out-of-phase ac susceptibility signal down to 1.8 K, the operating limit of our SQUID magnetometer.

Complex **2-1** and **2-2** are thus confirmed to possess an  $S = 3$  ground-state, which is an unusual ground state for an Fe<sup>III</sup><sub>6</sub> complex. Most of the Fe<sup>III</sup><sub>6</sub> complexes for which the ground state spin has been determined have an  $S = 0$  or  $S = 5$  ground state. In fact, it is not intuitively obvious how an  $S = 3$  ground state could arise for an Fe<sup>III</sup><sub>6</sub> complex, since it is clearly not the resultant of simple considerations of *spin-up* and *spin-down* alignment pictures. The usual qualitative rationalization in such cases is to say that spin frustration effects must be operative within the Fe<sub>3</sub> triangular sub-units. Spin frustration is here defined in the more general, chemical sense as the presence of competing exchange interactions of comparable magnitude that prevent (frustrate) the spin alignments preferred from the nature (ferro- or antiferromagnetic) of the exchange interactions between them. Thus, the qualitative argument would say that intermediate spin alignments ( $M_S = \pm 3/2, \pm 1/2$  for high-spin Fe<sup>III</sup>) are present at some number of the Fe atoms and this gives the observed  $S = 3$  ground state. While such qualitative arguments are undoubtedly correct, they are nevertheless less than satisfying. As mentioned earlier, there is the other Fe<sup>III</sup><sub>6</sub> complex in class (c), [Fe<sub>6</sub>O<sub>2</sub>Cl<sub>4</sub>(hmp)<sub>8</sub>](ClO<sub>4</sub>)<sub>2</sub> (**2-4**), and **2-4** was also found to have an  $S = 3$

ground state.<sup>55</sup> Seeking to understand the origin of this ground state for **2-4**, the authors carried out computational studies using irreducible tensor methods to obtain the various pairwise  $J_{ij}$  exchange parameters for each Fe<sub>i</sub>-Fe<sub>j</sub> pair and thus rationalize the  $S = 3$  ground state. However, these calculations led to a predicted  $S = 0$  ground state for **2-4**, in conflict with the experimental data. The authors suggested several reasons for this discrepancy, but the bottom line is that the origin of the unusual  $S = 3$  ground state for this class of Fe<sup>III</sup><sub>6</sub> complex has yet to be satisfactorily explained at a quantitative level. In order to do so for our present complex **2-1** and **2-2**, and by extension for **2-4**, we carried out computational studies on complex **2-1** using the ZILSH method.

### 2.3.3.3 Rationalization of the $S = 3$ ground state of Complex **2-1**

The spin alignments giving rise to the  $S = 3$  ground state of the Fe<sup>III</sup><sub>6</sub> complex **2-1** are not obvious because it is not a simple sum of *spin-up* and *spin-down* of  $S = 5/2$ . It is clear that spin frustration is likely taking place in the compound, and we need to know the exact spin alignments at each Fe ion. In such cases it is useful to consider the spin coupling  $\langle \hat{S}_A \cdot \hat{S}_B \rangle$ , which can provide a direct probe of spin frustration: if two Fe<sup>III</sup> ( $S = 5/2$ ) ions couple ferromagnetically, each has a  $z$  component  $S_z$  of  $+5/2$ , and the total spin  $S_T$  is 5. The spin coupling  $\langle \hat{S}_A \cdot \hat{S}_B \rangle$  between them, which can be calculated from eq. 2-8, has a value of  $+6.25$ . Similarly, if they couple

$$\langle \hat{S}_A \cdot \hat{S}_B \rangle = \frac{1}{2} [S_T(S_T + 1) - S_A(S_A + 1) - S_B(S_B + 1)] \quad (2-8)$$

antiferromagnetically, one has  $S_z = +5/2$ , the other has  $S_z = -5/2$ , and the total spin  $S_T$  is 0. The spin coupling  $\langle \hat{S}_A \cdot \hat{S}_B \rangle$  between them has a value of  $-8.75$ . The spin coupling indicates the actual alignment of  $z$  components  $S_{z,A}$  and  $S_{z,B}$  in the state, while the exchange constant  $J_{AB}$  indicates the preferred alignment.

When  $J_{AB}$  is negative but small, and a preferred antiparallel alignment is overwhelmed completely by competing interactions, then the two spins align parallel, each with  $S_z = +5/2$ , and  $\langle \hat{S}_A \cdot \hat{S}_B \rangle$  large and positive, on the order of the formal value of +6.25. Such a pathway is called frustrated, and the situation is called spin frustration: in general, if  $J_{AB}$  and  $\langle \hat{S}_A \cdot \hat{S}_B \rangle$  carry different signs, the A-B pathway is frustrated.

When the competing exchange interactions are not strong enough to totally frustrate the pathway under consideration, but also not weak enough to allow it to be in a preferred way, the spins do not point either straight up or straight down, and are in some intermediate z component such as  $\pm 3/2$  or  $\pm 1/2$ . The spin coupling  $\langle \hat{S}_A \cdot \hat{S}_B \rangle$  is then quite reduced in magnitude from the formal value of +6.25 or -8.75, but it can still be positive or negative, and thus the pathway might not be completely frustrated or satisfied. Therefore, for an antiferromagnetically coupled pathway ( $J_{AB} < 0$ ), there is a continuum ranging from completely frustrated on one end,  $\langle \hat{S}_A \cdot \hat{S}_B \rangle$  large and positive,  $S_{z,A} = +5/2$ ,  $S_{z,B} = +5/2$ , to completely satisfied on the other end,  $\langle \hat{S}_A \cdot \hat{S}_B \rangle$  large and negative,  $S_{z,A} = +5/2$ ,  $S_{z,B} = -5/2$ . In between these extremes are smaller values of  $\langle \hat{S}_A \cdot \hat{S}_B \rangle$ , and  $S_{z,A}$  and  $S_{z,B} \pm 3/2$  or  $\pm 1/2$  (Figure 2-15). Note that the two spins can still be aligned parallel if not completely frustrated (incomplete frustration,  $\langle \hat{S}_A \cdot \hat{S}_B \rangle$  positive but small), or antiparallel (incomplete satisfaction,  $\langle \hat{S}_A \cdot \hat{S}_B \rangle$  negative but small in magnitude). Both of these scenarios are taking place in complex **2-1**.  $J$  values for complex **2-1**, calculated by ZILSH method, are presented in Figure 2-16. In the triangular unit Fe1-Fe2-Fe3,  $J_{13} = -22\text{cm}^{-1}$ ,  $J_{23} = -17\text{cm}^{-1}$ , and  $J_{12} = -60\text{cm}^{-1}$ . The spin coupling  $\langle \hat{S}_A \cdot \hat{S}_B \rangle$  values are also given in Figure 2-16.

Considering both Figures 2-15 and 2-16, we can tell which pathways in the  $\text{Fe}_6$  complex are frustrated/satisfied and by how much; for example, the spin coupling  $\langle \hat{S}_A \cdot \hat{S}_B \rangle$  of the Fe1-Fe3 pathway is -3.69 (Figure 2-16), and the range where this value resides in Figure 2-15 shows that

the Fe1-Fe3 pathway is partially satisfied with actual spin alignments of  $S_{z,1} = +3/2$  and  $S_{z,2} = -3/2$ . With the same argument, spin alignments on each Fe ion were assigned as in Figure 2-16, with a net result of  $S_{z,1} = +3/2$ ,  $S_{z,2} = -3/2$ , and  $S_{z,3} = +3/2$ . Based on the symmetry of the complex, there are four Fe ions with  $S_z = +3/2$  and two with  $S_z = -3/2$ , and therefore in total  $S_T = 3$ . The two  $J$  values  $J_{13}$  and  $J_{23}$  in each triangular unit are similar enough that the pathway with a slightly weaker  $J$  is frustrated, but only partially, and the one with a slightly stronger  $J$  is satisfied, but also only partially.

As stated above, the other complex in class (c),  $[\text{Fe}_6\text{O}_2\text{Cl}_4(\text{hmp})_8](\text{ClO}_4)_2$  (**2-4**), was also experimentally found to have an  $S = 3$  ground state,<sup>55</sup> however, the theoretical calculations the authors carried out to rationalize the  $S = 3$  ground state actually predicted an  $S = 0$  ground state for the compound. This discrepancy results from the authors' assumption that each triangle is isosceles, and their calculation based on this assumption predicted an  $S = 0$  ground state for the  $\text{Fe}^{\text{III}}_6$  complex. In contrast, we treated each triangle as scalene and obtained  $J_{13} = -22\text{cm}^{-1}$ ,  $J_{23} = 17\text{cm}^{-1}$ ,  $J_{12} = -60\text{cm}^{-1}$ , and thus predicted an  $S = 3$  ground state. We therefore performed our calculation of the ground state again, using the assumption that each triangle is isosceles ( $J_{13} = J_{23} = 19.5\text{cm}^{-1}$ ,  $J_{12} = -60\text{cm}^{-1}$ ), and obtained an  $S = 0$  ground state for complex **2-1**. Therefore, in the literature, the experimentally observed  $S = 3$  ground state of complex **2-4** was not able to be rationalized because of the incorrect assumption that each triangle is isosceles. Although it seems like a valid assumption, only a small difference in the structure and the resulting small differences in  $J$  values change the ground state of the  $\text{Fe}_6$  complexes.

We further investigated how lowering the symmetry of the triangular units below isosceles influences the ground state of the  $\text{Fe}^{\text{III}}_6$  molecule; we kept all of the  $J$  values constant except for  $J_{23}$  (Figure 2-16) and calculated the ground state with various  $J_{23}$  values. Interestingly, the

ground state of the  $\text{Fe}^{\text{III}}_6$  molecule can be  $S_T = 0, 1, 2, 3, 4,$  and  $5,$  by successively reducing the  $J_{23}$  value in increments of  $0.5 \text{ cm}^{-1}$ ; therefore, by lowering the symmetry of triangular units below isosceles, the ground state of the  $\text{Fe}^{\text{III}}_6$  complex can change from  $S = 0$  to  $S = 5$  in succession (Table 2-2). By thoroughly examining the influence of the relative strength of  $J$  values on the *side* pathways of its triangular subunits ( $J_{13}$  and  $J_{23}$  in Figure 2-16) and the ground state  $S_T$  of the  $\text{Fe}^{\text{III}}_6$  complex, the possible  $S_T$  values with various  $J_{13}$  and  $J_{23}$  values were mapped, as shown in Figure 2-17. When the triangular unit (Fe1-Fe2-Fe3) is isosceles and the  $J$  values on the *side* pathways ( $J_{13}$  and  $J_{23}$ ) are equivalent, the  $\text{Fe}^{\text{III}}_6$  complex has an  $S = 0$  ground state. When  $J_{13}$  and  $J_{23}$  are different to a large extent, the  $\text{Fe}^{\text{III}}_6$  complex has an  $S = 5$  ground state. However, when  $J_{13}$  and  $J_{23}$  differ to a small extent, the  $\text{Fe}^{\text{III}}_6$  complex can have  $S$  values ranging from 1 to 4. In the case of complex **2-1**,  $J_{13}$  and  $J_{23}$  are at the right strength to give an  $S_T = 3$  ground state. Figure 2-17 shows that a minute deviation from the isosceles situation can lead to drastic changes in the ground states.

## 2.4 Conclusions

The bidentate N,O ligand  $\text{hmp}^-$  in noncarboxylate  $\text{Fe}^{\text{III}}$  chemistry has proven to be a useful route to new  $\text{Fe}^{\text{III}}$  clusters spanning  $\text{Fe}_4$  and  $\text{Fe}_6$  nuclearities and topologies that are both very rare. In particular, the reaction between  $\text{Fe}(\text{NO}_3)_3 \cdot 9\text{H}_2\text{O}$  and  $\text{hmpH}$  in basic media has led to  $[\text{Fe}_6\text{O}_2(\text{hmp})_{10}(\text{H}_2\text{O})_2](\text{NO}_3)_4$  (**2-1**) and  $[\text{Fe}_6\text{O}_2(\text{hmp})_8(\text{NO}_3)_4(\text{H}_2\text{O})_2](\text{NO}_3)_2$  (**2-2**), whereas a similar reaction in the presence of  $\text{NaN}_3$  gives the tetranuclear cluster  $[\text{Fe}_4(\text{N}_3)_6(\text{hmp})_6]$  (**2-3**). It is interesting that the azide ligands in **2-3** are terminal rather than bridging but, nevertheless, fostered formation of a product completely different from that of the nonazide products **2-1** and **2-2**. Magnetochemical characterization of **2-1** and **2-2** revealed that the  $\text{Fe}^{\text{III}}_6$  complex has an  $S = 3$  ground state, and this counterintuitive result was rationalized by ZILSH theoretical methods. Interestingly, we found that the ground state of the  $\text{Fe}^{\text{III}}_6$  complex is very sensitive to the relative

strength of the  $J$  values on the *side* pathways of its triangular subunits, and with a lowered symmetry of triangular units below isosceles, the molecule can present ground states of  $S_T = 0, 1, 2, 3, 4,$  and  $5$ . In complex **2-1**, the relative strength of the  $J$  values on the *side* pathways of its triangular subunits are found to be at the right strength to allow  $S_T = 3$  ground state. It will be interesting to see in the future work whether the ground state of the  $\text{Fe}^{\text{III}}_6$  complex can be altered by distorting its triangular units chemically or physically.

Table 2-1. Crystallographic Data for **2-1**·8MeCN, **2-2**·6MeCN and **2-3**·2MeOH.

parameter	<b>2-1</b>	<b>2-2</b>	<b>2-3</b>
formula	C <sub>76</sub> H <sub>88</sub> N <sub>22</sub> O <sub>26</sub> Fe <sub>6</sub>	C <sub>60</sub> H <sub>70</sub> N <sub>20</sub> O <sub>30</sub> Fe <sub>6</sub>	C <sub>38</sub> H <sub>44</sub> N <sub>24</sub> O <sub>8</sub> Fe <sub>4</sub>
fw, g mol <sup>-1</sup>	2060.78	1886.46	1188.37
crystal system	monoclinic	triclinic	monoclinic
space group	<i>C2/c</i>	$\bar{P}$	<i>P2<sub>1</sub>/c</i>
<i>a</i> , Å	29.655(3)	11.8677(8)	13.6914(10)
<i>b</i> , Å	13.0398(12)	13.0369(9)	14.1350(11)
<i>c</i> , Å	23.822(2)	13.9403(10)	13.6611(10)
$\alpha$ , deg	90	64.628(2)	90
$\beta$ , deg	91.672(2)	82.289(2)	104.942(1)
$\gamma$ , deg	90	73.042(2)	90
<i>V</i> , Å <sup>3</sup>	9207.7(15)	1863.9(2)	2554.4(3)
<i>Z</i>	4	1	2
<i>T</i> , °C	173(2)	173(2)	173(2)
radiation, Å <sup>a</sup>	0.71073	0.71073	0.71073
$\rho_{\text{calc}}$ , g cm <sup>-3</sup>	1.487	1.681	1.545
$\mu$ , mm <sup>-1</sup>	1.005	1.236	1.187
<i>R1</i> <sup>b,c</sup>	0.0733	0.0411	0.0482
<i>wR2</i> <sup>d</sup>	0.1775	0.1005	0.1156

<sup>a</sup> Graphite monochromator. <sup>b</sup>  $I > 2\sigma(I)$ . <sup>c</sup>  $R1 = 100\Sigma(|F_o| - |F_c|)/\Sigma|F_o|$ . <sup>d</sup>  $wR2 = 100[\Sigma[w(F_o^2 - F_c^2)^2]/\Sigma[w(F_o^2)^2]]^{1/2}$ ,  $w = 1/[\sigma^2(F_o^2) + [(ap)^2 + bp]$ , where  $p = [\max(F_o^2, O) + 2F_c^2]/3$ .

Table 2-2. Calculated ground states  $S_T$  of complex **2-1** with various  $J_{23}$  values: see the text for details.

$J_{23}$ ( $\text{cm}^{-1}$ )	$J_{13}$ ( $\text{cm}^{-1}$ )	$J_{12}$ ( $\text{cm}^{-1}$ )	$S_T$
-18.5	-22.0	-60.0	0
-18.0	-22.0	-60.0	1
-17.5	-22.0	-60.0	2
-17.0	-22.0	-60.0	3
-16.5	-22.0	-60.0	4
-16.0	-22.0	-60.0	5

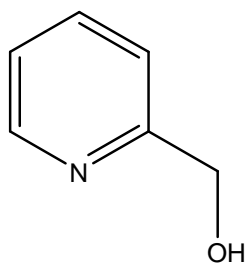


Figure 2-1. The structure of 2-(hydroxymethyl)pyridine (hmpH).

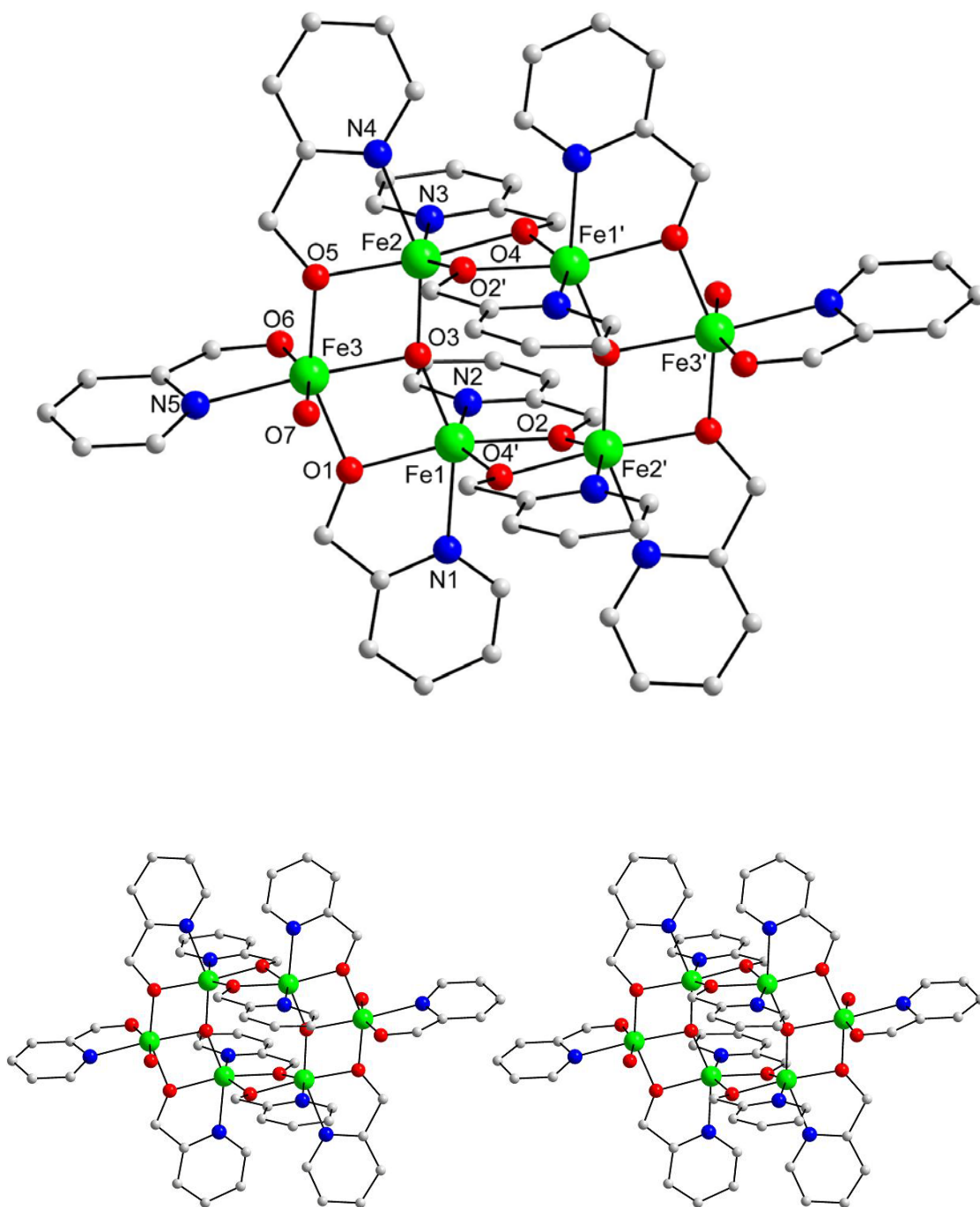


Figure 2-2. The structure of complex **2-1** (top) and a stereopair (bottom). Hydrogen atoms have been omitted for clarity. Color code: Fe<sup>III</sup> green; O red; N, blue; C grey.

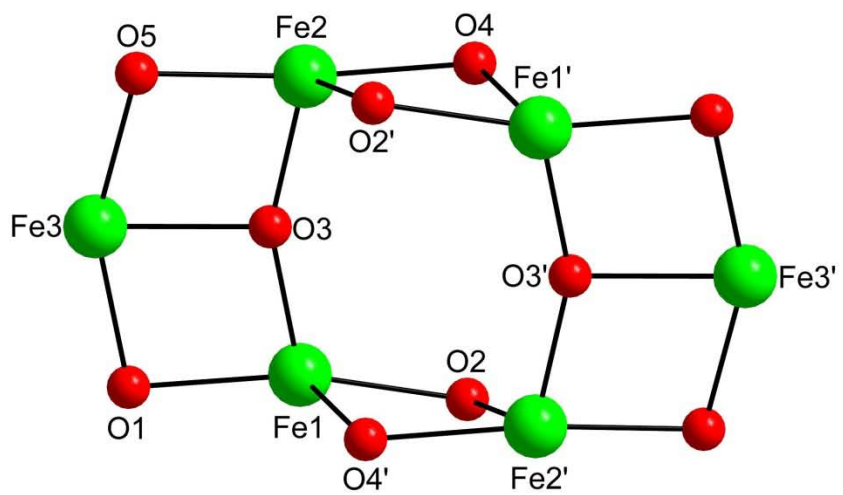


Figure 2-3. The fully labeled core of complex **2-1**. Color code: Fe<sup>III</sup> green; O red.

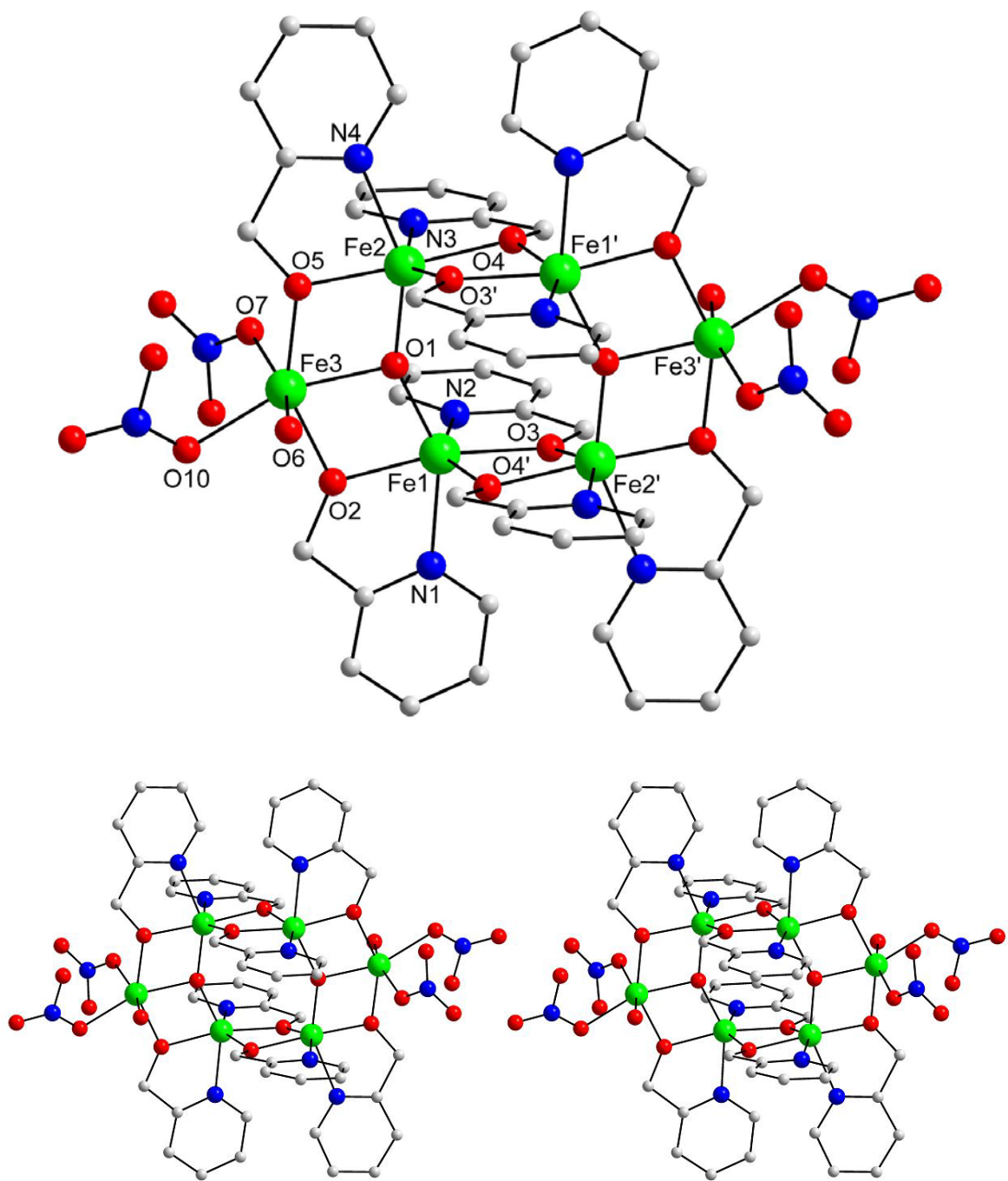


Figure 2-4. The structure of complex **2-2** (top) and a stereopair (bottom). Hydrogen atoms have been omitted for clarity. Color code: Fe<sup>III</sup> green; O red; N, blue; C grey.

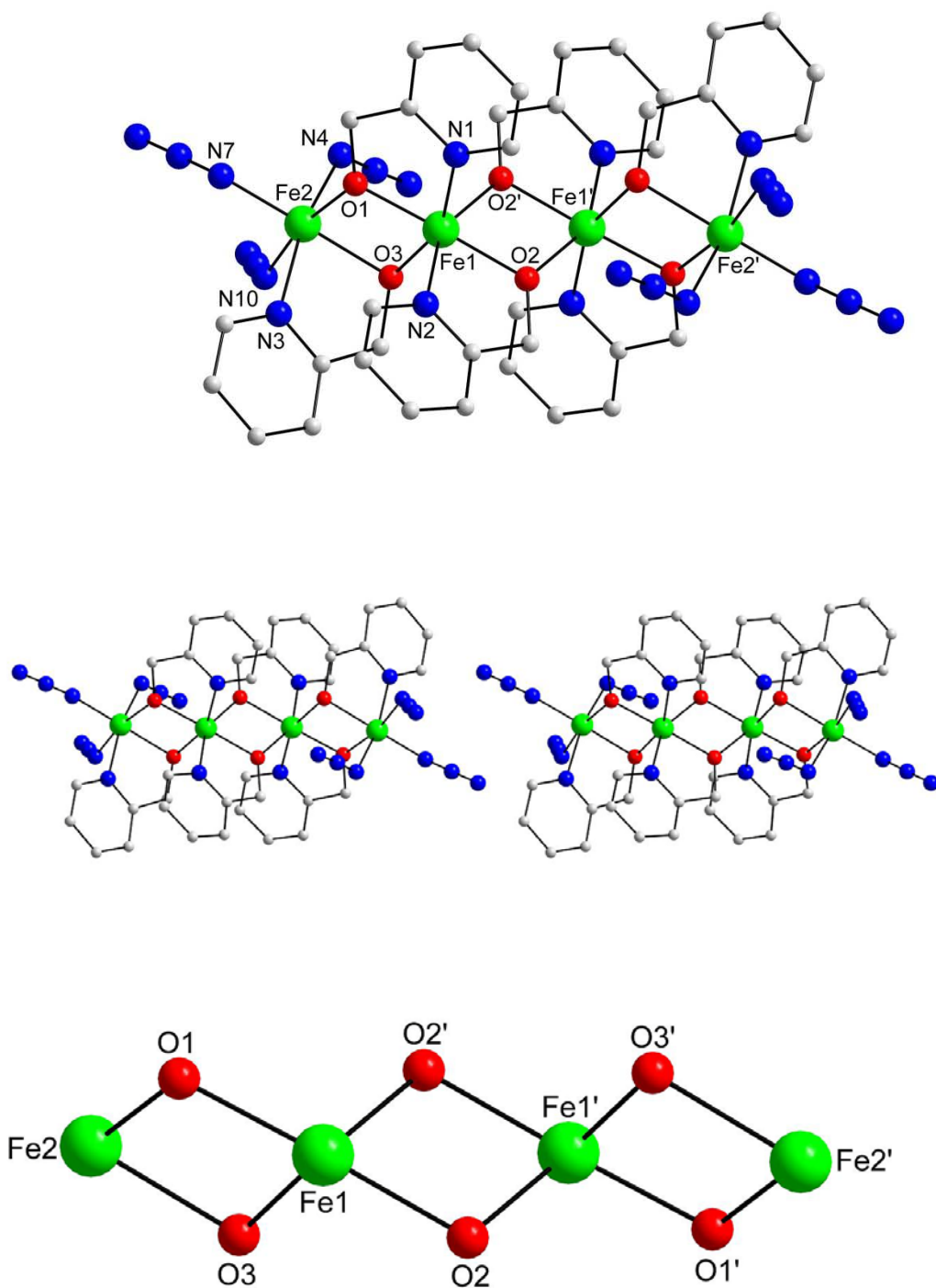


Figure 2-5. The structure of complex **2-3** (top), a stereopair (bottom), and the labeled core. Hydrogen atoms have been omitted for clarity. Color code: Fe<sup>III</sup> green; O red; N, blue; C grey.

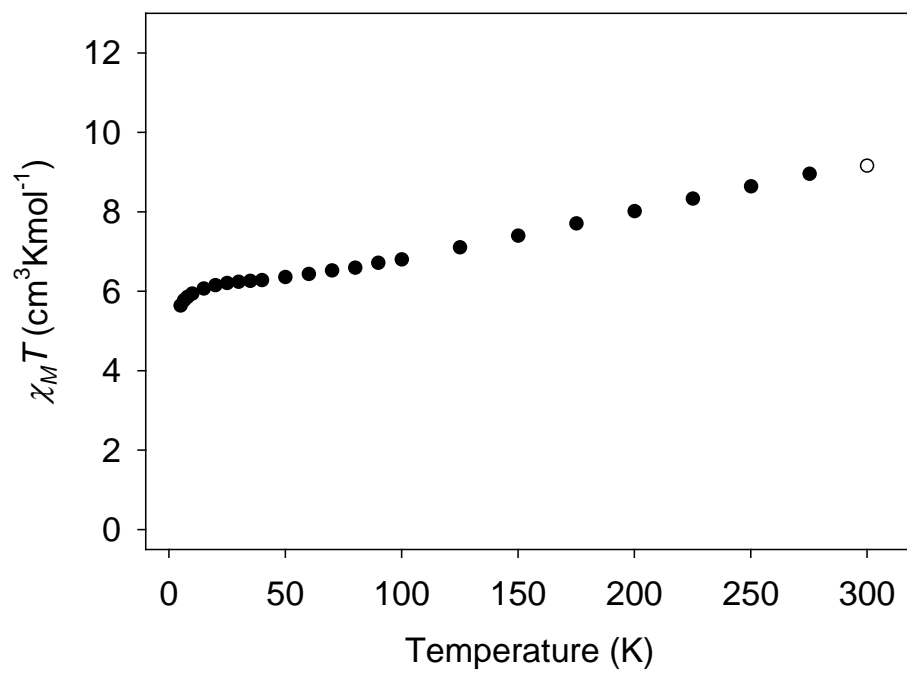


Figure 2-6. Plot of  $\chi_M T$  vs T for complex 2-1.

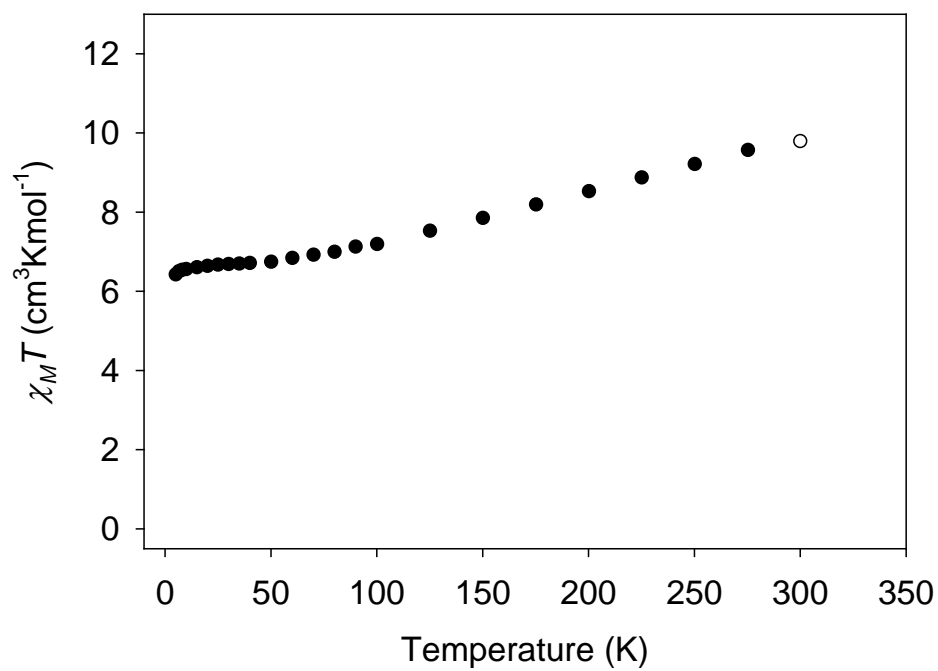


Figure 2-7. Plot of  $\chi_M T$  vs T for complex 2-2.

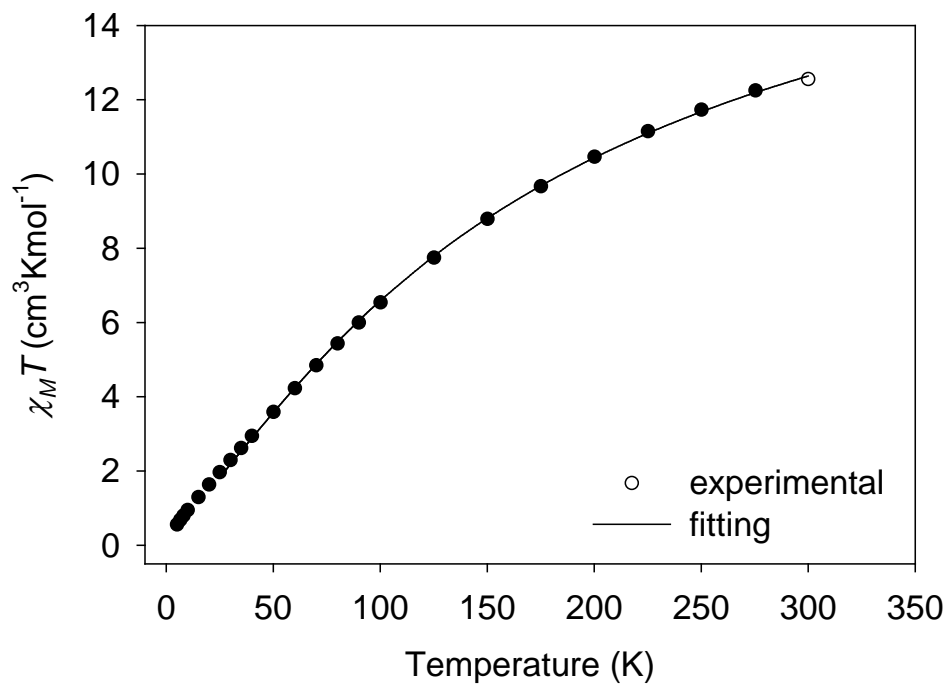


Figure 2-8. Plot of  $\chi_M T$  vs T for complex **2-3**. The solid line is the fit of the data; see the text for the fit parameters.

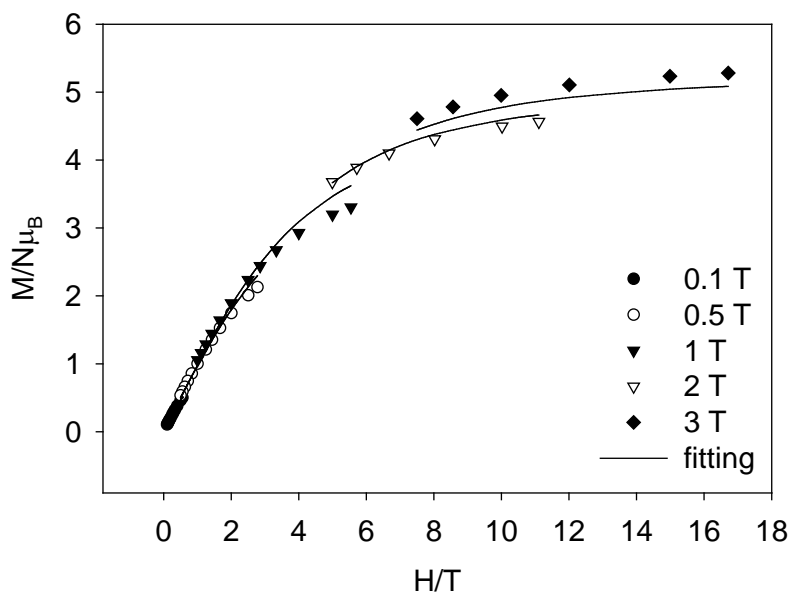


Figure 2-9. Reduced magnetization ( $M/N\mu_B$ ) vs  $H/T$  plot for complex **2-1**. The solid lines are the fit of the data; see the text for the fit parameters.

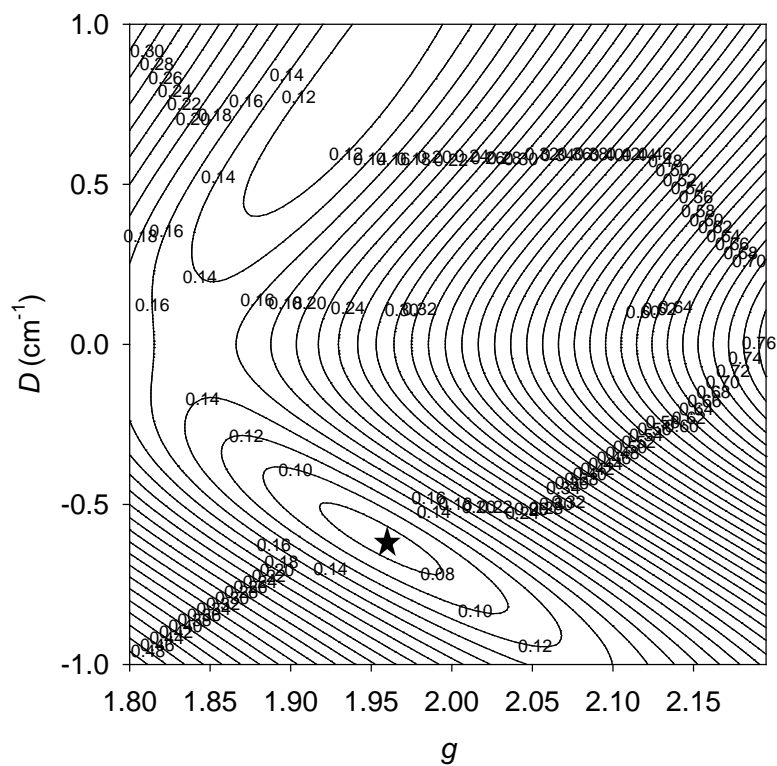


Figure 2-10. Two-dimensional contour plot of the root-mean-square error surface for the  $D$  vs  $g$  fit for complex **2-1**.

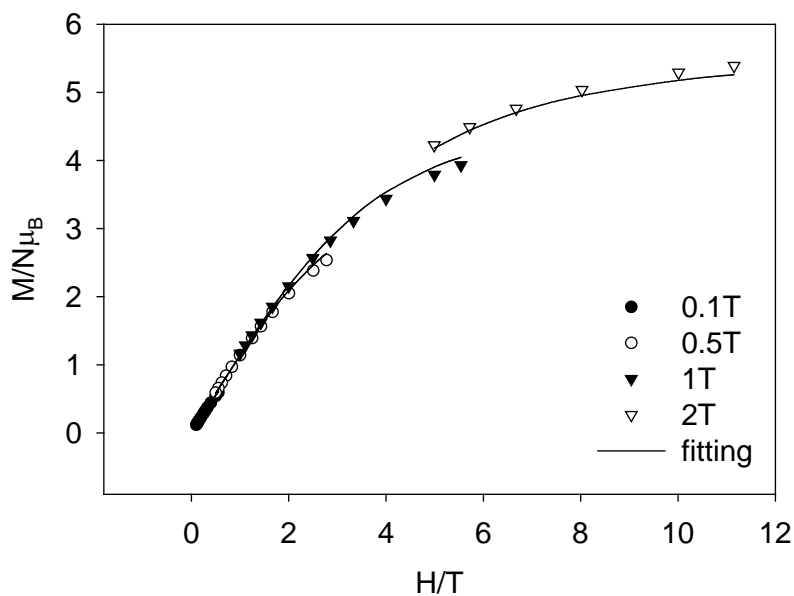


Figure 2-11. Reduced magnetization ( $M/N\mu_B$ ) vs  $H/T$  plot for complex **2-2**. The solid lines are the fit of the data; see the text for the fit parameters.

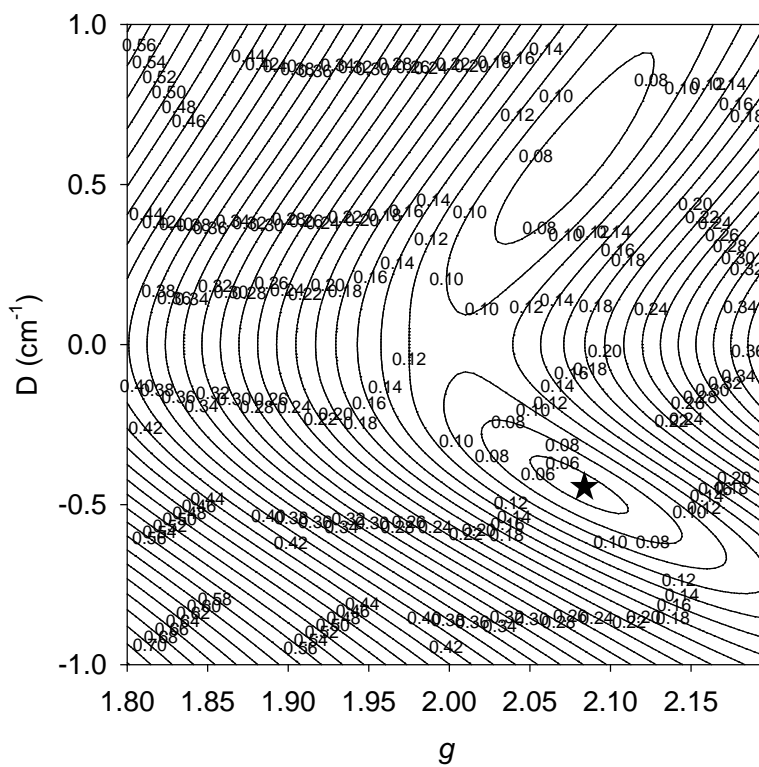


Figure 2-12. Two-dimensional contour plot of the root-mean-square error surface for the  $D$  vs  $g$  fit for complex **2-2**.

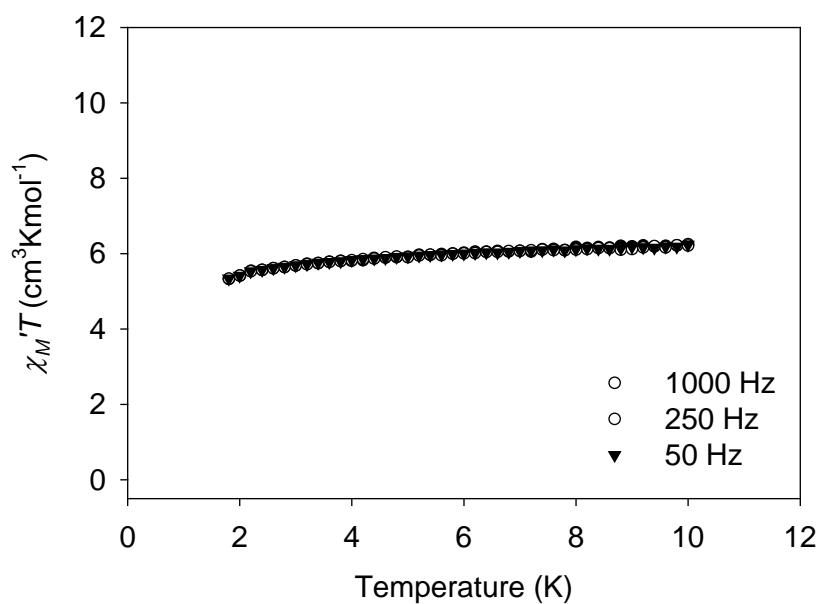


Figure 2-13. In-phase ac susceptibility ( $\chi_M'$ , plotted as  $\chi_M' T$  vs T) of complex **2-1** in a 3.5 Oe ac field oscillating at the indicated frequencies.

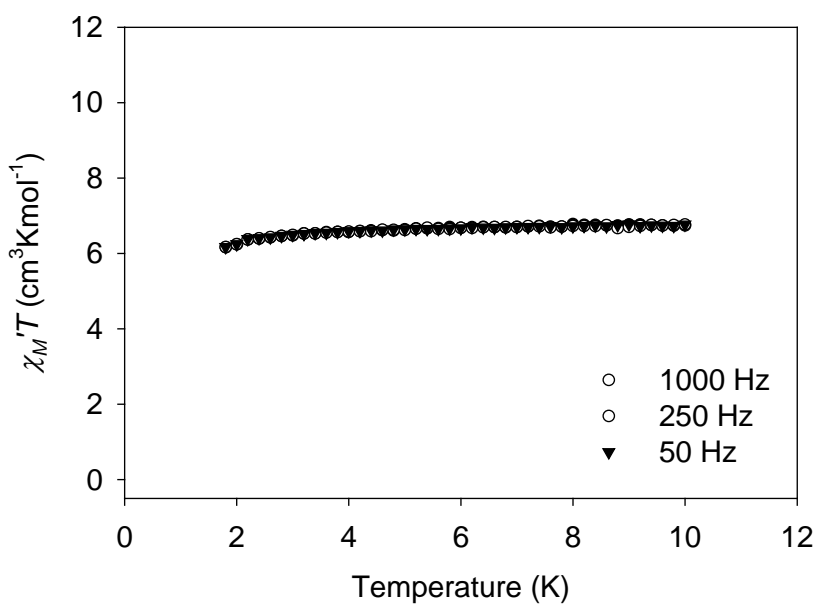


Figure 2-14. In-phase ac susceptibility ( $\chi_M'$ , plotted as  $\chi_M' T$  vs T) of complex **2-2** in a 3.5 Oe ac field oscillating at the indicated frequencies.

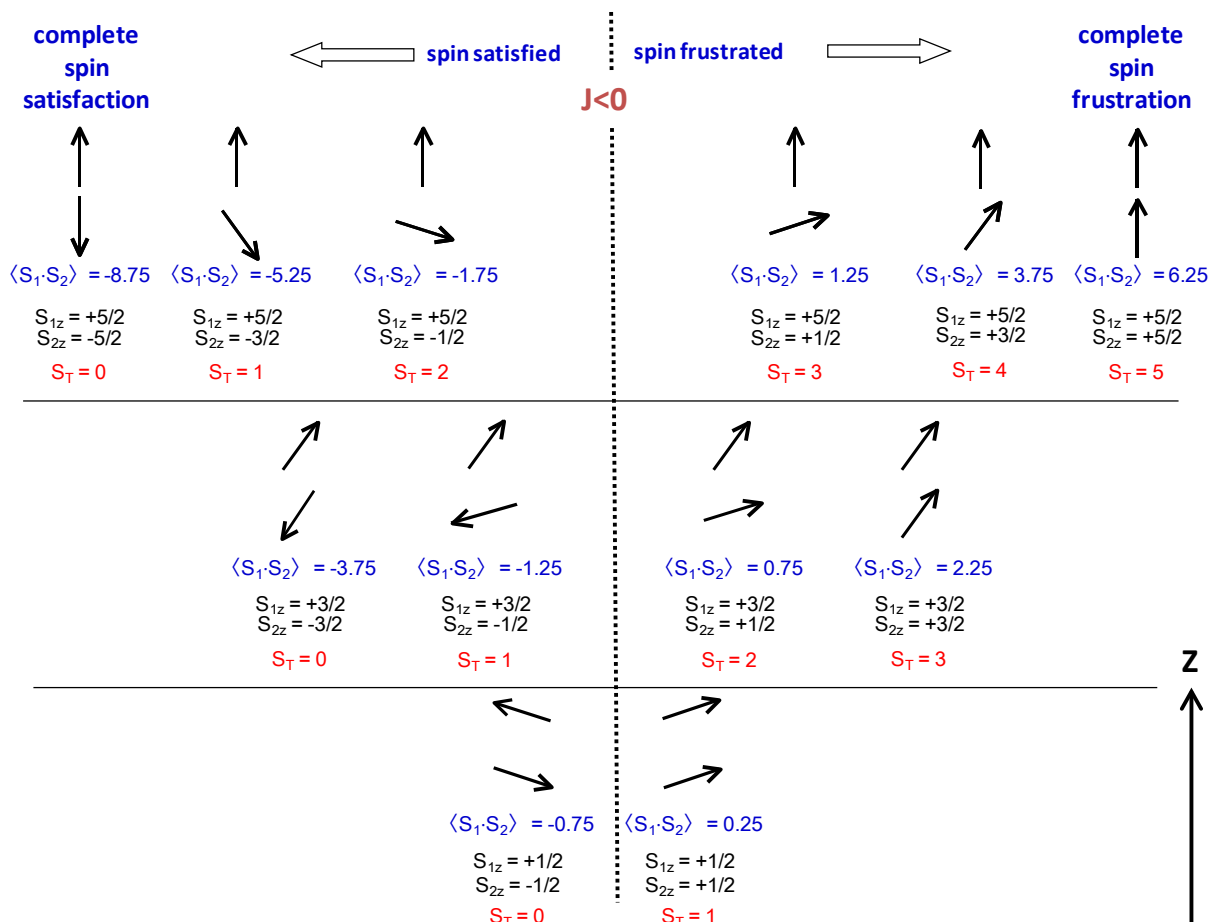


Figure 2-15. Scheme presenting a continuum of spin coupling values and spin alignments between completely satisfied situation and completely frustrated situation for an antiferromagnetically coupled pathway: see the text for details.

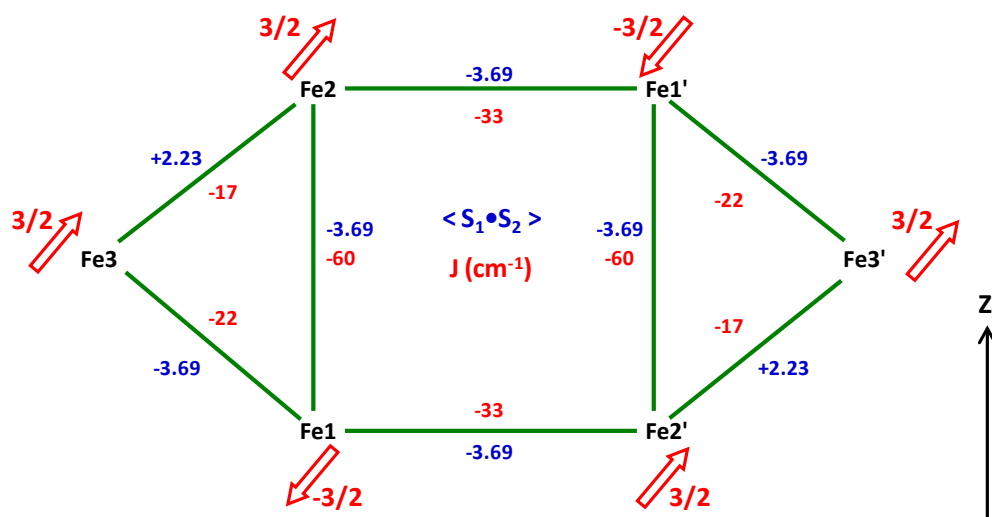


Figure 2-16. Diagrammatic scheme of the core structures of complex **2-1**, presenting the ZILSH exchange constants  $J$  and the spin coupling  $\langle \hat{S}_A \cdot \hat{S}_B \rangle$  for each Fe-Fe pathway and rationalizing the  $S = 3$  ground state of **2-1**: see the text for details.

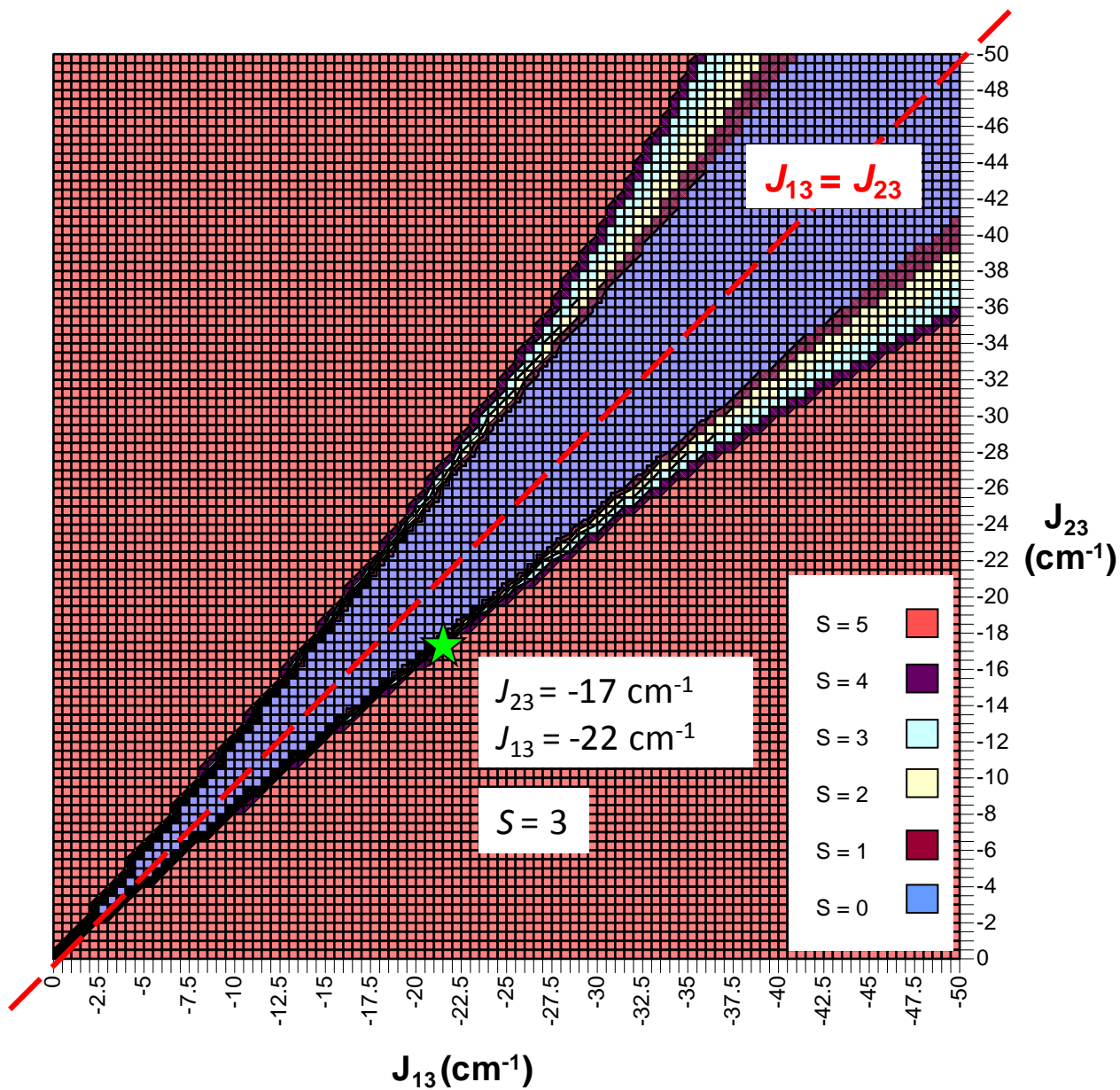


Figure 2-17. Mapping of the possible  $S_T$  values of **2-1** with various  $J_{13}$  and  $J_{23}$  values, presenting the influence of lowering of the symmetry of the triangular unit on the spin of the ground state.

CHAPTER 3  
UNUSUAL FE<sub>8</sub>, FE<sub>9</sub>, AND FE<sub>18</sub> STRUCTURAL TYPES FROM THE USE OF 2,6-  
PYRIDINEDIMETHANOL

**3.1 Introduction**

The systematic development of iron cluster chemistry over many years has led to a remarkable variety of species that have been of interest from several viewpoints, including structural aesthetics and spectroscopic and physical properties. From a biological viewpoint, the active sites of a variety of proteins such as hemerythrin, methane monooxygenase and ribonucleotide reductase have been shown to contain di-iron cores bridged by oxo or hydroxo ligands.<sup>22-24</sup> The protein ferritin has also received attention, owing to the biological importance of the role of this protein in the storage and recycling of iron, and a variety of compounds of high metal nuclearity that model the storage of iron in the protein have been synthesized.<sup>25-29</sup> Another interesting aspect of large polynuclear iron clusters is the potential for these clusters to possess large spin (*S*) values in their ground states due to a relatively large number of unpaired electrons of high-spin Fe<sup>III</sup> ions: The exchange interactions between these Fe<sup>III</sup> ions are normally antiferromagnetic, but with high enough Fe<sub>x</sub> nuclearities and appropriate topologies, such compounds can sometimes possess large ground-state spin values as a result of spin frustration effects among the various Fe<sub>2</sub> pairwise exchange pathways,<sup>40, 43, 117-123</sup> and can even occasionally function as single-molecule magnets (SMMs).<sup>12, 13, 19, 102, 124-129</sup> The latter are molecules that display slow magnetization relaxation rates and which, below a certain (blocking) temperature (*T<sub>B</sub>*), can function as single-domain magnetic particles of nanoscale dimensions.

For the above reasons, we have long been interested in the synthesis of polynuclear Fe<sub>x</sub> clusters. One approach to their synthesis is the hydrolysis or alcoholysis of either a ferric salt in the presence of carboxylate groups, or of a preformed small nuclearity Fe<sub>x</sub> carboxylate cluster, with or without other potentially chelating/bridging ligands. In line with this methodology, a

wide variety of potential ligands have been explored, and a large number of high nuclearity products, with nuclearities up to 64,<sup>130</sup> have been isolated.<sup>41, 112, 131-139</sup> The hydrolysis and alcoholysis reactions of ferric salts with appropriately chosen ligands in the absence of carboxylates are also a common approach to the synthesis of oxide/hydroxide/alkoxide-containing iron complexes, and have yielded various Fe<sub>x</sub> clusters, with nuclearities up to 17.<sup>121, 140-146</sup> We have been recently exploring the extension of this non-carboxylate Fe<sup>III</sup> chemistry as a synthetic route to high nuclearity products, with a particular interest in using pyridyl alcohols as potential chelates. Pyridyl alcohols have proven to be extremely versatile chelating and bridging groups that have yielded a number of 3d metal clusters with various structural motifs, large *S* values, and SMM behavior.<sup>44-47, 147-152</sup> In a previous chapter, we described the synthesis and properties of Fe<sub>4</sub> and Fe<sub>6</sub> complexes obtained from the employment of the pyridyl-alcohol, 2-(hydroxymethyl)pyridine (hmpH) in non-carboxylate Fe<sup>III</sup> chemistry.<sup>153</sup> We deliberately targeted non-carboxylate Fe<sup>III</sup> cluster products, and have successfully isolated new complexes which have not been isolated in the presence of carboxylate groups.<sup>54</sup> This initial success and the interesting products obtained encouraged us to extend the use of a different pyridyl-alcohol, 2,6-pyridinedimethanol (pdmH<sub>2</sub>) in Fe<sup>III</sup> cluster chemistry (Figure 3-1).

The ligand pdmH<sub>2</sub> has also proven to be very successful in Mn cluster chemistry, but surprisingly, there is no report of the use of pdmH<sub>2</sub> in Fe<sup>III</sup> cluster chemistry except for the heterometallic complexes.<sup>154</sup> We thus explored a number of reactions of Fe<sup>III</sup> and pdmH<sub>2</sub> in both the presence and the absence of carboxylate groups, and these efforts have led us to high nuclearity Fe<sub>8</sub>, Fe<sub>9</sub> and Fe<sub>18</sub> products, and ones that have particularly interesting structural features, especially the Fe<sub>18</sub> cluster. In the present chapter, we describe the syntheses, structures,

magnetochemical characterization, and high-frequency EPR spectra for these new Fe<sub>8</sub>, Fe<sub>9</sub> and Fe<sub>18</sub> clusters obtained from the use of pdmH<sub>2</sub>.

## 3.2 Experimental Section

### 3.2.1 Syntheses

All manipulations were performed under aerobic conditions using chemicals and solvents as received, unless otherwise stated. [Fe<sub>3</sub>O(O<sub>2</sub>CMe)<sub>6</sub>(py)<sub>3</sub>](NO<sub>3</sub>) was prepared as reported elsewhere.<sup>155-157</sup> *Safety note: Perchlorate salts are potentially explosive; such compounds should be synthesized and used in small quantities, and treated with utmost care at all times.*

**[Fe<sub>8</sub>O<sub>3</sub>(OMe)(pdm)<sub>4</sub>(pdmH)<sub>4</sub>(MeOH)<sub>2</sub>](ClO<sub>4</sub>)<sub>5</sub> (3-1).** To a stirred solution of pdmH<sub>2</sub> (0.14 g, 1.0 mmol) and NEt<sub>3</sub> (0.14 mL, 1.0 mmol) in MeOH (30 mL) was added solid Fe(ClO<sub>4</sub>)<sub>3</sub>·6H<sub>2</sub>O (0.46 g, 1.0 mmol). The resulting brown solution was stirred for 1 h and filtered, and the filtrate was layered with Et<sub>2</sub>O (30 mL). After 2 days, brown crystals of **3-1**·7MeOH were collected by filtration, washed with cold MeOH (2 × 5 mL) and Et<sub>2</sub>O (2 × 5 mL), and dried under vacuum; the yield was ~50%. Anal. Calcd (Found) for **3-1** (solvent-free): C, 32.38 (32.53); H, 3.27 (3.09); N, 5.12 (5.09). Selected IR data (cm<sup>-1</sup>): 3428 (mb), 1606 (m), 1582 (w), 1469 (w), 1438 (w), 1345 (w), 1265 (w), 1218 (w), 1144 (s), 1118 (s), 1089 (s), 786 (m), 720 (m), 676 (m), 628 (m), 592 (m), 510 (m), 467 (w), 430 (w).

**[Fe<sub>8</sub>O<sub>3</sub>(OEt)(pdm)<sub>4</sub>(pdmH)<sub>4</sub>(EtOH)<sub>2</sub>](ClO<sub>4</sub>)<sub>5</sub> (3-2).** This compound was made by a slight modification to the procedure for the methoxide analogue **3-1**. To a stirred solution of pdmH<sub>2</sub> (0.14 g, 1.0 mmol) and NEt<sub>3</sub> (0.14 mL, 1.0 mmol) in EtOH (30 mL) was added solid Fe(ClO<sub>4</sub>)<sub>3</sub>·6H<sub>2</sub>O (0.46 g, 1.0 mmol). The resulting orange solution was left stirring overnight, during which time a light brown-orange precipitate was obtained. The latter was collected by filtration, washed with the copious amount of EtOH and Et<sub>2</sub>O, and dried under vacuum; the yield

was ~65%. Anal. Calcd (Found) for **3-2**·H<sub>2</sub>O: C, 32.38 (32.53); H, 3.27 (3.09); N, 5.12 (5.09). Selected IR data (cm<sup>-1</sup>): 3405 (mb), 1607 (m), 1582 (w), 1470 (w), 1438 (w), 1346 (w), 1266 (w), 1218 (w), 1145 (s), 1111(s), 1088 (s), 786 (m), 754 (w), 723 (m), 677 (m), 627 (m), 592 (m), 541 (m), 508 (m), 470 (w), 436 (w).

**[Fe<sub>18</sub>O<sub>6</sub>(OH)<sub>8</sub>(pdm)<sub>10</sub>(pdmH)<sub>4</sub>(H<sub>2</sub>O)<sub>4</sub>](ClO<sub>4</sub>)<sub>10</sub> (3-3)**. Complex **3-2**, prepared and dried as described above, was then dissolved in MeCN (30 mL). The resulting brown solution was filtered, and the filtrate was carefully layered with Et<sub>2</sub>O/hexanes (1:1 v/v). After several days, brown crystals had grown and were collected by filtration, washed with cold MeCN (2 × 5 mL) and Et<sub>2</sub>O (2 × 5 mL), and dried under vacuum; the yield was ~10 %. Anal. Calcd (Found) for **3-3** (solvent-free): C, 27.84 (27.66); H, 2.81 (2.79); N, 4.64 (4.46). Selected IR data (cm<sup>-1</sup>): 3420 (mb), 1609 (m), 1582 (w), 1472 (w), 1438 (w), 1361 (w), 1346 (w), 1266 (w), 1216 (w), 1144 (s), 1190 (s), 1041 (s), 786 (w), 721 (m), 677 (m), 627 (m), 550 (m), 520 (m), 474 (m), 419 (m).

**[Fe<sub>9</sub>O<sub>4</sub>(OH)<sub>2</sub>(O<sub>2</sub>CMe)<sub>10</sub>(pdm)(pdmH)<sub>4</sub>](NO<sub>3</sub>) (3-4)**. To a stirred solution of pdmH<sub>2</sub> (0.035 g, 0.25 mmol) in CH<sub>2</sub>Cl<sub>2</sub> (30 mL) was added [Fe<sub>3</sub>O(O<sub>2</sub>CMe)<sub>6</sub>(py)<sub>3</sub>](NO<sub>3</sub>) (0.46 g, 0.25 mmol). The resulting brown solution was stirred for 2 h and filtered, and the filtrate was left to slowly concentrate by evaporation. X-ray quality crystals of **3-4**·7CH<sub>2</sub>Cl<sub>2</sub> slowly formed over a week. These were collected by filtration, washed with cold CH<sub>2</sub>Cl<sub>2</sub> and Et<sub>2</sub>O, and dried under vacuum; the yield was ~40%. Anal. Calcd (Found) for **3-4**·H<sub>2</sub>O: C, 33.69 (33.40); H, 3.75 (3.58); N, 4.29 (4.06). Selected IR data (cm<sup>-1</sup>): 3417 (mb), 1584 (s), 1541 (s), 1435 (s), 1385 (s), 1348 (m), 1268 (w), 1236 (w), 1219 (w), 1162 (w), 1114 (m), 1086 (m), 1050 (m), 1021 (m), 981 (w), 790 (w), 713 (m), 657 (s), 617 (m), 534 (m), 503 (m), 448 (m).

### 3.2.2 X-ray Crystallography

Data were collected on a Siemens SMART PLATFORM equipped with a CCD area detector and a graphite monochromator utilizing Mo-K $\alpha$  radiation ( $\lambda = 0.71073 \text{ \AA}$ ). Suitable crystals of **3-1**·7MeOH, **3-3**·7MeCN·3H<sub>2</sub>O, and **3-4**·7CH<sub>2</sub>Cl<sub>2</sub> were attached to glass fibers using silicone grease and transferred to a goniostat where they were cooled to 173 K for data collection. An initial search of reciprocal space revealed a monoclinic cell for **3-1**·7MeOH, **3-3**·7MeCN·3H<sub>2</sub>O, and **3-4**·7CH<sub>2</sub>Cl<sub>2</sub>; the choices of space groups  $P\bar{1}$ ,  $P2_1/n$ , and  $C_2$  were confirmed by the subsequent solution and refinement of the structures. Cell parameters were refined using up to 8192 reflections. A full sphere of data (1850 frames) was collected using the  $\omega$ -scan method (0.3° frame width). The first 50 frames were re-measured at the end of data collection to monitor instrument and crystal stability (maximum correction on I was < 1 %). Absorption corrections by integration were applied based on measured indexed crystal faces. The structures were solved by direct methods in *SHELXTL6*,<sup>158, 159</sup> and refined on  $F^2$  using full-matrix least-squares. The non-H atoms were treated anisotropically, whereas the H atoms were calculated in ideal positions and were riding on their respective carbon atoms. Unit cell parameters and structure solution and refinement data are listed in Table 3-1.

For **3-1**·7MeOH, the asymmetric unit consists of the complete Fe<sub>8</sub> cluster, five ClO<sub>4</sub><sup>-</sup> anions, and seven MeOH molecules of crystallization. A total of 1225 parameters were included in the structure refinement using 30354 reflections with  $I > 2\sigma(I)$  to yield R<sub>1</sub> and wR<sub>2</sub> of 7.02 and 16.66%, respectively.

For **3-3**·7MeCN·3H<sub>2</sub>O, the asymmetric unit consists of a half Fe<sub>18</sub> cluster (located on an inversion center), five perchlorate anions, three and a half acetonitrile solvent molecules and one and a half water molecules. Three half acetonitrile molecules are disordered against perchlorate

anions. Two perchlorate anions are fully disordered and each was refined in two parts. The third had its oxygen atoms disordered and also was refined in two parts. All hydroxyl and water protons were obtained from a Difference Fourier map and were riding on their parent atoms. A total of 1100 parameters were refined in the final cycle of refinement using 8269 reflections with  $I > 2\sigma(I)$  to yield  $R_1$  and  $wR_2$  of 8.50 and 21.96%, respectively.

For **3-4**·7CH<sub>2</sub>Cl<sub>2</sub>, the asymmetric unit consists of a half Fe<sub>9</sub> cluster cation, a half nitrate anion, three and a half dichloromethane solvent molecules. All half fragments are located on 2-fold rotation axes. The nitrate and the half dichloromethane as well as one of the latter located in general position are all disordered and each was refined in two parts. A total of 628 parameters were refined in the final cycle of refinement using 10062 reflections with  $I > 2\sigma(I)$  to yield  $R_1$  and  $wR_2$  of 4.22 and 11.61%, respectively.

### 3.2.3 Other Studies

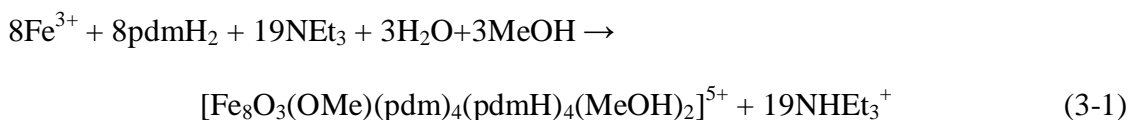
Infrared spectra were recorded in the solid state (KBr pellets) on a Nicolet Nexus 670 FTIR spectrometer in the 400-4000 cm<sup>-1</sup> range. Elemental analyses (C, H, and N) were performed by the in-house facilities of the University of Florida Chemistry Department. Variable-temperature dc and ac magnetic susceptibility data were collected on a Quantum Design MPMS-XL SQUID susceptometer equipped with a 7 Tesla magnet and operating in the 1.8–300 K range. Samples were embedded in solid eicosane to prevent torquing. Magnetization vs field and temperature data were fit using the program MAGNET.<sup>66</sup> Pascal's constants were used to estimate the diamagnetic corrections, which were subtracted from the experimental susceptibilities to give the molar paramagnetic susceptibilities ( $\chi_M$ ). High-Frequency Electron Paramagnetic Resonance (HF-EPR) measurements were carried out by the Hill group in the UF Physics Department, and were conducted on a crystal of complex **3-4**·7CH<sub>2</sub>Cl<sub>2</sub> in the 50 to 150

GHz frequency range, and at temperatures between 2 and 20 K, using a Millimeter-wave Vector Network Analyzer (MVNA) and a sensitive cavity perturbation technique described elsewhere.<sup>160, 161</sup> A dc magnetic field was provided by a 7 T horizontal field, split-pair superconducting magnet associated with a Quantum Design Physical Property Measurement System (PPMS); temperature control was achieved using an associated <sup>4</sup>He gas flow cryostat. Angle-dependent measurements were performed using a computer controlled stepper motor to rotate the EPR probe within the vertical split associated with the magnet.

### 3.3 Results and Discussion

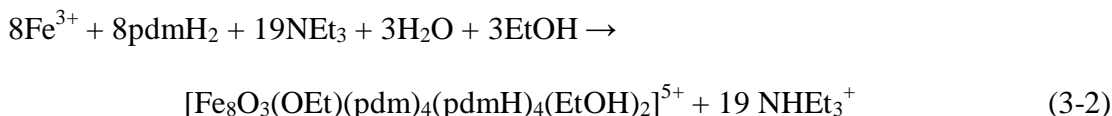
#### 3.3.1 Syntheses

Various reactions have been systematically explored with differing reagent ratios, reaction solvents, and other conditions before the following successful procedures were identified. The reaction of Fe(ClO<sub>4</sub>)<sub>3</sub>·6H<sub>2</sub>O and pdmH<sub>2</sub> in MeOH gave a brown solution from which were subsequently isolated large brown crystals of [Fe<sub>8</sub>O<sub>3</sub>(OMe)(pdm)<sub>4</sub>(pdmH)<sub>4</sub>(MeOH)<sub>2</sub>](ClO<sub>4</sub>)<sub>5</sub> (**3-1**) in ~50% yield. The formation of the cation of **3-1** is summarized in eq. 3-1. An increase of the NEt<sub>3</sub>:pdmH<sub>2</sub> ratio up to 3:1 gave comparable yields of complex **3-1** rather than a hoped for higher nuclearity product as a result of complete deprotonation of pdmH<sup>+</sup> groups. Further increases in the amount of NEt<sub>3</sub> led to amorphous, insoluble precipitates. Complex **3-1** was also obtained, but in lower yields (<30%), from reactions with Fe<sup>III</sup>:pdmH<sub>2</sub> ratios of 2:1, 3:1, and 1:2 in MeOH. Clearly, complex **3-1** is the preferred product of these reaction components under these conditions.

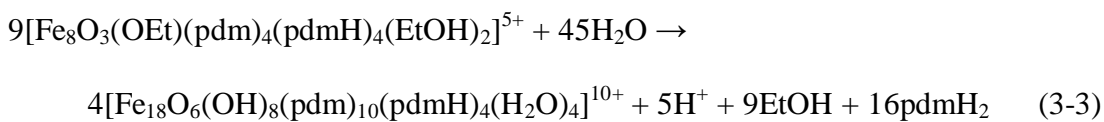


The corresponding reaction in EtOH solvent was then investigated and brown precipitate was obtained that was at first thought to be a different type of product from the very soluble **3-1**;

however, IR spectral similarities with **3-1** and elemental analysis data soon established that the product was indeed the analogous  $[\text{Fe}_8\text{O}_3(\text{OEt})(\text{pdm})_4(\text{pdmH})_4(\text{EtOH})_2](\text{ClO}_4)_5$  (**3-2**), and a crystal structure was not pursued. The formation of the cation is summarized in eq. 3-2.

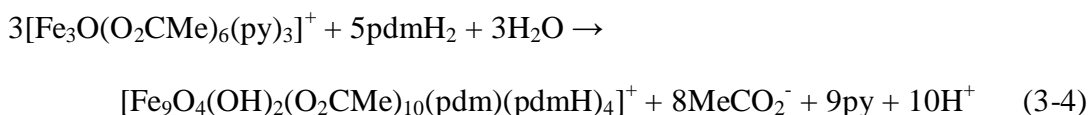


We have carried out a variety of investigations of the reaction system that leads to **3-1** and **3-2**. When the reaction mixtures were heated to reflux, light brown precipitates were formed in both MeOH and EtOH. Infrared spectra and elemental analysis data indicated the solids to contain  $\text{pdmH}^-$  and/or  $\text{pdm}^{2-}$  groups and to be different from **3-1** or **3-2**. We have not been able to characterize these products further, but we believe their insolubility indicates a polymeric structure. When the reaction medium was changed to MeCN, MeCN/alcohol or MeCN/water (without reflux), we were unable to isolate any pure, crystalline products. We therefore turned to exploring the reactivity properties of preformed **3-1** and **3-2**, and found them to be very sensitive to hydrolysis, which is consistent with their bridging alkoxide groups. Thus, dissolution of complex **3-2** in MeCN, and layering with  $\text{Et}_2\text{O}$ /hexanes gave well-formed brown crystals of  $[\text{Fe}_{18}\text{O}_6(\text{OH})_8(\text{pdm})_{10}(\text{pdmH})_4(\text{H}_2\text{O})_4](\text{ClO}_4)_{10}$  (**3-3**) in low (10%) yield. This is clearly a complicated hydrolysis and rearrangement reaction caused by the small amount of water in the MeCN; deliberate addition of more water did not give **3-3**, perhaps due to further hydrolysis. Nor, as implied above, did we obtain **3-3** directly by carrying out the preparative reaction for **3-2** in MeCN, MeCN/alcohol or MeCN/water. We thus settled for the low but reproducible yield of **3-3** obtained from preformed **3-2**. The overall transformation is summarized in eq. 3-3.



Complex **3-1** in MeCN was found to undergo the same transformation to **3-3**, as confirmed by IR spectral comparisons. The above reactions are summarized in Figure 3-2. Other solvents were also explored for the transformation of preformed **3-2**, and acetone was found to give complex **3-3** in comparable yields.

In earlier studies of the reactions of Fe<sup>III</sup> sources with pyridyl mono-alcohol chelate, 2-hydroxymethylpyridine (hmpH),<sup>182, 183</sup> the presence or absence of carboxylate groups has a profound effect on the identity of the product, giving structurally very different [Fe<sub>6</sub>O<sub>2</sub>(O<sub>2</sub>CBu<sup>t</sup>)<sub>6</sub>(hmp)<sub>6</sub>](NO<sub>3</sub>)<sub>2</sub> and [Fe<sub>6</sub>O<sub>2</sub>(NO<sub>3</sub>)<sub>2</sub>(hmp)<sub>8</sub>(H<sub>2</sub>O)<sub>2</sub>](NO<sub>3</sub>)<sub>2</sub> products, for example, from the reaction in MeCN of hmpH with [Fe<sub>3</sub>O(O<sub>2</sub>CBu<sup>t</sup>)<sub>6</sub>(H<sub>2</sub>O)<sub>3</sub>](NO<sub>3</sub>) or simple Fe<sup>III</sup> nitrate, respectively. We thus investigated this point in the present Fe<sup>III</sup>/pdmH<sub>2</sub> chemistry. Indeed, after investigating several reaction conditions and solvents, we found that the reaction of pdmH<sub>2</sub> with [Fe<sub>3</sub>O(O<sub>2</sub>CMe)<sub>6</sub>(py)<sub>3</sub>](NO<sub>3</sub>) in CH<sub>2</sub>Cl<sub>2</sub> gave the enneanuclear Fe<sup>III</sup> cluster [Fe<sub>9</sub>O<sub>4</sub>(OH)<sub>2</sub>(O<sub>2</sub>CMe)<sub>10</sub>(pdm)(pdmH)<sub>4</sub>](NO<sub>3</sub>) (**3-4**). Complex **3-4** was the only isolable product, in lower or comparable yield, from a number of reactions in which we varied the solvent, the Fe<sup>III</sup> starting material, and the reagent ratio. The formation of the cation of **3-4** is summarized in eq. 3-4.



Finally, since **3-3** and **3-4** both contain bridging hydroxide ions, we explored the analogous reactions also containing azide to see if azide groups might be incorporated in their place, as seen by Perlepes<sup>162, 163</sup> and coworkers for some Fe, Ni and Co clusters where bridging hydroxide groups could be replaced with end-on bridging azide. However, under our conditions, the only isolable products were again **3-3** and **3-4**.

### 3.3.2 Description of Structures

The partially labeled structure and a stereoview of the cation of complex  $[\text{Fe}_8\text{O}_3(\text{OMe})(\text{pdm})_4(\text{pdmH})_4(\text{MeOH})_2](\text{ClO}_4)_5$  (**3-1**) are presented in Figure 3-3, together with its labeled core. Selected interatomic distances and angles are listed in Table A-4. Complex **3-1** possesses a central  $[\text{Fe}_4(\mu_4\text{-O}^{2-})]$  tetrahedral subunit (Fe3, Fe6, Fe7, Fe8) fused to two  $[\text{Fe}_3(\mu_3\text{-O}^{2-})]$  triangular subunits (Fe4, Fe5, Fe6, and Fe1, Fe2, Fe8) at common atoms Fe6 and Fe8. The Fe- $\mu_4\text{-O}^{2-}$ -Fe angles range from 98.1(2) to 131.3(2)°, deviating significantly from the 109.5° ideal values of a tetrahedron. The Fe atoms are additionally bridged by the alkoxide arms of four  $\text{pdm}^{2-}$  and four  $\text{pdmH}^-$  groups. The  $\text{pdm}^{2-}$  groups are doubly deprotonated and tridentate-chelating to an Fe atom, with each of their alkoxide arms also bridging to adjacent Fe atoms; these groups are thus  $\eta^1:\eta^3:\eta^1:\mu_3$ . The  $\text{pdmH}^-$  groups are singly deprotonated and again tridentate-chelating to an Fe atom, but only the deprotonated alkoxide arm bridges to an adjacent Fe atom; these groups are thus  $\eta^1:\eta^3:\mu$ . In addition, there is a single  $\text{MeO}^-$  group bridging Fe6 and Fe8. The complex therefore contains a  $[\text{Fe}_8(\mu_4\text{-O})(\mu_3\text{-O})_2(\mu\text{-OMe})(\mu\text{-OR})_{12}]$  core. The ligation is completed by a terminal MeOH group on each of Fe atoms Fe1 and Fe5. The complete cation has only  $C_1$  crystallographic symmetry, but virtual  $C_2$  symmetry, the  $C_2$  axis passing through methoxide O atom O18 and central  $\mu_4\text{-O}^{2-}$  atom O19. The two  $[\text{Fe}_3(\mu_3\text{-O}^{2-})]^{7+}$  triangular units are essentially isosceles (Fe1...Fe2 = 3.133(2) Å, Fe1...Fe8 = 3.101(4) Å, Fe2...Fe8 = 3.529(1) Å, and Fe4...Fe5 = 3.129(2) Å, Fe5...Fe6 = 3.094(8) Å, Fe4...Fe6 = 3.541(4) Å), the long separation corresponding to the one not bridged by a  $\text{pdm}^{2-}$  or  $\text{pdmH}^-$  alkoxide group. This is also reflected in the geometry at the  $\mu_3\text{-O}^{2-}$  ions, O22 and O15, which have Y-shaped geometry (largest Fe-O-Fe angles of 138.1(2) and 139.4(2)°, respectively) rather than the trigonal planar geometry usually seen in triangular metal carboxylates;<sup>164, 165</sup> O22 and O15 are also 0.285 and 0.256 Å, respectively, above their  $\text{Fe}_3$  planes. Six of the Fe atoms (Fe2, Fe3, Fe4, Fe6, Fe7, and Fe8) are

six-coordinate with distorted octahedral geometries, whereas Fe1 and Fe5 are seven-coordinate with distorted pentagonal bipyramidal geometries. The Fe-N and Fe-O bond lengths are as expected for high-spin iron<sup>III</sup>.<sup>98, 110, 111</sup> Complex **3-1** presents a new structural type in a relatively small family of Fe<sup>III</sup> clusters with nuclearity of eight,<sup>73, 127, 166-174</sup> as well as being the first homometallic Fe<sup>III</sup> cluster with pdm<sup>2-</sup> and/or pdmH<sup>-</sup> groups.

The structure and a stereoview of [Fe<sub>18</sub>O<sub>6</sub>(OH)<sub>8</sub>(pdm)<sub>10</sub>(pdmH)<sub>4</sub>(H<sub>2</sub>O)<sub>4</sub>](ClO<sub>4</sub>)<sub>10</sub> (**3-3**) are presented in Figure 3-4, together with its labeled core. Selected interatomic distances and angles are listed in Table A-5. Complex **3-3** possesses a centrosymmetric [Fe<sub>18</sub>(μ<sub>4</sub>-O)<sub>4</sub>(μ<sub>3</sub>-O)<sub>2</sub>(μ<sub>3</sub>-OH)<sub>2</sub>(μ-OH)<sub>6</sub>(μ-OR)<sub>24</sub>] core containing four μ<sub>4</sub>-O<sup>2-</sup> (O1, O2), two μ<sub>3</sub>-O<sup>2-</sup> (O3), two μ<sub>3</sub>-OH<sup>-</sup> (O23) and six μ-OH<sup>-</sup> (O18, O19, O20) ions, whose protonation levels were confirmed by bond-valence-sum (BVS) calculations (Table 3-2). The Fe atoms are additionally bridged by the alkoxide arms of ten pdm<sup>2-</sup> and four pdmH<sup>-</sup> groups. The pdm<sup>2-</sup> groups are doubly-deprotonated and tridentate-chelating to an Fe atom, with each of their alkoxide arms also bridging to adjacent Fe atoms; these groups are thus η<sup>1</sup>:η<sup>3</sup>:η<sup>1</sup>:μ<sub>3</sub>. The pdmH<sup>-</sup> groups are singly-deprotonated and again tridentate-chelating to an Fe atom, but only the deprotonated alkoxide arm bridges to an adjacent Fe atom; these groups are thus η<sup>1</sup>:η<sup>3</sup>:μ. The ligation is completed by four terminal H<sub>2</sub>O groups on Fe6 and Fe6'. The eighteen Fe atoms are all six-coordinate with distorted octahedral geometries. The Fe-N and Fe-O bond lengths are as expected for high-spin Fe<sup>III</sup>.<sup>98, 110, 111</sup>

The core of **3-3** can be described as a central [Fe<sub>4</sub>O<sub>6</sub>] defective dicubane-like subunit (Fe1, Fe3, Fe1' and Fe3') that contains μ<sub>3</sub>-OH<sup>-</sup> (O23 and O23'), μ<sub>3</sub>-O<sup>2-</sup> (O3 and O3') and μ-alkoxide arms of μ<sub>3</sub>-pdm<sup>2-</sup> (O17 and O17') (Figure 3-4, bottom). On both sides of the central unit, the μ<sub>3</sub>-O<sup>2-</sup> is linked to [Fe<sub>7</sub>O<sub>11</sub>] units, which can be described as two [Fe<sub>4</sub>(μ<sub>4</sub>-O)] tetrahedra (O1, Fe2, Fe4, Fe5, Fe8, and O2, Fe6, Fe7, Fe8, Fe9) fused at Fe8. The Fe-μ<sub>4</sub>-O<sup>2-</sup>-Fe angles within these

tetrahedra range from 96.1 to 132.8°, deviating significantly from the 109.5° ideal values of a tetrahedron. The two [Fe<sub>3</sub>(μ<sub>3</sub>-O)] triangular units (Fe1, Fe2, Fe3) are essentially isosceles (Fe1···Fe2 = 3.066 Å, Fe1···Fe3 = 2.996 Å, Fe2···Fe3 = 3.555 Å), the long separation corresponding to the one not bridged by a pdm<sup>2-</sup> or OH<sup>-</sup> group. This is also reflected in the geometry at the μ<sub>3</sub>-O<sup>2-</sup> ions, O3, which have Y-shaped geometry (largest Fe-O-Fe angle of 141.7°) rather than the trigonal planar geometry usually seen in triangular metal carboxylates;<sup>164, 165</sup> O3 is also 0.272 Å above its Fe<sub>3</sub> plane.

Complex **3-3** joins a small family of only three previous Fe<sub>18</sub> clusters, two of which are molecular wheel complexes and one a ‘molecular chain’, i.e. with a discrete, serpentine-like extended structure.<sup>175-177</sup> Complex **3-3** is also the highest nuclearity non-carboxylate Fe<sup>III</sup> cluster discovered to date.

The structure and a stereoview of the cation of [Fe<sub>9</sub>O<sub>4</sub>(OH)<sub>2</sub>(O<sub>2</sub>CMe)<sub>10</sub>(pdm)(pdmH)<sub>4</sub>-(NO<sub>3</sub>) (**3-4**) viewed along the *ac* plane are presented in Figure 3-5. A labeled view along the *b*-axis of the structure and its core are shown in Figure 3-6. Selected interatomic distances and angles are listed in Table A-6. Complex **3-4** has imposed C<sub>2</sub> symmetry and contains a [Fe<sub>9</sub>(μ<sub>3</sub>-O)<sub>4</sub>(μ-OH)<sub>2</sub>(μ-OR)<sub>6</sub>] core held together by four μ<sub>3</sub>-O<sup>2-</sup> (O2, O3, O2', O3') and two μ-OH<sup>-</sup> (O1 and O1') ions, as confirmed by BVS calculations (Table 3-3). The Fe atoms are additionally bridged by the alkoxide arms of one pdm<sup>2-</sup> and four pdmH<sup>-</sup> groups, as well as ten acetates in the common η<sup>1</sup>:η<sup>1</sup>:μ bridging mode. The core can be described as an array of four vertex-fused [Fe<sub>3</sub>O] triangular units. Two of these (Fe1-Fe2-Fe5, and its symmetry partner) are scalene (Fe1···Fe2 = 3.507(1) Å, Fe1···Fe5 = 3.364(1) Å, and Fe2···Fe5 = 2.980(1) Å), and their central O<sup>2-</sup> atoms (O3, O3') are essentially (0.004 Å) in the Fe<sub>3</sub> plane. The other two triangular units (Fe2-Fe3-Fe4, and their symmetry partner) are also scalene (Fe2···Fe3 = 3.508(1) Å, Fe2···Fe4 =

3.284(1) Å, Fe3...Fe4 = 2.939(1) Å), but with their O<sup>2-</sup> atoms distinctly out (0.206 Å) of their Fe<sub>3</sub> plane. In each case, the shortest Fe...Fe separation is the bridged by both a μ<sub>3</sub>-O<sup>2-</sup> and a deprotonated pdmH<sup>-</sup> alkoxide arm. All Fe atoms are six-coordinate with octahedral geometry except for the Fe atom in the center (Fe1), which is five-coordinate with distorted trigonal bipyramidal geometry, pdm<sup>2-</sup> O atoms O18 and O18' occupying the axial positions. The Fe-N and Fe-O bond lengths in complex **3-4** are as expected for high-spin Fe<sup>III</sup>.<sup>98, 110, 111</sup> There are several Fe<sub>9</sub> clusters known in the literature,<sup>119, 120, 136, 178-182</sup> but none of them have the same Fe<sub>9</sub> topology as **3-4**.

### 3.3.3 Magnetochemistry

#### 3.3.3.1 Direct current magnetic susceptibility studies

Variable-temperature magnetic susceptibility measurements were performed on powdered polycrystalline samples of **3-1**, **3-3**, and **3-4**·H<sub>2</sub>O, restrained in eicosane to prevent torquing, in a 1 kG (0.1 T) field and in the 5.0–300 K range.

For **3-1**,  $\chi_{MT}$  decreases steeply from 11.77 cm<sup>3</sup>Kmol<sup>-1</sup> at 300 K to 0.67 cm<sup>3</sup>Kmol<sup>-1</sup> at 5.0 K (Figure 3-7). The 300 K value is much less than the spin-only ( $g = 2$ ) value of 35.00 cm<sup>3</sup>Kmol<sup>-1</sup> for eight non-interacting Fe<sup>III</sup> ions, indicating the presence of strong antiferromagnetic interactions, as expected for oxo-bridged Fe<sup>III</sup> systems, and an  $S = 0$  ground state.

For **3-3**,  $\chi_{MT}$  decreases with decreasing temperature from 26.23 cm<sup>3</sup>Kmol<sup>-1</sup> at 300 K to 8.47 cm<sup>3</sup>Kmol<sup>-1</sup> at 25 K and then increases slightly to 9.05 cm<sup>3</sup>Kmol<sup>-1</sup> at 5.0 K (Figure 3-8). The 300 K value is much less than the spin-only ( $g = 2$ ) value of 78.75 cm<sup>3</sup>Kmol<sup>-1</sup> for eighteen non-interacting Fe<sup>III</sup> ions, indicating dominant antiferromagnetic exchange interactions. The 5.0 K value is close to the spin-only ( $g = 2$ ) value of a complex with an  $S = 4$  ground state (10.00 cm<sup>3</sup>Kmol<sup>-1</sup>).

For **3-4**,  $\chi_M T$  steadily decreases with decreasing temperature from 11.97 cm<sup>3</sup>Kmol<sup>-1</sup> at 300 K to 4.17 cm<sup>3</sup>Kmol<sup>-1</sup> at 5.0 K (Figure 3-9). The 300 K value is much less than the spin-only ( $g = 2$ ) value of 39.38 cm<sup>3</sup>Kmol<sup>-1</sup> for nine non-interacting Fe<sup>III</sup> ions, indicating dominant antiferromagnetic exchange interactions. The 5.0 K value is close to the spin-only ( $g = 2$ ) value of a complex with an  $S = 5/2$  ground state (4.38 cm<sup>3</sup>Kmol<sup>-1</sup>).

To confirm the indicated  $S = 4$  and  $S = 5/2$  ground states of **3-3** and **3-4**, respectively, and to estimate the magnitude of the zero-field splitting parameter  $D$ , magnetization vs dc field measurements were made on restrained samples at applied magnetic fields and temperatures in the 1–70 kG and 1.8–10.0 K ranges, respectively. The obtained magnetization ( $M$ ) data for **3-3** are plotted as reduced magnetization ( $M/N\mu_B$ ) vs  $H/T$  in Figure 3-10, where  $N$  is Avogadro's number and  $\mu_B$  is the Bohr magneton. They were fit using the program MAGNET<sup>66</sup> to a model that assumes only the ground state is populated at these temperatures and magnetic fields, includes axial zero-field splitting ( $D\hat{S}_z^2$ ) and the Zeeman interaction, and incorporates a full powder average. The corresponding spin Hamiltonian is given by eq. 3-5, where  $\hat{S}_z$  is the easy-axis spin operator,  $g$  is the Landé  $g$  factor, and  $\mu_0$  is the vacuum permeability. Only data

$$\mathcal{H} = D\hat{S}_z^2 + g\mu_B\mu_0\hat{S}\cdot H \quad (3-5)$$

collected at fields up to 2 T were employed in the final fit, because satisfactory fits could not be obtained using data collected at higher fields. Such problems are typical for high nuclearity complexes that have low-lying excited states with  $S$  greater than that of the ground state and whose  $M_S$  levels thus approach those of the ground state with increasing applied fields. The resulting best fit is shown as the solid lines in Figure 3-10 and was obtained with  $S = 4$ ,  $g = 1.94$ , and  $D = -0.24$  cm<sup>-1</sup>. Alternative fits with  $S = 3$  or 5 were rejected because they gave unreasonable values of  $g$ . In order to examine the obtained fit quality, we calculated the root-mean-square  $D$  vs

$g$  error surface using the program GRID,<sup>116</sup> which calculates the relative difference between the experimental  $M/N\mu_B$  data and those calculated for various combinations of  $D$  and  $g$ . The obtained error surface, plotted as a two-dimensional contour plot in Figure 3-11, in fact exhibits two minima, one with positive  $D$  and the other with a negative one. This is as is typically found in such fits, which are not very sensitive to the sign of  $D$ . Nevertheless, the fit with  $D < 0$  clearly has the smaller relative error, suggesting the true sign of  $D$  is negative. Examination of the stretched nature of the contour lines around the best-fit position, corresponding to a somewhat soft minimum, allows the reliability in the fit parameters to be estimated as  $S = 4$ ,  $g = 1.94(1)$ , and  $D = -0.24(3) \text{ cm}^{-1}$ .

The  $M/N\mu_B$  vs  $H/T$  plot for **3-4** is shown in Figure 3-12, and we were able to obtain an excellent fit with the program MAGNET using all the data collected up to 7 tesla. This suggests that the ground state of **3-4** is relatively well isolated from the nearest excited states. The obtained error surface for the fit, plotted as a two-dimensional contour plot in Figure 3-13, again exhibits two minima, both of which are much softer (more poorly defined) than those for **3-3**: one has fit parameters of  $S = 5/2$ ,  $g = 1.94(3)$  and  $D = -0.63(9) \text{ cm}^{-1}$  (solid lines in Figure 3-12), and another with positive  $D$  and fit parameters  $S = 5/2$ ,  $g = 1.96(3)$  and  $D = +0.89(12) \text{ cm}^{-1}$ . However, unlike for **3-3**, the two fits for **3-4** are essentially of equal quality, and it is thus not possible, on the basis of these magnetization fits, to conclude the more likely sign of the axial anisotropy parameter  $D$  for **3-4**.

### 3.3.3.2 Alternating current magnetic susceptibility studies

As we have described before on multiple occasions,<sup>152, 183-186</sup> ac susceptibility studies are a powerful complement to dc studies for determining the ground state of a system, because they preclude any complications arising from the presence of a dc field. In an ac experiment, a weak magnetic field (typically in the 1-5 Oe range) oscillating at some ac frequency is applied to a

sample to investigate its magnetization relaxation dynamics. If the magnetization vector can relax fast enough to keep up with the oscillating field, then there is no out-of-phase susceptibility signal ( $\chi_M''$ ), and the in-phase susceptibility ( $\chi_M'$ ) is equal to the dc susceptibility. If a significant barrier (vs  $kT$ ) to magnetization relaxation is present, however, then there is a nonzero  $\chi_M''$  signal and the in-phase signal decreases; such frequency-dependent  $\chi_M''$  signals are suggestive of a SMM.

The ac data for complex **3-3** were collected in the 1.8-15 K range in a zero dc field and a 3.5 Oe ac field oscillating at frequencies in the 50-1000 Hz range. The in-phase ac susceptibility, plotted as  $\chi_M'T$  vs  $T$ , is shown in Figure 3-14 (there were no out-of phase ac signals down to 1.8 K, the operating limit of our SQUID magnetometer). The  $\chi_M'T$  of **3-3** is  $8.87 \text{ cm}^3\text{Kmol}^{-1}$  at 15 K, increases steadily to a plateau of  $10.0 \text{ cm}^3\text{Kmol}^{-1}$  at 1.8 K as excited states are depopulated, and the 1.8 K value is as expected for an  $S = 4$  ground state with  $g = 2.0$ . Complex **3-3** is thus confirmed to possess an  $S = 4$  ground state.

The in-phase  $\chi_M'T$  vs  $T$  plot for complex **3-4** is shown in Figure 3-15, and it is essentially temperature-independent at  $\sim 4.3 \text{ cm}^3\text{Kmol}^{-1}$ , except for a tiny decrease at the lowest temperatures assignable to very weak intermolecular interactions. The  $\chi_M'T$  vs  $T$  plot thus supports the conclusion from the dc reduced magnetization fit of a well isolated ground state for **3-4**. The value of  $\sim 4.3 \text{ cm}^3\text{Kmol}^{-1}$  is as expected for an  $S = 5/2$  ground state with  $g \sim 2$ ;  $S = 3/2$  and  $7/2$  would give  $\chi_M'T = 2.63$  and  $7.88 \text{ cm}^3\text{Kmol}^{-1}$ , respectively.

### 3.3.3.3 Rationalization of the $S = 5/2$ Ground State of Complex 3-4

It is of interest to try to rationalize the observed  $S = 4$  and  $5/2$  ground states of **3-3** and **3-4**, respectively. However, the high nuclearity and low symmetry of **3-3** make it impossible for this compound. An  $S = 4$  ground state cannot result from simple spin-up/spin-down alignment of

spins, and it is clear that many intermediate spin alignments must be present as a result of extensive spin frustration effects present in the many Fe<sub>3</sub> triangular sub-units in the core.

The smaller size and C<sub>2</sub> symmetry of **3-4** allow more satisfying conclusions to be reached. The nuclearity is still too high to allow the experimental  $\chi_M T$  vs  $T$  data to be fit by matrix diagonalization of the appropriate spin Hamiltonian involving the eight symmetry-independent nearest-neighbor Fe exchange interactions,  $J_{ij}$ ; this would involve diagonalizing a matrix of dimensions slightly greater than  $1 \times 10^7$  by  $1 \times 10^7$ . We thus estimated the  $J_{ij}$  values using the magnetostructural correlation of Gorun and Lippard,<sup>187</sup> which is based on the bridging Fe-O-Fe bond distances. The resulting  $J_{ij}$  values ( $\mathcal{H} = -2J_{ij}\hat{S}_i \cdot \hat{S}_j$  convention) calculated for each Fe<sub>i</sub>-Fe<sub>j</sub> interaction are shown in Figure 3-16, where the viewpoint is that of Figure 3-6 (bottom). As expected, all interactions are antiferromagnetic and span a range from -6.0 to -41.2 cm<sup>-1</sup>. Consideration of spin frustration (competing exchange interactions) within each Fe<sub>3</sub> triangular sub-unit leads to the qualitative conclusions of the individual spin alignments shown in Figure 3-16. In almost all cases, one of the interactions is significantly weaker (by a factor of two or more) than the other two interactions, allowing us to conclude that this interaction will clearly be frustrated and the spin alignments therefore determined by the other two. The weaker, frustrated interactions are shown in blue. The exception is  $J_{34}$  (-25.4 cm<sup>-1</sup>), which is within ~4 cm<sup>-1</sup> of  $J_{23}$  (-29.6 cm<sup>-1</sup>) but we propose the Fe3 spin is nevertheless locked parallel to the Fe4 spin by the combined stronger  $J_{23}$  and  $J_{35}$  interactions. We thus offer Figure 3-16 as a rationalization of the  $S = 5/2$  ground state of **3-4**, which can be summarized as an outer  $S = 0$  loop of four antiparallel-aligned Fe<sub>2</sub> pairs of  $S = 5$  spins, and an inner  $S = 5/2$  Fe1 spin, giving the overall  $S = 5/2$  spin of the complete molecule. No doubt other spin alignments involving some spins in intermediate alignments also significantly contribute to the ground state spin wavefunction of the molecule,

but we believe Figure 3-16 describes the main component, on the basis of the calculated  $J_{ij}$  values at least.

#### 3.3.3.4 Single-Crystal, High Frequency EPR (HFEP) Spectroscopy

HFEP studies were carried out by the Hill group in the UF Physics Department. For an independent means of confirming the ground state spin,  $S$ , as well as the sign and magnitude of the axial ZFS parameter  $D$ , HFEP measurements were carried out on a single crystal of **3-4-7**CH<sub>2</sub>Cl<sub>2</sub>. As shown in the previous section, ac susceptibility and dc magnetization measurements can provide good estimates of  $S$  and  $D$ , but HFEP measurements provide much more accurate and reliable values, particularly in the case of  $D$ . Furthermore, the sign of  $D$  can be determined unambiguously from EPR studies, which is not easy to do from fits of powder magnetization data, as stated.<sup>188</sup>

Sample alignment was first achieved by performing in-situ rotation of the sample in order to locate extrema (easy/hard directions) among plots of the angle-dependent EPR peak positions. Once aligned, measurements were performed as a function of frequency and temperature so as to provide data sets that maximally constrain the ZFS parameters. Figure 3-17(a) displays a series of angle-dependent HFEP spectra at 91.3 GHz; the data in the figure focus on a narrow angle interval either side of one of the extrema. Based on previous studies of similar Fe<sup>III</sup> complexes,<sup>60,</sup><sup>188</sup> we identify this particular orientation as the hard plane. Upon closer inspection of the data, it is apparent that most of the peaks are split into doublets (see e.g. the two vertical arrows between 4.5 and 5 T). Furthermore, the angle-dependence of the two peaks in each doublet appears to be slightly different. This is most clearly illustrated in Figure 3-17(b), which plots the locations of the two peaks associated with the highest field resonance observed above 4.5 T. From these plots, we conclude that the crystal employed in this study possesses two hard planes. The X-ray crystal structure shows only one orientation of molecules in the unit cell of **3-4-7**CH<sub>2</sub>Cl<sub>2</sub>, ruling out

different orientations as the cause of the HFEPR peak doubling. We thus conclude (a posteriori) that the sample used for the HFEPR investigation was twinned, leading to the two rotation patterns observed in Figure 3-17(b). Although this complicates the analysis slightly, it does not preclude an accurate determination of  $S$  and  $D$ . Indeed, the procedures employed in this investigation have been applied successfully to many other samples for which two or more molecular orientations exist.<sup>227, 228</sup> The angle-dependent plots in Figure 3-17(a) indicate that the field intersects the hard planes associated with the twinned crystal roughly  $5^\circ$  apart. Furthermore, the fact that the maxima occur at different magnetic field values is indicative of the presence of transverse ZFS interactions, i.e. the field intersects the two hard planes at different orientations with respect to the hard/medium axes associated with the twinned crystal.<sup>189, 190</sup> Thus, in some sense, more information is obtained than would otherwise have been the case for a single crystal. However, characterization of the transverse ZFS terms would require very time consuming two-axis rotation studies,<sup>191, 192</sup> which is well beyond the scope of the present investigation.

Given that only a single-axis rotation capability was employed for these experiments, perfect easy-axis alignment is never guaranteed. However, by rotating the sample  $90^\circ$  from one of the hard planes, one can usually achieve a sufficient parallel field component ( $B_z$ ) for accessing the  $z$ -component of the HFEPR spectrum from which the axial ZFS is easily extracted. Indeed, extrapolation of simulations to zero-field enables very tight constraints on the axial ZFS parameters  $D$  and  $B_4^0$  (see below). However, the obtained  $g$  value is not so reliable. For these investigations, we rotated  $90^\circ$  away from the hard plane located at  $-7^\circ$  in Figure 3-17(b) due to the fact that the corresponding peak is stronger than for the other hard plane.

Figure 3-18 displays a series of HFEPR spectra for **3-4-7**CH<sub>2</sub>Cl<sub>2</sub> at different temperatures in the 2 to 20 K range, and with the field aligned closer to the easy-axes of the twinned crystal

than for the data in Figure 3-17. Two series of resonances can be seen (labeled  $\alpha$  and  $\beta$ ), corresponding to the two different orientations within the twinned sample. The various peaks can be identified by virtue of the fact that they occur in pairs exhibiting essentially the same temperature dependence, and from the subsequent simulations (see below). For some of the peak assignments, subscripts are included with the label indicating the approximate magnitude of  $M_S$  associated with the level from which the transition is excited. At the lowest temperature, the strongest peaks in each series ( $\alpha_{5/2}$  and  $\beta_{5/2}$ ) are observed at the lowest field, which indicates that they correspond to excitations from the lowest levels within the ground state  $S$  multiplet. This observation confirms the negative sign of  $D$ .<sup>60</sup> However, even at the lowest temperature of 2 K, significant populations exist among excited  $M_S$  levels due to the relatively weak ZFS in this complex.

Figure 3-19 displays the frequency dependence of HFEPR peak positions for **3-4·7**CH<sub>2</sub>Cl<sub>2</sub> corresponding to the same field orientation as the spectra displayed in Figure 3-18. The red and blue squares correspond to the  $\alpha$  and  $\beta$  resonances, respectively. The red and blue solid lines are the corresponding best simulations of the frequency dependence, obtained via exact diagonalization of eq. 3-5. The primary adjustable parameters used for these simulations were the spin,  $S = 5/2$ , a single axial ZFS parameter  $D = -0.48(1) \text{ cm}^{-1}$ , and the field orientation relative to the two easy- axes of the twinned crystal ( $16^\circ$  and  $38^\circ$ , see Figure 3-19). The  $g$  value was held constant and assumed to be isotropic (2.00), as expected for Fe<sup>III</sup>, and inclusion of a rhombic ZFS parameter  $E$  ( $\sim 0.07 \text{ cm}^{-1}$ ) slightly improved agreement among the weak higher- field resonances; inclusion of a fourth-order axial  $B_4^0$  term did not, however, improve the simulations.

The uncertainty associated with the rhombic parameter is considerable, because the plane of field rotation relative to the two crystals is not known. Nevertheless, the improvement in the

simulations in Figure 3-19 upon inclusion of a rhombic term is consistent with indications from the hard plane measurements that complex **3-4** possesses a significant rhombic anisotropy. In contrast, the obtained  $D$  value is very reliable, as evidenced by the excellent agreement between the lower field peak positions and the corresponding simulations. We note the different field misalignment angles (relative to the two easy-axes) found from the simulations in Figure 3-19. This indicates that the two components of the twinned crystal are significantly misaligned, and that it was fortuitous that the field intersected the two hard planes in relatively close proximity; see Figure 3-17(b). Note that the  $D = -0.48(1) \text{ cm}^{-1}$  obtained from HF-EPR is significantly different from the  $-0.63(9) \text{ cm}^{-1}$  value obtained from the fits of powder magnetization data, emphasizing again the need for studies by a technique such as EPR when more reliable and accurate values are required.

Finally, we comment on the  $S = 5/2$  ground state spin assignment based on HF-EPR. The spectra in Figure 3-18 exhibit significant  $M_S$ -dependent peak broadening. This behavior may be attributed to  $D$ -strain, most likely resulting from solvent or ligand disorder that, in turn, causes inhomogeneous broadening of the transitions.<sup>193-195</sup> Within this picture, one can understand the fact that the sharpest resonance corresponds to the  $M_S = -\frac{1}{2}$  to  $M_S = +\frac{1}{2}$  transition ( $\alpha_{1/2}$ ), since there is no ZFS associated with these two Kramers levels.<sup>102</sup> In fact, the  $\alpha_{1/2}$  resonance becomes very sharp at higher fields/frequencies (not shown), presumably due to reduced dipolar field fluctuations. On the basis that the  $M_S = -\frac{1}{2}$  to  $M_S = +\frac{1}{2}$  assignment can be made with near 100% certainty, our confidence in the spin  $S = 5/2$  ground state assignment is equally robust.

### 3.4 Conclusions

The first ever employment of the tridentate O,N,O ligands  $\text{pdm}^{2-}/\text{pdmH}^-$  in homometallic  $\text{Fe}^{\text{III}}$  chemistry has led to three interesting new  $\text{Fe}_8$  (**3-1**),  $\text{Fe}_{18}$  (**3-3**) and  $\text{Fe}_9$  (**3-4**) clusters, all of

which are of an unprecedented structural type. The Fe<sub>18</sub> complex **3-3** is the highest nuclearity complex to date in non-carboxylate Fe<sup>III</sup> chemistry and can be obtained readily from hydrolysis of [Fe<sub>8</sub>O<sub>3</sub>(OEt)(pdm)<sub>4</sub>(pdmH)<sub>4</sub>(EtOH)<sub>2</sub>](ClO<sub>4</sub>)<sub>5</sub> (**3-2**) or its MeO-/MeOH analogue (**3-1**), but we have not been able to prepare it directly from simple Fe<sup>III</sup> salts. It has an unusual cigar-like core, and we see no reason why longer, higher nuclearity analogues might not be accessible. The complexes have  $S = 0$  (**3-1**), 4 (**3-3**) and 5/2 (**3-4**) ground states, the latter two clearly arising from spin frustration effects within the many Fe<sub>3</sub> triangular sub-units; the  $S$  value for **3-3** is impossible to rationalize but that for **3-4** can be rationalized on the basis of the exchange interactions predicted from published magnetostructural correlations. The magnetization fits for **3-3** gave a value for  $D$  of  $-0.24(3) \text{ cm}^{-1}$ , whereas for **3-4**, equally good fits were obtained with positive and negative  $D$  values and with large uncertainties in  $D$ , emphasizing the difficulty of determining the sign of  $D$  for Fe<sup>III</sup> clusters from such measurements. However, use of the powerful HFEPR spectroscopic technique both identified the true  $D$  value of **3-4** to be negative, and provided a reliable value of  $-0.48(1) \text{ cm}^{-1}$ .

The combined results demonstrate the usefulness of pdmH<sub>2</sub>, which is poorly explored in Fe<sup>III</sup> chemistry, to give interesting new high nuclearity products, and shows once again that the presence or absence of carboxylates can have a marked effect on the obtained products. We also find it of interest that preformed alkoxide-containing clusters can undergo mild hydrolysis to yield clusters not accessible directly from simple starting materials, suggesting a possible means of targeted nuclearity increase of known compounds.

Table 3-1. Crystallographic Data for **3-1**·7MeOH, **3-3**·7MeCN·H<sub>2</sub>O and **3-4**·7CH<sub>2</sub>Cl<sub>2</sub>.

parameter	<b>3-1</b>	<b>3-3</b>	<b>3-4</b>
formula	C <sub>66</sub> H <sub>99</sub> N <sub>8</sub> O <sub>42</sub> Cl <sub>5</sub> Fe <sub>8</sub>	C <sub>112</sub> H <sub>145</sub> Cl <sub>10</sub> Fe <sub>18</sub> N <sub>21</sub> O <sub>89</sub>	C <sub>62</sub> H <sub>79</sub> C <sub>114</sub> Fe <sub>9</sub> N <sub>6</sub> O <sub>39</sub>
fw, g mol <sup>-1</sup>	2300.58	4569.29	2531.26
crystal system	triclinic	monoclinic	monoclinic
space group	<i>P</i> $\bar{1}$	<i>P</i> 2 <sub>1</sub> / <i>n</i>	<i>C</i> <sub>2</sub>
<i>a</i> , Å	13.6178(14)	26.3129(17)	25.150(2)
<i>b</i> , Å	18.6824(19)	13.9984(9)	15.3942(13)
<i>c</i> , Å	19.069(2)	27.3080(18)	14.1502(12)
$\alpha$ , deg	78.547(2)	90	90
$\beta$ , deg	76.319(2)	116.9220(10)	115.8900(10)
$\gamma$ , deg	87.39(2)	90	90
<i>V</i> , Å <sup>3</sup>	4619.9(8)	8968.5(10)	4928.7(7)
<i>Z</i>	2	2	2
<i>T</i> , °C	173(2)	173(2)	173(2)
radiation, Å <sup>a</sup>	0.71073	0.71073	0.71073
$\rho_{\text{calc}}$ , g cm <sup>-3</sup>	1.654	1.692	1.706
$\mu$ , mm <sup>-1</sup>	1.457	1.657	1.747
<i>R</i> 1 <sup>b,c</sup>	0.0702	0.0850	0.0422
<i>wR</i> 2 <sup>d</sup>	0.1666	0.2196	0.1161

<sup>a</sup> Graphite monochromator. <sup>b</sup>  $I > 2\sigma(I)$ . <sup>c</sup>  $R1 = 100\Sigma(|F_o| - |F_c|)/\Sigma|F_o|$ . <sup>d</sup>  $wR2 = 100[\Sigma[w(F_o^2 - F_c^2)^2]/\Sigma[w(F_o^2)^2]]^{1/2}$ ,  $w = 1/[\sigma^2(F_o^2) + [(ap)^2 + bp]$ , where  $p = [\max(F_o^2, O) + 2F_c^2]/3$ .

Table 3-2. Bond Valence Sums for Selected O Atoms in Complex **3-3**.<sup>a</sup>

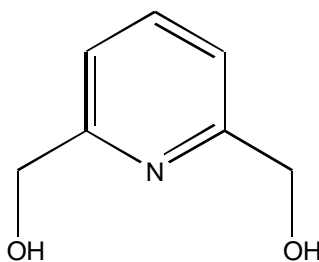
atom	BVS	assgt.	atom	BVS	assgt.
O1	1.79	O <sup>2-</sup>	O20	1.19	OH <sup>-</sup>
O2	1.82	O <sup>2-</sup>	O21	0.39	H <sub>2</sub> O
O3	2.11	O <sup>2-</sup>	O22	0.34	H <sub>2</sub> O
O18	1.11	OH <sup>-</sup>	O23	1.16	OH <sup>-</sup>
O19	1.14	OH <sup>-</sup>			

<sup>a</sup> The oxygen atom is an O<sup>2-</sup> if the BVS is ~1.8-2.0, an OH<sup>-</sup> if the BVS is ~1.0-1.2, and an H<sub>2</sub>O if the BVS is ~0.2-0.4.

Table 3-3. Bond Valence Sums for Selected O Atoms in Complex **3-4**.<sup>a</sup>

atom	BVS	assgt.
O1	1.17	OH <sup>-</sup>
O2	2.08	O <sup>2-</sup>
O3	2.02	O <sup>2-</sup>

<sup>a</sup> The oxygen atom is an O<sup>2-</sup> if the BVS is ~1.8-2.0, an OH<sup>-</sup> if the BVS is ~1.0-1.2, and an H<sub>2</sub>O if the BVS is ~0.2-0.4.



**pdmH<sub>2</sub>**

Figure 3-1. Structure of ligand: 2,6-pyridinedimethanol (pdmH<sub>2</sub>).

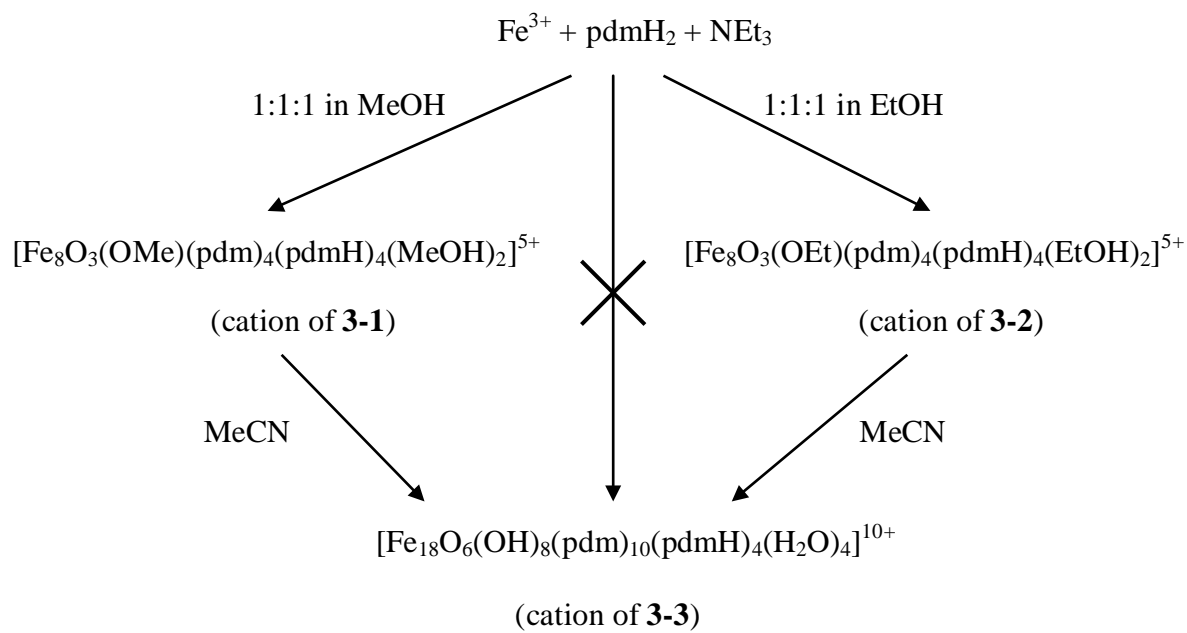


Figure 3-2. Summary of the reactions concerning **3-1**, **3-2** and **3-3**.

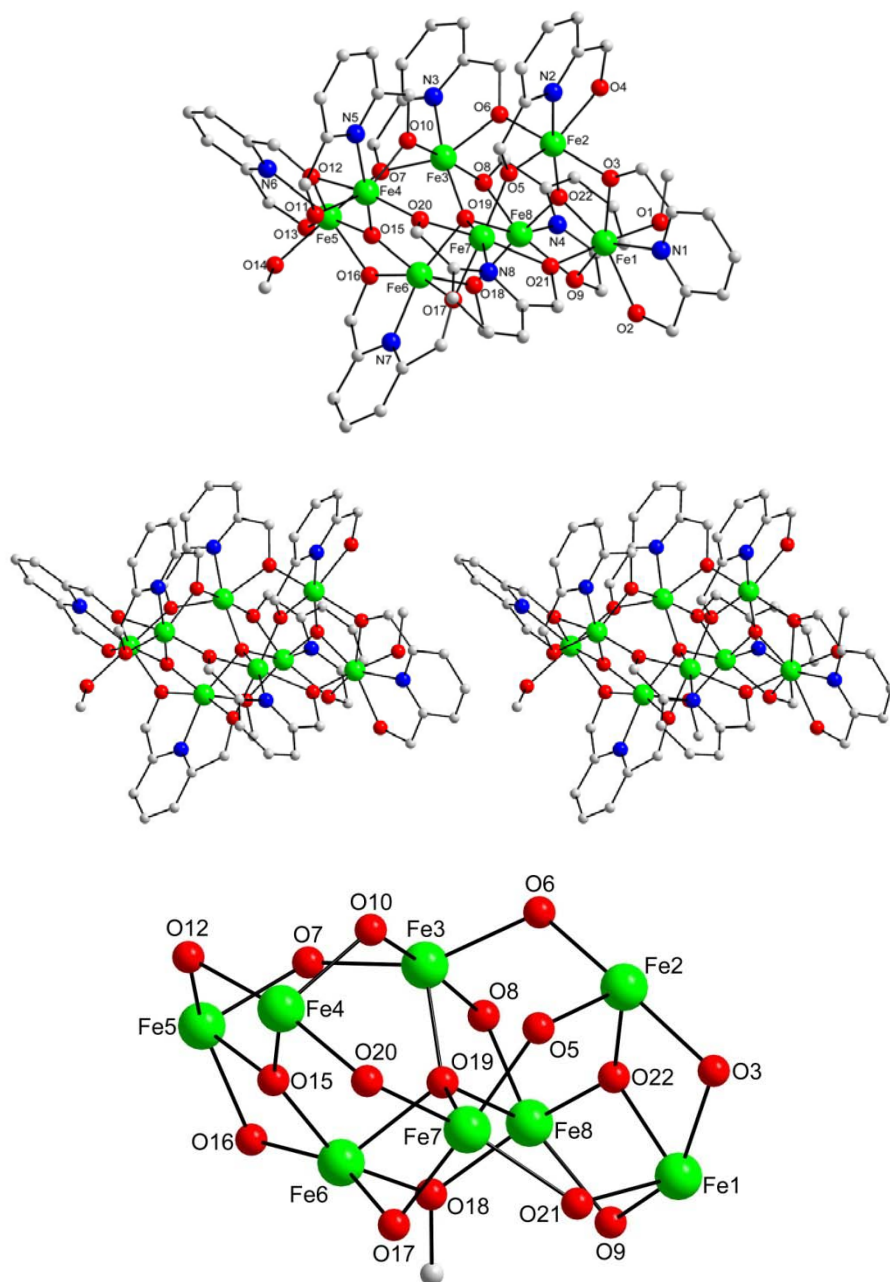


Figure 3-3. The structure of complex **3-1** (top), a stereopair (middle), and the labeled core. Hydrogen atoms have been omitted for clarity. Color code: Fe<sup>III</sup> green; O red; N blue; C gray.

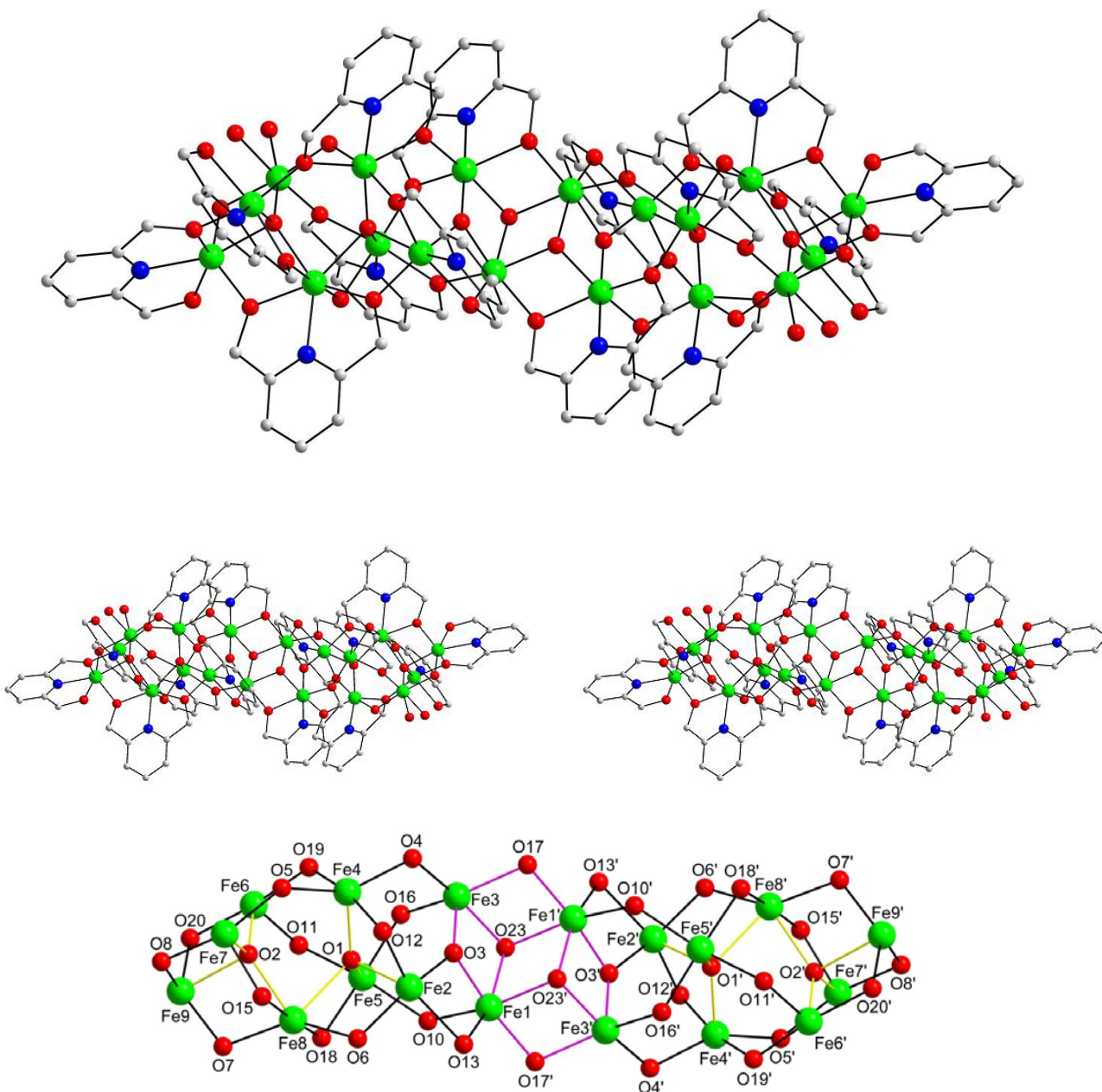


Figure 3-4. The structure of complex **3-3** (top), a stereopair (middle), and the labeled core. Hydrogen atoms have been omitted for clarity. Color code: Fe<sup>III</sup> green; O red; N blue; C gray.

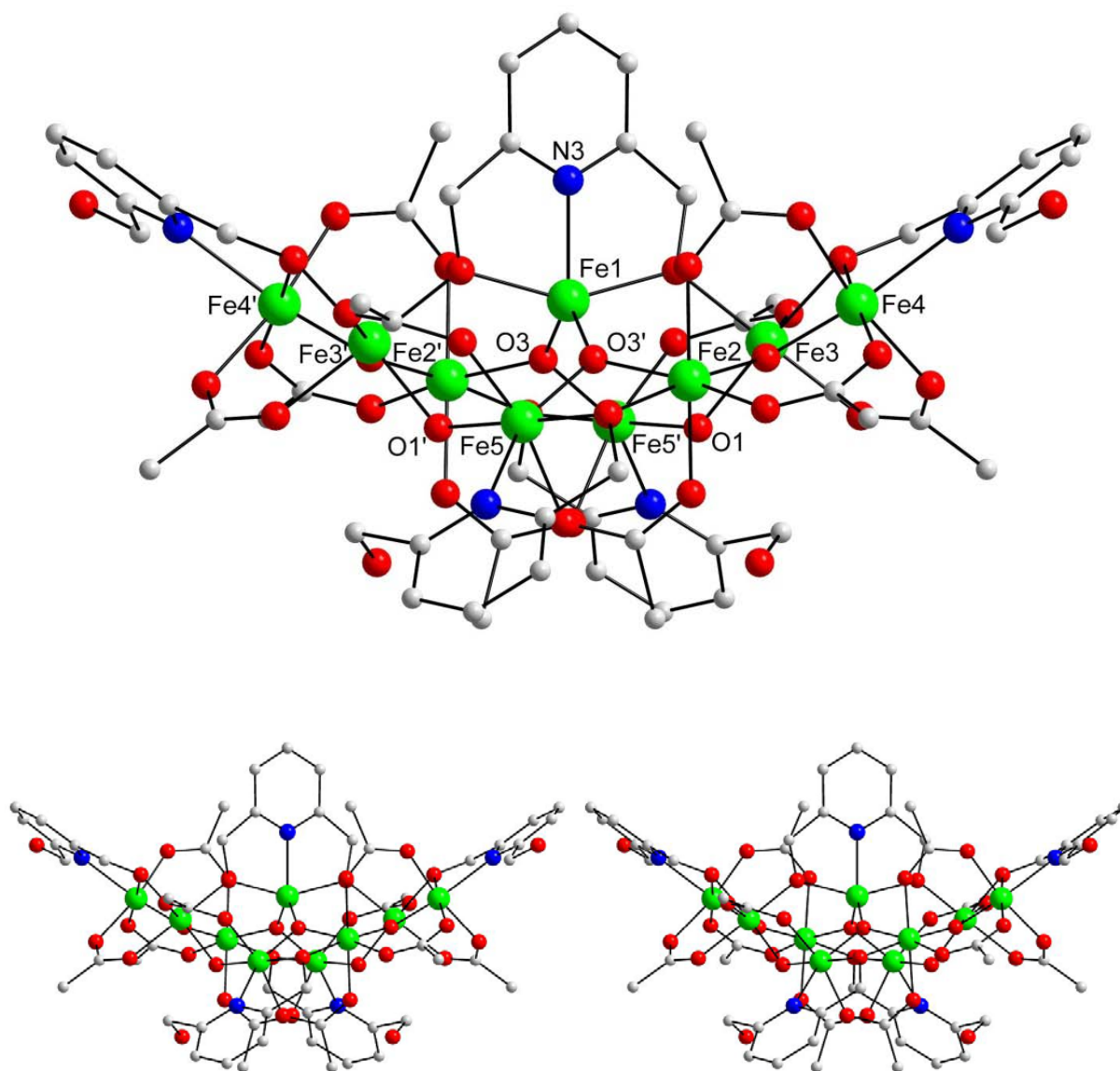


Figure 3-5. The structure of complex **3-4** (top), and a stereopair (bottom), viewed along the *ab*-plane. Hydrogen atoms have been omitted for clarity. Color code: Fe<sup>III</sup> green; O red; N blue; C grey.

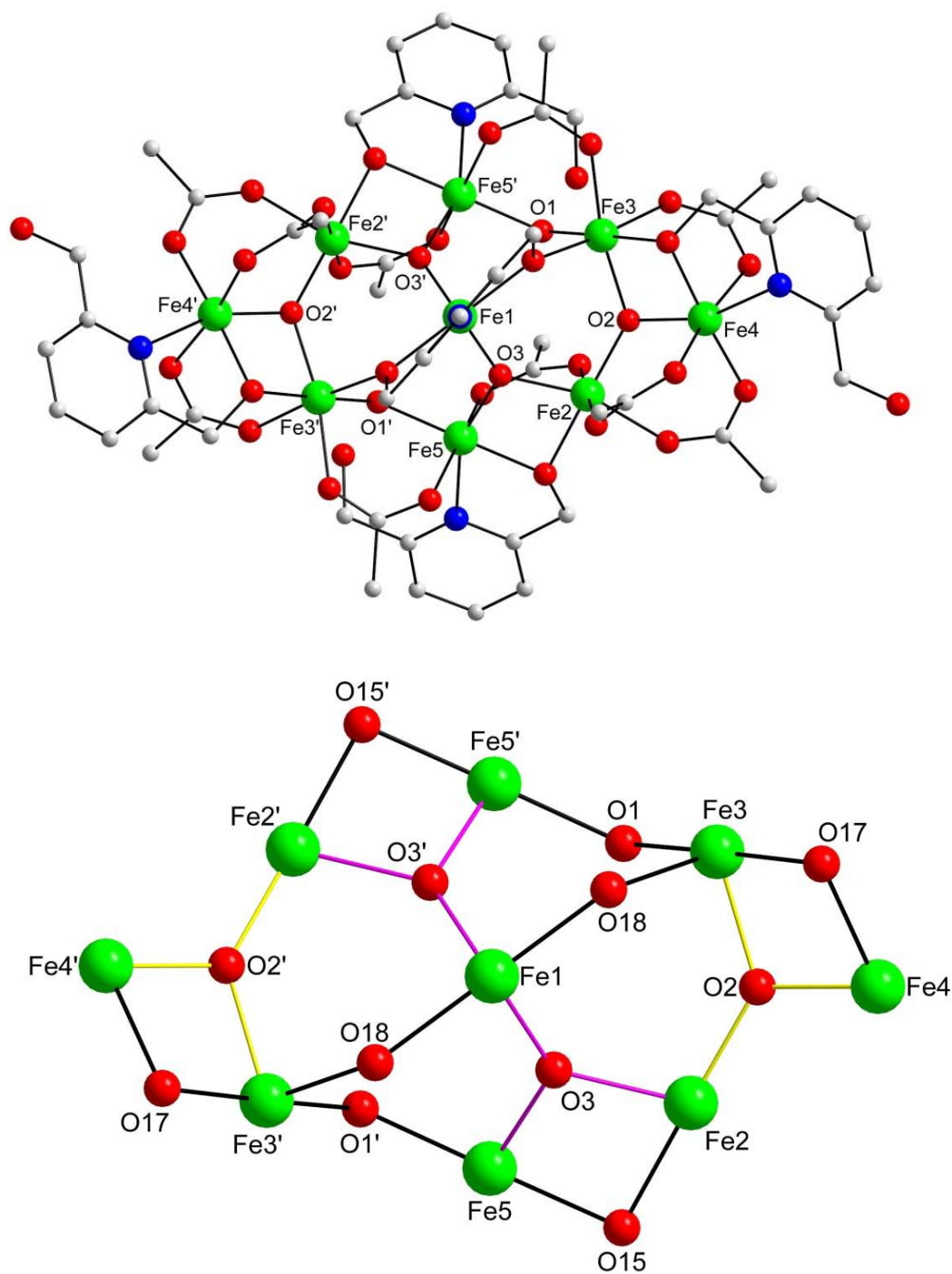


Figure 3-6. The structure of complex **3-4** (top), and its labeled core (bottom), viewed along the b-axis. Hydrogen atoms have been omitted for clarity. Color code: Fe<sup>III</sup> green; O red; N blue; C grey.

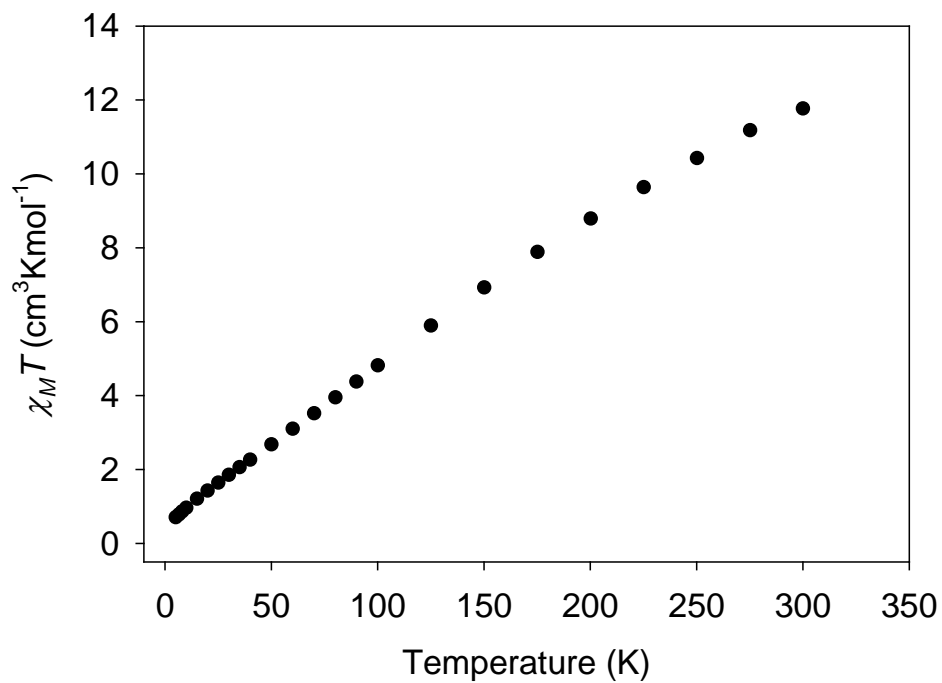


Figure 3-7. Plot of  $\chi_M T$  vs T for complex **3-1**.

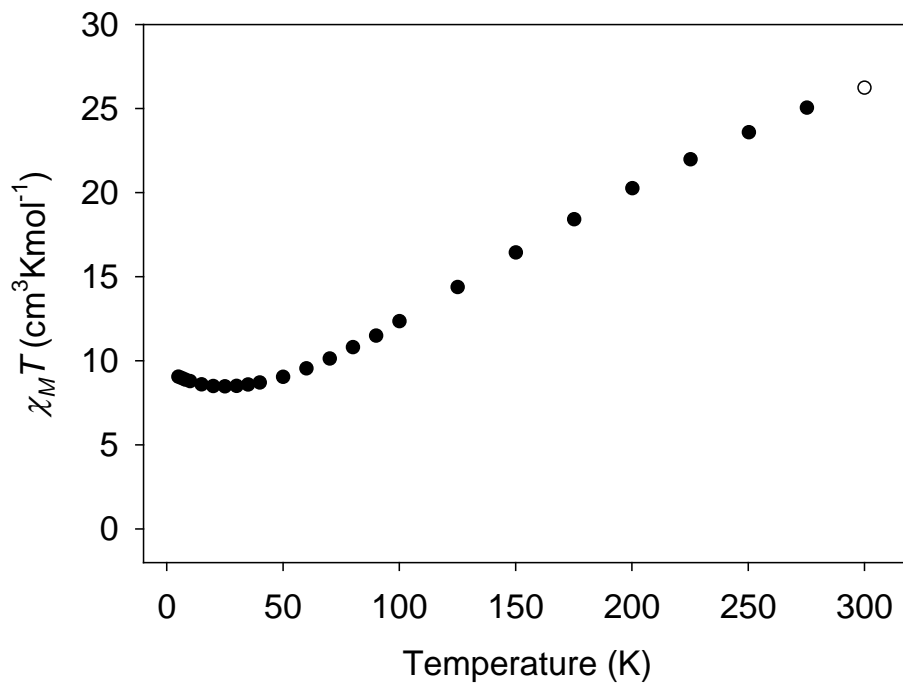


Figure 3-8. Plot of  $\chi_M T$  vs T for complex **3-3**.

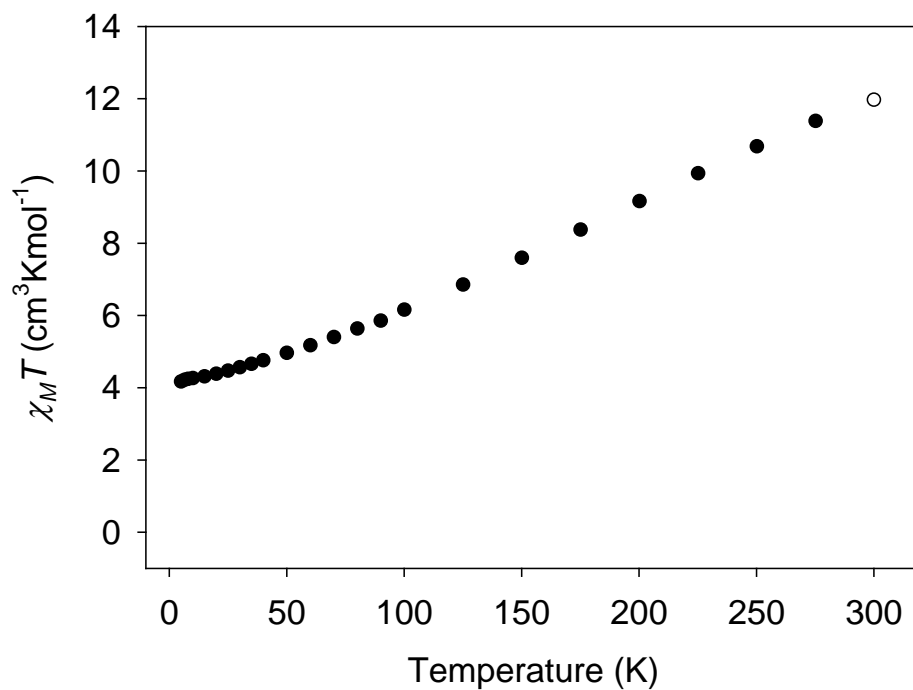


Figure 3-9. Plot of  $\chi_M T$  vs T for complex 3-4.

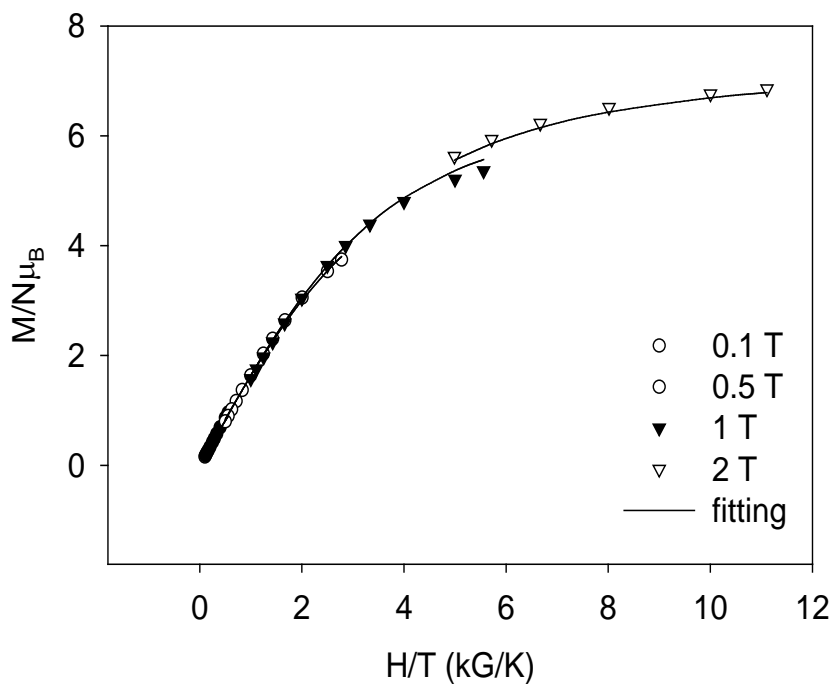


Figure 3-10. Reduced magnetization ( $M/N\mu_B$ ) vs  $H/T$  plot for complex 3-3. The solid lines are the fit of the data; see the text for the fit parameters.

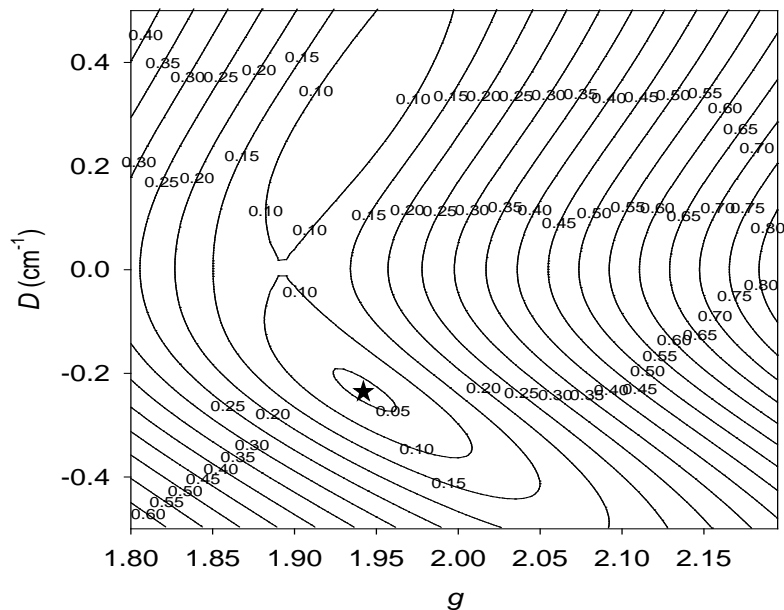


Figure 3-11. Two-dimensional contour plot of the root-mean-square error surface for the  $D$  vs  $g$  fit for complex **3-3**.

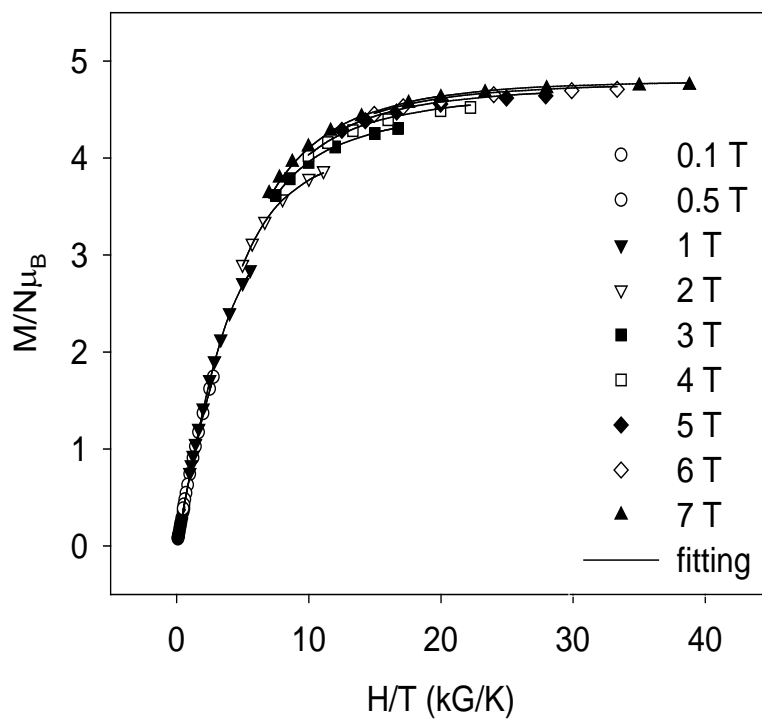


Figure 3-12. Reduced magnetization ( $M/N\mu_B$ ) vs  $H/T$  plot for complex **3-4**. The solid lines are the fit of the data; see the text for the fit parameters.

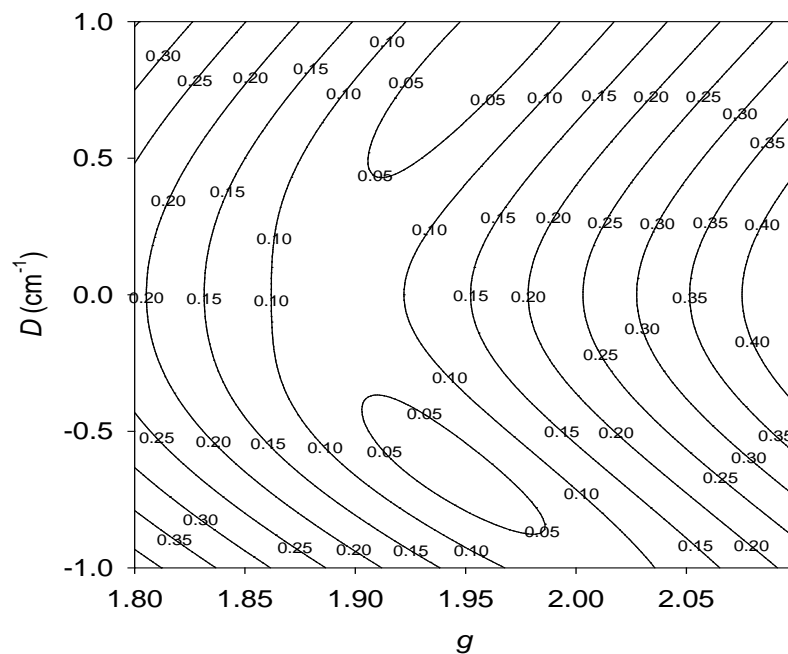


Figure 3-13. Two-dimensional contour plot of the root-mean-square error surface for the  $D$  vs  $g$  fit for complex 3-4.

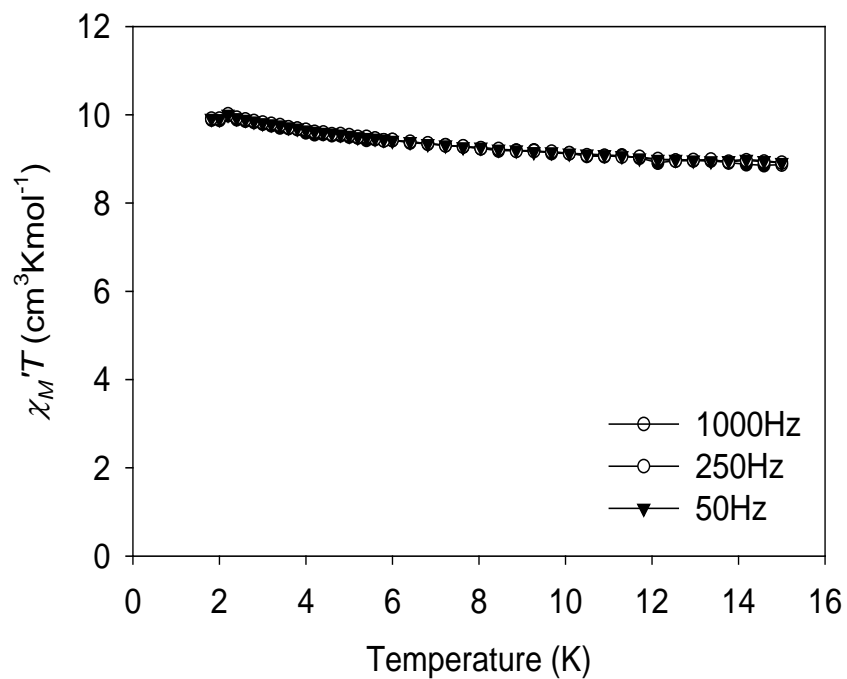


Figure 3-14. In-phase ac susceptibility ( $\chi_M'$ , plotted as  $\chi_M' T$  vs  $T$ ) of complex 3-3 in a 3.5 Oe ac field oscillating at the indicated frequencies.

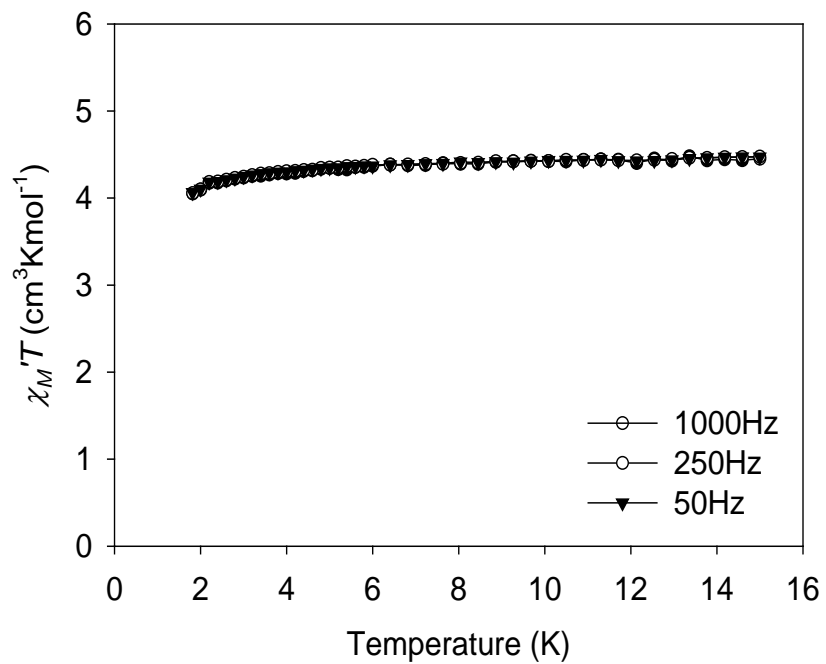


Figure 3-15. In-phase ac susceptibility ( $\chi_M'$ , plotted as  $\chi_M' T$  vs T) of complex **3-4** in a 3.5 Oe ac field oscillating at the indicated frequencies.

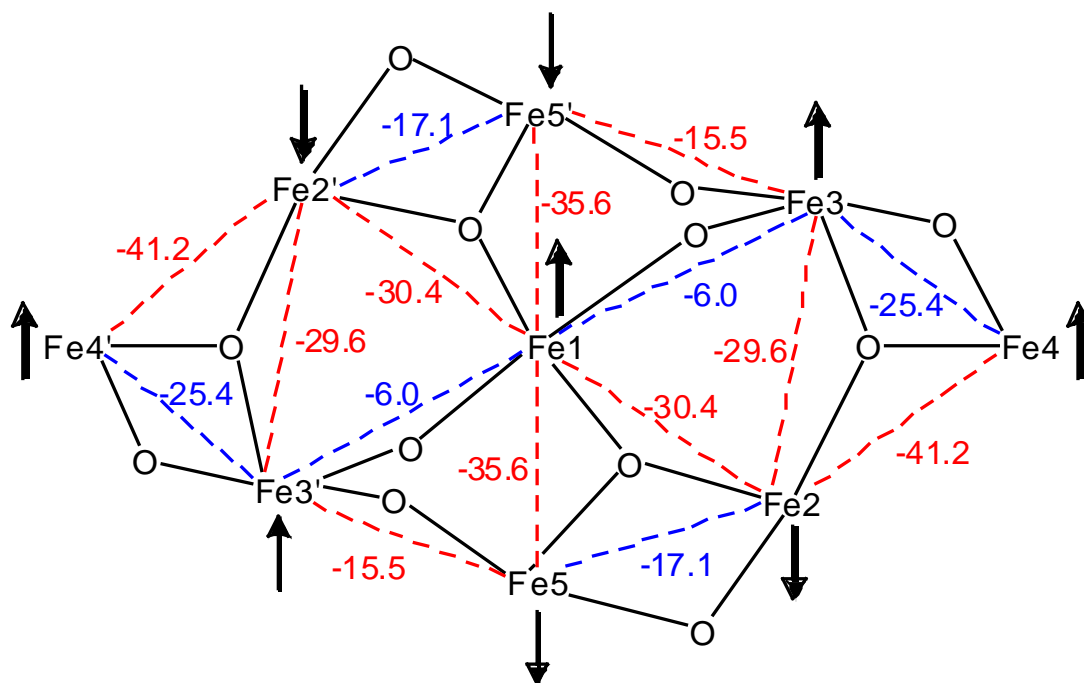


Figure 3-16. Rationalization of the  $S = 5/2$  ground state of **3-4**, on the basis of the predicted magnitudes of the various pairwise  $J_{ij}$  exchange constants and the resulting spin frustration effects; frustrated interactions are shown in blue. The viewpoint and atom labels are those of Figure 3-6 (bottom).

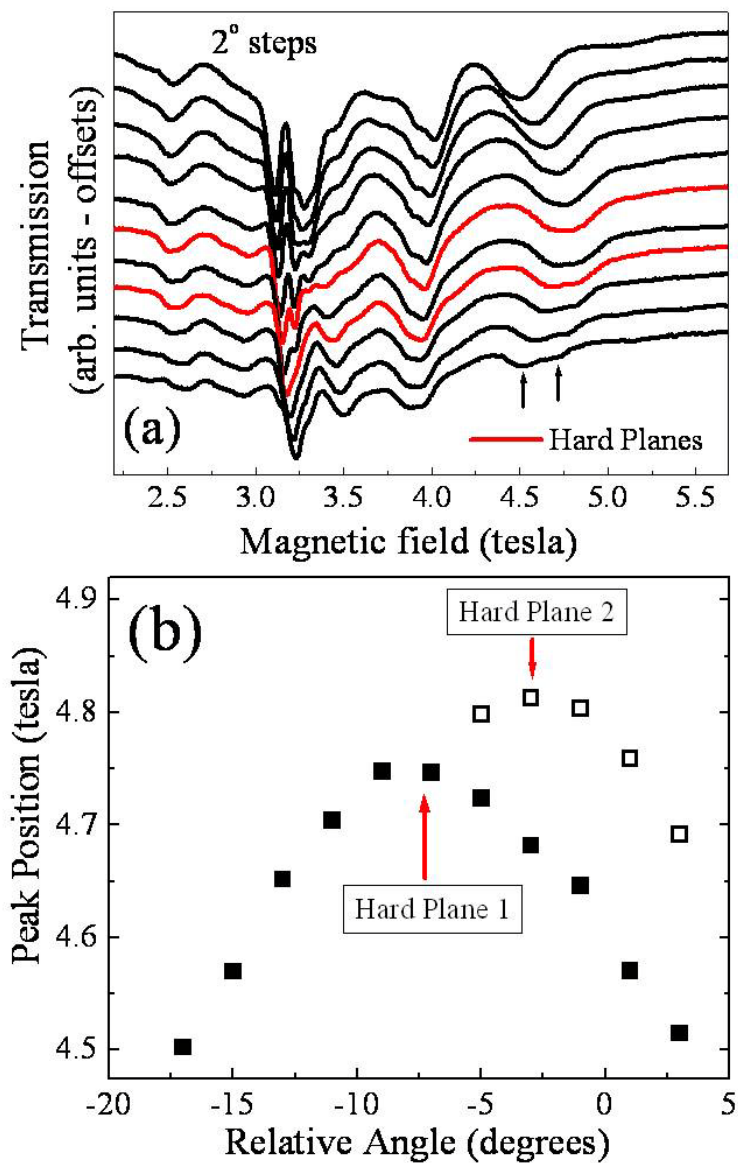


Figure 3-17. (a) Angle-dependent HFEPR spectra ( $2^\circ$  steps) for complex **3-4** obtained at 8 K and 91.3 GHz. The red traces correspond to the hard planes of two crystals in the twinned sample (see main text). (b) Plot of the peak positions associated with the highest field doublet observed in (a); see main text for explanation.

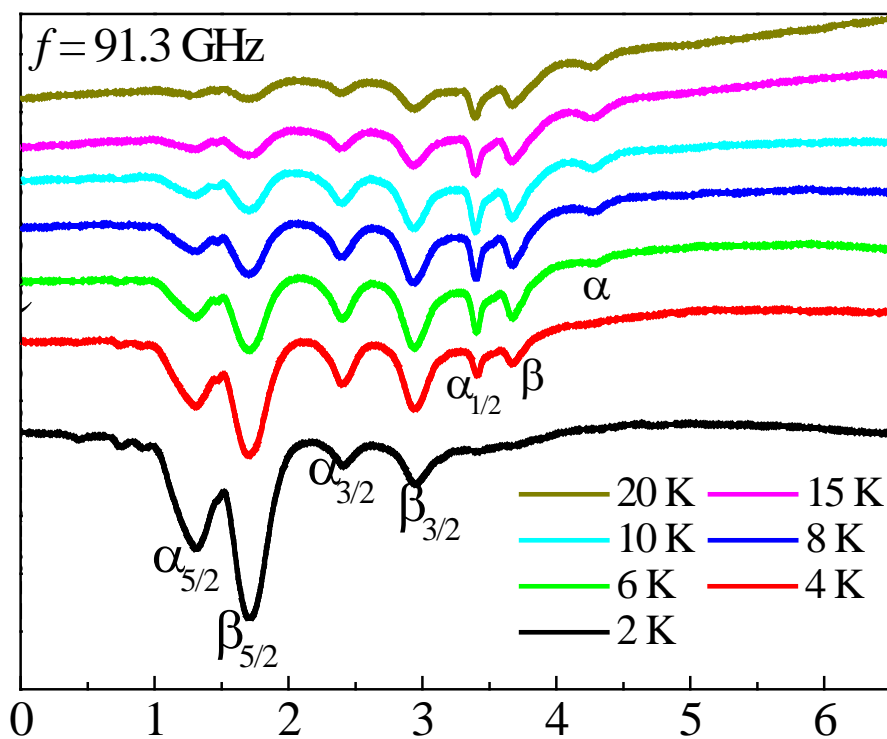


Figure 3-18. 91.3 GHz temperature dependent HFEPR spectra for complex **3-4** with the applied field aligned closer to the easy-axes of the two crystals in comparison to the data in Figure 3-17. The labels  $\alpha$  and  $\beta$  differentiate resonances originating from the two crystals in the twinned sample; for some of the peaks, subscripts are included with the label indicating the approximate magnitude of ms associated with the level from which the transition is excited.

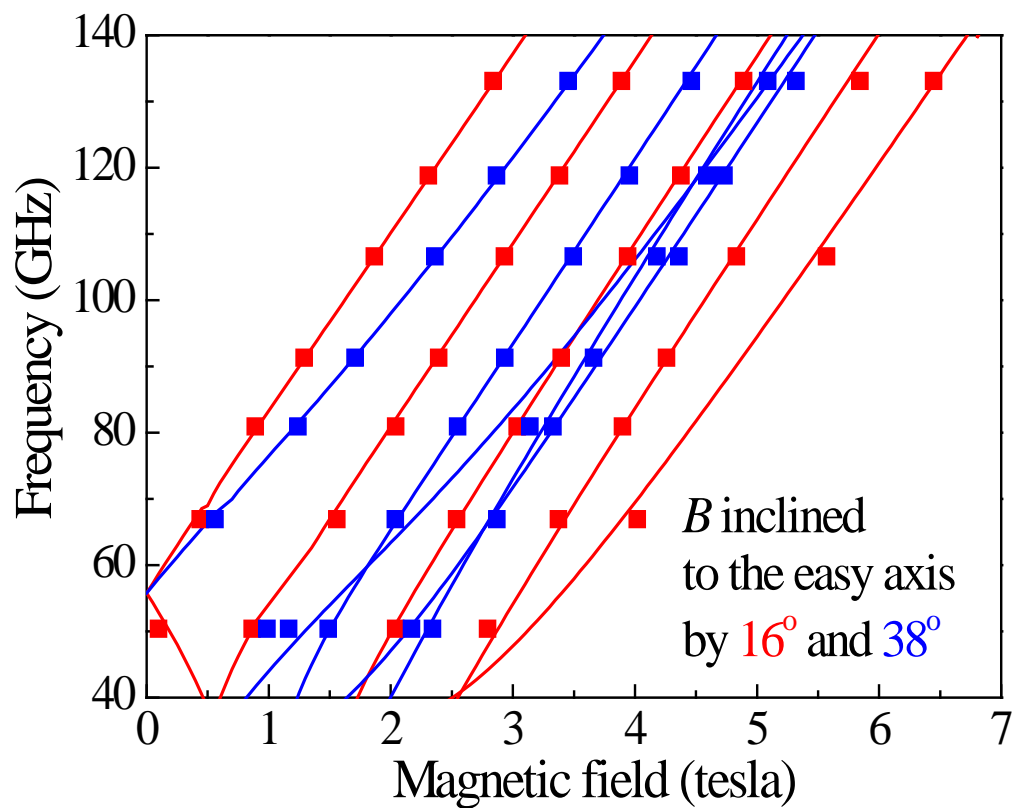


Figure 3-19. Frequency dependence of the HFEPR peak positions for complex **3-4** corresponding to the same field orientation as the spectra displayed in Figure 3-17. The red and blue squares correspond the  $\alpha$  and  $\beta$  resonances, respectively. Meanwhile, the red and blue curves represent the corresponding best simulations of the frequency dependence; see text for further explanation.

## CHAPTER 4

### MN CLUSTERS FROM THE USE OF BULKY PYRIDYLALCOHOLS: STRUCTURAL AND MAGNETIC STUDIES

#### 4.1 Introduction

The synthesis and characterization of 3*d* transition metal clusters with various nuclearities and metal topologies have been of great interest due to their interesting physical properties as well as the intrinsic architectural beauty and aesthetically pleasing structures they possess.<sup>196</sup> In particular, they often have large ground-state spin and easy-axis-type magnetic anisotropy, which provides a significant energy barrier to reversal of the magnetization vector. Thus, at sufficiently low temperatures they function as nanoscale magnetic particles, and they therefore represent a molecular approach to nanomagnetism.<sup>12, 13, 33-35, 197</sup> Such single-molecule magnets (SMMs) not only exhibit hysteresis in magnetization versus dc field scans, the diagnostic property of a classical magnet, but also fascinating quantum mechanical properties such as quantum tunneling of magnetization (QTM)<sup>18, 198</sup> and quantum phase interference.<sup>199-201</sup>

The first SMM discovered was  $[\text{Mn}_{12}\text{O}_{12}(\text{O}_2\text{CMe})_{16}(\text{H}_2\text{O})_4]$ ,<sup>15, 17, 18</sup> and its synthetic manipulation has provided a very well studied family of related complexes.<sup>12</sup> Since the discovery of  $\text{Mn}_{12}$  complexes, many polynuclear complexes containing 3*d* transition metals have been reported to be SMMs,<sup>124, 153, 154, 202, 203</sup> with most of them containing primarily  $\text{Mn}^{\text{III}}$  ions. This is because Mn clusters often display relatively large ground-state *S* values, as well as negative *D* values (easy-axis anisotropy) associated with the presence of Jahn-Teller (JT) distorted  $\text{Mn}^{\text{III}}$  atoms. In addition, some of these molecules have unique structures, such as the giant  $\text{Mn}_{84}$  SMM with a torus structure.<sup>204</sup>

For the above reasons, we and others have explored and successfully developed many new routes for the synthesis of polynuclear Mn complexes, with nuclearities as high as 84.<sup>204</sup> These procedures have included comproportionation reactions of simple starting materials,<sup>46, 205, 206</sup>

reductive aggregation of permanganate ions,<sup>207-209</sup> aggregation of clusters having smaller nuclearities,<sup>186, 210, 211</sup> reductive aggregation or fragmentation of preformed clusters,<sup>212, 213</sup> electrochemical oxidation,<sup>214-216</sup> and ligand substitution of preformed species,<sup>217-219</sup> among others. As part of this work, a wide variety of potentially chelating and/or bridging ligands were explored in order to foster the formation of high nuclearity products.<sup>44, 45, 147, 151,190, 220-238</sup> Among these are pyridyl alcohols, especially 2-(hydroxymethyl)pyridine (hmpH, Figure 4-1),<sup>44, 45, 147, 151,190</sup> which has proven to be an extremely versatile chelating and bridging group that has yielded a number of 3d metal clusters with various structural motifs, large *S* values, and SMM behavior. In order to explore new Mn cluster chemistry from such ligands, we have initiated a project in which the steric bulk of chelates such as hmpH has been increased by the addition of bulky groups at positions that we expect to influence the identity of obtained cluster products. In the present chapter, we describe the use in Mn cluster chemistry of an hmpH derivative in which two bulky phenyl or methyl groups have been added onto the CH<sub>2</sub> unit. The resulting molecules, diphenyl-hmpH (dphmpH; IUPAC name is diphenyl (pyridine-2-yl)methanol) and dimethyl-hmpH (dmhmpH, IUPAC name is 2-(pyridine-2-yl)propan-2-ol) are shown in Figure 4-1.

We anticipated that the use of dphmpH and dmhmpH in metal cluster chemistry would give products distinctly different from those with hmpH, and have therefore explored their use initially in Mn chemistry. Note that dphmpH has only been used for the synthesis of mononuclear Zr, W, and Mo complexes;<sup>239-241</sup> dmhmpH has only been employed for the synthesis of mononuclear complexes of V, Zr, Mo, and W, and dinuclear complexes of Ni and W.<sup>242-248</sup> In this work, we have deliberately targeted higher nuclearity Mn products by exploring reactions of dphmpH and dmhmpH with Mn<sup>II</sup> salts under slightly basic conditions. This has

successfully led to new Mn<sub>4</sub>, Mn<sub>6</sub>, Mn<sub>7</sub>, Mn<sub>11</sub>, and Mn<sub>12</sub> clusters, and their syntheses, structures, and magnetochemical characterization are described in this chapter.

## 4.2 Experimental Section

### 4.2.1 Syntheses

All preparations were performed under aerobic conditions except for the synthesis of dphmpH and dmhmpH, which were carried out as previously reported.<sup>249, 250</sup> All chemicals were used as received. *Safety note: Perchlorate salts are potentially explosive; such compounds should be synthesized and used in small quantities, and treated with utmost care at all times.*

**[Mn<sub>4</sub>O<sub>2</sub>(O<sub>2</sub>CBu<sup>t</sup>)<sub>5</sub>(dphmp)<sub>3</sub>] (4-1).** To a stirred solution of dphmpH (0.26 g, 1.0 mmol) and NEt<sub>3</sub> (0.42 mL, 3.0 mmol) in MeCN/MeOH (30 mL, 5:1 v/v) was added solid MnCl<sub>2</sub>·4H<sub>2</sub>O (0.20 g, 1.0 mmol) and NaO<sub>2</sub>CBu<sup>t</sup>·H<sub>2</sub>O (0.25 g, 2.0 mmol). The mixture was stirred overnight, filtered to remove NaCl, and the filtrate layered with Et<sub>2</sub>O (60 mL). X-ray quality crystals of **4-1**·2MeCN slowly grew over 5 days in 55% yield. These were collected by filtration, washed with cold MeCN (2 × 3 mL) and Et<sub>2</sub>O (2 × 5 mL), and dried under vacuum. Anal. Calc. (Found) for **4-1**·2MeCN·H<sub>2</sub>O (C<sub>83</sub>H<sub>93</sub>N<sub>5</sub>Mn<sub>4</sub>O<sub>15</sub>): C, 61.52 (61.10); H, 5.78 (5.99); N, 4.32 (3.93). Selected IR data (cm<sup>-1</sup>): 3446(mb), 3059(w), 3020(w), 2956(m), 2926(m), 2896(w), 2867(w), 2361(m), 2337(m), 1603(s), 1578(m), 1564(s), 1481(s), 1445(w), 1406(s), 1369(m), 1356(m), 1224(m), 1168(w), 1111(w), 1082(w), 1402(m), 1024(m), 953(w), 930(w), 907(w), 891(w), 778(m), 750(w), 703(m), 683(m), 659(m), 648(m), 635(m), 607(m), 597(m), 541(w), 525(w), 492(w), 463(w), 434(m).

**[Mn<sub>6</sub>O<sub>4</sub>(OMe)<sub>2</sub>(O<sub>2</sub>CPh)<sub>4</sub>(dphmp)<sub>4</sub>] (4-2). Method A.** To a stirred solution of dphmpH (0.26 g, 1.0 mmol) and NEt<sub>3</sub> (0.42 mL, 3.0 mmol) in MeCN/MeOH (30 mL, 5:1 v/v) was added solid Mn(O<sub>2</sub>CPh)<sub>2</sub> (0.33 g, 1.0 mmol). The resulting dark brown solution was stirred overnight, filtered, and the filtrate left undisturbed to concentrate slowly by evaporation. X-ray quality

crystals of **4-2**·3MeCN slowly grew over 2 weeks in 20% yield. These were collected by filtration, washed with cold MeCN (2 × 3 mL) and Et<sub>2</sub>O (2 × 5 mL), and dried under vacuum. Anal. Calc. (Found) for **4-2**·2H<sub>2</sub>O (C<sub>120</sub>H<sub>86</sub>N<sub>4</sub>Mn<sub>6</sub>O<sub>20</sub>): C, 60.73 (60.51); H, 4.30 (3.96); N, 2.78 (3.09). Selected IR data (cm<sup>-1</sup>): 3415(mb), 3057(w), 2935(w), 2739(w), 2677(w), 2491(w), 1598(s), 1561(s), 1489(w), 1475(w), 1445(w), 1389(s), 1251(w), 1170(m), 1044(m), 1024(m), 951(w), 928(w), 910(w), 841(w), 774(m), 707(m), 681(m), 661(m), 633(m), 607(m), 582(m), 529(m), 461(w), 433(w).

**Method B.** To a stirred solution of dphmpH (0.26 g, 1.0 mmol) and NEt<sub>3</sub> (0.42 mL, 3.0 mmol) in MeCN/MeOH (30 mL, 5:1 v/v) was added solid MnCl<sub>2</sub>·4H<sub>2</sub>O (0.20 g, 1.00 mmol) and NaO<sub>2</sub>CPh (0.29 g, 2.00 mmol). The mixture was stirred overnight, filtered to remove NaCl, and the filtrate left undisturbed to concentrate slowly by evaporation. X-ray quality crystals of **4-2**·3MeCN slowly grew over 2 weeks in 15% yield. These were collected by filtration, washed with cold MeCN (2 × 3 mL) and Et<sub>2</sub>O (2 × 5 mL), and dried under vacuum; the product was identified by IR spectral comparison as identical with material from Method A.

**[Mn<sub>11</sub>O<sub>7</sub>(OMe)<sub>7</sub>(O<sub>2</sub>CPh)<sub>7</sub>(dphmp)<sub>4</sub>(MeOH)<sub>2</sub>] (4-3).** **Method A.** To a stirred solution of dphmpH (0.26 g, 1.0 mmol) and NEt<sub>3</sub> (0.42 mL, 3.0 mmol) in MeCN/MeOH (30 mL, 1:29 v/v) was added solid Mn(O<sub>2</sub>CPh)<sub>2</sub> (0.33 g, 1.0 mmol). The resulting dark brown solution was stirred overnight, filtered, and the filtrate left undisturbed to concentrate slowly by evaporation. X-ray quality crystals of **4-3**·4MeCN slowly grew over 2 weeks in 25% yield. These were collected by filtration, washed with cold MeCN (2 × 3 mL) and Et<sub>2</sub>O (2 × 5 mL), and dried under vacuum. Dried solid analyzed as solvent-free. Anal. Calc. (Found) for **4-3** (solvent-free) (C<sub>130</sub>H<sub>120</sub>N<sub>4</sub>Mn<sub>11</sub>O<sub>34</sub>): C, 54.09 (53.89); H, 4.19 (3.98); N, 1.94 (1.91). Selected IR data (cm<sup>-1</sup>): 3417(mb), 3059(w), 2919(w), 2809(w), 1598(s), 1557(s), 1490(w), 1474(w), 1445(w), 1390(s),

1252(w), 1171(w), 1048(m), 953(w), 930(w), 910(w), 836(w), 773(w), 706(m), 680(m), 680(m), 657(w), 634(m), 592(m), 565(m), 468(w), 425(w).

**Method B.** To a stirred solution of dphmpH (0.26 g, 1.0 mmol) and  $\text{NEt}_3$  (0.42 mL, 3.0 mmol) in MeCN/MeOH (30 mL, 1:29 v/v) was added solid  $\text{MnCl}_2 \cdot 4\text{H}_2\text{O}$  (0.20 g, 1.0 mmol) and  $\text{NaO}_2\text{CPh}$  (0.29 g, 2.0 mmol). The mixture was stirred overnight, filtered to remove NaCl, and the filtrate left undisturbed to concentrate slowly by evaporation. X-ray quality crystals of **4-3**·3MeCN slowly grew over 2 weeks in 20% yield. These were collected by filtration, washed with cold MeCN ( $2 \times 3$  mL) and  $\text{Et}_2\text{O}$  ( $2 \times 5$  mL), and dried under vacuum; the product was identified by IR spectral comparison as identical with material from Method A.

**[Mn<sub>7</sub>O<sub>3</sub>(OH)<sub>3</sub>(O<sub>2</sub>CBu<sup>t</sup>)<sub>7</sub>(dmhmp)<sub>4</sub>] (4-4).** To a stirred solution of dmhmpH (0.14 g, 1.0 mmol) and  $\text{NEt}_3$  (0.14 mL, 1.0 mmol) in a solvent mixture comprised of MeCN/MeOH (27 mL, 25:2 v/v) was added solid  $\text{MnCl}_2 \cdot 4\text{H}_2\text{O}$  (0.20 g, 1.0 mmol) and  $\text{NaO}_2\text{CBu}^t \cdot \text{H}_2\text{O}$  (0.25 g, 2.0 mmol). The mixture was stirred overnight and filtered to remove NaCl, and the filtrate was left undisturbed to concentrate slowly by evaporation. X-ray quality crystals of **4-4**·7MeCN slowly grew over 2 weeks in 50% yield. These were collected by filtration, washed with cold MeCN ( $2 \times 3$  mL), and dried under vacuum. Anal. Calc. (Found) for **4-4**·MeCN ( $\text{C}_{69}\text{H}_{113}\text{N}_5\text{Mn}_7\text{O}_{24}$ ): C, 46.53 (46.93); H, 6.39 (6.32); N, 3.93 (3.51). Selected IR data ( $\text{cm}^{-1}$ ): 3423(wb), 2956(m), 2926(w), 2868(w), 1595(s), 1545(s), 1482(s), 1458(w), 1415(s), 1358(s), 1277(w), 1225(w), 1181(m), 1123(m), 1101(w), 1502(w), 1032(w), 982(m), 889(w), 782(m), 757(w), 741(w), 661(s), 611(m), 563(m), 516(w), 436(w).

**[Mn<sub>12</sub>O<sub>7</sub>(OH)(OMe)<sub>2</sub>(O<sub>2</sub>CPh)<sub>12</sub>(dmhmp)<sub>4</sub>(H<sub>2</sub>O)] (4-5).** **Method A.** To a stirred solution of dmhmpH (0.14 g, 1.0 mmol) and  $\text{NEt}_3$  (0.42 mL, 3.0 mmol) in a solvent mixture comprised of  $\text{CH}_2\text{Cl}_2/\text{MeOH}$  (31 mL, 30:1 v/v) was added solid  $\text{Mn}(\text{O}_2\text{CPh})_2$  (0.33 g, 1.0 mmol). The

resulting dark brown solution was stirred overnight and filtered, and the filtrate was layered with Et<sub>2</sub>O (60 mL). X-ray quality crystals of **4-5**·3CH<sub>2</sub>Cl<sub>2</sub> slowly grew over 2 weeks in 55% yield. These were collected by filtration, washed with Et<sub>2</sub>O (2 × 5 mL), and dried under vacuum. Anal. Calc. (Found) for **4-5**·3H<sub>2</sub>O (C<sub>118</sub>H<sub>119</sub>N<sub>4</sub>Mn<sub>12</sub>O<sub>42</sub>): C, 48.46 (48.34); H, 4.10 (3.84); N, 1.92 (1.83). Selected IR data (cm<sup>-1</sup>): 3434(mb), 3063(w), 2974(m), 2922(m), 2813(w), 1603(s), 1565(s), 1483(m), 1401(s), 1305(w), 1278(w), 1252(w), 1180(m), 1123(m), 1101(w), 1067(w), 1052(m), 1027(m), 978(m), 936(w), 885(w), 839(w), 816(w), 782(m), 717(s), 667(s), 620(s), 557(s), 463(m), 433(m).

**Method B.** To a stirred solution of dmhmpH (0.14 g, 1.0 mmol) and NEt<sub>3</sub> (0.42 mL, 3.0 mmol) in a solvent mixture comprised of MeCN/MeOH (30 mL, 5:1 v/v) was added solid Mn(O<sub>2</sub>CPh)<sub>2</sub> (0.33 g, 1.0 mmol). The resulting dark brown solution was stirred for 3 hours and filtered, and the filtrate was left undisturbed. Brown crystals were obtained after 3 days in 45 % yeild. These were collected by filtration, washed with cold MeCN (2 × 3 mL) and Et<sub>2</sub>O (2 × 5 mL), and dried under vacuum; the product was identified by IR spectral comparison with material from Method A.

**(HNEt<sub>3</sub>)[NaMn<sub>6</sub>O<sub>4</sub>(dmhmp)<sub>6</sub>(N<sub>3</sub>)<sub>4</sub>](ClO<sub>4</sub>)<sub>2</sub> (4-6).** To a stirred solution of dmhmpH (0.28 g, 2.0 mmol), NaN<sub>3</sub> (0.13 g, 2.0 mmol) and NEt<sub>3</sub> (0.28 mL, 2.0 mmol) in a solvent mixture comprised of MeCN/MeOH (21 mL, 20:1 v/v) was added solid Mn(ClO<sub>4</sub>)<sub>2</sub>·6H<sub>2</sub>O (0.72g, 2.0 mmol). The obtained solution was stirred for 2 hours, filtered, and the filtrate layered with Et<sub>2</sub>O. Red crystals of **4-6**·Et<sub>2</sub>O grew over a week in 50% yield. These were collected by filtration, washed with cold MeCN (2 × 3 mL) and Et<sub>2</sub>O (2 × 5 mL), and dried under vacuum. Anal. Calc. (Found) for **4-6**·Et<sub>2</sub>O (C<sub>58</sub>H<sub>92</sub>Cl<sub>2</sub>N<sub>19</sub>Mn<sub>6</sub>NaO<sub>19</sub>): C, 39.07 (39.29); H, 5.20 (4.82); N, 14.93 (15.14). Selected IR data (cm<sup>-1</sup>): 3438(wb), 2970(m), 2678(w), 2058(s), 1610(m), 1485(w),

1437(w), 1322(m), 1281(w), 1253(w), 1181(m), 1122(s), 1092(s), 1055(m), 1030(m), 986(m), 883(w), 790(w), 760(w), 740(w), 675(m), 662(s), 626(s), 603(m), 563(w), 530(w), 500(w), 425(w).

#### 4.2.2 X-ray Crystallography

Data were collected on a Siemens SMART PLATFORM equipped with a CCD area detector and a graphite monochromator utilizing Mo-K $\alpha$  radiation ( $\lambda = 0.71073 \text{ \AA}$ ). Suitable crystals of **4-1**·2MeCN, **4-2**·3MeCN, **4-3**·4MeCN, **4-4**·7MeCN, **4-5**·3CH<sub>2</sub>Cl<sub>2</sub>, and **4-6**·Et<sub>2</sub>O were attached to glass fibers using silicone grease and transferred to a goniostat where they were cooled to 173 K for data collection. Cell parameters were refined using up to 8192 reflections. A full sphere of data (1850 frames) was collected using the  $\omega$ -scan method (0.3° frame width). The first 50 frames were remeasured at the end of data collection to monitor instrument and crystal stability (maximum correction on  $I$  was < 1 %). Absorption corrections by integration were applied based on measured indexed crystal faces. The structure was solved by Direct Methods in *SHELXTL6*,<sup>64</sup> and refined on  $F^2$  using full-matrix least squares. The non-H atoms were treated anisotropically, whereas the H atoms were calculated in ideal positions and refined as riding on their respective C atoms.

For **4-1**·2MeCN, the asymmetric unit contains the Mn<sub>4</sub> cluster and two MeCN molecules. A total of 979 parameters were refined in the final least-squares cycle using 14826 reflections with  $I > 2\sigma(I)$  to yield R<sub>1</sub> and wR<sub>2</sub> of 6.28 and 15.09%, respectively.

For **4-2**·3MeCN, the asymmetric unit contains two half Mn<sub>6</sub> clusters, and three MeCN molecules. The latter were disordered and could not be modeled properly, thus program SQUEEZE,<sup>65</sup> a part of the PLATON package of crystallographic software, was used to calculate the solvent disorder area and remove its contribution to the overall intensity data. A total of 1171

parameters were refined in the final least-squares cycle using 6680 reflections with  $I > 2\sigma(I)$  to yield  $R_1$  and  $wR_2$  of 8.07 and 18.53%, respectively.

For **4-3**·4MeCN, the asymmetric unit contains the  $Mn_{11}$  cluster and four MeCN molecules. The latter were disordered and could not be modeled properly, thus program SQUEEZE was again used to calculate the solvent disorder area and remove its contribution to the overall intensity data. The O22 position of the  $Mn_{11}$  cluster is disordered between an OH and a methoxy group. The protons of the two coordinated MeOH groups were obtained from a difference Fourier map and refined freely. A total of 1637 parameters were refined in the final least-squares cycle using 12365 reflections with  $I > 2\sigma(I)$  to yield  $R_1$  and  $wR_2$  of 5.66 and 10.18%, respectively.

For **4-4**·7MeCN, the asymmetric unit consists of a  $Mn_7$  cluster and seven acetonitrile solvent molecules. The latter were disordered and could not be modeled properly, thus program SQUEEZE was used to calculate the solvent disorder area and remove its contribution to the overall intensity data. The three protons H4, 5 and 6, on O4, 5 and 6 were obtained from a Difference Fourier map and H4 and H6 were refined freely but H5 was refined riding on O5. A total of 915 parameters were refined in the final cycle of refinement using 14701 reflections with  $I > 2\sigma(I)$  to yield  $R_1$  and  $wR_2$  of 8.59 and 16.20%, respectively.

For **4-5**·3CH<sub>2</sub>Cl<sub>2</sub>, the asymmetric unit consists of a  $Mn_{12}$  cluster and three disordered dichloromethane solvent molecules. The latter were disordered and could not be modeled properly, thus program SQUEEZE was used to calculate the solvent disorder area and remove its contribution to the overall intensity data. The benzoate ligands at Carbon atoms 81 and 91 are disordered and each was refined in two positions with their site occupation factors fixed at 0.5 (after refining to near 50%). The phenyl rings of the disordered benzoate ligands were idealized

to a hexagonal shape. A total of 30912 parameters were refined in the final cycle of refinement using 16954 reflections with  $I > 2\sigma(I)$  to yield  $R_1$  and  $wR_2$  of 4.19 and 11.64%, respectively.

For **4-6**·Et<sub>2</sub>O, the asymmetric unit consists of 1/3 Mn<sub>6</sub>Na clusters, two 1/3 perchlorate anions, 1/3 triethylamino cation and a 1/3 ether molecule also located on a 3-fold rotation axis. Both anions, ether and the amino cation are disordered and each was refined in two parts with their site occupation factors tied to a total on 1. Each species lies on a 3-fold rotation axis. A total of 343 parameters were refined in the final cycle of refinement using 3565 reflections with  $I > 2\sigma(I)$  to yield  $R_1$  and  $wR_2$  of 2.93 and 7.30%, respectively. Unit cell data and details of the structure refinements for **4-1** to **4-3** are collected in Table 4-1, **4-4** to **4-6** in Table 4-2.

### 4.2.3 Other Studies

Infrared spectra were recorded in the solid state (KBr pellets) on a Nicolet Nexus 670 FTIR spectrometer in the 400-4000 cm<sup>-1</sup> range. Elemental analyses (C, H and N) were performed by the in-house facilities of the University of Florida, Chemistry Department.

Variable-temperature DC and AC magnetic susceptibility data were collected on a Quantum Design MPMS-XL SQUID susceptometer equipped with a 7 T magnet and operating in the 1.8–300 K range. Samples were embedded in solid eicosane to prevent torquing. Magnetization vs. field and temperature data was fit using the program MAGNET. Pascal's constants<sup>251</sup> were used to estimate the diamagnetic corrections, which were subtracted from the experimental susceptibilities to give the molar paramagnetic susceptibility ( $\chi_M$ ). Magnetic studies below 1.8 K were carried out on single crystals using a micro-SQUID apparatus operating down to 0.04 K.

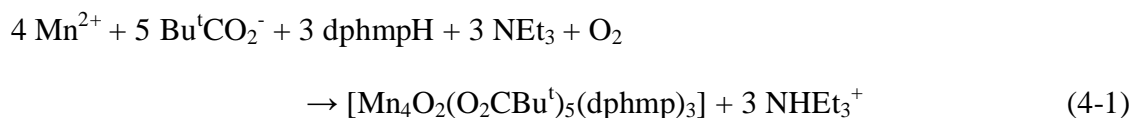
## 4.3 Results and Discussion

### 4.3.1 Syntheses

One strategy to make clusters containing Mn<sup>III</sup> ions is to oxidize simple Mn<sup>II</sup> salts by atmospheric O<sub>2</sub> under prevailing basic conditions in the presence of potentially chelating ligands. In Mn/hmpH chemistry, this strategy has led to the isolation of a series of clusters possessing an [Mn<sub>4</sub>(hmp)<sub>6</sub>]<sup>4+</sup> core.<sup>148-150, 252-254</sup> Therefore, we decided to also employ this strategy with the bulkier derivatives dmhmpH and dphmpH, and a variety of reaction ratios, reagents, and other conditions were investigated before the following procedures were developed.

#### 4.3.1.1 Reactions with dphmpH

The reaction of dphmpH with MnCl<sub>2</sub>·4H<sub>2</sub>O, NaO<sub>2</sub>CBu<sup>t</sup>·H<sub>2</sub>O and NEt<sub>3</sub> in a 1:1:2:3 ratio in MeCN/MeOH (5:1) afforded a brown solution from which was subsequently obtained the tetranuclear complex [Mn<sub>4</sub>O<sub>2</sub>(O<sub>2</sub>CBu<sup>t</sup>)<sub>5</sub>(dphmp)<sub>3</sub>] (**4-1**) in 55% yield; the mixed solvent system was used to ensure adequate solubility of all reagents. A picture of crystals of **4-1** is shown in Figure 4-2. The formation of **4-1** is summarized in eq. 4-1, assuming atmospheric O<sub>2</sub> as the oxidizing agent. Small variations in the Mn/dphmpH/Bu<sup>t</sup>CO<sub>2</sub><sup>-</sup> ratio still gave complex **4-1**, which clearly is a preferred product of these components and with pivalate. We also employed other

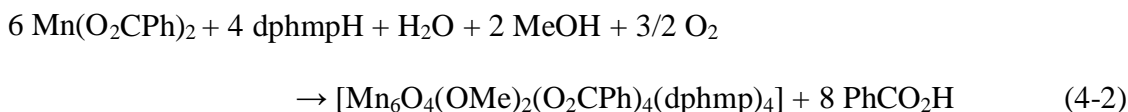


Mn salts, e.g., NO<sub>3</sub><sup>-</sup> or ClO<sub>4</sub><sup>-</sup>, but again obtained complex **4-1** in every case. We then investigated the identity of Mn/dphmp<sup>-</sup> products as a function of carboxylate groups.

The reaction of dphmpH with Mn(O<sub>2</sub>CPh)<sub>2</sub> and NEt<sub>3</sub> in a 1:1:3 ratio in MeCN/MeOH (5:1) gave a brown solution from which was subsequently isolated the hexanuclear complex [Mn<sub>6</sub>O<sub>4</sub>(OMe)<sub>2</sub>(O<sub>2</sub>CPh)<sub>4</sub>(dphmp)<sub>4</sub>] (**4-2**) in 20% yield (Method A). A picture of crystals of **4-2** is

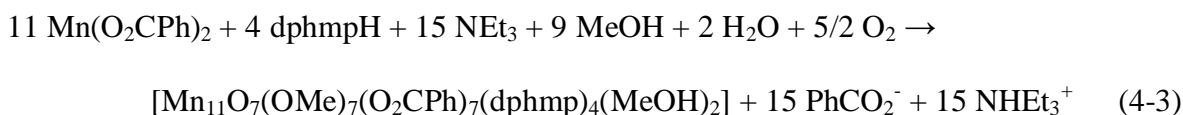
shown in Figure 4-3. The similar reaction of dphmpH with  $\text{MnCl}_2 \cdot 4\text{H}_2\text{O}$ ,  $\text{NaO}_2\text{CPh}$  and  $\text{NEt}_3$  in a 1:1:2:3 ratio in  $\text{MeCN}/\text{MeOH}$  (5:1) also gave **4-2** in a slightly lower yield of 15% (Method B).

Its formation via Method A is summarized in eq. 4-2. Increasing or decreasing the amount of dphmpH also gave complex **4-2**, but at a lower purity. The low yield of the reaction clearly



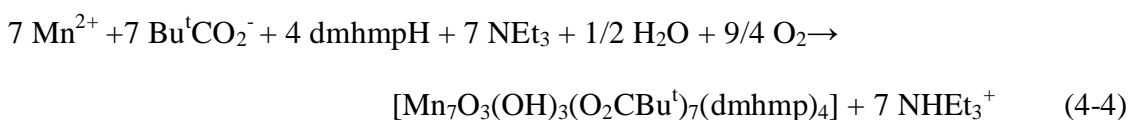
indicates, as with many other reactions in  $\text{Mn}^{\text{III}}$  chemistry, that the reaction solution probably contains a complicated mixture of several species in equilibrium, with factors such as relative solubility, lattice energies, crystallization kinetics, and others determining the identity of the product that crystallizes. One (or more) of these factors is undoubtedly the reason that changing the carboxylate used from pivalate to benzoate causes a major change in the identity of the product from **4-1** to **4-2**. Along these lines, it is worth noting that we were unable to isolate any pure product from the use of  $\text{Mn}(\text{O}_2\text{CMe})_2 \cdot 4\text{H}_2\text{O}$  in an otherwise identical reaction system.

We also investigated the identity of the product as a function of the solvent composition. When the reaction that gives **4-2** was carried out with less  $\text{MeOH}$ , the product was still **4-2** but in an appreciably lower yield. However, at the other extreme, when the reaction was performed in predominantly  $\text{MeOH}$ , namely  $\text{MeCN}/\text{MeOH}$  (1:29), the undecanuclear complex  $[\text{Mn}_{11}\text{O}_7(\text{OMe})_7(\text{O}_2\text{CPh})_7(\text{dphmp})_4(\text{MeOH})_2]$  (**4-3**) was obtained in 25% yield. The small amount of  $\text{MeCN}$  was found beneficial in obtaining well-formed, X-ray quality crystals. A picture of crystals of **4-3** is shown in Figure 4-4. Its formation is summarized in eq. 4-3.



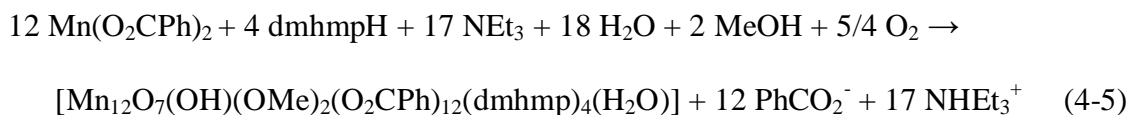
### 4.3.1.2 Reactions with dmhmpH

The reaction of dmhmpH with  $\text{MnCl}_2 \cdot 4\text{H}_2\text{O}$ ,  $\text{NaO}_2\text{CBu}^t \cdot \text{H}_2\text{O}$  and  $\text{NEt}_3$  in a 1:1:2:1 ratio in MeCN/MeOH afforded a brown solution from which was subsequently obtained the heptanuclear complex  $[\text{Mn}_7\text{O}_3(\text{OH})_3(\text{O}_2\text{CBu}^t)_7(\text{dmhmp})_4]$  (**4-4**) in 50%. A picture of crystals of **4-4** is shown in Figure 4-5. Its formation is summarized in eq. 4-4, assuming atmospheric  $\text{O}_2$  as the oxidizing agent. The mixed solvent system was needed to ensure adequate solubility for all reagents. Small variations in the Mn/dmhmpH/ $\text{Bu}^t\text{CO}_2^-$  ratio also gave complex **4-4**, which



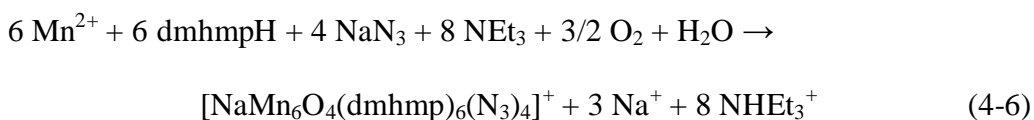
clearly is a preferred product of these components and with pivalate. We also employed other Mn salts, e.g.,  $\text{NO}_3^-$  or  $\text{ClO}_4^-$ , but again obtained complex **4-4** in every case. We then investigated the identity of product as a function of carboxylate groups.

The reaction of dmhmpH with  $\text{Mn}(\text{O}_2\text{CPh})_2$  and  $\text{NEt}_3$  in a 1:1:3 ratio in  $\text{CH}_2\text{Cl}_2/\text{MeOH}$  (30/1) gave a brown solution from which was isolated the dodecanuclear complex  $[\text{Mn}_{12}\text{O}_7(\text{OH})(\text{OMe})_2(\text{O}_2\text{CPh})_{12}(\text{dmhmp})_4(\text{H}_2\text{O})]$  (**4-5**) in 55% yield (Method A). A picture of crystals of **4-5** is shown in Figure 4-6. The same reaction in MeCN/MeOH (25/5) also gave **4-5** in a slightly lower yield of 45 % (Method B). Its formation is summarized in eq. 4-5.



In our previous work in Mn/hmpH chemistry, we often observed the strong tendency of the hmp<sup>-</sup> alkoxide arm to bridge two or even three Mn atoms, without the need for other chelating/bridging groups to form metal clusters. For example, a series of Mn clusters possessing an  $[\text{Mn}_4(\text{hmp})_6]^{4+}$  core were isolated from the reactions of  $\text{MnX}_2$  ( $\text{X} = \text{Cl}^-$ ,  $\text{NO}_3^-$ , or  $\text{ClO}_4^-$ ) and hmpH under basic conditions.<sup>148-150, 252-254</sup> Among the six hmp<sup>-</sup> alkoxide arms in the

$[\text{Mn}_4(\text{hmp})_6]^{4+}$  core, two are in the  $\mu_3$ -bridging modes and four are in the  $\mu$ -bridging mode. We therefore tried non-carboxylate reactions using dmhmpH to see whether identical or similar non-carboxylate clusters with  $\mu$ -/ $\mu_3$ - alkoxide arms of dmhmp<sup>-</sup> are obtained. We have attempted a variety of dmhmpH reactions by differing Mn starting materials, reagent ratios, solvents, and other conditions; however, we were unable to isolate any pure, crystalline materials from these non-carboxylate reactions. Pure, crystalline materials were only isolated after the addition of carboxylate groups to the reactions, as stated above. The use of azide is an exception to this statement; when NaN<sub>3</sub> was added to the non-carboxylate reactions, a Mn/dmhmp<sup>-</sup>/N<sub>3</sub><sup>-</sup> product was successfully isolated. The reaction of dmhmpH with Mn(ClO<sub>4</sub>)<sub>2</sub>·6H<sub>2</sub>O, NaN<sub>3</sub>, and NEt<sub>3</sub> in a 1:1:1:1 ratio in MeCN/MeOH (20:1) afforded a reddish brown solution from which was subsequently obtained the hexanuclear complex (HNEt<sub>3</sub>)[NaMn<sub>6</sub>O<sub>4</sub>(dmhmp)<sub>4</sub>(N<sub>3</sub>)<sub>4</sub>](ClO<sub>4</sub>)<sub>2</sub> (**4-6**) in 50% yield; the mixed solvent system was used to ensure the adequate solubility of all reagents. A picture of crystals of **4-6** is shown in Figure 4-7. The formation of **4-6** is summarized in eq. 4-6



Interestingly, the use of hmpH in an otherwise identical reaction system has led to the isolation of [Mn<sub>10</sub>O<sub>4</sub>(N<sub>3</sub>)<sub>4</sub>(hmp)<sub>12</sub>](ClO<sub>4</sub>)<sub>2</sub>·MeCN (**4-7**).<sup>44</sup> Both **4-6** and **4-7** present very symmetric structures, and **4-6** is the inner core of **4-7** (vide infra); i.e., by using the bulky derivative of hmpH, part of the core of the known structure was isolated.

### 4.3.2 Description of Structures

The partially labeled structure of [Mn<sub>4</sub>O<sub>2</sub>(O<sub>2</sub>CBu<sup>t</sup>)<sub>5</sub>(dphmp)<sub>3</sub>] (**4-1**) is shown in Figure 4-8; selected interatomic distances and angles are listed in Table A-7.

Complex **4-1** crystallizes in the rare triclinic space group *P1* and possesses a near-planar Mn<sub>4</sub> unit bridged by μ<sub>3</sub>-O<sup>2-</sup> ions O1 and O2 above and below the Mn<sub>4</sub> plane. A [Mn<sub>4</sub>(μ<sub>3</sub>-O)<sub>2</sub>]<sup>8+</sup> core containing an exactly planar Mn<sub>4</sub> rhombus is what we have described as a ‘planar butterfly’ unit in the past,<sup>38, 255, 256</sup> to emphasize its relationship to the related [Mn<sub>4</sub>O<sub>2</sub>]<sup>8+</sup> complexes with a true butterfly (i.e. V-shaped) Mn<sub>4</sub> topology, such as that in the hmp<sup>-</sup> cluster anion [Mn<sub>4</sub>O<sub>2</sub>(O<sub>2</sub>CPh)<sub>7</sub>(hmp)<sub>2</sub>]<sup>-</sup> (**4-8**, Figure 4-9) with virtual C<sub>2</sub> symmetry.<sup>257</sup> In both the butterfly and planar-butterfly complexes obtained previously, including **4-8**, each Mn<sub>2</sub> edge of the [Mn<sub>4</sub>(μ<sub>3</sub>-O)<sub>2</sub>] core is bridged by one or two carboxylate groups and each ‘wingtip’ Mn atom is chelated by bidentate ligand. The butterfly vs planar-butterfly difference is caused by the presence or absence, respectively, of a η<sup>1</sup>:η<sup>1</sup>:μ-carboxylate group bridging the two central (‘body’) Mn atoms. Complex **4-1** is overall similar to these previous complexes in possessing a dphmp<sup>-</sup> chelate on wingtip atoms Mn1 and Mn2, and bridging Bu<sup>t</sup>CO<sub>2</sub><sup>-</sup> groups, but differs in having an unusually low symmetry as a result of (i) possessing a third dphmp<sup>-</sup> group in a η<sup>1</sup>:η<sup>2</sup>:μ bridging mode, chelating ‘body’ atom Mn3 and bridging to Mn2 with its deprotonated alkoxide arm in a very asymmetric manner (Mn3-O5 = 1.887(3) Å vs Mn2-O5 = 2.505(3) Å); and (ii) the carboxylate group bridging Mn2 and Mn4 also bonds weakly to Mn3 (Mn3-O12 = 2.784(3) Å vs Mn4-O12 = 2.282(3) Å) and is thus in an approximately η<sup>2</sup>:η<sup>1</sup>:μ<sub>3</sub> binding mode. As a result, the Mn<sub>4</sub> topology of **4-1** is intermediate between the true planar-butterfly and V-shaped butterfly topologies observed previously. Charge considerations and the metric parameters indicate all Mn atoms to be Mn<sup>III</sup>, as confirmed by BVS calculations<sup>258, 259</sup> (Table 4-3). All Mn atoms are six-coordinate with near-octahedral geometries, and undergo the expected Jahn-Teller (JT) axial elongation; the elongation axes at Mn2 and Mn3 contain the long bonds mentioned above, with O12 also lying on the JT elongation axis of Mn4. For Mn1, the JT axis is O6-Mn1-O8.

The partially labeled structure and a stereoview of  $[\text{Mn}_6\text{O}_4(\text{OMe})_2(\text{O}_2\text{CPh})_4(\text{dphmp})_4]$  (**4-2**) are presented in Figure 4-10; selected interatomic distances and angles are listed in Table A-8. Complex **4-2** crystallizes in the triclinic space group  $P\bar{1}$ , with two essentially superimposable independent molecules in the unit cell, both lying on inversion centers; only one will therefore be discussed below. The centrosymmetric molecule consists of a  $[\text{Mn}_6\text{O}_4(\text{OMe})_2]^{8+}$  core with peripheral ligation provided by six bridging  $\text{PhCO}_2^-$  and four bidentate, chelating  $\text{dphmp}^-$  groups. The core has a face-sharing double-cubane structure, containing two  $\mu_3\text{-O}^{2-}$ , two  $\mu_4\text{-O}^{2-}$ , and two  $\mu_3\text{-MeO}^-$  ions bridging the six Mn atoms. This is a very unusual and very rare structural type, and there has been only one previous report of a complex with this dicubane-like  $\text{Mn}_6$  core, namely  $[\text{Mn}_6\text{O}_4(\text{OMe})_2(\text{OAc})_4(\text{Mesalim})_4]$  ( $\text{Mesalim}^- = \text{methyl salicylimidate anion}$ ).<sup>260</sup> The Mn atoms in **4-2** are all six-coordinate with near-octahedral geometry, and charge considerations and the metric parameters indicate they are all  $\text{Mn}^{\text{III}}$ , as confirmed by BVS calculations (Table 4-4). The  $\text{Mn}^{\text{III}}$  atoms thus all display JT axial elongations. Normally, the latter avoid Mn-oxide bonds, almost always the strongest and shortest in the molecule, but this is not possible for every Mn atom in **4-2** because of the double-cubane topology: for Mn2 and Mn3 (and their symmetry related partners), the JT axes are those containing the O atoms of the  $\mu_3\text{-MeO}^-$  ions, but for Mn1 and Mn1', the JT elongation axes contain a  $\mu_4\text{-O}^{2-}$  ion O2' or O2, respectively; the location of all JT axes are indicated as yellow bonds in Figure 4-4. The JT axes of Mn1, Mn1', Mn3, and Mn3' are oriented nearly parallel to each other, and perpendicular to those of Mn2 and Mn2'; they are thus all oriented in the xy planes, if the z axis is defined as the long axis of the double-cubane. There are no significant intermolecular interactions.

The complete structure and a stereoview of  $[\text{Mn}_{11}\text{O}_7(\text{OMe})_7(\text{O}_2\text{CPh})_7(\text{dphmp})_4(\text{MeOH})_2]$  (**4-3**) are shown in Figure 4-11, and its labeled core in Figure 4-12; selected interatomic distances

and angles are listed in Table A-9. Complex **4-3** possesses a  $[\text{Mn}_{11}(\mu_4\text{-O})_4(\mu_3\text{-O})_5(\mu\text{-OR})_6]$  core containing four  $\mu_4\text{-O}^{2-}$  (O30, O31, O33, and O34), three  $\mu_3\text{-O}^{2-}$  (O28, O29 and O32), two  $\mu_3\text{-MeO}^-$  (O17 and O19), five  $\mu\text{-MeO}^-$  (O18, O20, O21, O22, and O25), and one  $\mu\text{-RO}^-$  alkoxide arm (O1) of a  $\eta^1:\eta^2:\mu\text{-dphmp}^-$  group that is chelating on Mn2 and bridging to Mn3 in a very asymmetric manner (Mn2-O1 = 1.879(1) Å vs Mn3-O1 = 2.415(2) Å). The other three dphmp<sup>-</sup> groups are bound as  $\eta^2$  chelates. Six of the seven benzoates are bridging two Mn<sup>III</sup> atoms in the common  $\eta^1:\eta^1:\mu$ -bridging mode, and the seventh is bound terminally to Mn<sup>II</sup> atom Mn11 and hydrogen-bonds to one of the two terminal MeOH groups on Mn11 that complete the ligation. The Mn oxidation states were deduced from charge considerations and the metric parameters, and confirmed by BVS calculations (Table 4-5).

The core of **4-3** can be described as consisting of a  $[\text{Mn}_4\text{O}_3(\text{OMe})]$  cubane (Mn4, Mn7, Mn8, and Mn9) linked on one side to the Mn<sup>II</sup> atom (Mn11) by a cubane  $\text{O}^{2-}$  and two  $\mu\text{-MeO}^-$  groups. On the other side, the cubane face is linked to a  $[\text{Mn}_5\text{O}_7]$  unit which can be described as a central  $[\text{Mn}_4\text{O}_3]$  defective cubane (Mn2, Mn3 and Mn5) sharing two of its faces with two other defective cubanes (Mn1, Mn2, Mn5 and Mn3, Mn5, Mn6), the latter of which is linked by  $\mu_3\text{-O}^{2-}$  ion O28 to another Mn atom (Mn10) that is also attached to the cubane by a  $\mu\text{-MeO}^-$  group. It is thus interesting that **4-3** bears some structural similarity to **4-2** in containing a cubane unit. Complex **4-3** is the first example of this low symmetry Mn<sub>11</sub> topology, and in fact joins only a very small family of Mn/O clusters with a nuclearity of eleven.<sup>50, 261</sup>

The structure and a stereoview of  $[\text{Mn}_7\text{O}_3(\text{OH})_3(\text{O}_2\text{CBu}^t)_7(\text{dmhmp})_4]$  (**4-4**) are shown in Figure 4-13, and its core in Figure 4-14. Selected interatomic distances and angles are listed in Table A-10. The complex contains an  $[\text{Mn}_7(\mu_4\text{-O})(\mu_3\text{-O})_2(\mu\text{-O})_5]$  core comprising a  $[\text{Mn}_4(\mu_3\text{-O})_2]$  butterfly-like unit and a  $[\text{Mn}_4(\mu_4\text{-O})]$  tetrahedral unit fused at shared Mn atom Mn1 (Figure 4-

14). Note that the butterfly unit is related to  $[\text{Mn}_4\text{O}_2(\text{O}_2\text{CPh})_7(\text{hmp})_2]^-$  (**4-8**, Figure 4-9), which has an  $\text{hmp}^-$  group chelating to each ‘wing-tip’  $\text{Mn}^{\text{III}}$  atom, as do two of the  $\text{dmhmp}^-$  groups in **4-4**. One of the latter and the two other  $\text{dmhmp}^-$  groups each bound in a  $\eta^1:\eta^2:\mu$  mode, chelating to a  $\text{Mn}^{\text{III}}$  of the tetrahedral unit and bridging with their O atom to the  $\text{Mn}^{\text{II}}$  atom, Mn7. Two additional  $\text{OH}^-$  ions, O4 and O5, bridge between the ‘body’ Mn atoms of the butterfly unit and Mn5 and Mn2, respectively. Ligation is completed by six  $\eta^1:\eta^1:\mu$  pivalate groups bridging  $\text{Mn}^{\text{III}}\text{Mn}^{\text{III}}$  pairs, a chelating pivalate on  $\text{Mn}^{\text{II}}$  atom Mn7, and a terminal  $\text{OH}^-$  ion (O6) on Mn6.

Charge considerations, the metric parameters, and the presence of  $\text{Mn}^{\text{III}}$  Jahn-Teller (JT) distortions (axial elongations) indicate a  $\text{Mn}^{\text{II}}\text{Mn}^{\text{III}}_6$  description, as confirmed by bond valence sum (BVS) calculations (Table 4-6). BVS calculations were also performed on the inorganic O atoms to identify their degree of protonation and thus distinguish  $\text{O}^{2-}$ ,  $\text{OH}^-$ , and  $\text{H}_2\text{O}$  situations (Table 4-7). These confirm three  $\text{O}^{2-}$  ions (one  $\mu_4\text{-O}^{2-}$  (O2) and two  $\mu_3\text{-O}^{2-}$  (O1 and O3) ions), and three  $\text{OH}^-$  ions (a terminal  $\text{OH}^-$  (O6) and two  $\mu\text{-OH}^-$  O4 and O5 ions). The BVS value of 0.63 for O6 is a little lower than expected for a  $\text{OH}^-$  ion, but is consistent with it acting as an acceptor atom for two hydrogen-bonds with  $\mu\text{-OH}^-$  ions O4 and O5 ( $\text{O4}\dots\text{O6} = 2.711(5)$  Å,  $\text{O5}\dots\text{O6} = 2.767(5)$  Å). All the Mn atoms are six-coordinate with distorted octahedral geometry; Mn2 and Mn5 are very distorted, with one JT elongated bond being particularly long ( $\text{Mn2-O15} = 2.588(3)$  Å,  $\text{Mn5-O13} = 2.522(3)$  Å).

The structure and a stereoview of  $[\text{Mn}_{12}\text{O}_7(\text{OH})(\text{OMe})_2(\text{O}_2\text{CPh})_{12}(\text{dmhmp})_4(\text{H}_2\text{O})]$  (**4-5**) are shown in Figure 4-15, and its core in Figure 4-16. Selected interatomic distances and angles are listed in Table A-11. The complex is mixed-valent  $\text{Mn}^{\text{II}}_3\text{Mn}^{\text{III}}_9$ , as indicated by the metric parameters and confirmed by BVS calculations (Table 4-8), and contains an  $[\text{Mn}_{12}(\mu_4\text{-O})_4(\mu_3\text{-O})_5(\mu\text{-O})_7]$  core consisting of a central  $[\text{Mn}_4(\mu_4\text{-O})_2(\mu_3\text{-O})_4]$  face-sharing incomplete dicubane

(Mn1, Mn2, Mn3, Mn4), and on either side of this is attached a  $[\text{Mn}_4(\mu_4\text{-O})]$  tetrahedral unit. There is an interesting asymmetry in that the tetrahedral unit is  $\text{Mn}^{\text{II}}\text{Mn}^{\text{III}}_3$  on one side and  $\text{Mn}^{\text{II}}_2\text{Mn}^{\text{III}}_2$  on the other. BVS calculations were performed on the inorganic O atoms to assess their degree of protonation (Table 4-9), and there are four  $\mu_4\text{-O}^{2-}$  (O1, O6, O7, O8), three  $\mu_3\text{-O}^{2-}$  (O2, O4, O5), one  $\mu_3\text{-OH}^-$  (O3), one  $\mu_3\text{-MeO}^-$  (O38), one  $\mu\text{-MeO}^-$  (O39), four  $\mu\text{-RO}^-$  alkoxide arms (O9, O10, O11, O12) of  $\eta^1:\eta^2:\mu\text{-dmhmp}^-$  groups, and a terminal water molecule (O37). Two additional  $\mu\text{-O}$  atoms are provided by benzoate groups bridging in  $\mu_3$  modes (O22 and O16). Peripheral ligation is provided by twelve benzoate groups exhibiting four binding modes: eight bridge two Mn atoms in the common  $\eta^1:\eta^1:\mu$  mode; two bridge three Mn atoms in the rarer  $\eta^2:\eta^1:\mu_3$  mode; one chelates  $\text{Mn}^{\text{II}}$  atom Mn12; and one is terminally bound to  $\text{Mn}^{\text{II}}$  atom Mn6, with its inbound O atom (O30) statically disordered between forming a H-bond to the nearby water (O37) ( $\text{O30}\dots\text{O37} = 2.654(5) \text{ \AA}$ ) or the  $\mu_3\text{-OH}^-$  (O3) group ( $\text{O30}\dots\text{O3} = 2.713(3) \text{ \AA}$ ). The four dmhmp<sup>-</sup> groups all bind in a  $\eta^1:\eta^2:\mu$  mode, as in **4-4**. The Mn atoms are six-coordinate with distorted octahedral geometry, except for Mn11, which is five-coordinate unless a long sixth bond ( $\text{Mn11-O24} = 2.842(3) \text{ \AA}$ ) is included.

It is interesting to note that the  $\text{Mn}_x$  topologies of **4-4** and **4-5** are related, consisting of one (**4-4**) or two (**4-5**)  $[\text{Mn}_4(\mu_4\text{-O})]$  tetrahedral units attached to a second type of unit: in **4-4**, the latter is an  $[\text{Mn}_3(\mu_3\text{-O})]$  triangular unit (which forms a butterfly with one of the Mn atoms of the tetrahedral unit), whereas in **4-5**, it is two edge-sharing  $[\text{Mn}_3(\mu_3\text{-O})]$  triangular units (the core of the incomplete face-sharing dicubane).

It is also of interest that  $\text{Mn}_{12}$  benzoate complex **4-5** is similar to a reported  $\text{Mn}_{12}$  benzoate complex with hmp<sup>-</sup>,  $[\text{Mn}_{12}\text{O}_8\text{Cl}_4(\text{O}_2\text{CPh})_8(\text{hmp})_6]$  (**4-9**).<sup>151</sup> Disregarding differences such as  $\text{MeO}^-$  in **4-5** vs  $\text{Cl}^-$  in **4-9**, and looking instead at the overall structures, the two complexes are

similar in that both consist of a central face-sharing incomplete dicubane on either side of which are two tetrahedral units attached to the oxide ions of the former. However, there is a major difference in that **4-9** is centrosymmetric whereas **4-5** is unusually asymmetric, in both the distribution and binding modes of many ligands, and in the Mn oxidation state distribution, being  $[\text{Mn}^{\text{II}}_3\text{Mn}^{\text{III}}_9]$  in **4-5** and  $[\text{Mn}^{\text{II}}_2\text{Mn}^{\text{III}}_{10}]$  in **4-9**. In both cases, however, the  $\text{dmhmp}^-$  and  $\text{hmp}^-$  groups are all bound in the same  $\eta^1:\eta^2:\mu$  modes.

The structure and a stereoview of  $[\text{NaMn}_6\text{O}_4(\text{dmhmp})_4(\text{N}_3)_4](\text{ClO}_4)$  (**4-6**) are shown in Figure 4-17, together with its labeled core. Selected interatomic distances and angles are listed in Table A-12. Complex **4-6** crystallizes in the trigonal space group  $P31c$ . The structure of **4-6** consists of a  $\text{Mn}_6$  octahedron with four nonadjacent faces bridged by  $\mu_3\text{-N}_3^-$  ions, and among the other four faces, three are bridged by  $\mu_3\text{-O}^{2-}$  ions (O1), with the other one bridged by the  $\mu_4\text{-O}^{2-}$  ion (O3), the latter being bound to a Na ion. Alternatively, the  $[\text{Mn}_6\text{O}_4(\text{N}_3)_4]^{6+}$  core can be described as a tetrahedron with a  $\text{N}_3^-$  at each vertex, a Mn at the midpoint of each edge, and an  $\text{O}^{2-}$  bridging each face. The  $\text{O}^{2-}$  ions lie 0.44 Å (O1) and 0.35 Å (O3) above the  $\text{Mn}_3$  planes they bridge. Charge consideration and qualitative inspection of the metric parameters indicate a  $\text{Mn}^{\text{III}}_6$  metal oxidation-state description. All Mn ions are six-coordinate with distorted octahedral geometry. As expected for the high-spin  $\text{Mn}^{\text{III}}$  ( $d^4$ ) in near-octahedral geometry, there is a Jahn-Teller (JT) distortion, and it takes the form of an axial elongation of the two trans Mn- $\text{N}_3$  bonds; the JT axes form the edge in the tetrahedral description of  $[\text{Mn}_6\text{O}_4(\text{N}_3)_4]^{6+}$ . Ligation is completed by six  $\text{dmhmp}^-$  groups. Three of them chelate to Mn atoms (Mn2), and the other three both chelate to Mn atoms (Mn1) and bridge with their alkoxide arms to the Na atom; these groups are thus  $\eta^1:\eta^2:\mu$ . The Na ion is further bound to a nitrogen atom (N6) of an azide group of a neighboring molecule, thus linking  $\text{Mn}_6$  units to form a one-dimensional chain (Figure 4-18). The

molecule has a crystallographic  $C_3$  rotation axis passing thorough the  $N_3^- \cdots Na^+ \cdots \mu_4-O^{2-}$  (O3) bonds. There are two previous examples of  $Mn_6$  complexes with a  $[Mn_6O_4(\mu_3-X)_4]$  face-capped octahedral topology in the literature, with X being Cl or Br.<sup>262</sup>

It is interesting that the  $Mn_6$  topology of **4-6** is related to the previously reported decanuclear  $Mn/hmp^-/N_3^-$  cluster,  $[Mn_{10}O_4(N_3)_4(hmp)_{12}](ClO_4)_2 \cdot MeCN$  (**4-7**),<sup>44</sup> in that both consist of a  $Mn_6$  octahedron with four nonadjacent faces bridged by  $\mu_3-N_3^-$  ions: in **4-6**, among the other four faces, three are bridged by  $\mu_3-O^{2-}$  ions, and the other one is bridged by a  $\mu_4-O^{2-}$  ion, the latter of which is bound to a Na ion. In **4-7**, the four remaining faces of the  $Mn_6$  octahedron are bridged by four  $\mu_4-O^{2-}$  ions, which also bridge to four external  $Mn^{II}$  ions that thus cap the four non-adjacent faces of the octahedron. Therefore, we found that the use of bulky  $hmpH$ ,  $dnhmpH$ , led to the isolation of the inner core of this known  $hmpH$  product.

### 4.3.3 Magnetochemistry

#### 4.3.3.1 Direct current magnetic susceptibility studies

Variable temperature magnetic susceptibility measurements were performed on microcrystalline powder samples of complexes **4-1**·2MeCN·H<sub>2</sub>O, **4-2**·2H<sub>2</sub>O, **4-3**, **4-4**·MeCN, **4-5**·3H<sub>2</sub>O, and **4-6**·Et<sub>2</sub>O in a 1 kG (0.1 T) dc field and in the 5.0-300 K range. The samples were restrained in eicosane to prevent torquing in the applied field.

The obtained data for complex **4-1**·2MeCN·H<sub>2</sub>O are shown as a  $\chi_M T$  versus  $T$  plot in Figure 4-19.  $\chi_M T$  gradually decreases from 7.57 cm<sup>3</sup>Kmol<sup>-1</sup> at 300 K to 4.99 cm<sup>3</sup>Kmol<sup>-1</sup> at 40.0 K and then decreases more rapidly to 1.72 cm<sup>3</sup>Kmol<sup>-1</sup> at 5.0 K. The 300 K value is much smaller than the spin-only ( $g = 2$ ) value of 12 cm<sup>3</sup>Kmol<sup>-1</sup> for four noninteracting  $Mn^{III}$  atoms, indicating the presence of dominant antiferromagnetic exchange interactions within the molecule.  $\chi_M T$  is clearly heading for zero at the lowest temperatures, indicating that complex **4-1** possesses an  $S =$

0 ground state. Because of this and the low symmetry of the molecule, which requires five separate  $Mn_2$  pairwise exchange parameters ( $J_{ij}$ ) to describe its exchange coupling (and more if interactions with next-nearest neighbors are included), we did not pursue fits of the  $\chi_M T$  vs  $T$  data by matrix diagonalization to determine the values of the exchange interactions.

Unfortunately, the more convenient Kambe vector coupling method cannot be applied to such a low symmetry molecule. In any case, the exchange interactions are expected to be weak, based on the many previous magnetic studies of such molecules that we have reported, making accurate determinations of so many independent  $J$  values problematic, to say the least.

For complex **4-2**·2H<sub>2</sub>O,  $\chi_M T$  gradually decreases from 13.8 cm<sup>3</sup>Kmol<sup>-1</sup> at 300 K to 6.64 cm<sup>3</sup>Kmol<sup>-1</sup> at 5.0 K (Figure 4-20). The 300 K value is again much smaller than the spin-only ( $g = 2$ ) value of 18 cm<sup>3</sup>Kmol<sup>-1</sup> for six noninteracting Mn<sup>III</sup> atoms, indicating the presence of at least some strong antiferromagnetic interactions. However, the plot is clearly not heading to zero at 0 K, indicating that **4-2** has a ground state with  $S > 0$ , and the 5.0 K value is close to the spin-only value of 6.00 cm<sup>3</sup>Kmol<sup>-1</sup> expected for an  $S = 3$  ground state. Although complex **4-2** is more symmetric than **4-1**, it is still not possible to apply the Kambe method for fitting the  $\chi_M T$  vs  $T$  data. We thus chose to confirm the ground state by ac studies, as will be described below (vide infra).

For complex **4-3**,  $\chi_M T$  steadily decreases from 29.4 cm<sup>3</sup>Kmol<sup>-1</sup> at 300 K to 19.9 cm<sup>3</sup>Kmol<sup>-1</sup> at 50.0 K, and then decreases more rapidly to 8.14 cm<sup>3</sup>Kmol<sup>-1</sup> at 5.0 K (Figure 4-21). The 300 K value is much smaller than the spin-only value of 34.4 cm<sup>3</sup>Kmol<sup>-1</sup> for one Mn<sup>II</sup> and ten Mn<sup>III</sup> noninteracting atoms indicating the presence of dominant antiferromagnetic interactions. As for **4-2**·2H<sub>2</sub>O, the  $\chi_M T$  at 5.0 K of **4-3** is not heading for zero at 0 K, indicating an  $S > 0$  ground state,

and the value at 5 K can be compared with the spin-only ( $g = 2$ ) values of 4.38 and 7.88  $\text{cm}^3\text{Kmol}^{-1}$  expected for  $S = 5/2$  and  $7/2$  states, respectively.

For complex **4-4**·MeCN,  $\chi_{MT}$  gradually decreases from 16.22  $\text{cm}^3\text{Kmol}^{-1}$  at 300 K to a value of 13.44  $\text{cm}^3\text{Kmol}^{-1}$  at 25.0 K and then rapidly decreases to 10.11  $\text{cm}^3\text{Kmol}^{-1}$  at 5.0 K (Figure 4-22). The 300 K value is much less than the spin-only ( $g = 2$ ) value of 22.38  $\text{cm}^3\text{Kmol}^{-1}$  for six  $\text{Mn}^{\text{III}}$  and one  $\text{Mn}^{\text{II}}$  noninteracting ions, indicating the presence of dominant antiferromagnetic exchange interactions. However, the plot is clearly not heading to zero at 0 K, indicating that **4-4** has a ground state with  $S > 0$ , and the value at 5 K can be compared with the spin-only ( $g = 2$ ) values of 7.88  $\text{cm}^3\text{Kmol}^{-1}$  expected for  $S = 7/2$  state.

For complex **4-5**·3H<sub>2</sub>O,  $\chi_{MT}$  gradually decreases from 29.94  $\text{cm}^3\text{Kmol}^{-1}$  at 300 K to a minimum of 20.69  $\text{cm}^3\text{Kmol}^{-1}$  at 40.0 K, and then increases to 23.75  $\text{cm}^3\text{Kmol}^{-1}$  at 5 K (Figure 4-23). The 300 K value is much less than the spin-only ( $g = 2$ ) value of 40.13  $\text{cm}^3\text{Kmol}^{-1}$  for three  $\text{Mn}^{\text{II}}$  and nine  $\text{Mn}^{\text{III}}$  non-interacting ions, indicating the presence of antiferromagnetic interactions, but the  $\chi_{MT}$  versus  $T$  profile suggests there may also be significant ferromagnetic interactions as well. The 5.0 K value is indicative of an  $S = 13/2$  ground state (expected  $\chi_{MT} = 24.38 \text{ cm}^3\text{Kmol}^{-1}$  for  $g = 2$ ).

For complex **4-6**·Et<sub>2</sub>O,  $\chi_{MT}$  gradually increases from 26.32  $\text{cm}^3\text{Kmol}^{-1}$  at 300 K to a near-plateau value of  $\sim 77 \text{ cm}^3\text{mol}^{-1}\text{K}$  at 40-20 K and then slightly decreases to  $74.23 \text{ cm}^3\text{mol}^{-1}\text{K}$  at 5.0 K (Figure 4-24). The 300 K value is larger than the spin-only ( $g = 2$ ) value of 18  $\text{cm}^3\text{Kmol}^{-1}$  for six  $\text{Mn}^{\text{III}}$  noninteracting ions, indicating the presence of dominant ferromagnetic exchange interactions. The  $\chi_{MT}$  near-plateau value in the 20-40 K range appears to be heading for a final value of  $\sim 78 \text{ cm}^3\text{mol}^{-1}\text{K}$ , the spin-only ( $g = 2$ ) value of a species with an  $S = 12$  ground state, before exhibiting the final decrease at temperatures below 10 K. The latter decrease is likely due

to a combination of zero-field splitting (ZFS), Zeeman effects, and any weak intermolecular interactions. The metal ions are thus clearly involved in magnetic exchange interactions, and the data were thus fit to the theoretical  $\chi_M T$  vs  $T$  expression derived from the spin Hamiltonian appropriate for a  $Mn_6$  octahedron; this is given in eq. 4-7, where  $S_i$  refers to the spin of metal

$$\begin{aligned} \hat{H} = & -2J_{\text{cis}}(\hat{S}_1 \cdot \hat{S}_2 + \hat{S}_1 \cdot \hat{S}_3 + \hat{S}_1 \cdot \hat{S}_4 + \hat{S}_1 \cdot \hat{S}_6 + \hat{S}_2 \cdot \hat{S}_3 + \hat{S}_2 \cdot \hat{S}_5 + \hat{S}_2 \cdot \hat{S}_6 \\ & + \hat{S}_3 \cdot \hat{S}_4 + \hat{S}_3 \cdot \hat{S}_5 + \hat{S}_4 \cdot \hat{S}_5 + \hat{S}_4 \cdot \hat{S}_6 + \hat{S}_5 \cdot \hat{S}_6) - 2J_{\text{trans}}(\hat{S}_1 \cdot \hat{S}_5 + \hat{S}_2 \cdot \hat{S}_4 + \hat{S}_3 \cdot \hat{S}_6) \end{aligned} \quad (4-7)$$

$Mn_i$ , and  $J_{\text{cis}}$  and  $J_{\text{trans}}$  are the pairwise exchange parameters for adjacent and opposite metals of the octahedron, respectively; the Mn labeling scheme of Figure 4-25 was employed. Note that we assume that the interaction with the  $Na^+$  ion causes minimal change to the  $J$  values. This Hamiltonian can be transformed into an equivalent form (eq. 4-8) by use of the Kambe vector coupling method<sup>263</sup> and the substitutions  $\hat{S}_A = \hat{S}_1 + \hat{S}_5$ ,  $\hat{S}_B = \hat{S}_2 + \hat{S}_4$ ,  $\hat{S}_C = \hat{S}_3 + \hat{S}_6$  and  $\hat{S}_T = \hat{S}_A + \hat{S}_B + \hat{S}_C$  where  $S_T$  is the resultant spin of the complete molecule.

$$\begin{aligned} \hat{H} = & -J_{\text{cis}}(\hat{S}_T^2 - \hat{S}_A^2 - \hat{S}_B^2 - \hat{S}_C^2) - J_{\text{trans}}(\hat{S}_A^2 + \hat{S}_B^2 + \\ & \hat{S}_C^2 - \hat{S}_1^2 - \hat{S}_2^2 - \hat{S}_3^2 - \hat{S}_4^2 - \hat{S}_5^2 - \hat{S}_6^2) \end{aligned} \quad (4-8)$$

From eq. 4-8 can be obtained the energy expression (eq. 4-9) for the energies,  $E(S_T)$ , of each  $S_T$  state; constant terms contributing equally to all states have been omitted from eq. 4-9.

$$\begin{aligned} E(S_T) = & -J_{\text{cis}}[S_T(S_T+1) - S_A(S_A+1) - S_B(S_B+1) - S_C(S_C+1)] \\ & - J_{\text{trans}}[\hat{S}_A(\hat{S}_A+1) + \hat{S}_B(\hat{S}_B+1) + \hat{S}_C(\hat{S}_C+1)] \end{aligned} \quad (4-9)$$

An expression for the molar paramagnetic susceptibility,  $\chi_M$ , was derived using the above and the Van Vleck equation,<sup>264</sup> and assuming an isotropic  $g$  tensor (Appendix C-1). This was then used to fit the experimental  $\chi_M T$  vs  $T$  data in Figure 4-18 as a function of the two exchange parameters  $J_{\text{cis}}$  and  $J_{\text{trans}}$ , and the  $g$  factor. Only data for the 20.0-300 K range were used, since the model does not incorporate ZFS and other minor effects and therefore cannot reproduce the

decrease at lower temperatures. Good fits were obtained with fit parameters of  $J_{\text{cis}} = 5.75 \text{ cm}^{-1}$ ,  $J_{\text{trans}} \approx 0 \text{ cm}^{-1}$ , and  $g = 1.99$ , with temperature independent paramagnetism (TIP) held constant at  $600 \times 10^{-6} \text{ cm}^3 \text{ mol}^{-1}$ . The fit indicates that  $\text{Mn}_6$  complex **4-6** has an  $S_{\text{T}} = 12$  ground state. In the notation  $|S_{\text{T}}, S_{\text{A}}, S_{\text{B}}, S_{\text{C}}\rangle$  this is the  $|12, 4, 4, 4\rangle$  state in which all six  $\text{Mn}^{\text{III}}$  spins are aligned parallel. The first excited state is a triply degenerate set of  $S_{\text{T}} = 11$  states comprising the  $|11, 3, 4, 4\rangle$ ,  $|11, 4, 3, 4\rangle$ , and  $|11, 4, 4, 3\rangle$  states at  $92 \text{ cm}^{-1}$  above the ground state. The  $S = 12$  ground state in the  $\text{Mn}_6$  complexes is thus well-isolated from the nearest excited state.

To confirm the indicated  $S = 3, 5/2, 7/2, 13/2$ , and  $12$  ground states of complex **4-2**, **4-3**, **4-4**, **4-5**, and **4-6**, respectively, and to estimate the magnitude of the zero-field splitting parameter  $D$ , magnetization vs dc field measurements were made on restrained samples at applied magnetic fields and temperatures in the 1–70 kG and 1.8–10.0 K ranges, respectively. We then attempted to fit the data, using the program MAGNET,<sup>66</sup> by diagonalization of the spin Hamiltonian matrix assuming only the ground state is populated, incorporating axial anisotropy ( $D\hat{S}_z^2$ ) and Zeeman terms, and employing a full powder average. The corresponding spin Hamiltonian is given by eq. 4-10, where  $\hat{S}_z$  is the easy-axis spin operator,  $g$  is the Landé  $g$  factor,  $\mu_{\text{B}}$  is the Bohr magneton, and  $\mu_0$  is the vacuum permeability. However, for complex **4-2**, **4-3**, and **4-4**, we could not get an

$$\mathcal{H} = D\hat{S}_z^2 + g\mu_{\text{B}}\mu_0\hat{S}\cdot H \quad (4-10)$$

acceptable fit using data collected over the whole field range. This is commonly due to the presence of low-lying excited states because (i) the excited states are close enough to the ground state that they are populated even at very low temperatures, and/or (ii) even higher-lying excited states whose  $S$  is greater than the ground-state become populated as their larger  $M_S$  levels rapidly decrease in energy in the applied dc field and approach (or even cross) those of the ground state. Either (or both) of these two effects will lead to poor fits because the fitting program assumes

population of only the ground state. A common solution is to use only data collected at low fields ( $\leq 1.0$  T), as we showed for many mixed-valence  $\text{Mn}^{\text{II}}/\text{Mn}^{\text{III}}$  clusters,<sup>183, 184, 265</sup> but for **4-2**, **4-3**, and **4-4** it was still not possible to obtain a satisfactory fit assuming only the ground state is populated in this temperature range, suggesting particularly low-lying excited states. Thus, we turned to ac susceptibility measurements, which are a powerful complement to dc studies for determining the ground state of a system, because they preclude complications from a dc field (*vide infra*).<sup>152, 185, 186</sup>

For complex **4-5**·3H<sub>2</sub>O, again we could not obtain a satisfactory fit using all data up to 7 T, but this time we were able to get around the problem from excited states by using only data collected up to 2 T. These are shown as a reduced magnetization ( $M/N\mu_{\text{B}}$ ) vs  $H/T$  plot in Figure 4-20, where  $N$  is Avogadro's number, and the fit (solid lines in Figure 4-26) gave  $S = 13/2$ ,  $D = -0.18 \text{ cm}^{-1}$ , and  $g = 1.97$ . Alternative fits with  $S = 11/2$  or  $15/2$  were rejected because they gave unreasonable values of  $g$ . The root-mean-square  $D$  vs  $g$  error surface for the fit was generated using the program GRID,<sup>116</sup> and is shown as a 2-D contour plot in Figure 4-27 for the  $D = -0.3$  to  $0.3 \text{ cm}^{-1}$  and  $g = 1.8$  to  $2.2$  ranges. Two soft fitting minima are observed with positive and negative  $D$  values, with the latter being clearly superior and indicating  $D$  to be negative. From the shape and orientation of the contour describing the region of minimum error, we estimate the uncertainties in the fit parameters as  $S = 13/2$ ,  $D = -0.18(2) \text{ cm}^{-1}$  and  $g = 1.97(2)$ .

The  $M/N\mu_{\text{B}}$  vs  $H/T$  plot for complex **4-6**·MeCN is shown in Figure 4-28, and we were able to obtain an excellent fit with the program MAGNET using all the data collected up to 7 tesla. This suggests that the ground state of **4-6** is relatively well isolated from the nearest excited states, as suggested also from the obtained  $J$  values (*vide supra*). The best fit is shown as the solid lines in Figure 4-28 and was obtained with  $S = 12$ ,  $g = 2.00$ , and  $D = 0.05 \text{ cm}^{-1}$ . An equally

good fit was also obtained with  $S = 12$ ,  $g = 2.00$  and  $D = -0.03 \text{ cm}^{-1}$ . It is common to obtain two acceptable fits of magnetization data for a given  $S$  value, one with  $D > 0$  and the other with  $D < 0$ , since magnetization fits are not very sensitive to the sign of  $D$ . Alternative fits with  $S = 11$  were rejected because they gave unreasonable values of  $g$  and  $D$ .

The obtained error surface for the fit, plotted as a 2-dimensional contour plot in Figure 4-29, exhibits the two minima, one with positive  $D$  and the other with a negative one, but this time the two fits are essentially of equal quality, and it is thus not possible on the basis of these magnetization fits to conclude the more likely sign of the axial anisotropy parameter  $D$  for **4-6**.

The ZFS of the ground state of a polynuclear  $\text{Mn}^{\text{III}}$  complex is largely a consequence of the vectorial addition of the single-ion ZFS tensors. A large Jahn-Teller (JT) distortion is typically seen in an octahedral  $\text{Mn}^{\text{III}}$  ion, in which a unique axis is formed by two noticeably longer Mn-L bond distances. This axis often defines the unique axis of the magnetic structure of the  $\text{Mn}^{\text{III}}$  ion. Single-ion ZFS in  $\text{Mn}^{\text{III}}$  ions can be very large; for example, high-frequency EPR experiments have shown that  $D = -4.52 \text{ cm}^{-1}$  for  $\text{Mn}(\text{acac})_3$ , where acac is the anion of 2,4-pentanedione, and  $D = -5.90 \text{ cm}^{-1}$  for  $\text{Mn}(\text{taa})$ , where taa is the trianion of tris(1-(2-azoly1)-2-azabuten-4-yl)amine. When all JT axes are oriented parallel, the resultant ZFS of a  $\text{Mn}^{\text{III}}_x$  complex will be quite large; for example, in  $[\text{Mn}_{12}\text{O}_{12}(\text{O}_2\text{CR})_{16}(\text{H}_2\text{O})_4]$  complexes (8  $\text{Mn}^{\text{III}}$ , 4  $\text{Mn}^{\text{IV}}$ ), the 8  $\text{Mn}^{\text{III}}$  ions have their JT axes essentially parallel, and the net ZFS in the molecule is fairly large ( $D \sim -0.5 \text{ cm}^{-1}$ ).<sup>217, 266</sup> On the other hand, when the JT axes do not all point in the same direction, the resultant ZFS will be small, as the contributions from the individual sites partially or completely cancel out. In the  $\text{Mn}_6$  complexes **4-6**, because of the high symmetry of the molecule, the vectorial addition of single ion anisotropies sums to zero. This clearly explains the experimental observation of  $D \sim 0$  for **4-6**.

#### 4.3.3.2 Alternating current magnetic susceptibility studies

Ac susceptibility studies are a powerful complement to dc studies for determining the ground state spin of a system, because they preclude complications arising from the presence of a dc field. They were performed for complex **4-2**·2H<sub>2</sub>O, **4-3**, **4-4**·MeCN, **4-5**·3H<sub>2</sub>O, and **4-6**·Et<sub>2</sub>O, respectively, in the 1.8-15 K range using a 3.5 G ac field oscillating at frequencies in the 50-1000 Hz range.

For **4-2**·2H<sub>2</sub>O, the obtained in-phase  $\chi_M' T$  and out-of-phase  $\chi_M''$  ac susceptibility data are shown in Figure 4-30.  $\chi_M' T$  decreases significantly with decreasing temperature indicating population of one or more excited states and rationalizing the problematic fits of dc magnetization data. In particular, a decreasing  $\chi_M' T$  vs  $T$  plot with decreasing  $T$  is indicative of the population of low-lying excited states with  $S$  values greater than the ground-state  $S$  and this rationalizing the problematic fits of dc magnetization data. Extrapolation of the plot from above 4 K to 0 K, where only the ground state will be populated, gives a  $\chi_M' T$  value of  $\sim 6 \text{ cm}^3 \text{ K mol}^{-1}$ , which is the value expected for an  $S = 3$  state with  $g \sim 2.0$ . This conclusion is the same as that reached from the dc study, and provides an independent confirmation that complex **4-2** possesses an  $S = 3$  ground state.

The out-of-phase ( $\chi_M''$ ) susceptibility in Figure 4-30 (bottom) is zero until  $\sim 3$  K, and then shows a small frequency-dependent rise. The  $\chi_M''$  signal in Figure 4-24 is weak and parallels a tiny drop in the in-phase  $\chi_M' T$ ; nevertheless, the  $\chi_M'' : \chi_M' T$  ratio is small ( $\sim 1.5\%$ ), and the  $\chi_M''$  signal is clearly just the small tail of a much stronger  $\chi_M''$  peak whose maximum is below the 1.8 K operating limit of our SQUID magnetometer. The data thus suggest that complex **4-2** exhibits the slow magnetization relaxation dynamics of a SMM, but with only a very small barrier. It would thus require single-crystal micro-SQUID studies down to 40 mK to better study the SMM

properties, but these were not pursued given the only small barrier evident and the many such studies on other SMMs with small barriers already reported.

For **4-3**, the in-phase  $\chi_M' T$  and out-of-phase  $\chi_M''$  data are shown in Figure 4-31. The  $\chi_M' T$  vs  $T$  plot in Figure 4-25 (top) decreases very rapidly with decreasing temperature, supporting a very high density of low-lying excited states consistent with the higher nuclearity of this complex and again rationalizing the unsatisfactory fits of dc magnetization data. The steeply decreasing and curving plot makes extrapolation to 0 K trickier, but it appears to be heading for a  $\chi_M' T$  value in the 4 – 5 cm<sup>3</sup>Kmol<sup>-1</sup> range consistent with an  $S = 5/2$  ground state (4.38 cm<sup>3</sup>Kmol<sup>-1</sup> for  $g = 2$ ) suggesting this is the ground state of the molecule; the spin-only  $\chi_M' T$  values  $S = 3/2$  and  $7/2$  states are 1.88 and 7.88 cm<sup>3</sup>Kmol<sup>-1</sup>, significantly different than the experimental value. We conclude that complex **4-3** has an  $S = 5/2$  ground state. Below ~ 3 K, there is a small dip in the  $\chi_M' T$  signal concomitant with the appearance of a frequency-dependent  $\chi_M''$  signal (Figure 4-31, bottom). As for **4-2**, it appears that **4-3** has a very small magnetization relaxation barrier that leads to  $\chi_M''$  signals whose peaks lie well below 1.8 K. This suggests that **4-3** is also a SMM, but again one with only a very small barrier, and we thus did not pursue further characterization.

For **4-4**, the obtained in-phase ac susceptibility data ( $\chi_M'$ , plotted as  $\chi_M' T$ ) are shown in Figure 4-32. The  $\chi_M' T$  vs  $T$  plot of Figure 4-32 decreases significantly with decreasing temperature, again indicating population of one or more excited states with  $S$  greater than the ground state  $S$ , rationalizing the problematic fits of dc magnetization data. Extrapolation of the plot to 0 K, where only the ground state will be populated, gives a  $\chi_M' T$  value of ~7 cm<sup>3</sup>Kmol<sup>-1</sup>, which is the value expected for an  $S = 7/2$  state with  $g$  slightly less than 2, as expected for a Mn<sup>II</sup>/Mn<sup>III</sup> complex. Extrapolation of a steeply sloping plot to 0 K can be fairly unreliable, especially for large  $S$  ground states and even in the absence (as here) of significant

intermolecular interactions, but the data for **4-4** clearly distinguish the  $S = 5/2$ ,  $7/2$ , and  $9/2$  possibilities, whose  $\chi_M'T$  values are 4.38, 7.35, and  $12.38 \text{ cm}^3\text{Kmol}^{-1}$ , respectively, for  $g = 2$ . We thus feel confident in our conclusion that **4-4** has an  $S = 7/2$  ground state. Complex **4-4** exhibited no out-of-phase ( $\chi_M''$ ) ac signal down to 1.8 K, indicating that it does not exhibit a significant barrier (vs  $kT$ ) to magnetization relaxation, i.e., it is not an SMM.

The in-phase ( $\chi_M'T$ ) and out-of-phase ( $\chi_M''$ ) ac susceptibilities for **4-5** are shown in Figure 4-33.  $\chi_M'T$  increases with decreasing temperature below 15 K to a plateau of  $\sim 24.5 \text{ cm}^3\text{Kmol}^{-1}$  in the 4-5 K region, and then exhibits a frequency-dependent decrease below 3 K. The plateau value is clearly indicative of an  $S = 13/2$  ground state with  $g \sim 2.0$ , in agreement with the dc magnetization fit.  $S = 11/2$  and  $15/2$  ground states would be expected to give  $\chi_M'T$  values of 17.9 and  $31.9 \text{ cm}^3\text{Kmol}^{-1}$ , respectively, clearly very different from the experimental value. We conclude that complex **4-5** has an  $S = 13/2$  ground state. The frequency-dependent decrease in  $\chi_M'T$  below 3 K is accompanied by the appearance of frequency-dependent out-of-phase  $\chi_M''$  signals below 3 K, clearly the tails of peaks whose maxima are at  $< 1.8$  K. If the magnetization vector relaxes fast enough to keep up with the oscillating ac field, there will be no  $\chi_M''$  signal, but if the relaxation barrier is significant compared to thermal energy ( $kT$ ), then there is a nonzero  $\chi_M''$  signal and the in-phase signal decreases. Such frequency-dependent ac signals are an indication of the superparamagnet-like slow relaxation of a single-molecule magnet (SMM). To confirm whether **4-5** is an SMM, studies were carried out on a single crystal down to 0.04 K (*vide infra*).

The obtained in-phase  $\chi_M'$  signal for **4-6** is plotted as  $\chi_M'T$  in Figure 4-34, and can be seen to be almost temperature-independent, confirming a well-isolated ground state, before decreasing slightly below  $\sim 5$  K. Extrapolating to 0 K the data from above 5 K (to avoid lower temperature

effects from the slight anisotropy and weak intermolecular interactions) gives a value of  $\sim 78 \text{ cm}^3 \text{ K mol}^{-1}$ , which is consistent with an  $S = 12$  ground state and  $g \sim 2$ , in excellent agreement with the reduced magnetization fit. We conclude that complex **4-6** does indeed have an  $S = 12$  ground state. There is no out-of-phase ac susceptibility signal down to 1.8 K, the operating limit of our SQUID magnetometer.

#### 4.3.3.3 Hysteresis Studies below 1.8 K.

Magnetization vs applied dc field studies down to 0.04 K were carried out using a micro-SQUID apparatus and single crystals of **4-5**·3CH<sub>2</sub>Cl<sub>2</sub> that had been kept in contact with their mother liquor.<sup>3267</sup> Magnetization vs field hysteresis, the diagnostic property of a magnet, was observed below 0.7 K (Figure 4-35). The hysteresis loops exhibit increasing coercivity with increasing field sweep rate at a constant temperature (Figure 4-35, top), and increasing coercivity with decreasing temperature at a constant sweep rate (Figure 4-35, bottom), as expected for the superparamagnet-like properties of a SMM. These loops thus confirm complex **4-5**·3CH<sub>2</sub>Cl<sub>2</sub> to be a new addition to the family of SMMs.

The most dominating feature of the hysteresis loops in Figure 4-35 is the large step at zero field due to quantum tunneling of the magnetization (QTM) through the anisotropy barrier. The large zero-field step indicates that QTM in zero field is fast, and this is consistent with the low symmetry of the molecule, which introduces a significant rhombic (transverse) anisotropy into the spin Hamiltonian, i.e.  $E(\hat{S}_x^2 - \hat{S}_y^2)$ , where  $E$  is the rhombic zero-field splitting parameter. The greater is the transverse anisotropy, the greater will be the mixing of levels on either of the anisotropy barrier, leading to increased rates of QTM. The fast relaxation at zero field precludes magnetization decay vs time studies to provide relaxation rate vs  $T$  kinetic data; we cannot therefore construct an Arrhenius plot from which could be determined the effective barrier to magnetization relaxation,  $U_{\text{eff}}$ .

#### 4.3.4 Structural Comparison of hmp<sup>-</sup>, dmhmp<sup>-</sup>, and dphmp<sup>-</sup> Mn<sub>x</sub> Products.

The initial objective of this work was to explore whether the introduction of bulky substituents at the CH<sub>2</sub> position of hmpH might lead to products distinctly different from those previously obtained from hmpH, and this has been found to be the case. None of the products obtained to date containing bulky dphmp<sup>-</sup> or dmhmp<sup>-</sup> are structurally the same as those obtained previously with hmp<sup>-</sup>. Instead, all six products of the present study have been found to be prototypical or very rare structural types in Mn cluster chemistry. However, Mn chemistry is already known to be amazingly fickle, with obtained products often changing dramatically when reaction conditions such as the identity of the solvent or the carboxylate are changed (for reasons discussed above). Thus, the simple fact that dphmp<sup>-</sup> and dmhmp<sup>-</sup> give different products from hmp<sup>-</sup> is not in itself so surprising. A much more pertinent and useful question to ask is whether there is anything systematically different between the products with hmp<sup>-</sup> and its bulky derivatives? The answer is yes – the bulky derivatives, dmhmp<sup>-</sup> and especially dphmp<sup>-</sup>, are exhibiting distinctly different binding modes that can be directly assigned to the presence of the Ph and Me groups and which consequently lead to the different structural types of products. The various types of known Mn clusters containing hmp<sup>-</sup> are listed in Table 4-10, together with complexes **4-1** – **4-6** from this work, and the binding modes of the alkoxide O atom. Immediately apparent is a strong tendency of the hmp<sup>-</sup> alkoxide arm to bridge two and even three Mn atoms in most of the [Mn<sub>4</sub>(hmp)<sub>6</sub>]<sup>4+</sup>- and [Mn<sub>4</sub>(hmp)<sub>4</sub>]<sup>6+</sup>-containing complexes, as well as [Mn<sub>7</sub>(OH)<sub>3</sub>(hmp)<sub>9</sub>Cl<sub>3</sub>]<sup>2+</sup> and [Mn<sub>10</sub>O<sub>4</sub>(OH)<sub>2</sub>(O<sub>2</sub>CMe)<sub>8</sub>(hmp)<sub>8</sub>]<sup>4+</sup>.<sup>44, 51, 147-150, 252-254</sup> The carboxylate-rich anion [Mn<sub>4</sub>O<sub>2</sub>(O<sub>2</sub>CPh)<sub>7</sub>(hmp)<sub>2</sub>]<sup>-</sup> is the exception that proves the rule in containing only chelating hmp<sup>-</sup> groups. This preference of the numerous hmp<sup>-</sup> groups in these many complexes to almost all favor a bridging mode for their alkoxide group is as expected for mid- and late-transition metals. In contrast, for Mn/dphmp<sup>-</sup> complexes **4-1** – **4-3**, nine of the

eleven dphmp<sup>-</sup> groups bind in non-bridging, chelate modes. Even the tenth and eleventh, the ostensibly bridging dphmp<sup>-</sup> group bridges very asymmetrically, as described above (complex **4-1**: Mn3-O5 = 1.887(3) vs Mn2-O5 = 2.505(3) Å; complex **4-3**: Mn2-O1 = 1.879(1) Å vs Mn3-O1 = 2.415(2) Å), and perhaps are best described as semi-bridging. Thus, although the number of dphmp<sup>-</sup> products is admittedly limited to date, we believe the trend is nevertheless clear: the influence of the two bulky Ph groups next to the alkoxide O atom disfavors the adoption of a bridging mode. We believe this is primarily due to steric effects, but there will also be an electronic effect of the electron-withdrawing Ph groups that lowers the basicity of the O atom. Thus, with dphmp<sup>-</sup> favoring a chelating mode, it is not surprising that its Mn clusters are distinctly different from those obtained with hmp<sup>-</sup>. It now also makes sense that the Mn<sub>6</sub> core of complex **4-2** is the same as that found previously in [Mn<sub>6</sub>O<sub>4</sub>(OMe)<sub>2</sub>(OAc)<sub>4</sub>(Mesalim)<sub>4</sub>], where the Mesalim<sup>-</sup> anion is a bidentate chelate. On the other hand, the dmhmp<sup>-</sup> products show an increased preference for dmhmp<sup>-</sup> bridging modes as in the hmp<sup>-</sup> products; in the three Mn/dmhmp<sup>-</sup> complexes **4-4** – **4-6**, ten of the fourteen dmhmp<sup>-</sup> groups exhibit bridging (μ) modes as a result of both the smaller size of Me (vs Ph) groups and their electron-donating rather than withdrawing character. Although we have not observed the μ<sub>3</sub>-bridging mode in dmhmp<sup>-</sup> products, it is apparent that the tendency of the alkoxide oxygen to bridge metal ions, which was lost when adding Ph groups to the alcohol arm, was restored in dmhmp<sup>-</sup>. However, the two Me groups at the CH<sub>2</sub> position of hmpH still provide sufficient steric differences with hmp<sup>-</sup> to lead to new products. It is thus interesting that Mn/dmhmp<sup>-</sup> products bear some structural similarity to Mn/hmp<sup>-</sup> products, as a result of dmhmp<sup>-</sup> acting as a perturbed hmp<sup>-</sup>.

#### 4.4 Conclusions

The introduction of two bulky phenyl or methyl groups onto the CH<sub>2</sub> group of hmp<sup>-</sup> has proven to be a route to new Mn clusters not accessible with hmp<sup>-</sup> itself, and with prototypical or very rare structures. In contrast to hmp<sup>-</sup>, the bulkier dphmp<sup>-</sup> favors a chelating, non-bridging binding mode, and as a result, products with alternative bridging ligands such as carboxylates filling up coordination sites are readily obtained. This is in contrast to hmp<sup>-</sup>, which favors chelating/bridging binding modes and whose higher denticity will often preclude the incorporation of additional bridging groups such as carboxylates. The reluctance of dphmp<sup>-</sup> to adopt a bridging mode is clearly due to the nearby steric bulk of the two Ph groups, and perhaps their electron-withdrawing effect on the O atom. On the other hand, the less bulky dmhmp<sup>-</sup> functions as a chelating and bridging ligand, as does hmp<sup>-</sup>, but yields products that are structurally distinct from any seen in Mn/hmp<sup>-</sup> chemistry as a result of sufficient steric differences with hmp<sup>-</sup>. The combined results support our initial idea that (i) the addition of bulky groups near the functional groups of known ligands could lead to the isolation of new cluster products, and (ii) the use of different bulky group sizes leads to the formation of different clusters. It would be interesting to investigate whether the binding mode, and thus the identity of the obtained Mn clusters, can be altered in a targeted way by modifying the size and electronic effects of the two substituents.

Table 4-1. Crystallographic Data for **4-1**·2MeCN, **4-2**·3MeCN and **4-3**·4MeCN.

	<b>4-1</b>	<b>4-2</b>	<b>4-3</b>
formula <sup>a</sup>	C <sub>83</sub> H <sub>93</sub> Mn <sub>4</sub> N <sub>5</sub> O <sub>15</sub>	C <sub>108</sub> H <sub>96</sub> Mn <sub>6</sub> N <sub>7</sub> O <sub>18</sub>	C <sub>138</sub> H <sub>133</sub> Mn <sub>11</sub> N <sub>8</sub> O <sub>34</sub>
fw, g mol <sup>-1</sup> <sup>a</sup>	1620.38	2019.56	3051.86
crystal system	Triclinic	Triclinic	Triclinic
space group	<i>P</i> 1	<i>P</i> $\bar{1}$	<i>P</i> $\bar{1}$
<i>a</i> , Å	13.1020(16)	13.5311(19)	17.0807(15)
<i>b</i> , Å	13.6590(17)	13.6589(18)	18.5090(16)
<i>c</i> , Å	14.6292(18)	27.034(4)	21.0431(18)
$\alpha$ , deg	63.067(2)	98.178(3)	94.9260(10)
$\beta$ , deg	63.803(2)	90.914(3)	93.104(2)
$\gamma$ , deg	65.072(2)	105.032(3)	96.2410(10)
<i>V</i> , Å <sup>3</sup>	2012.4(4)	4769.1(11)	6575.3(10)
<i>Z</i>	1	2	2
<i>T</i> , K	173(2)	173(2)	173(2)
radiation, Å <sup>b</sup>	0.71073	0.71073	0.71073
$\rho_{\text{calc}}$ , g cm <sup>-3</sup>	1.337	1.469	1.541
$\mu$ , mm <sup>-1</sup>	0.680	0.845	1.100
<i>R</i> 1 <sup>c,d</sup>	0.0628	0.0807	0.0566
<i>wR</i> 2 <sup>e</sup>	0.1509	0.1853	0.1018

<sup>a</sup> Graphite monochromator. <sup>b</sup>  $I > 2\sigma(I)$ . <sup>c</sup>  $R1 = 100\Sigma(|F_o| - |F_c|)/\Sigma|F_o|$ . <sup>d</sup>  $wR2 = 100[\Sigma[w(F_o^2 - F_c^2)^2]/\Sigma[w(F_o^2)^2]]^{1/2}$ ,  $w = 1/[\sigma^2(F_o^2) + [(ap)^2 + bp]$ , where  $p = [\max(F_o^2, O) + 2F_c^2]/3$ .

Table 4-2. Crystallographic Data for **4-4**·7MeCN **4-5**·3CH<sub>2</sub>Cl<sub>2</sub> and **4-6**·Et<sub>2</sub>O.

parameter	<b>4-4</b>	<b>4-5</b>	<b>4-6</b>
formula	C <sub>67</sub> H <sub>106</sub> Mn <sub>7</sub> N <sub>4</sub> O <sub>24</sub>	C <sub>118</sub> H <sub>108</sub> Mn <sub>12</sub> N <sub>4</sub> O <sub>39</sub>	C <sub>58</sub> H <sub>86</sub> Cl <sub>2</sub> Mn <sub>6</sub> N <sub>19</sub> NaO <sub>19</sub>
fw, g mol <sup>-1</sup>	1736.14	2865.36	1776.99
crystal system	Triclinic	Triclinic	Trigonal
space group	<i>P</i> $\bar{1}$	<i>P</i> $\bar{1}$	<i>P</i> 3 <i>1c</i>
<i>a</i> , Å	14.396(3)	15.9055(12)	14.0257(7)
<i>b</i> , Å	15.169(3)	17.0160(13)	14.0257(7)
<i>c</i> , Å	25.551(6)	27.771(2)	23.328(2)
$\alpha$ , deg	77.295(4)	107.1080(10)	90
$\beta$ , deg	88.592(4)	99.8710(10)	90
$\gamma$ , deg	63.557(3)	108.4790(10)	120
<i>V</i> , Å <sup>3</sup>	4856.3(18)	6516.3(9)	3974.3(5)
<i>Z</i>	2	2	2
<i>T</i> , °C	173(2)	173(2)	173(2)
radiation, Å <sup>a</sup>	0.71073	0.71073	0.71073
$\rho_{\text{calc}}$ , g cm <sup>-3</sup>	1.187	1.460	1.485
$\mu$ , mm <sup>-1</sup>	0.940	1.197	1.072
<i>R</i> 1 <sup>b,c</sup>	0.0610	0.0419	0.0293
<i>wR</i> 2 <sup>d</sup>	0.1538	0.1164	0.0730

<sup>a</sup> Graphite monochromator. <sup>b</sup>  $I > 2\sigma(I)$ . <sup>c</sup>  $R1 = 100\Sigma(|F_o| - |F_c|)/\Sigma|F_o|$ . <sup>d</sup>  $wR2 = 100[\Sigma[w(F_o^2 - F_c^2)^2]/\Sigma[w(F_o^2)^2]]^{1/2}$ ,  $w = 1/[\sigma^2(F_o^2) + [(ap)^2 + bp]$ , where  $p = [\max(F_o^2, O) + 2F_c^2]/3$ .

Table 4-3. Bond Valence Sums for the Mn Atoms in Complex **4-1**<sup>a</sup>

atom	Mn <sup>II</sup>	Mn <sup>III</sup>	Mn <sup>IV</sup>
Mn1	3.22	<u>2.98</u>	3.08
Mn2	3.13	<u>2.89</u>	2.99
Mn3	3.23	<u>2.99</u>	3.08
Mn4	3.20	<u>2.92</u>	3.07

<sup>a</sup> The underlined value is the one closest to the charge for which it was calculated, and the nearest whole number can be taken as the oxidation state of that atom.

Table 4-4. Bond Valence Sums for the Mn Atoms in Complex **4-2**<sup>a</sup>

atom	Mn <sup>II</sup>	Mn <sup>III</sup>	Mn <sup>IV</sup>
Mn1	3.15	<u>2.88</u>	3.02
Mn2	3.15	<u>2.91</u>	3.00
Mn3	3.15	<u>2.92</u>	3.01

<sup>a</sup> The underlined value is the one closest to the charge for which it was calculated, and the nearest whole number can be taken as the oxidation state of that atom.

Table 4-5. Bond Valence Sums for the Mn Atoms in Complex **4-3**<sup>a</sup>

atom	Mn <sup>II</sup>	Mn <sup>III</sup>	Mn <sup>IV</sup>
Mn1	3.18	<u>2.95</u>	3.04
Mn2	3.28	<u>3.03</u>	3.13
Mn3	3.13	<u>2.89</u>	2.98
Mn4	3.12	<u>2.86</u>	3.00
Mn5	3.23	<u>2.96</u>	3.11
Mn6	3.15	<u>2.88</u>	3.02
Mn7	3.16	<u>2.89</u>	3.03
Mn8	3.14	<u>2.87</u>	3.01
Mn9	3.17	<u>2.90</u>	3.05
Mn10	3.26	<u>3.02</u>	3.12
Mn11	<u>1.98</u>	1.81	1.90

<sup>a</sup> The underlined value is the one closest to the charge for which it was calculated, and the nearest whole number can be taken as the oxidation state of that atom.

Table 4-6. Bond Valence Sums for the Mn Atoms in Complex **4-4**<sup>a</sup>

	Mn <sup>II</sup>	Mn <sup>III</sup>	Mn <sup>IV</sup>
Mn1	3.32	<u>3.07</u>	3.06
Mn2	3.13	<u>2.90</u>	2.89
Mn3	3.13	<u>2.86</u>	3.01
Mn4	3.12	<u>2.85</u>	2.99
Mn5	3.16	<u>2.93</u>	2.92
Mn6	3.25	<u>3.00</u>	3.00
Mn7	<u>1.80</u>	1.65	1.73

<sup>a</sup> The underlined value is the one closest to the charge for which it was calculated, and the nearest whole number can be taken as the oxidation state of that atom.

Table 4-7. Bond Valence Sums for the Inorganic Oxygen Atoms in Complex **4-4**<sup>a</sup>

atom	BVS	assgt <sup>a</sup>
O1	1.85	O <sup>2-</sup>
O2	1.98	O <sup>2-</sup>
O3	1.79	O <sup>2-</sup>
O4	0.93	OH <sup>-</sup>
O5	0.93	OH <sup>-</sup>
O6	0.63	OH <sup>-</sup>

<sup>a</sup> The oxygen atom is an O<sup>2-</sup> if the BVS is ~1.8-2.0, an OH<sup>-</sup> if the BVS is ~0.9-1.2, and an H<sub>2</sub>O if the BVS is ~0.2-0.4, although these numbers may vary a little due to hydrogen-bonding.

Table 4-8. Bond Valence Sums for the Mn Atoms in Complex **4-5**<sup>a</sup>

	Mn <sup>II</sup>	Mn <sup>III</sup>	Mn <sup>IV</sup>
Mn1	3.13	<u>2.86</u>	3.01
Mn2	3.17	<u>2.90</u>	3.05
Mn3	3.12	<u>2.85</u>	3.00
Mn4	3.20	<u>2.93</u>	3.07
Mn5	3.22	<u>2.97</u>	2.97
Mn6	<u>1.87</u>	1.71	1.80
Mn7	<u>1.81</u>	1.66	1.74
Mn8	3.27	<u>3.02</u>	3.02
Mn9	3.32	<u>3.07</u>	3.07
Mn10	3.26	<u>3.01</u>	3.01
Mn11	3.14	<u>2.87</u>	3.01
Mn12	<u>1.92</u>	1.76	1.84

<sup>a</sup> The oxygen atom is an O<sup>2-</sup> if the BVS is ~1.8-2.0, an OH<sup>-</sup> if the BVS is ~0.9-1.2, and an H<sub>2</sub>O if the BVS is ~0.2-0.4, although these numbers may vary a little due to hydrogen-bonding.

Table 4-9. Bond Valence Sums for the Inorganic Oxygen Atoms in Complex **4-5**<sup>a</sup>

atom	BVS	assgt <sup>a</sup>
O1	1.73	O <sup>2-</sup>
O2	1.88	O <sup>2-</sup>
O3	1.07	OH <sup>-</sup>
O4	1.85	O <sup>2-</sup>
O5	1.67	O <sup>2-</sup>
O6	1.73	O <sup>2-</sup>
O7	1.73	O <sup>2-</sup>
O8	1.93	O <sup>2-</sup>
O37	0.27	H <sub>2</sub> O

<sup>a</sup> The oxygen atom is an O<sup>2-</sup> if the BVS is ~1.8-2.0, an OH<sup>-</sup> if the BVS is ~0.9-1.2, and an H<sub>2</sub>O if the BVS is ~0.2-0.4, although these numbers may vary a little due to hydrogen-bonding.

Table 4-10. Complexes with hmp-, dmhmp-, or dphmp-, and the Alkoxide O Atom Binding Mode

Complex <sup>a</sup>	n ( $\mu_n$ -O) <sup>b</sup>	Ref
[Mn <sub>4</sub> O <sub>2</sub> (O <sub>2</sub> CPh) <sub>7</sub> (hmp) <sub>2</sub> ] <sup>-</sup>	1	257
[Mn <sub>4</sub> (hmp) <sub>6</sub> X <sub>4-x</sub> (solv) <sub>x</sub> ] <sup>z+</sup> <sup>c</sup>	3	148-150, 252-254
[Mn <sub>4</sub> (6-Me-hmp) <sub>6</sub> Cl <sub>4</sub> ]	3	148
[Mn <sub>4</sub> (hmp) <sub>4</sub> Br <sub>2</sub> (OMe) <sub>2</sub> (dcn) <sub>2</sub> ]	3	150
[Mn <sub>4</sub> (hmp) <sub>4</sub> (acac) <sub>2</sub> (MeO) <sub>2</sub> ] <sup>2+</sup>	2	51
[Mn <sub>7</sub> (OH) <sub>3</sub> (hmp) <sub>9</sub> Cl <sub>3</sub> ] <sup>2+</sup>	2, 3	45, 147
[Mn <sub>10</sub> O <sub>4</sub> (OH) <sub>2</sub> (O <sub>2</sub> CMe) <sub>8</sub> (hmp) <sub>8</sub> ] <sup>4+</sup>	2, 3	45
[Mn <sub>10</sub> O <sub>4</sub> (N <sub>3</sub> ) <sub>4</sub> (hmp) <sub>12</sub> ] <sup>2+</sup>	2	44
[Mn <sub>12</sub> O <sub>8</sub> Cl <sub>4</sub> (O <sub>2</sub> CPh) <sub>8</sub> (hmp) <sub>6</sub> ]	2	151
[Mn <sub>21</sub> O <sub>14</sub> (OH) <sub>2</sub> (O <sub>2</sub> CMe) <sub>16</sub> (hmp) <sub>8</sub> (pic) <sub>2</sub> (py)(H <sub>2</sub> O)] <sup>4+</sup>	2	152
[Mn <sub>7</sub> O <sub>3</sub> (OH) <sub>3</sub> (O <sub>2</sub> CBu <sup>t</sup> ) <sub>7</sub> (dmhmp) <sub>4</sub> ] ( <b>4-4</b> )	1, 2	t.w.
[Mn <sub>12</sub> O <sub>7</sub> (OH)(OMe) <sub>2</sub> (O <sub>2</sub> CPh) <sub>12</sub> (dmhmp) <sub>4</sub> (H <sub>2</sub> O)] ( <b>4-5</b> )	2	t.w.
[Mn <sub>6</sub> O <sub>4</sub> (dmhmp) <sub>6</sub> (N <sub>3</sub> ) <sub>4</sub> ] ( <b>4-6</b> )	1, 2	t.w.
[Mn <sub>4</sub> O <sub>2</sub> (O <sub>2</sub> CBu <sup>t</sup> ) <sub>5</sub> (dphmp) <sub>3</sub> ] ( <b>4-1</b> )	1, 2	t.w.
[Mn <sub>6</sub> O <sub>4</sub> (OMe) <sub>2</sub> (O <sub>2</sub> CPh) <sub>4</sub> (dphmp) <sub>4</sub> ] ( <b>4-2</b> )	1	t.w.
[Mn <sub>11</sub> O <sub>7</sub> (OMe) <sub>7</sub> (O <sub>2</sub> CPh) <sub>7</sub> (dphmp) <sub>4</sub> (MeOH) <sub>2</sub> ] ( <b>4-3</b> )	1, 2	t.w.

<sup>a</sup> Counterions omitted. <sup>b</sup> bridging mode of the hmp<sup>-</sup>, dmhmp<sup>-</sup>, or dphmp<sup>-</sup> O atom;  $\mu_1$ -O indicates a non-bridging (terminal) mode. <sup>c</sup> Many complexes, varying in the content of monodentate anionic ligand X<sup>-</sup> and solvent molecules (solv). t.w. = this work.

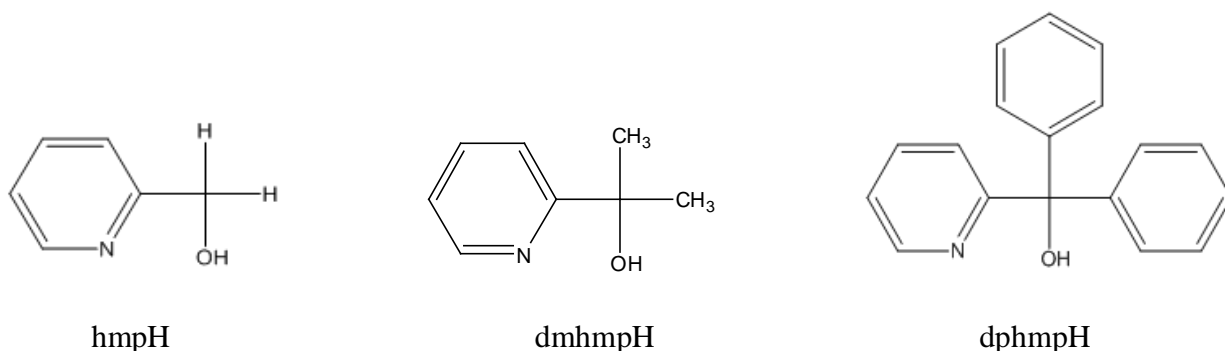


Figure 4-1. Structure of ligands: 2-(hydroxymethyl)pyridine (hmpH), 2-(pyridine-2-yl)propan-2-ol (dmhmpH), and diphenyl (pyridine-2-yl)methanol (dphmpH).

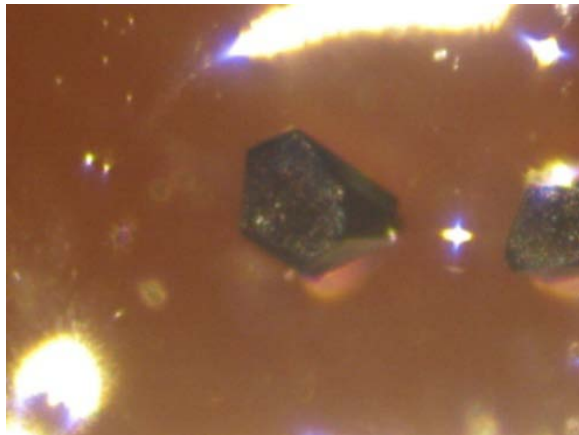


Figure 4-2. A picture of crystals of **4-1**.

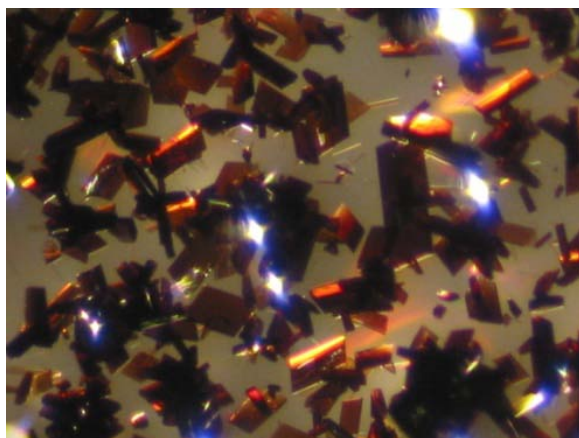


Figure 4-3. A picture of crystals of **4-2**.

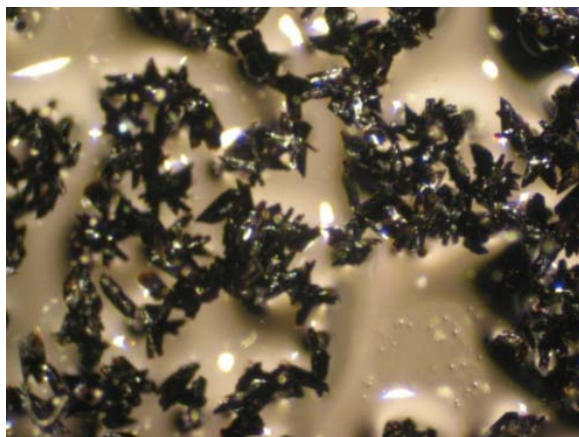


Figure 4-4. A picture of crystals of **4-3**.



Figure 4-5. A picture of crystals of **4-4**.

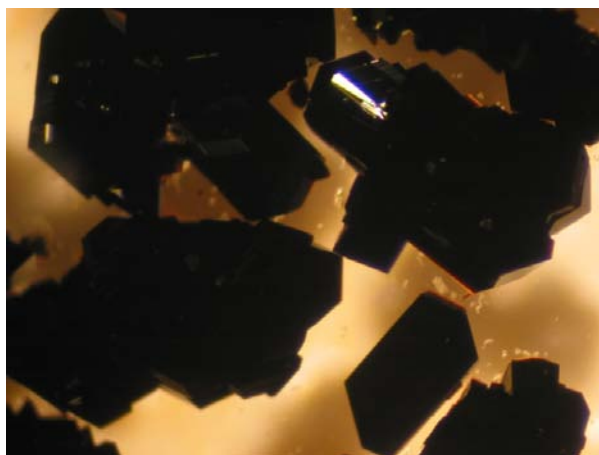


Figure 4-6. A picture of crystals of **4-5**.

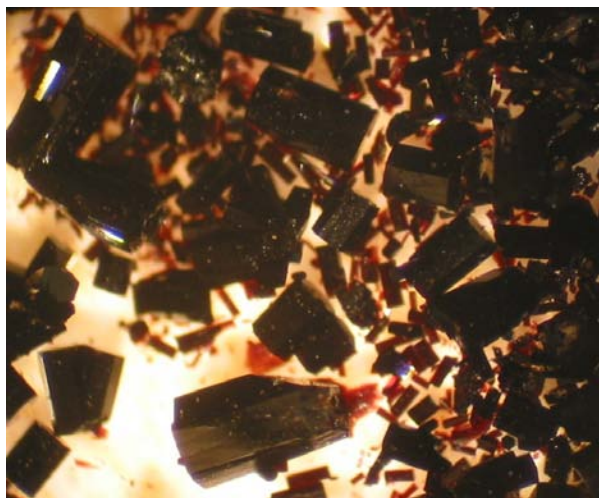


Figure 4-7. A picture of crystals of **4-6**.

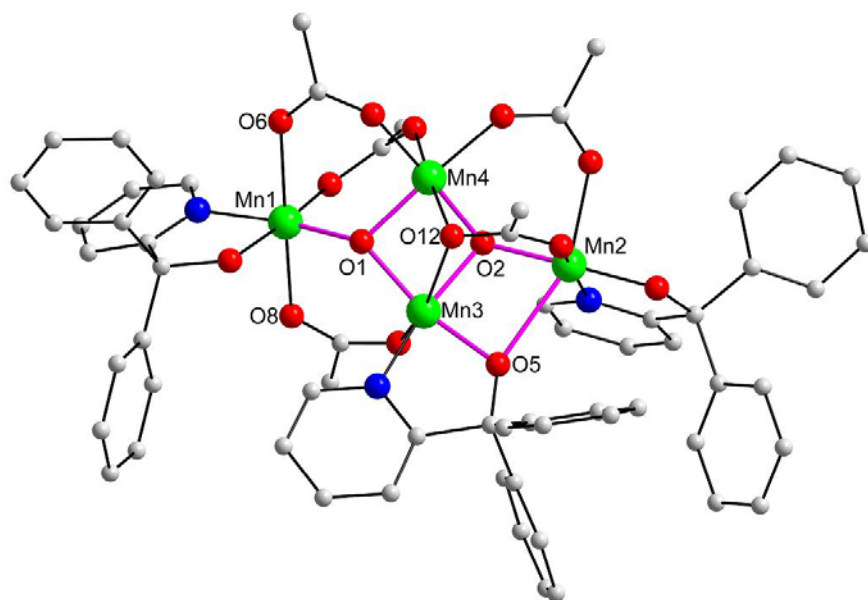


Figure 4-8. The structure of complex **4-1**, with core Mn–O bonds shown in purple. Hydrogen atoms and methyl groups on pivalates have been omitted for clarity. Color code: Mn<sup>III</sup> green; O red; N blue; C gray.

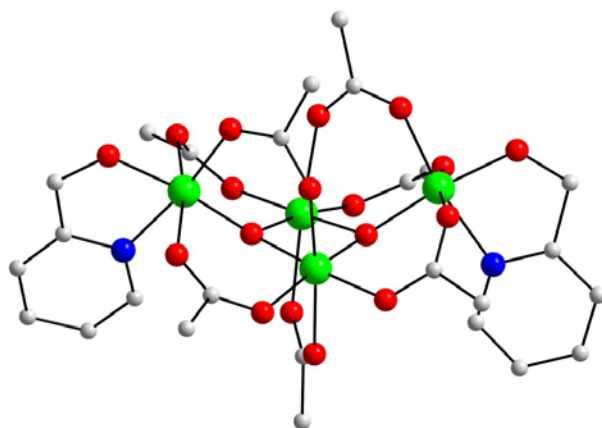


Figure 4-9. The structure of complex **4-8**, with core Mn–O bonds shown in purple. Hydrogen atoms and methyl groups on pivalates have been omitted for clarity. Color code: Mn<sup>III</sup> green; O red; N blue; C gray.

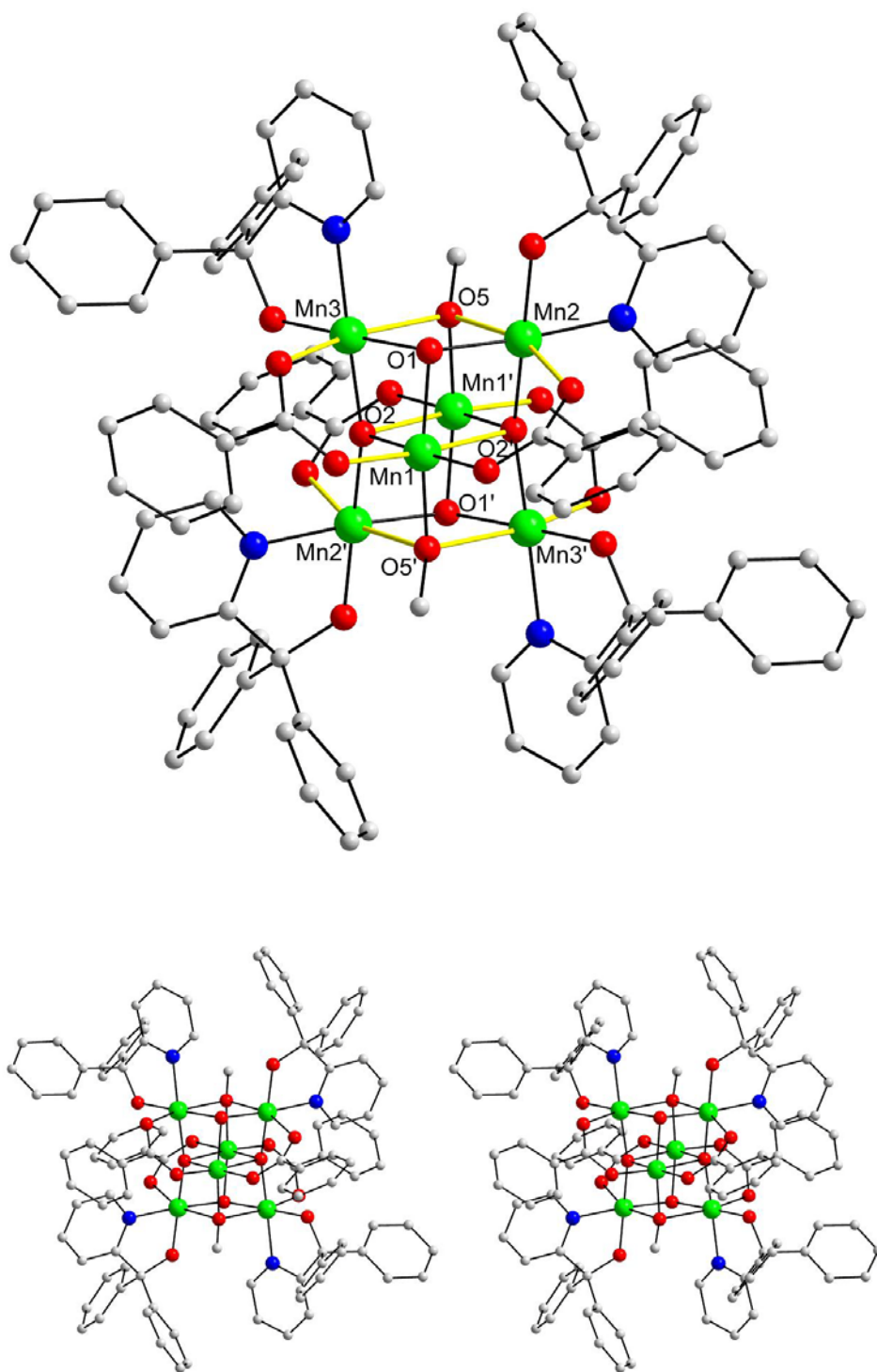


Figure 4-10. The structure of complex **4-2** with the Mn<sup>III</sup> Jahn–Teller elongation axes shown as yellow bonds (top), and a stereopair (bottom). Hydrogen atoms have been omitted for clarity. Color code: Mn<sup>III</sup> green; O red; N blue; C gray.

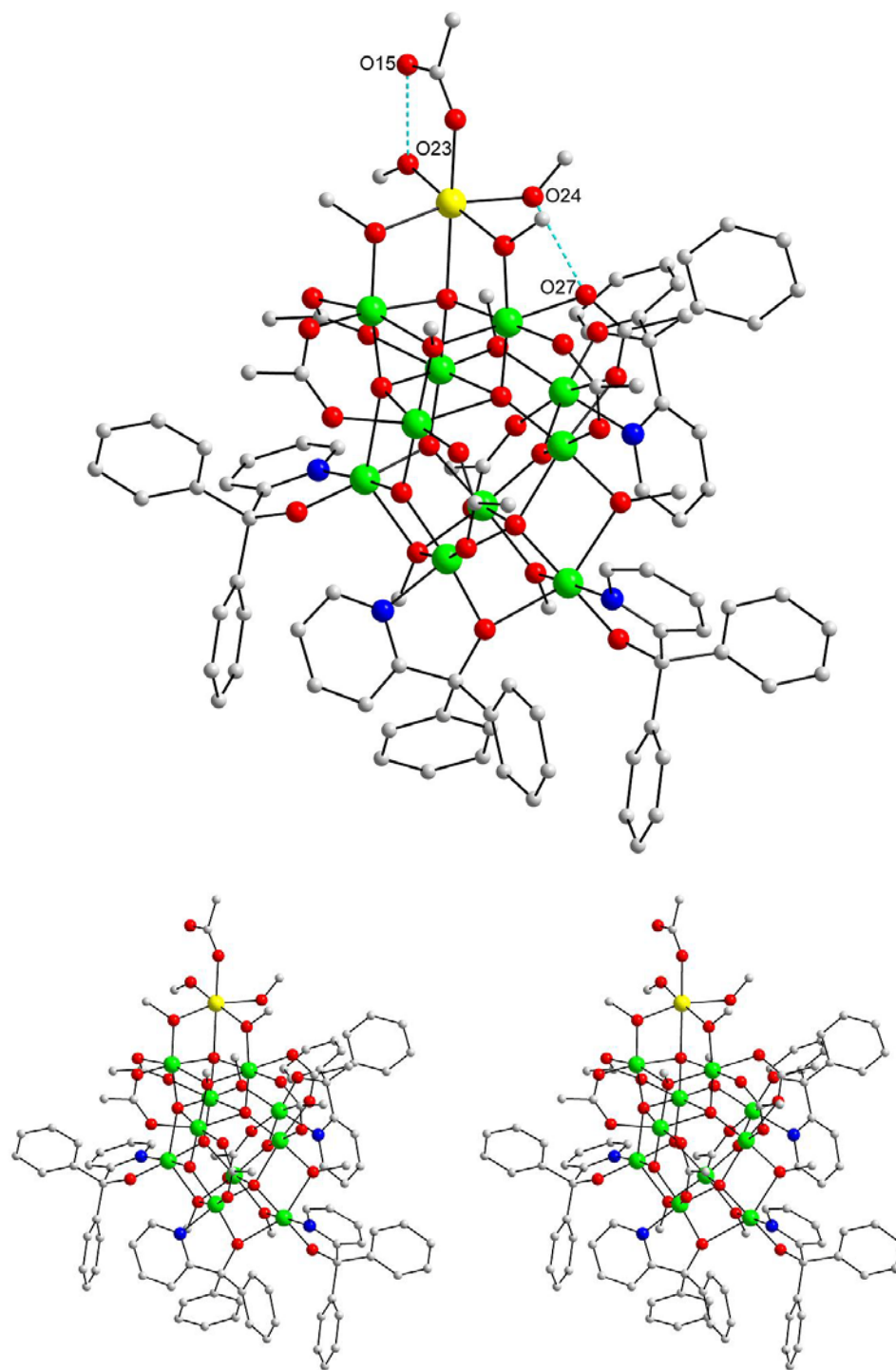


Figure 4-11. The structure of complex **4-3** with intramolecular hydrogen-bonds shown as dashed lines (top), and a stereopair (bottom). Hydrogen atoms and benzoate phenyl rings (except for the ipso carbon atoms) have been omitted for clarity. Color code: Mn<sup>II</sup> yellow; Mn<sup>III</sup> green; O red; N blue; C gray.

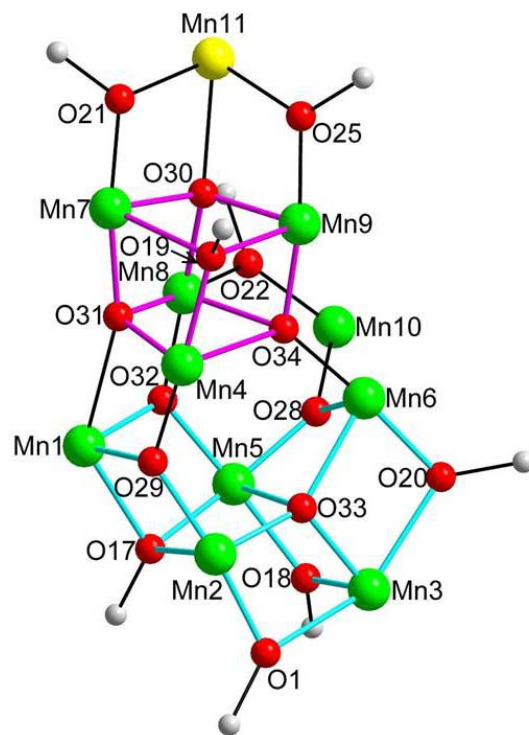


Figure 4-12. The fully labeled core of complex **4-3**. Color code: Mn<sup>II</sup> yellow; Mn<sup>III</sup> green; O red; C gray.

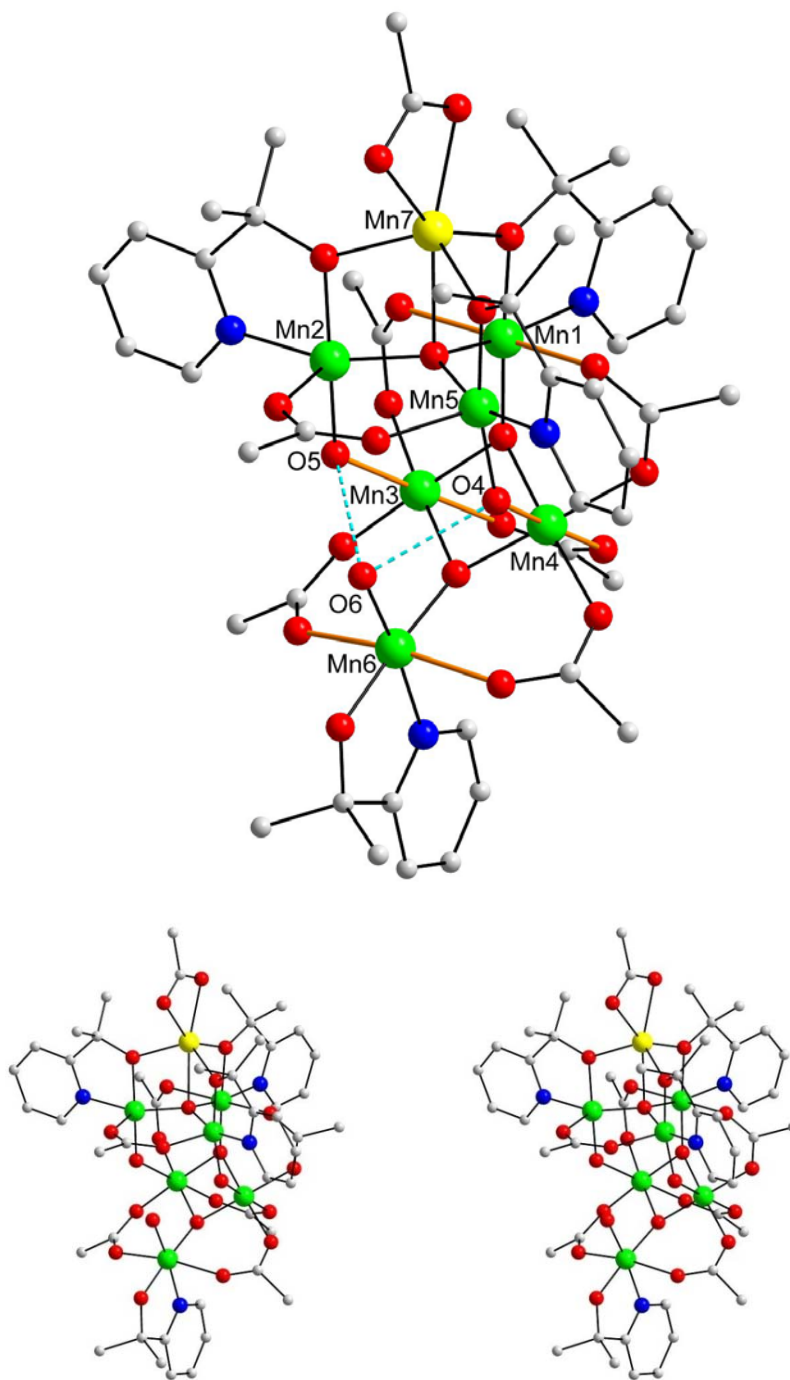


Figure 4-13. The structure of complex **4-4** with intramolecular hydrogen-bonds shown as dashed lines (top), and a stereopair. The thicker orange bonds indicate the positions of the  $\text{Mn}^{\text{III}}$  Jahn–Teller elongation axes. Hydrogen atoms and methyl groups on pivalate groups have been omitted for clarity. Color code:  $\text{Mn}^{\text{II}}$  yellow;  $\text{Mn}^{\text{III}}$  green; O red; N blue; C grey.

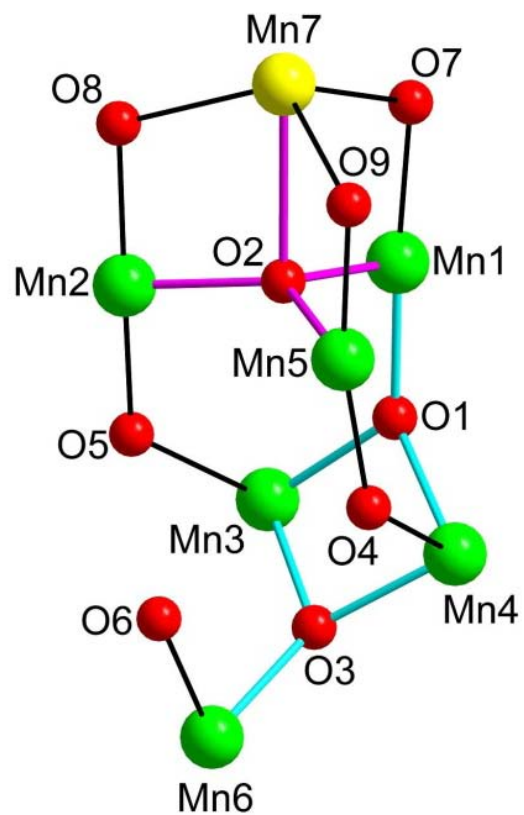


Figure 4-14. The fully labeled core of complex **4-4**. Color code: Mn<sup>II</sup> yellow; Mn<sup>III</sup> green; O red.

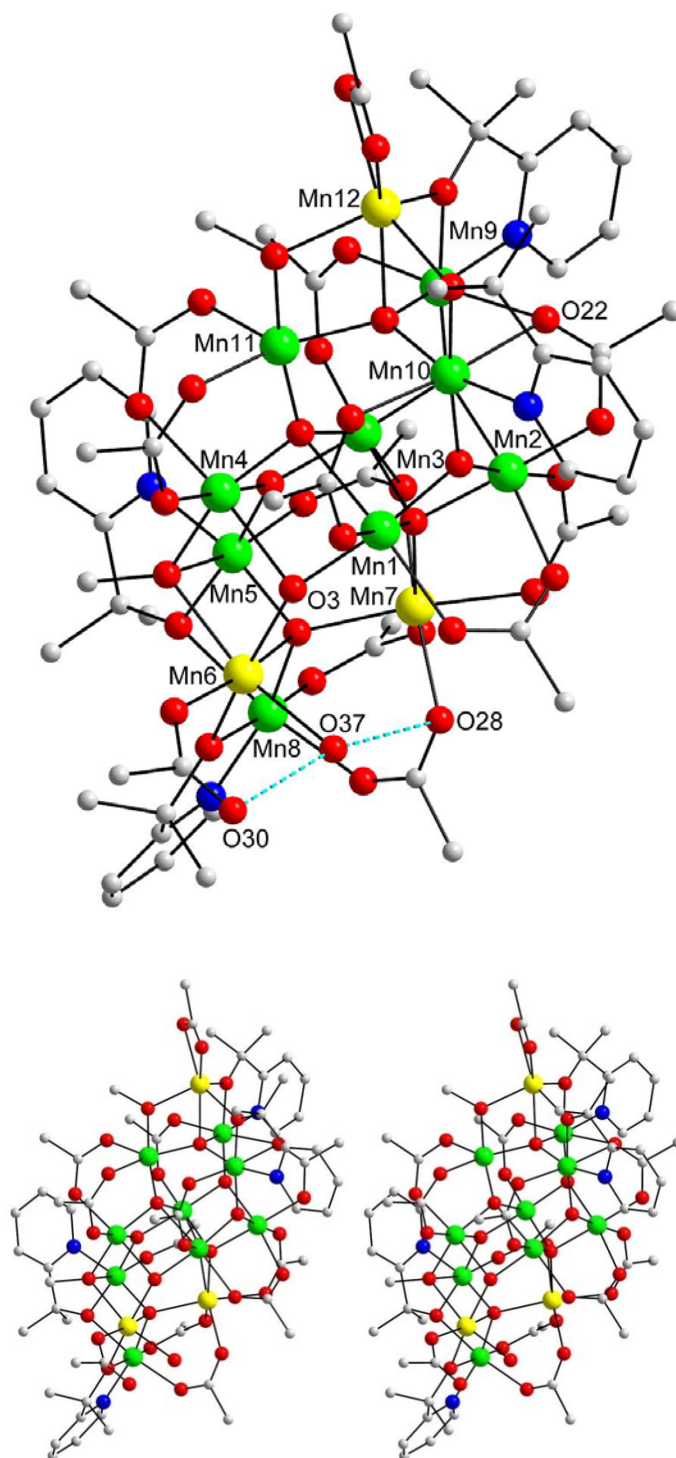


Figure 4-15. The structure of complex **4-5** with intramolecular hydrogen-bonds shown as dashed lines (top), and a stereopair (bottom). Hydrogen atoms and phenyl rings (except for the ipso carbon atoms) on benzoate groups have been omitted for clarity. Color code: Mn<sup>II</sup> yellow; Mn<sup>III</sup> green; O red; C gray; N blue.

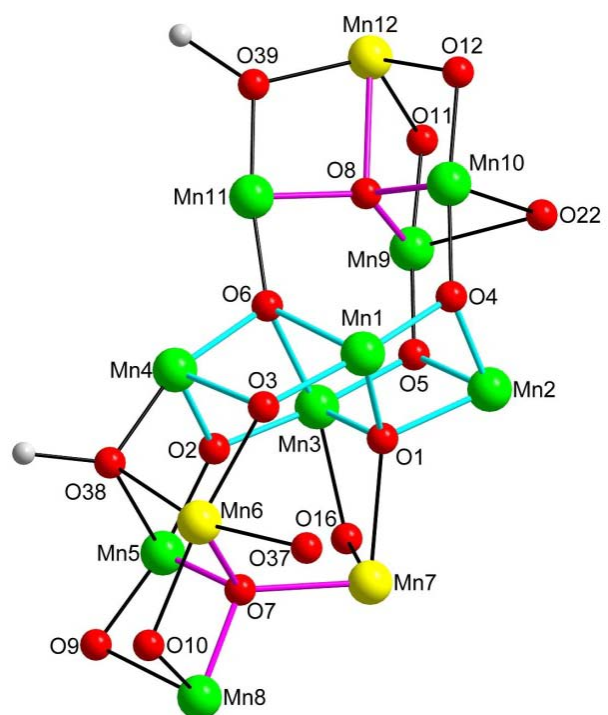


Figure 4-16. The fully labeled core of complex **4-5**. Color code: Mn<sup>II</sup> yellow; Mn<sup>III</sup> green; O red; C gray.

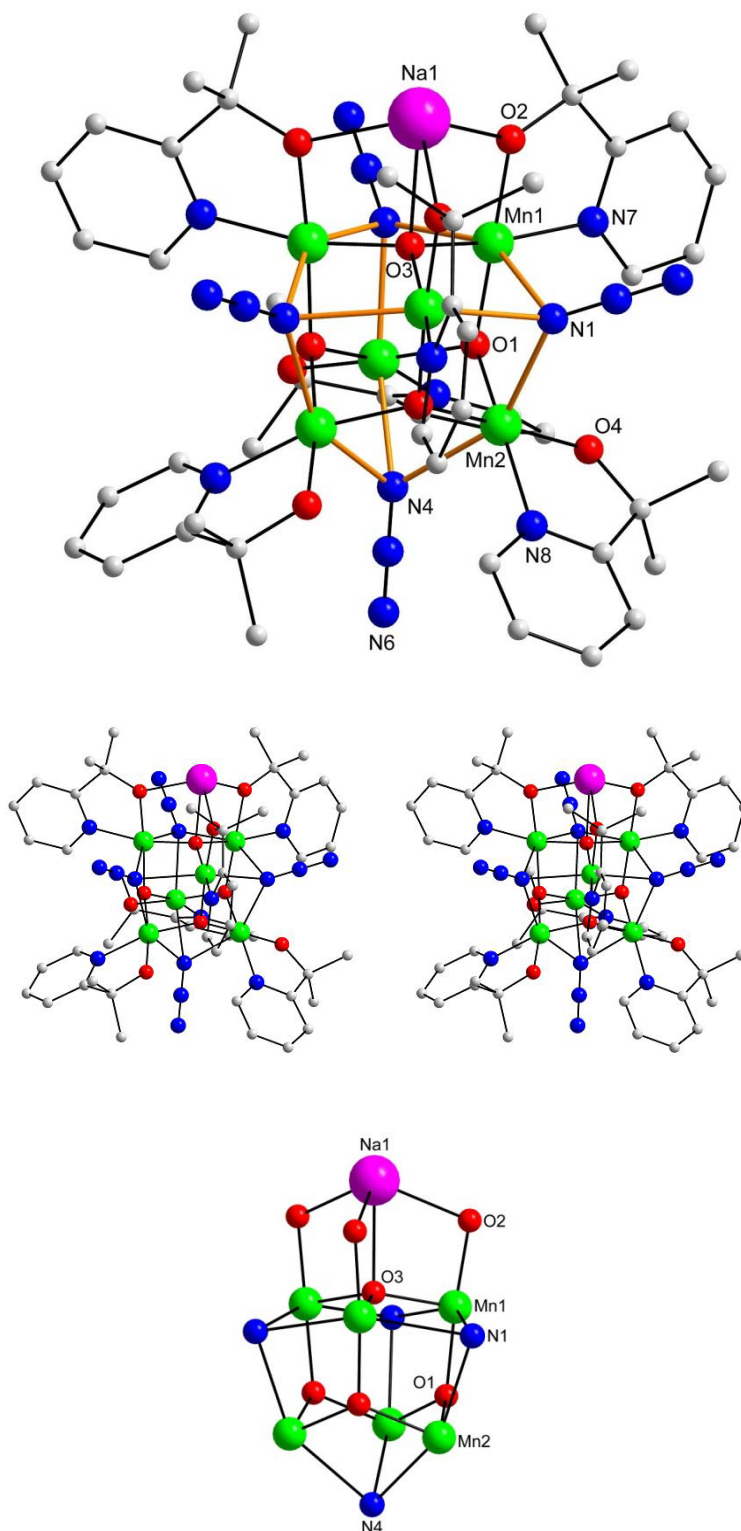


Figure 4-17. The structure of complex **4-6** (top), a stereopair (middle), and the labeled core (bottom). The thicker orange bonds indicate the positions of the Mn<sup>III</sup> Jahn–Teller elongation axes. Hydrogen atoms have been omitted for clarity. Color code: Mn<sup>III</sup> green; O red; C gray; N blue; Na Purple.

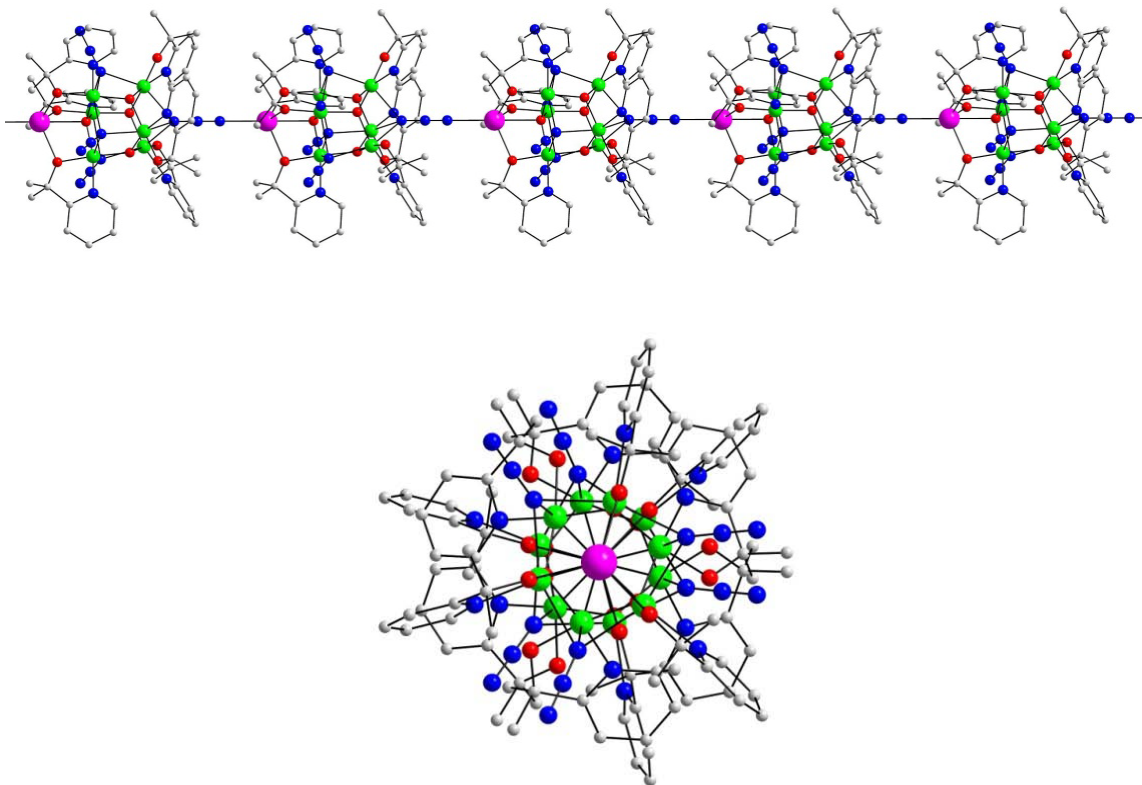


Figure 4-18. 1 D chain of complex **4-6** viewed perpendicular (top) and parallel (bottom) to c-axis. Hydrogen atoms have been omitted for clarity. Mn<sup>III</sup> green; O red; C gray; N blue; Na Purple

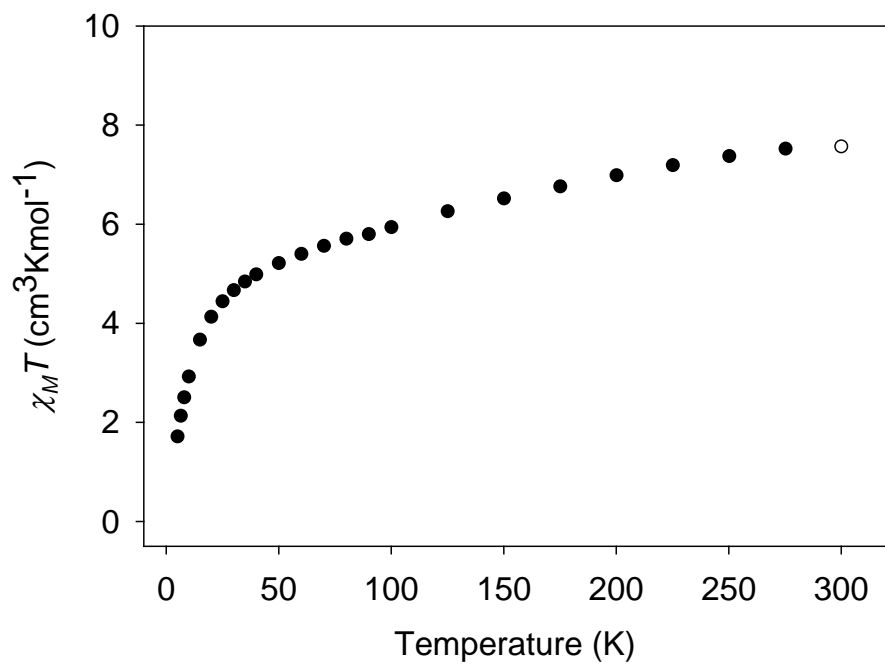


Figure 4-19. Plots of  $\chi_M T$  vs. T for complexes **4-1**.

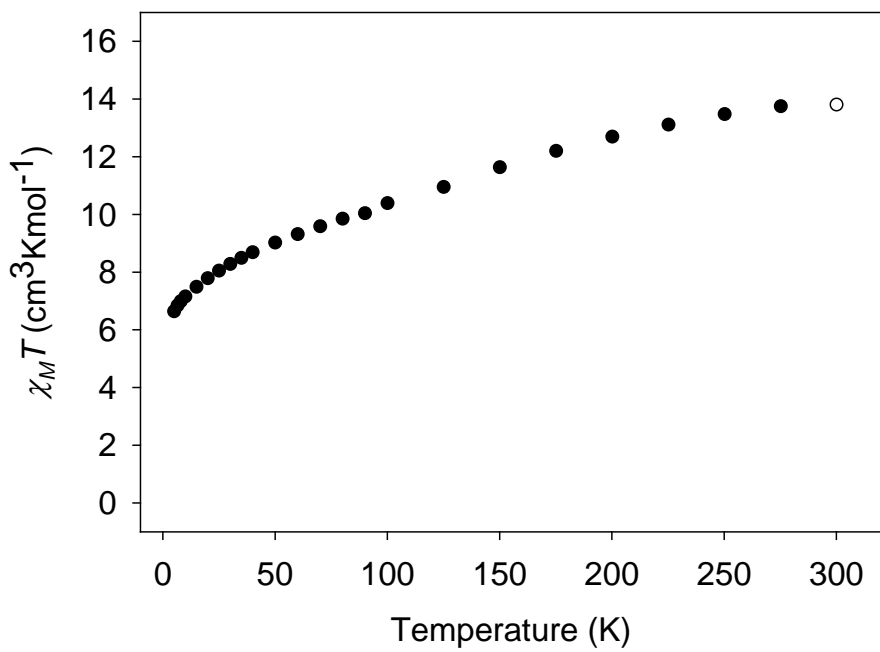


Figure 4-20. Plots of  $\chi_M T$  vs. T for complexes **4-2**.

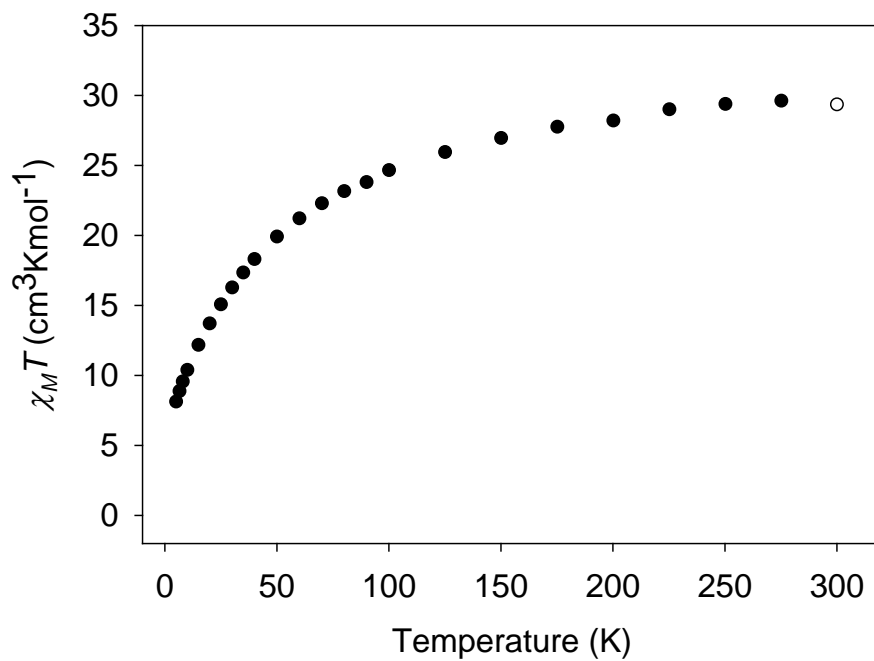


Figure 4-21. Plots of  $\chi_M T$  vs. T for complexes **4-3**.

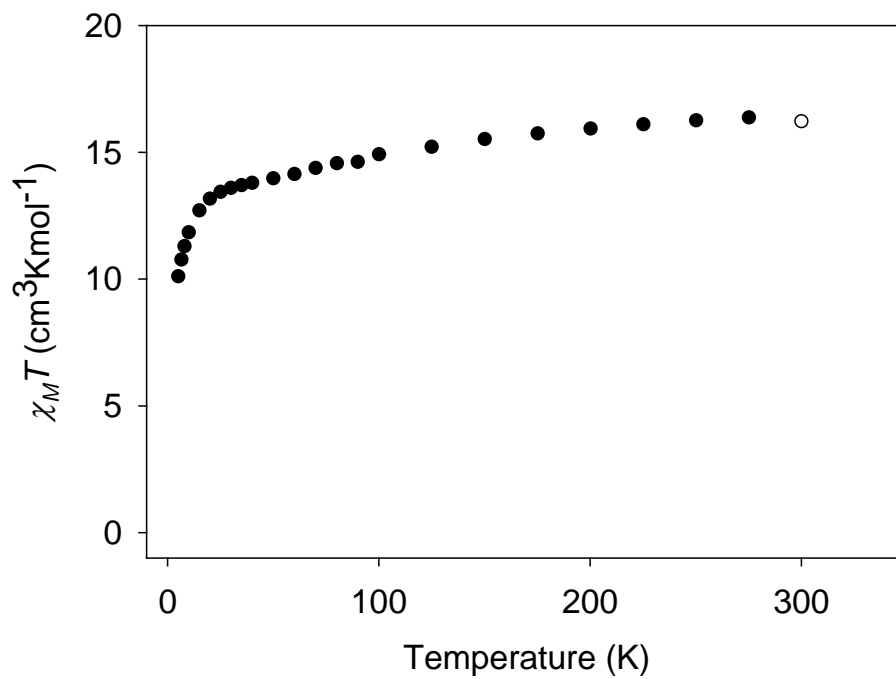


Figure 4-22. Plots of  $\chi_M T$  vs. T for complexes **4-4**.

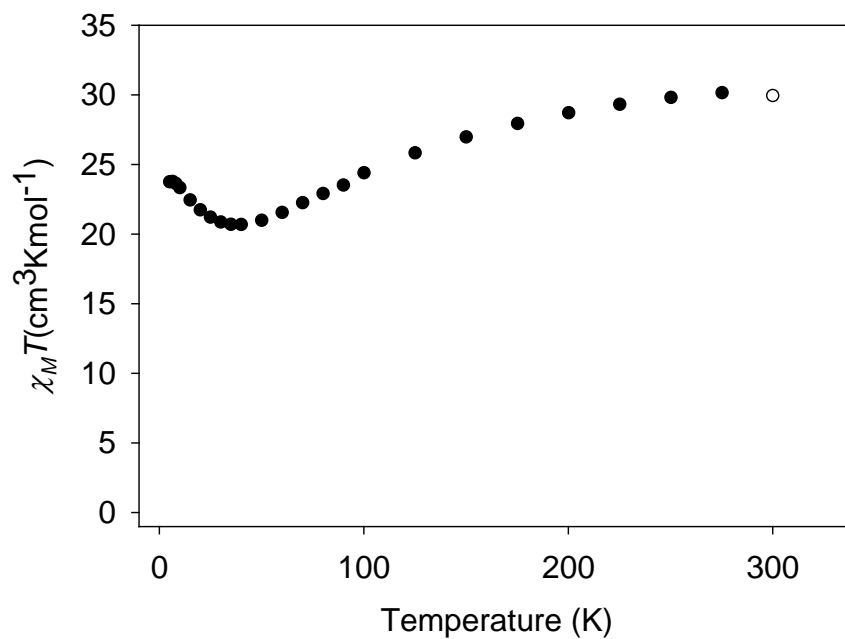


Figure 4-23. Plots of  $\chi_M T$  vs. T for complexes 4-5.

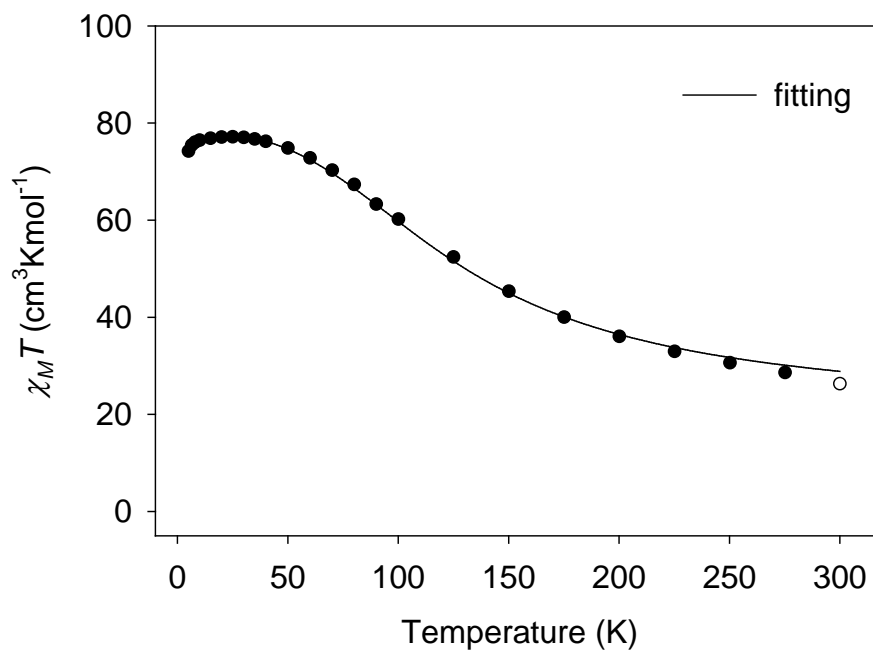


Figure 4-24. Plots of  $\chi_M T$  vs. T for complexes 4-6. The solid line is the fit of the data; see the text for the fit parameters

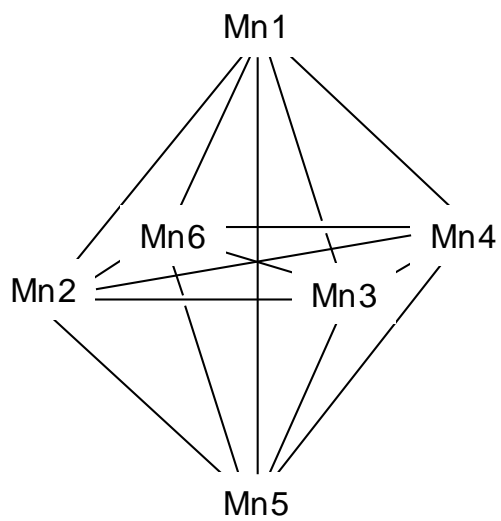


Figure 4-25. Mn labeling scheme employed in eq.4-7.

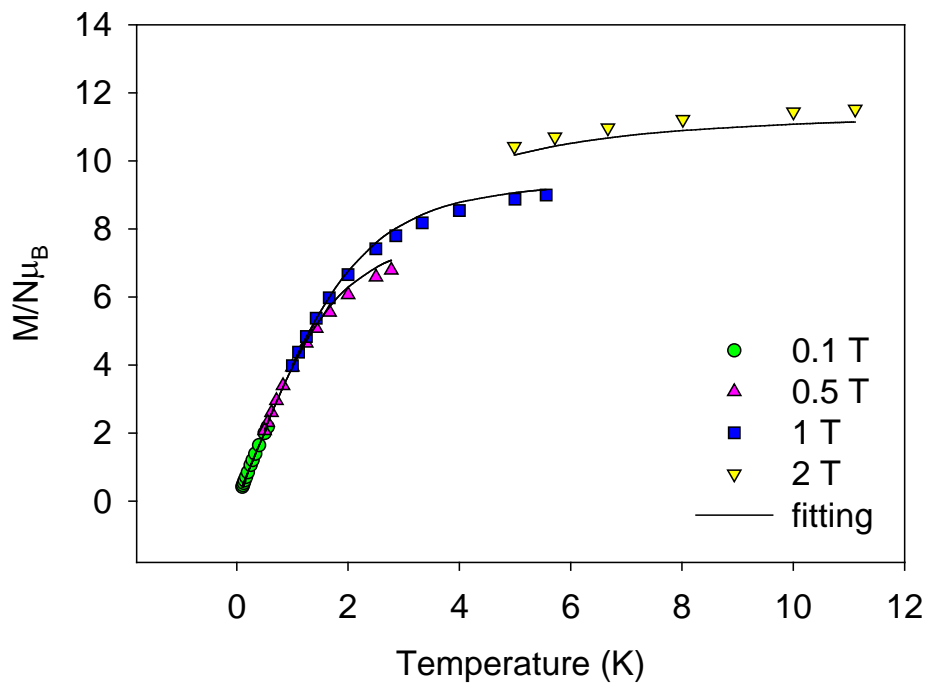


Figure 4-26. Plots of reduced magnetization ( $M/N\mu_B$ ) vs  $H/T$  for complex 4-5. The solid lines are the fit of the data; see the text for the fit parameters.

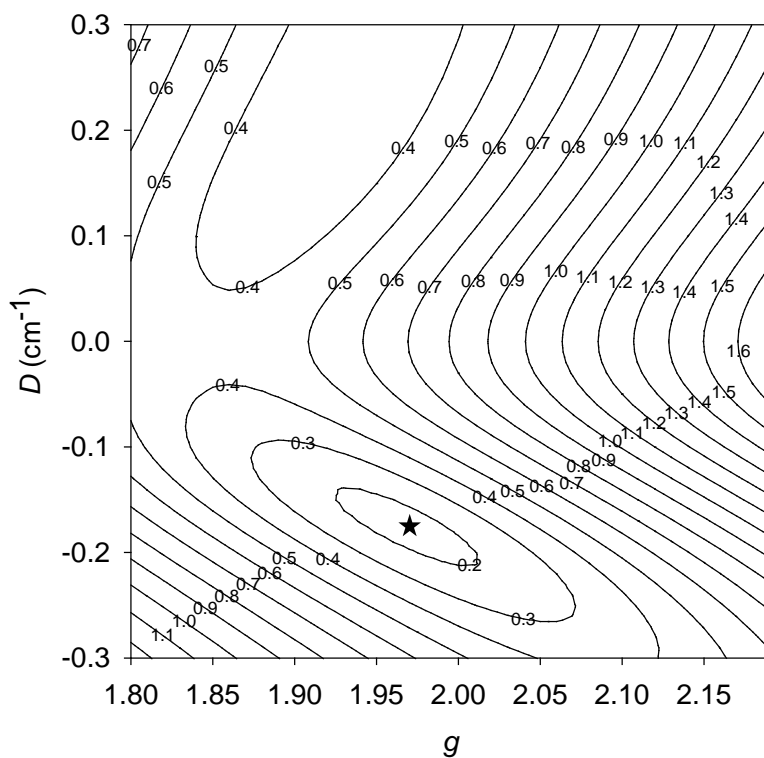


Figure 4-27. Two-dimensional contour plot of the root-mean-square error surface for the  $D$  vs  $g$  fit for complex 4-5.

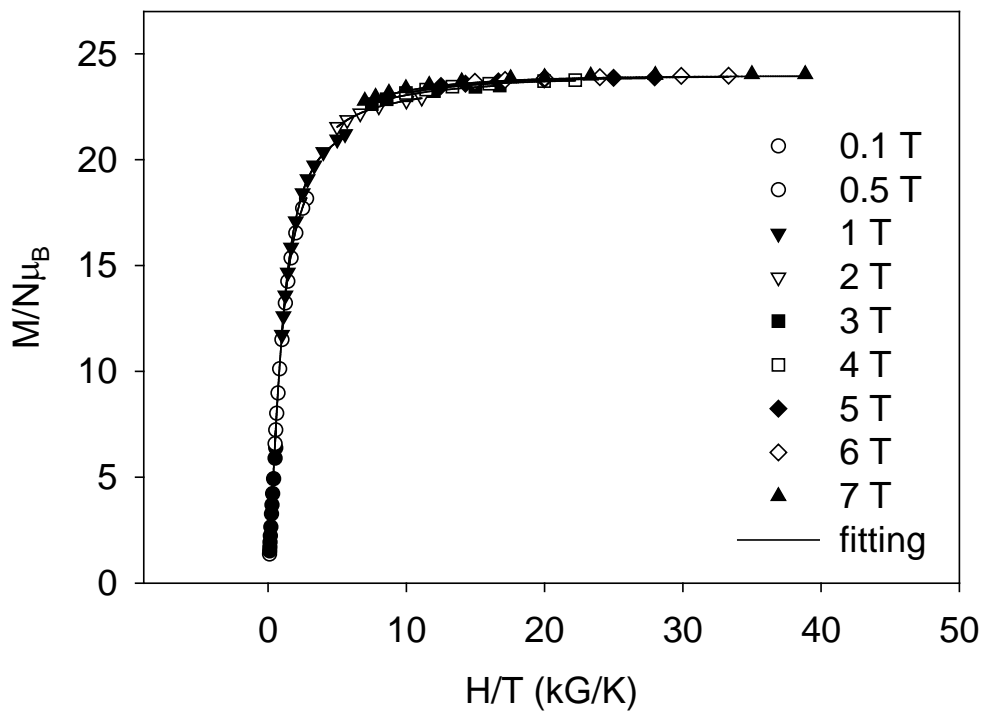


Figure 4-28. Plots of reduced magnetization ( $M/N\mu_B$ ) vs  $H/T$  for complex 4-6. The solid lines are the fit of the data; see the text for the fit parameters.

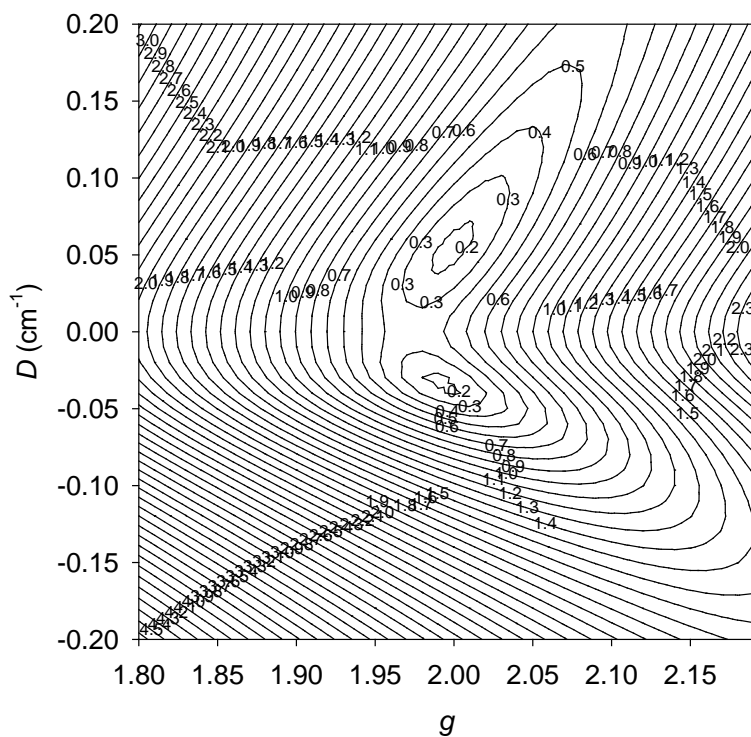


Figure 4-29. Two-dimensional contour plot of the root-mean-square error surface for the  $D$  vs  $g$  fit for complex 4-6.

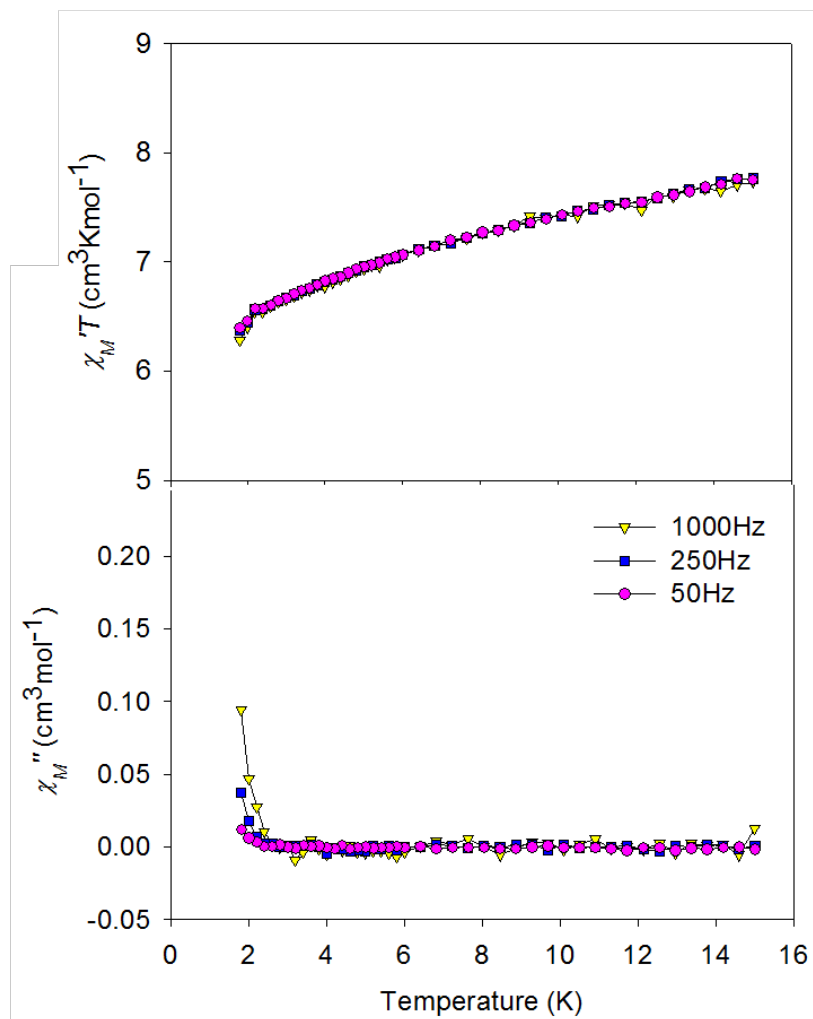


Figure 4-30. AC susceptibility of complex **4-2** in a 3.5 G field oscillating at the indicated frequencies: (top) in-phase signal ( $\chi_M'$ ) plotted as  $\chi_M' T$  vs  $T$ ; and (bottom) out-of-phase signal  $\chi_M''$  vs  $T$ .

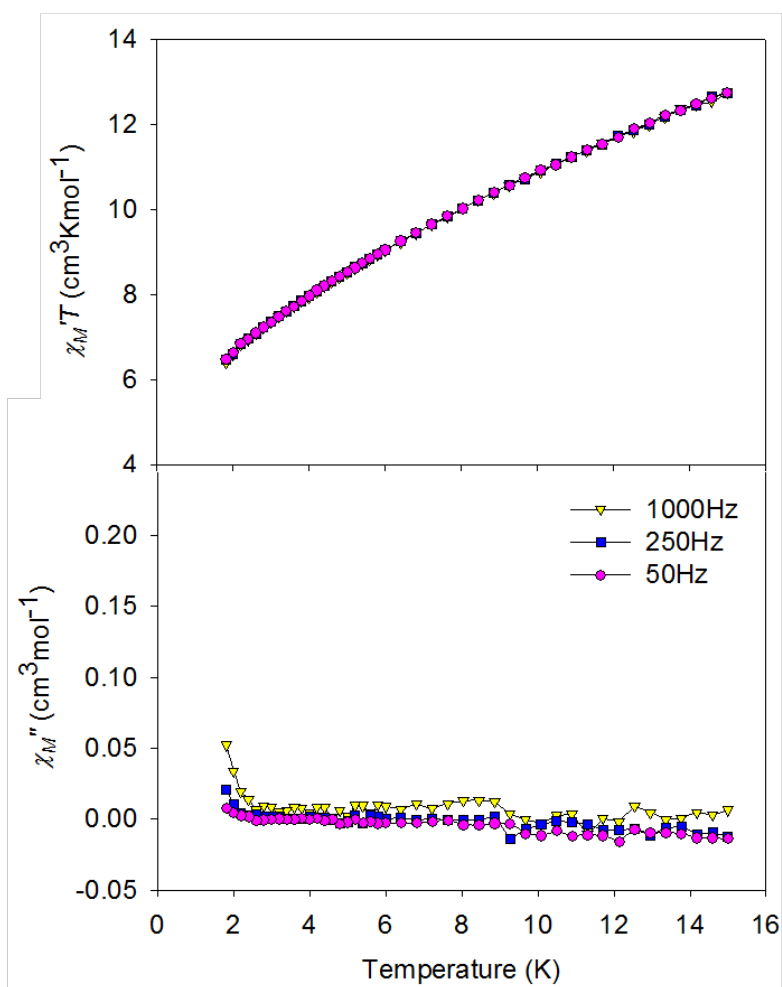


Figure 4-31. AC susceptibility of complex **4-3** in a 3.5 G field oscillating at the indicated frequencies: (top) in-phase signal ( $\chi_M'$ ) plotted as  $\chi_M' T$  vs T; and (bottom) out-of-phase signal  $\chi_M''$  vs T.

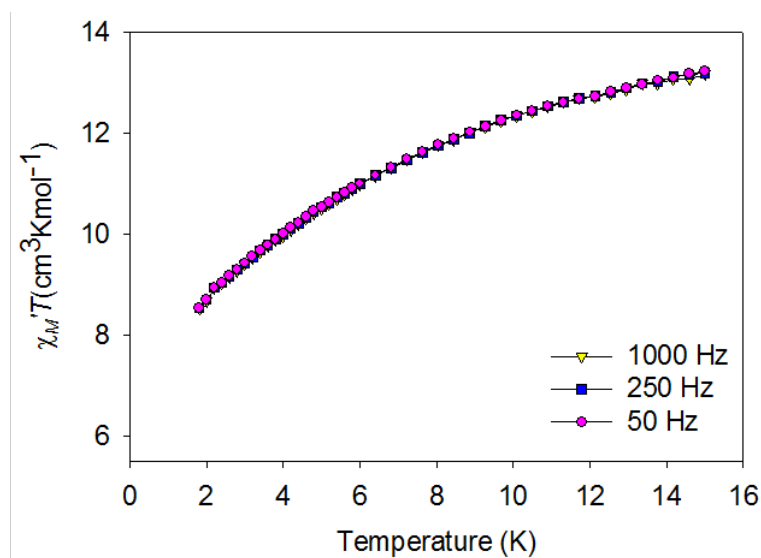


Figure 4-32. In-phase ac susceptibility ( $\chi_M'$ , plotted as  $\chi_M' T$  vs  $T$ ) of complex **4-4** in a 3.5 G ac field oscillating at the indicated frequencies.

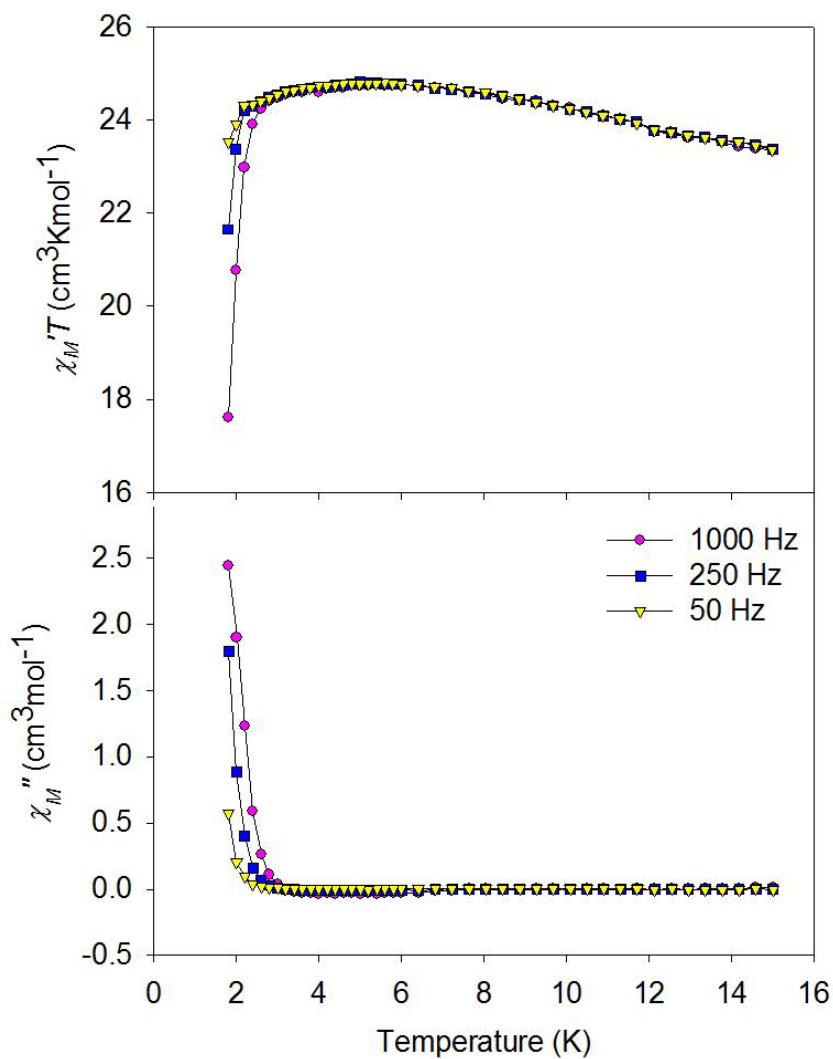


Figure 4-33. AC susceptibility of complex **4-5** in a 3.5 G field oscillating at the indicated frequencies: (top) in-phase signal ( $\chi_M'$ ) plotted as  $\chi_M' T$  vs T; and (bottom) out-of-phase signal  $\chi_M''$  vs T.

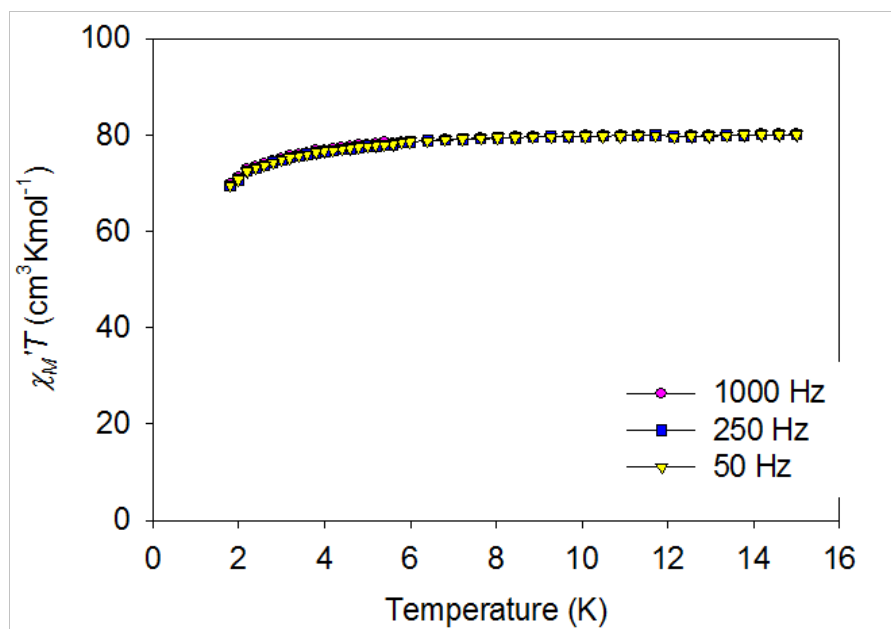


Figure 4-34. In-phase ac susceptibility ( $\chi_M'$ , plotted as  $\chi_M' T$  vs  $T$ ) of complex **4-6** in a 3.5 G ac field oscillating at the indicated frequencies.

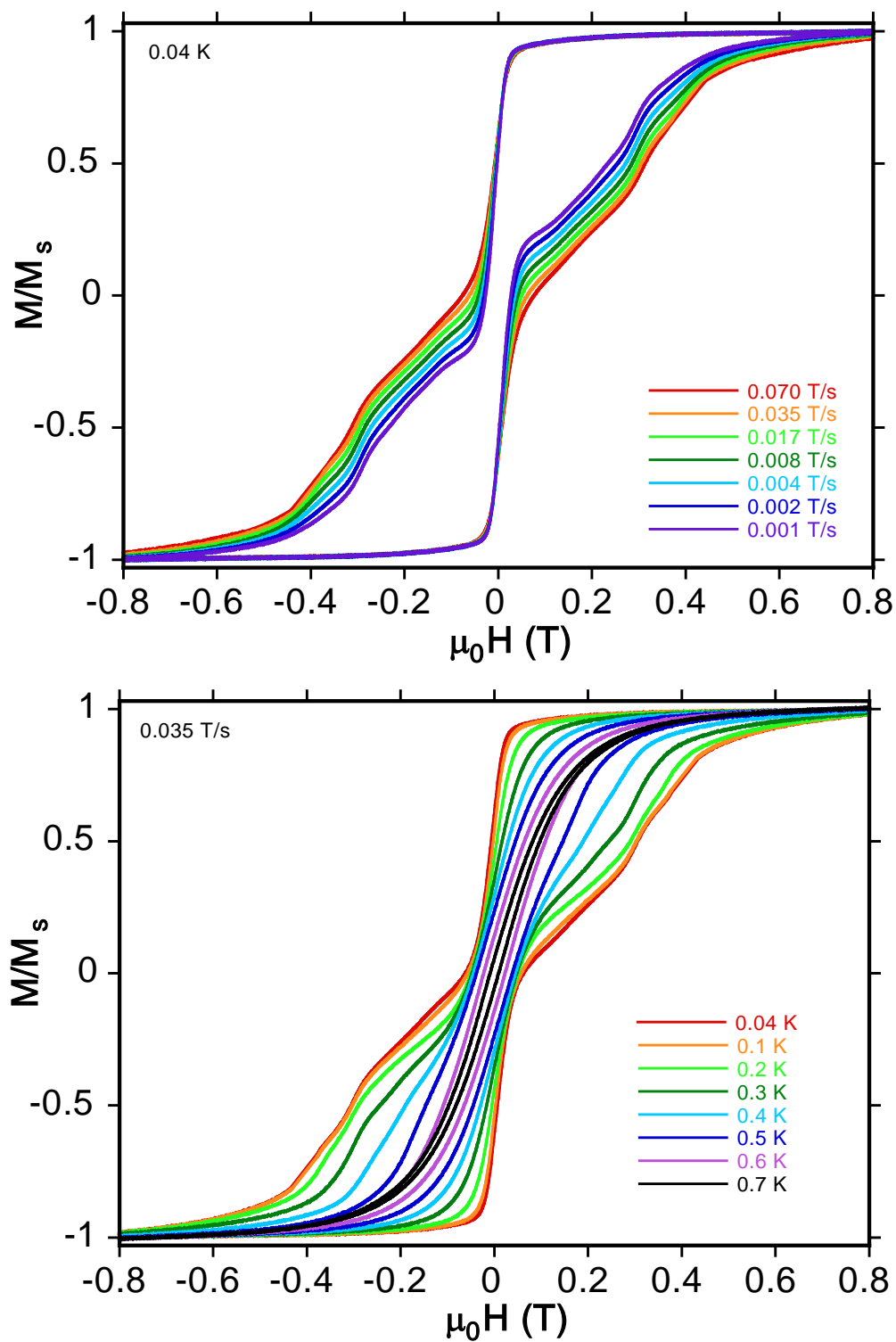


Figure 4-35. Single-crystal magnetization ( $M$ ) vs dc field ( $H$ ) hysteresis loops for a single crystal of  $4-5 \cdot 3\text{CH}_2\text{Cl}_2$  at different scan rates (top) and temperatures (bottom).

CHAPTER 5  
NEW MN<sub>4</sub> AND MN<sub>7</sub> CLUSTERS FROM THE USE OF PHENYLDIPYRIDIN-2-  
YLMETHANOL

**5.1 Introduction**

There continues to be great interest in the synthesis and characterization of high-nuclearity 3d transition metal clusters. In some cases, this is because of their relevance to bioinorganic chemistry as models for the metallosites of various proteins and enzymes, whereas in other cases it is their importance to molecular magnetism that drives this interest. And in many instances, the intrinsic architectural beauty and aesthetically pleasing structures of metal clusters is itself the primary interest within the field of supramolecular chemistry.<sup>196</sup> In manganese chemistry, for example, Mn carboxylate clusters are of bioinorganic interest because of their relevance to elucidating the nature and mechanism of action of the water oxidizing complex (WOC) on the donor side of photosystem II in green plants and cyanobacteria.<sup>269-272</sup> The WOC comprises a pentanuclear Mn<sub>4</sub>Ca cluster, the exact structure of which is still unclear, and which is responsible for the light-driven, oxidative coupling of two molecules of water into dioxygen.<sup>273, 274</sup> Secondly, some polynuclear Mn compounds have been found to be single-molecule magnets (SMMs), which are individual molecules capable of functioning as nanoscale magnetic particles and thus represent a molecular approach to nanomagnetism.<sup>12, 13</sup> Such molecules behave as magnets below their blocking temperature ( $T_B$ ), exhibiting hysteresis in magnetization versus dc field scans. This magnetic behavior of SMMs results from the combination of a large ground spin state ( $S$ ) with a large and negative Ising (or easy-axis) type of magnetoanisotropy, as measured by the axial zero-field splitting parameter  $D$ .

As a result of the above, there is a continuing search for new synthetic methods that can yield new polynuclear Mn/O complexes. In the design of potentially new synthetic routes to polynuclear metal complexes, the choice of the ligands and bridging groups is always a key

issue. Accordingly, we and others have explored a wide variety of potentially chelating and/or bridging ligands that might foster formation of high nuclearity products, and have successfully isolated and studied new cluster products. Examples include aliphatic or aromatic alcohols,<sup>185, 186, 212, 220-222, 232-234, 275-287</sup> alcohol amines,<sup>226-231, 288-293</sup> di-2-pyridylketone,<sup>236-238, 294-301</sup> pyridyl alcohols,<sup>44-46, 49, 151,302</sup> pyridyl ketone oximes,<sup>190, 235, 303-313</sup> salicylaldoximes,<sup>206, 223-225, 314-325</sup> and others.<sup>326-334</sup> As a new ligand design strategy to isolate new polynuclear metal complexes, in the previous chapter we reported the use of derivatives of a pyridyl alcohol, 2-(hydroxymethyl) pyridine (hmpH, Figure 5-1), in which two phenyl or two methyl or groups have been added onto the CH<sub>2</sub> unit. The resulting molecules, diphenyl-hmpH (dphmpH; IUPAC name is diphenyl (pyridine-2-yl)methanol) and dimethyl-hmpH (dmhmpH, IUPAC name is 2-(pyridine-2-yl)propan-2-ol) have given distinctly different products from those obtained from hmpH.<sup>335</sup> As a further expansion of our ligand design strategy, in this chapter we describe the use in Mn cluster chemistry of an hmpH derivative in which one phenyl and one pyridyl groups have been added onto the CH<sub>2</sub> unit of hmpH. The resulting molecule, phenyldipyridin-2-ylmethanol (pdpH), is shown in Figure 5-1, and is now a potentially tridentate chelating/bridging group, in contrast to hmpH, dmhmpH, and dphmpH. It was thus anticipated that pdpH would thus give distinctly different products than obtained previously with other chelates.

Note that pdpH has been employed to date in the literature only for the synthesis of a mononuclear complex of In.<sup>336</sup> In the present investigation, we have deliberately targeted higher nuclearity Mn products by exploring the reactions between pdpH and Mn starting materials under basic conditions. This has successfully led to Mn<sub>4</sub> and Mn<sub>7</sub> cluster products containing chelating and bridging pdpH<sup>-</sup>. The syntheses, structures, and electrochemical and magnetochemical characterization of these complexes are described in this chapter.

## 5.2 Experimental Section

### 5.2.1 Syntheses

All preparations were performed under aerobic conditions using chemicals as received, except for the synthesis of pdpmH, which was carried out as previously reported.<sup>337</sup>

$[\text{Mn}_{12}\text{O}_{12}(\text{O}_2\text{CMe})_{16}(\text{H}_2\text{O})_4]\cdot 2\text{MeCO}_2\text{H}\cdot 4\text{H}_2\text{O}$  and  $\text{NBu}^n_4\text{MnO}_4$  were prepared as previously reported.<sup>17, 338, 339</sup> *Safety note: Perchlorate salts are potentially explosive; such compounds should be synthesized and used in small quantities, and treated with utmost care at all times.*

**$[\text{Mn}_4\text{O}_4(\text{O}_2\text{CMe})_3(\text{pdpm})_3]$  (5-1). Method A.** To a stirred solution of pdpmH (0.17 g, 0.65 mmol) in MeCN (20 mL) was added  $[\text{Mn}_{12}\text{O}_{12}(\text{O}_2\text{CMe})_{16}(\text{H}_2\text{O})_4]\cdot 2\text{MeCO}_2\text{H}\cdot 4\text{H}_2\text{O}$  (0.20 g, 0.11 mmol). The dark brown solution was stirred for 3 hours, and filtered to remove undissolved solid. Vapor diffusion of  $\text{Et}_2\text{O}$  into the filtrate gave X-ray quality crystals of **5-1** $\cdot 0.5\text{MeCN}$  after 2 weeks. These were collected by filtration, washed with  $\text{Et}_2\text{O}$ , and dried in vacuo; the yield was ~5%. Anal. Calc. (Found) for **5-1** (solvent-free): C, 55.00 (54.74); H, 3.89 (3.74); N, 6.75 (6.55). Selected IR data ( $\text{cm}^{-1}$ ): 3446 (m), 3054 (w), 1585 (s), 1569 (s), 1491 (m), 1473 (m), 1428 (s), 1410 (s), 1338 (m), 1296 (w), 1254 (w), 1179 (w), 1098 (m), 1053 (s), 1034 (m), 995 (w), 947 (w), 928 (w), 776 (m), 730 (w), 683 (s), 665 (s), 619 (s), 581 (s), 548 (m).

**Method B.** To a stirred solution of pdpmH (0.20 g, 0.75 mmol),  $\text{Mn}(\text{O}_2\text{CMe})_2\cdot 4\text{H}_2\text{O}$  (0.17 g, 0.70 mmol) and acetic acid (0.07 mL, 1.2 mmol) in MeCN (25 mL) was added  $\text{NBu}^n_4\text{MnO}_4$  (0.11 g, 0.3 mmol) in small portions, resulting in a dark purple solution that quickly turned dark brown. After being stirred at 60 °C for 15 min, the solution was cooled to room temperature, filtered, and the filtrate left undisturbed to concentrate slowly by evaporation. X-ray quality crystals of **5-1** $\cdot 0.5\text{MeCN}$  slowly grew over 2 weeks in 20% yield. These were collected by filtration, washed with cold MeCN ( $2 \times 3$  mL) and  $\text{Et}_2\text{O}$  ( $2 \times 5$  mL), and dried under vacuum; the product was identified by IR spectral comparison and elemental analysis as identical with

material from Method A. Anal. Calc. (Found) for **5-1**·H<sub>2</sub>O: C, 54.55 (54.56); H, 3.99 (3.82); N, 6.66 (6.95).

**Method C.** To a stirred solution of pdpmH (0.20 g, 0.75 mmol), Mn(O<sub>2</sub>CMe)<sub>2</sub>·4H<sub>2</sub>O (0.15 g, 0.60 mmol) and acetic acid (0.09 mL, 1.6 mmol) in MeCN (25 mL) was added NBu<sup>n</sup><sub>4</sub>MnO<sub>4</sub> (0.14 g, 0.4 mmol) in small portions, resulting in a dark purple solution that quickly turned dark brown. After being stirred at 60 °C for 15 min, the solution was cooled to room temperature, during which time dark brown microcrystalline solid began to deposit. When crystallization was judged complete the solid was collected by filtration, washed with MeCN (2 × 5 mL), and dried under vacuum; the yield was ~50%. The product was identified by IR spectral comparison and elemental analysis as identical with material from Method A. Anal. Calc. (Found) for **5-1**·H<sub>2</sub>O: C, 54.21 (53.92); H, 3.99 (3.96); N, 6.66 (6.58).

**[Mn<sub>7</sub>O<sub>4</sub>(pdpm)<sub>6</sub>(N<sub>3</sub>)<sub>4</sub>](ClO<sub>4</sub>)<sub>2</sub> (**5-2**).** Solid NaN<sub>3</sub> (0.13 g, 2.0 mmol) was added to a stirred, pale yellow solution of pdpmH (0.52 g, 2.0 mmol) and NEt<sub>3</sub> (0.28 mL, 2.0 mmol) in MeCN/MeOH (21 mL, 20:1 v/v). To this solution was added solid Mn(ClO<sub>4</sub>)<sub>2</sub>·6H<sub>2</sub>O (0.50 g, 2.0 mmol), which caused a rapid color change to dark brown. The resulting dark brown solution was stirred for a further 2 h and filtered, and the filtrate was layered with Et<sub>2</sub>O. After 3 days, X-ray quality dark red crystals of **5-2**·2MeCN appeared and were collected by filtration, washed with MeCN (2 × 5 mL) and Et<sub>2</sub>O (2 × 5 mL), and dried in vacuo; the yield was ~50%. Anal. Calc. (Found) for **5-2**·5H<sub>2</sub>O: C, 49.41 (49.02); H, 3.82 (3.42); N, 13.56 (13.24). Selected IR data (cm<sup>-1</sup>): 3424(wb), 3057(wb), 2060(s), 1603(m), 1567(w), 1490(w), 1467(m), 1446(w), 1432(m), 1312(m), 1229(m), 1253(w), 1229(w), 1202(w), 1156(w), 1089(s), 1049(s), 1009(m), 958(w), 931(w), 907(w), 778(m), 750(w), 731(w), 703(s), 663(s), 637(s), 624(s), 588(m), 542(m), 496(w), 470(w) 426(w), 409(w).

### 5.2.2 X-Ray Crystallography

Data were collected on a Siemens SMART PLATFORM equipped with a CCD area detector and a graphite monochromator utilizing Mo-K $\alpha$  radiation ( $\lambda = 0.71073 \text{ \AA}$ ). Suitable crystals of **5-1**·0.5MeCN and **5-2**·2MeCN were attached to glass fibers using silicone grease and transferred to a goniostat where they were cooled to 173 K for data collection. Cell parameters were refined using up to 8192 reflections. A full sphere of data (1850 frames) was collected using the  $\omega$ -scan method (0.3° frame width). The first 50 frames were remeasured at the end of data collection to monitor instrument and crystal stability (maximum correction on I was < 1 %). Absorption corrections by integration were applied based on measured indexed crystal faces. The structure was solved by the direct methods in *SHELXTL6*,<sup>64</sup> and refined using full-matrix least squares. The non-H atoms were treated anisotropically, whereas the hydrogen atoms were calculated in ideal positions and were riding on their respective carbon atoms. Refinement was done using F<sup>2</sup>.

For **5-1**·0.5MeCN, the asymmetric unit consists of a Mn<sub>4</sub> cluster and a half acetonitrile solvent molecule. A total of 39377 parameters were refined in the final cycle of refinement using 12489 reflections with  $I > 2\sigma(I)$  to yield R<sub>1</sub> and wR<sub>2</sub> of 3.75 and 8.35%, respectively.

For **5-2**·2MeCN, the structure is twinned with a twin law being a 2-fold rotation around the c-axis with a basf value of 0.127. The asymmetric unit consists of a 1/3 Mn<sub>7</sub> cluster, two 1/3 perchlorate anions (disordered around a 3-fold axis), a 1/3 acetonitrile solvent molecule and another disordered in two parts with a common methyl group. The cluster itself has two disordered regions. In one, the terminal nitrogen of an azide, N6/N6' was refined in two parts with a fixed site occupation distribution of 0.2/0.133, and the second is where an aryl group is disordered and refined in two parts with equal site occupation factors fixed at 50%. There were

several constraints applied namely keeping all distances in the N4-N5-N6/N6' equivalent using the SADI command. The two acetonitrile solvent molecules also constrained to maintain equivalent bond lengths in each anion. Also, the displacement parameters of the oxygen atoms of each anion were set to be equivalent by EADP. A total of 485 parameters were refined in the final cycle of refinement using 4738 reflections with  $I > 2\sigma(I)$  to yield  $R_1$  and  $wR_2$  of 7.47 and 21.97%, respectively. Unit cell data and details of the structure refinements for the two complexes are listed in Table 5-1.

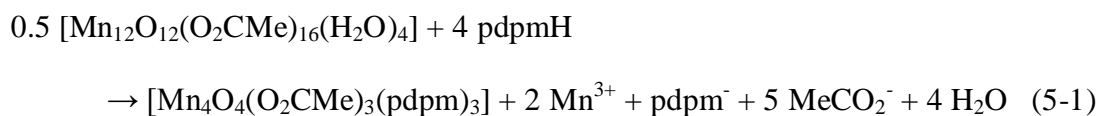
### 5.2.3 Other Studies

Infrared spectra were recorded in the solid state (KBr pellets) on a Nicolet Nexus 670 FTIR spectrometer in the 400-4000  $\text{cm}^{-1}$  range. Elemental analyses (C, H and N) were performed by the in-house facilities of the University of Florida, Chemistry Department. Electrochemical studies were performed under argon using a BAS model CV-50W voltammetric analyzer and a standard three-electrode assembly (glassy carbon working, Pt wire auxiliary, and Ag wire reference) in 0.1 M  $\text{NBu}_4\text{PF}_6$   $\text{CH}_2\text{Cl}_2$  solution. Quoted potentials are vs the ferrocene / ferrocenium couple, used as an internal standard. Variable-temperature DC and AC magnetic susceptibility data were collected at the University of Florida using a Quantum Design MPMS-XL SQUID susceptometer equipped with a 7 T magnet and operating in the 1.8–300 K range. Samples were embedded in solid eicosane to prevent torquing. Magnetization vs. field and temperature data was fit using the program MAGNET. Pascal's constants<sup>251</sup> were used to estimate the diamagnetic correction, which was subtracted from the experimental susceptibility to give the molar paramagnetic susceptibility ( $\chi_M$ ).

## 5.3 Results and Discussion

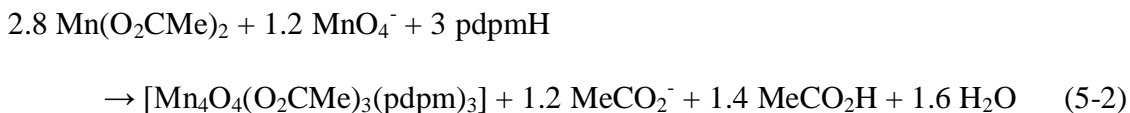
### 5.3.1 Syntheses

Our initial attempts to use pdpmH in polynuclear Mn cluster syntheses involved the oxidation reactions of simple Mn<sup>II</sup> salts by atmospheric O<sub>2</sub> under basic conditions in the presence of carboxylate groups. This approach has proven to be successful in Mn/dphmpH and Mn/dmhmpH chemistry resulting in various Mn clusters with nuclearities ranging from 4 to 12. Therefore, a variety of reaction ratios, reagents, solvents and other conditions were investigated; however, despite many attempts, we were unable to isolate any pure, crystalline products. We thus turned our attention to the reactions with preformed Mn clusters, and subsequently developed the following procedure. The reaction of [Mn<sub>12</sub>O<sub>12</sub>(O<sub>2</sub>CMe)<sub>16</sub>(H<sub>2</sub>O)<sub>4</sub>].2MeCO<sub>2</sub>H·4H<sub>2</sub>O in MeCN with 6 equiv of pdpmH afforded a dark brown solution from which was subsequently obtained the new mixed valent [Mn<sup>III</sup><sub>2</sub>Mn<sup>IV</sup><sub>2</sub>] complex [Mn<sub>4</sub>O<sub>4</sub>(O<sub>2</sub>CMe)<sub>3</sub>(pdpm)<sub>3</sub>] (**5-1**). Its formation is summarized in eq. 5-1.

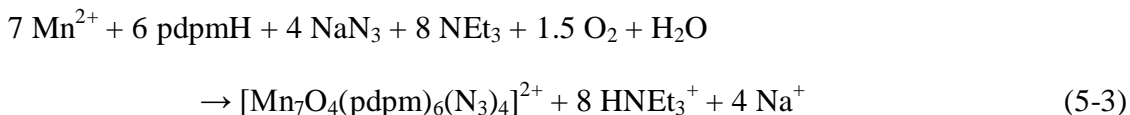


However, the yield of complex **5-1** was only ~5% and attempts to increase the yield were unsuccessful; thus, a better route to this compound was sought and subsequently developed. Complex **5-1** is composed of two Mn<sup>III</sup> and two Mn<sup>IV</sup> ions. It is generally not easy to obtain the Mn<sup>IV</sup> oxidation state by simple aerobic oxidation reactions starting with Mn<sup>II</sup> sources. A commonly used synthetic procedure for the preparation of high oxidation state manganese clusters is the comproportionation reaction of a Mn<sup>II</sup> source with MnO<sub>4</sub><sup>-</sup> in the presence of appropriate ligand groups. This is a convenient general procedure involving oxidation of Mn<sup>II</sup> ions and concomitant reduction of Mn<sup>VII</sup> ions, producing a product at the Mn<sup>III</sup> and/or Mn<sup>IV</sup> oxidation level. The Mn<sup>II</sup>/Mn<sup>VII</sup> reaction ratio can readily be varied, and mixed-valent

Mn<sup>IV</sup>/Mn<sup>III</sup> and Mn<sup>III</sup>/Mn<sup>II</sup> complexes can also be obtained.<sup>51, 148, 340</sup> In line with this approach, we investigated the comproportionation reactions of Mn<sup>II</sup> and Mn<sup>VII</sup> sources in the presence of pdpmH, and successfully developed the following procedures for **5-1** with a higher yield. The reaction of Mn(O<sub>2</sub>CMe)<sub>2</sub>·4H<sub>2</sub>O, NBu<sup>n</sup><sub>4</sub>MnO<sub>4</sub>, and pdpmH in the molar ratio of 0.7:0.3:0.75 in MeCN/MeCO<sub>2</sub>H afforded a dark brown solution from which dark brown crystals of complex **5-1** were isolated in ~20% yield (Method B). This ratio of reagents is that calculated to give a Mn<sub>4</sub> complex in the Mn<sup>III</sup><sub>2</sub>Mn<sup>IV</sup><sub>2</sub> oxidation state and with three pdpmH ligands. After subsequent reactions exploring the effect of varying the reagents ratio, the increased ratio of Mn<sup>VII</sup>/Mn<sup>II</sup> was found to afford a better yield of ~50%; Mn(O<sub>2</sub>CMe)<sub>2</sub>·4H<sub>2</sub>O, NBu<sup>n</sup><sub>4</sub>MnO<sub>4</sub>, and pdpmH in the molar ratio of 0.6:0.4:0.75 in MeCN/MeCO<sub>2</sub>H (Method C). The overall reaction is summarized in eq.5-2.



The ligand pdpmH was also explored in non-carboxylate Mn chemistry in the presence of N<sub>3</sub><sup>-</sup>. The reaction of Mn(ClO<sub>4</sub>)<sub>2</sub>·6H<sub>2</sub>O, NaN<sub>3</sub>, pdpmH, and NEt<sub>3</sub> in MeCN/MeOH afforded a dark red solution and subsequent isolation of **5-2** in 50% yield; its formation is summarized in eq. 5-3.



This reaction is an oxidation, undoubtedly by O<sub>2</sub> under the prevailing basic conditions, and has been balanced accordingly. With the identity of **5-2** established, we also tried several other Mn<sup>II</sup>/pdpmH/NEt<sub>3</sub>/N<sub>3</sub><sup>-</sup> ratios, particularly with a large excess of MnX<sub>2</sub> (X = Cl<sup>-</sup>, NO<sub>3</sub><sup>-</sup>, ClO<sub>4</sub><sup>-</sup>), to see if higher nuclearity azide-containing products might be obtained, but in all cases complex **5-2** was the isolated product. It is of interest that this reaction procedure is same as the ones for

$[\text{Mn}_{10}\text{O}_4(\text{N}_3)_4(\text{hmp})_{12}](\text{ClO}_4)_2 \cdot \text{MeCN}$  (**4-7**) and  $(\text{HNEt}_3)[\text{NaMn}_6\text{O}_4(\text{dmhmp})_6(\text{N}_3)_4] \cdot (\text{ClO}_4)_2$  (**4-6**), and these complexes all presents  $[\text{Mn}_6\text{O}_4(\text{N}_3)_4]^{6+}$  tetrahedral units, and they all possess their highest possible ground state spin (vide infra).

### 5.3.2 Description of Structures

The partially labeled structure and a stereoview of  $[\text{Mn}_4\text{O}_4(\text{O}_2\text{CMe})_3(\text{pdp}_m)_3]$  (**5-1**) are shown in Figure 5-2; selected interatomic distances and angles are listed in Table A-13. Complex **5-1** crystallizes in orthorhombic space group  $P2_12_12_1$ . The molecule consists of a  $[\text{Mn}_4\text{O}_4]$  core with peripheral ligation provided by three chelating  $\text{pdp}_m^-$  and three  $\mu$ -bridging  $\text{MeCO}_2^-$  groups. The core has a cubane structure consisting of four Mn atoms and four  $\mu_3\text{-O}^{2-}$  ions. Charge considerations and the metric parameters indicate a  $2\text{Mn}^{\text{III}}, 2\text{Mn}^{\text{IV}}$  metal oxidation state description, as confirmed by BVS calculations (Table 5-2), which identified Mn2 and Mn4 as the  $\text{Mn}^{\text{IV}}$  atoms and the others as  $\text{Mn}^{\text{III}}$ . The latter was consistent with the Jahn–Teller (JT) axial elongations at Mn1 and Mn3. Normally, the JT axial elongations avoid Mn-oxide bonds, almost always the strongest and shortest in the molecule, but this is not possible for every Mn atom in **5-1** because of the  $[\text{Mn}_4\text{O}_4]$  cubane topology. The locations of two JT axes are indicated as yellow bonds in Figure 5-2. The JT axes of Mn1 and Mn3 are oriented nearly perpendicular to each other. BVS calculations were also performed on the inorganic O atoms to identify their degree of protonation and thus distinguish  $\text{O}^{2-}$ ,  $\text{OH}^-$ , and  $\text{H}_2\text{O}$  situations (Table 5-3), and these confirm four  $\text{O}^{2-}$  ions. The BVS value of 1.53 for O1 is slightly lower than expected for an  $\text{O}^{2-}$  ion, but is consistent with it being positioned on the JT elongation axis of Mn3, which presents unusually long Mn- $\text{O}^{2-}$  distance ( $\text{Mn3}\cdots\text{O1} = 2.297(2)$  Å). All Mn atoms are six-coordinate with distorted octahedral geometry.

Complex **5-1** contains three  $\text{pdp}_m^-$  ligands, and one of two pyridine rings in each  $\text{pdp}_m^-$  is unbound, i.e.,  $\text{pdp}_m^-$  is serving as a bidentate chelate. Interestingly, the unbound pyridine rings

are not protonated either. This is because they are sterically hindered by the neighboring phenyl and pyridyl rings of the same ligand, as shown in the spacefilling diagram in Figure 5-3. The structure of **5-1** is similar to those previously reported for other  $[\text{Mn}_4\text{O}_3\text{X}]^{6+}$  ( $\text{X} = \text{Cl}^-, \text{Br}^-$ )-containing complexes that also present a cubane arrangement of four Mn atoms (1  $\text{Mn}^{\text{IV}}$  and 3  $\text{Mn}^{\text{III}}$ ), with three  $\mu_3\text{-O}^{2-}$  ions and one  $\mu_3\text{-X}$  ion,<sup>341, 342</sup> with the exception that complex **5-1** comprises 2  $\text{Mn}^{\text{IV}}$  and 2  $\text{Mn}^{\text{III}}$ . There has been only one previous report of a  $\text{Mn}_4$  cubane complex with a  $\text{Mn}^{\text{III}}_2\text{Mn}^{\text{IV}}_2$  oxidation state description, namely  $[\text{Mn}_4\text{O}_4(\text{O}_2\text{PPh}_2)_6]$ .<sup>343-345</sup>

The complete structure and a stereoview of the cation of  $[\text{Mn}_7\text{O}_4(\text{pdpm})_6(\text{N}_3)_4](\text{ClO}_4)_2$  (**5-2**) are shown in Figure 5-4, and its labeled core in Figure 5-5; selected interatomic distances and angles are listed in Table A-14. Complex **5-2** crystallizes in rhombohedral space group  $R\bar{3}$ . The core of the cluster consists of an  $[\text{Mn}_6\text{O}_4(\text{N}_3)_4]^{6+}$  super-tetrahedron with an  $\text{N}_3^-$  at each vertex, a Mn at the midpoint of each edge, and an  $\text{O}^{2-}$  bridging each face; to one of the latter  $\text{O}^{2-}$  ions an additional  $\text{Mn}^{\text{II}}$  atom is attached, making the  $\text{O}^{2-}$  ion  $\mu_4$ . The  $\text{Mn}^{\text{II}}$  atom is additionally bridged to the  $\text{Mn}^{\text{III}}_3\text{O}$  face by three alkoxide arms of  $\text{pdpm}^-$  groups; thus overall, the complex contains a  $[\text{Mn}_7(\mu_4\text{-O})(\mu_3\text{-O})_3(\mu_3\text{-N}_3)_4(\mu\text{-OR})_3]^{5+}$  core. Complex **5-2** contains six  $\text{pdpm}^-$  groups; three of them chelate to  $\text{Mn}^{\text{III}}$  ions (Mn2), with one of two pyridine groups of the ligand being unbound, and thus these  $\text{pdpm}^-$  groups are serving as bidentate chelates. The other three  $\text{pdpm}^-$  both chelate to  $\text{Mn}^{\text{III}}$  ions (Mn1) and bridge with their alkoxide arm to  $\text{Mn}^{\text{II}}$  ion (Mn3) which is also coordinated by the pyridine rings of the  $\text{pdpm}^-$  groups, thus these  $\text{pdpm}^-$  groups are serving as tridentate ligand. The molecule has a crystallographic  $C_3$  rotation axis passing thorough the  $\text{Mn}^{\text{II}}$  ion,  $\mu_4\text{-O}^{2-}$  ion bridging the Mn1 atoms (O4), and  $\mu_3\text{-N}$  atom of azide ion bridging the Mn2 atoms (N4).

Charge considerations and a qualitative inspection of the metric parameters indicate an  $[\text{Mn}^{\text{II}}\text{Mn}^{\text{III}}_6]$  metal oxidation-state description. As expected for high-spin  $\text{Mn}^{\text{III}}$  ( $d^4$ ) in near-octahedral geometry, there is a Jahn-Teller (JT) distortion, and it takes the form of an axial elongation of the two trans Mn-N<sub>3</sub> bonds; the JT axes are the edges of the virtual tetrahedron  $[\text{Mn}_6\text{O}_4(\text{N}_3)_4]^{6+}$ . Each Mn ion is six-coordinate with distorted octahedral geometry except for the  $\text{Mn}^{\text{II}}$  ion which is seven-coordinate.

### 5.3.3 Electrochemistry

The electrochemical properties of the cubane-like complex **5-1** were investigated by cyclic voltammetry (CV) in 0.1M  $\text{NBu}_4\text{PF}_6$  solution in  $\text{CH}_2\text{Cl}_2$ . The obtained CV of **5-1** is shown in Figure 5-6, where the potential is quoted vs  $\text{Fc}/\text{Fc}^+$ , which was used as an internal reference. The complex shows a reversible oxidation process at a potential of 660 mV with anodic vs cathodic peak separation of 300 mV at a scan rate of 100 mV/sec. In addition, one irreversible reduction process was observed at -600 mV. The reversible oxidation process observed for **5-1** indicates the accessibility of the oxidation states outlined in eq.5-4.



To study the scan rate dependence of the reversible oxidation process of **5-1**, CV of complex **5-1** was recorded in the appropriate potential range at 20 different scan rates between 30 and 600 mV/sec (Figure 5-7). From the linear dependence of anodic peak current,  $i_a$ , vs the square root of the scan rate,  $v^{1/2}$  (Figure 5-8) it was confirmed that the oxidation/reduction process in eq.5-4 is reversible.

### 5.3.4 Magnetochemistry

#### 5.3.4.1 Direct current magnetic susceptibility studies

Variable-temperature magnetic susceptibility measurements were performed on microcrystalline powder samples of complex **5-1**·H<sub>2</sub>O and **5-2**·5H<sub>2</sub>O, restrained in eicosane to prevent torquing, in a 1 kG (0.1 T) field and in the 5.0-300 K range.

For **5-1**·H<sub>2</sub>O,  $\chi_M T$  steadily decreases from 6.28 cm<sup>3</sup>Kmol<sup>-1</sup> at 300 K to 0.63 cm<sup>3</sup>Kmol<sup>-1</sup> at 5.0 K (Figure 5-9). If there were no exchange interactions between the metal ions in a 2Mn<sup>III</sup>2Mn<sup>IV</sup> complex, the spin-only ( $g = 2$ )  $\chi_M T$  value would be 9.75 cm<sup>3</sup>Kmol<sup>-1</sup>, and it would be temperature independent. The metal ions are clearly involved in antiferromagnetic exchange interactions, and the data were thus fit to the appropriate theoretical  $\chi_M T$  vs  $T$  expression. The latter was derived from the spin Hamiltonian of eq. 5-5, where  $J_1 = J(\text{Mn}^{\text{IV}} \cdots \text{Mn}^{\text{IV}})$ ,  $J_2 = J(\text{Mn}^{\text{IV}} \cdots \text{Mn}^{\text{III}})$ ,  $J_3 = J(\text{Mn}^{\text{III}} \cdots \text{Mn}^{\text{III}})$ ,  $S_1 = S_3 = S(\text{Mn}^{\text{III}}) = 2$ , and  $S_2 = S_4 = S(\text{Mn}^{\text{IV}}) = 3/2$ , by employing an equivalent operator approach based on the Kambe vector coupling method.<sup>263</sup> The substitutions employed were  $\hat{S}_A = \hat{S}_2 + \hat{S}_4$ ,  $\hat{S}_B = \hat{S}_1 + \hat{S}_3$  and  $\hat{S}_T = \hat{S}_A + \hat{S}_B$ .

$$\hat{H} = -2J_2(S_1 \cdot S_2 + S_1 \cdot S_4 + S_2 \cdot S_3 + S_3 \cdot S_4) - 2J_1 S_2 \cdot S_4 - 2J_3 S_1 \cdot S_3 \quad (5-5)$$

This gives the equivalent form of eq. 5-5 that is given in eq.5-6

$$\hat{H} = -J_2(S_T^2 - S_A^2 - S_B^2) - J_1(S_A^2 - S_2^2 - S_4^2) - J_3(S_B^2 - S_1^2 - S_3^2) \quad (5-6)$$

Eq. 5-6 leads to the eigenvalue expression of eq. 5-7, which gives the energy,  $E(S_T)$ , of each of the possible total spin states,  $S_T$ , of the Mn<sup>III</sup><sub>2</sub>Mn<sup>IV</sup><sub>2</sub> complex.

$$E(S_T) = -J_2[S_T(S_T+1) - S_A(S_A+1) - S_B(S_B+1)] - J_1[S_A(S_A+1)] - J_3[S_B(S_B+1)] \quad (5-7)$$

An expression for the molar paramagnetic susceptibility,  $\chi_M$ , was derived using the above and the Van Vleck equation,<sup>264</sup> and assuming an isotropic  $g$  tensor (Appendix C-2). This equation was then used to fit the experimental  $\chi_M T$  vs  $T$  data in Figure 5-9 as a function of the

three exchange parameters  $J_1$ ,  $J_2$  and  $J_3$  and the  $g$  factor. The contribution from temperature independent paramagnetism (TIP) was held constant at  $400 \times 10^{-6} \text{ cm}^3 \text{ mol}^{-1}$ . The obtained fit is shown as the solid lines in Figure 5-9: the fitting parameters are  $J_1 = -16.1 \text{ cm}^{-1}$ ,  $J_2 = -9.67 \text{ cm}^{-1}$ ,  $J_3 = -8.26 \text{ cm}^{-1}$  and  $g = 2.01$ . These values yield an  $S = 0$  ground state for complex **5-1**. In  $|S_T, S_A, S_B\rangle$  notation, the ground state is  $|0, 0, 0\rangle$ , and the first and second excited states are  $|0, 1, 1\rangle$  and  $|1, 0, 1\rangle$ , and 10 and 17  $\text{cm}^{-1}$  above the ground state, respectively.

For **5-2**·5H<sub>2</sub>O,  $\chi_{MT}$  gradually increases from  $30.59 \text{ cm}^3 \text{ K mol}^{-1}$  at 300 K to a value of  $102.81 \text{ cm}^3 \text{ mol}^{-1} \text{ K}$  at 8 K, and then slightly decreases to 102.09 at 5.0 K (Figure 5-10). The 300 K value is larger than the spin-only ( $g = 2$ ) value of  $22.38 \text{ cm}^3 \text{ K mol}^{-1}$  for one Mn<sup>II</sup> and six Mn<sup>III</sup> noninteracting ions, indicating the presence of dominant ferromagnetic exchange interactions. The  $\chi_{MT}$  value at 5.0 K is consistent with an  $S = 29/2$  ground state and a  $g$  slightly less than 2.0; the spin-only value is  $\sim 112 \text{ cm}^3 \text{ mol}^{-1} \text{ K}$ , and  $S = 29/2$  is the maximum value for a Mn<sup>II</sup>Mn<sup>III</sup><sub>6</sub> cluster, indicating a complete ferromagnetic system.

In order to confirm the calculated  $S = 12$  ground state of complex **5-2** and to estimate the magnitude of the zero-field splitting parameter  $D$ , magnetization vs dc field measurements were made on restrained samples at applied magnetic fields and temperatures in the 1–70 kG and 1.8–10.0 K ranges, respectively. The resulting data were fit, using the program MAGNET,<sup>66</sup> by diagonalization of the spin Hamiltonian matrix assuming that only the ground state is populated, incorporating axial anisotropy ( $D\hat{S}_z^2$ ) and Zeeman terms, and employing a full powder average. The corresponding spin Hamiltonian is given by eq.5- 8, where  $\hat{S}_z$  is the easy-axis spin operator,  $g$  is the Landé  $g$  factor,  $\mu_B$  is the Bohr magneton, and  $\mu_0$  is the vacuum permeability.

$$H = D\hat{S}_z^2 + g\mu_B\mu_0\hat{S}\cdot H \quad (5-8)$$

The resulting data are shown in Figure 5-11 as a reduced magnetization ( $M/N\mu_B$ ) versus  $H/T$  plot, where  $N$  is Avogadro's number. The data show that the isofield lines almost superimpose, indicating that the ground state is only slightly zero-field split. The data were fit using the program MAGNET (vide supra) using all the data collected up to 7 tesla. This suggests that the ground state of **5-2** is relatively well isolated from the nearest excited states. The best fit is shown as the solid lines in Figure 5-11 and was obtained with  $S = 29/2$ ,  $g = 1.89$ , and  $D = -0.03 \text{ cm}^{-1}$ . An equally good fit was also obtained with  $S = 29/2$ ,  $g = 1.89$  and  $D = -0.02 \text{ cm}^{-1}$ . Alternative fits with  $S = 27/2$  were rejected because they gave unreasonable values of  $g$ . It is common to obtain two acceptable fits of magnetization data for a given  $S$  value, one with  $D > 0$  and the other with  $D < 0$ , because magnetization fits are not very sensitive to the sign of  $D$ .

To assess which is the superior fit and also to ensure that the true global minimum had been located, we calculated the root-mean-square  $D$  versus  $g$  error surface using the program GRID,<sup>116</sup> which calculates the relative difference between the experimental  $M/N\mu_B$  data and those calculated for various combinations of  $D$  and  $g$ . The error surface, plotted as a two-dimensional contour plot in Figure 5-12, shows the two minima with positive and negative  $D$  values, but with essentially equal quality; thus, it would require more sensitive techniques such as EPR spectroscopy or magnetization measurements on oriented single-crystals to confirm the sign of  $D$ . However,  $D$  values for  $\text{Mn}^{\text{III}}/\text{Mn}^{\text{IV}}$  clusters are essentially always negative, and thus very likely the situation here.

#### **5.3.4.2 Alternating current magnetic susceptibility studies**

We collected ac susceptibility data on **5-2**·5H<sub>2</sub>O in the 1.8-15 K range using a 3.5 G ac field oscillating at frequencies in the 50-1000 Hz range. The obtained in-phase  $\chi_M'$  signal for **5-2** is plotted as  $\chi_M' T$  in Figure 5-13, and can be seen to be almost temperature-independent,

indicating a well isolated ground state. Extrapolating the data to 0 K gives a value of  $\sim 103 \text{ cm}^3 \text{ K mol}^{-1}$ , which is consistent with an  $S = 29/2$  ground state and  $g \sim 1.91$ , in excellent agreement with the reduced magnetization fit. We conclude that complex **5-2** does indeed have an  $S = 29/2$  ground state, and that all exchange interactions in the molecule are ferromagnetic. It is worth noting that **5-2** and  $(\text{HNEt}_3)[\text{NaMn}_6\text{O}_4(\text{dmhmp})_6(\text{N}_3)_4] \cdot (\text{ClO}_4)_2$  (**4-6**) in Chapter 4, as well as two previous examples of  $\text{Mn}_6$  complexes with a  $[\text{Mn}_6\text{O}_4(\mu_3\text{-X})_4]$  face-capped octahedral topology with X being Cl or Br,<sup>262</sup> all present ferromagnetic exchange interactions within the molecules. There is no out-of-phase ac susceptibility signal down to 1.8 K, the operating limit of our SQUID magnetometer.

#### 5.4 Conclusions

The tridentate N,N,O ligand  $\text{pdpm}^-$  in polynuclear Mn chemistry has provided new mixed-valent Mn clusters spanning  $\text{Mn}_4$  and  $\text{Mn}_7$  nuclearities and topologies that are either very rare or prototypical. In particular, the reaction of  $[\text{Mn}_{12}\text{O}_{12}(\text{O}_2\text{CMe})_{16}(\text{H}_2\text{O})_4]$  and  $\text{pdpmH}$  in MeCN has led to the isolation of the tetranuclear complex  $[\text{Mn}_4\text{O}_4(\text{O}_2\text{CMe})_3(\text{pdpm})_3]$  (**5-1**). The complex presents a cubane structure with rare Mn oxidation states: 2  $\text{Mn}^{\text{III}}$  and 2  $\text{Mn}^{\text{IV}}$ . Subsequently, a better preparation of complex **5-1** with a higher yield was developed by the comproportionation reaction between  $\text{Mn}(\text{O}_2\text{CMe})_2$  and  $\text{MnO}_4^-$  in the presence of  $\text{pdpmH}$ . Non-carboxylate Mn chemistry was also explored with  $\text{pdpmH}$ , and a new heptanuclear complex  $[\text{Mn}_7\text{O}_4(\text{pdpm})_6(\text{N}_3)_4](\text{ClO}_4)_2$  (**5-2**) was isolated. Interestingly in both **5-1** and **5-2**, potentially tridentate ligand  $\text{pdpmH}$  mainly acts as bidentate chelate. The reluctance of  $\text{pdpm}^-$  to serve as a tridentate ligand is due to the nearby steric bulk of the Ph and pyridine rings. Magnetochemical characterization of these complexes revealed that **5-1** and **5-2** have ground state spin values of  $S = 0$  and  $29/2$ ,

respectively. The combined results emphasize the potential of our ligand design strategy, and it will be interesting to extend this idea to other alkoxide-containing chelating/bridging ligands.

Table 5-1. Crystallographic Data for **5-1**·0.5MeCN and **5-2**·2MeCN.

parameter	<b>5-1</b>	<b>5-2</b>
formula	C <sub>58</sub> H <sub>49.5</sub> Mn <sub>4</sub> N <sub>6.5</sub> O <sub>13</sub>	C <sub>106</sub> H <sub>84</sub> Cl <sub>2</sub> Mn <sub>7</sub> N <sub>26</sub> O <sub>18</sub>
fw, g mol <sup>-1</sup>	1265.30	2465.47
crystal system	Orthorhombic	Rhombohedral
space group	<i>P2<sub>1</sub>2<sub>1</sub>2<sub>1</sub></i>	<i>R</i> $\bar{3}$
<i>a</i> , Å	12.440(3)	19.2878(8)
<i>b</i> , Å	19.761(4)	19.2878(8)
<i>c</i> , Å	22.399(5)	59.757(5)
$\alpha$ , deg	90	90
$\beta$ , deg	90	90
$\gamma$ , deg	90	120
<i>V</i> , Å <sup>3</sup>	5506.3(19)	19252.4(19)
<i>Z</i>	4	6
<i>T</i> , °C	173(2)	100(2)
radiation, Å <sup>a</sup>	0.71073	0.71073
$\rho_{\text{calc}}$ , g cm <sup>-3</sup>	1.526	1.276
$\mu$ , mm <sup>-1</sup>	0.968	0.775
<i>R1</i> <sup>b,c</sup>	0.0375	0.0747
<i>wR2</i> <sup>d</sup>	0.0835	0.2197

<sup>a</sup> Graphite monochromator. <sup>b</sup>  $I > 2\sigma(I)$ . <sup>c</sup>  $R1 = 100\Sigma(|F_o| - |F_c|)/\Sigma|F_o|$ . <sup>d</sup>  $wR2 = 100[\Sigma[w(F_o^2 - F_c^2)^2]/\Sigma[w(F_o^2)^2]]^{1/2}$ ,  $w = 1/[\sigma^2(F_o^2) + [(ap)^2 + bp]$ , where  $p = [\max(F_o^2, O) + 2F_c^2]/3$ .

Table 5-2. Bond Valence Sums for the Mn Atoms in Complex **5-1**<sup>a</sup>

	Mn <sup>II</sup>	Mn <sup>III</sup>	Mn <sup>IV</sup>
Mn1	3.17	<u>2.90</u>	3.04
Mn2	4.02	3.71	<u>3.84</u>
Mn3	3.28	<u>3.03</u>	3.13
Mn4	4.16	3.84	<u>3.98</u>

<sup>a</sup> The underlined value is the one closest to the charge for which it was calculated, and the nearest whole number can be taken as the oxidation state of that atom.

Table 5-3. . BVS for Selected O Atoms in **5-1**<sup>a</sup>

atom	BVS	assgt <sup>a</sup>
O1	1.53	O <sup>2-</sup>
O2	1.70	O <sup>2-</sup>
O3	1.75	O <sup>2-</sup>
O4	1.85	O <sup>2-</sup>

<sup>a</sup> The O atom is an O<sup>2-</sup> if the BVS is ~1.8 – 2.0, an OH<sup>-</sup> if it ~1.0 – 1.2, and an H<sub>2</sub>O if it is ~ 0.2 – 0.4, although the ranges can be affected slightly by H-bonding.

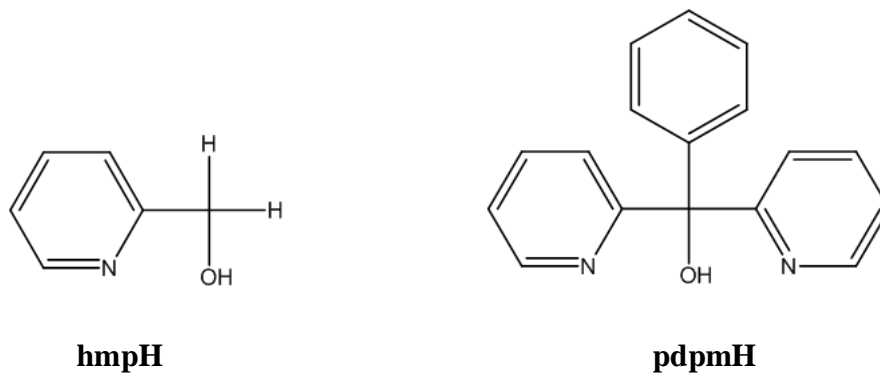


Figure 5-1. Structure of ligands: 2-(hydroxymethyl)pyridine (hmpH) and phenyldipyridin-2-ylmethanol (pdpmH).

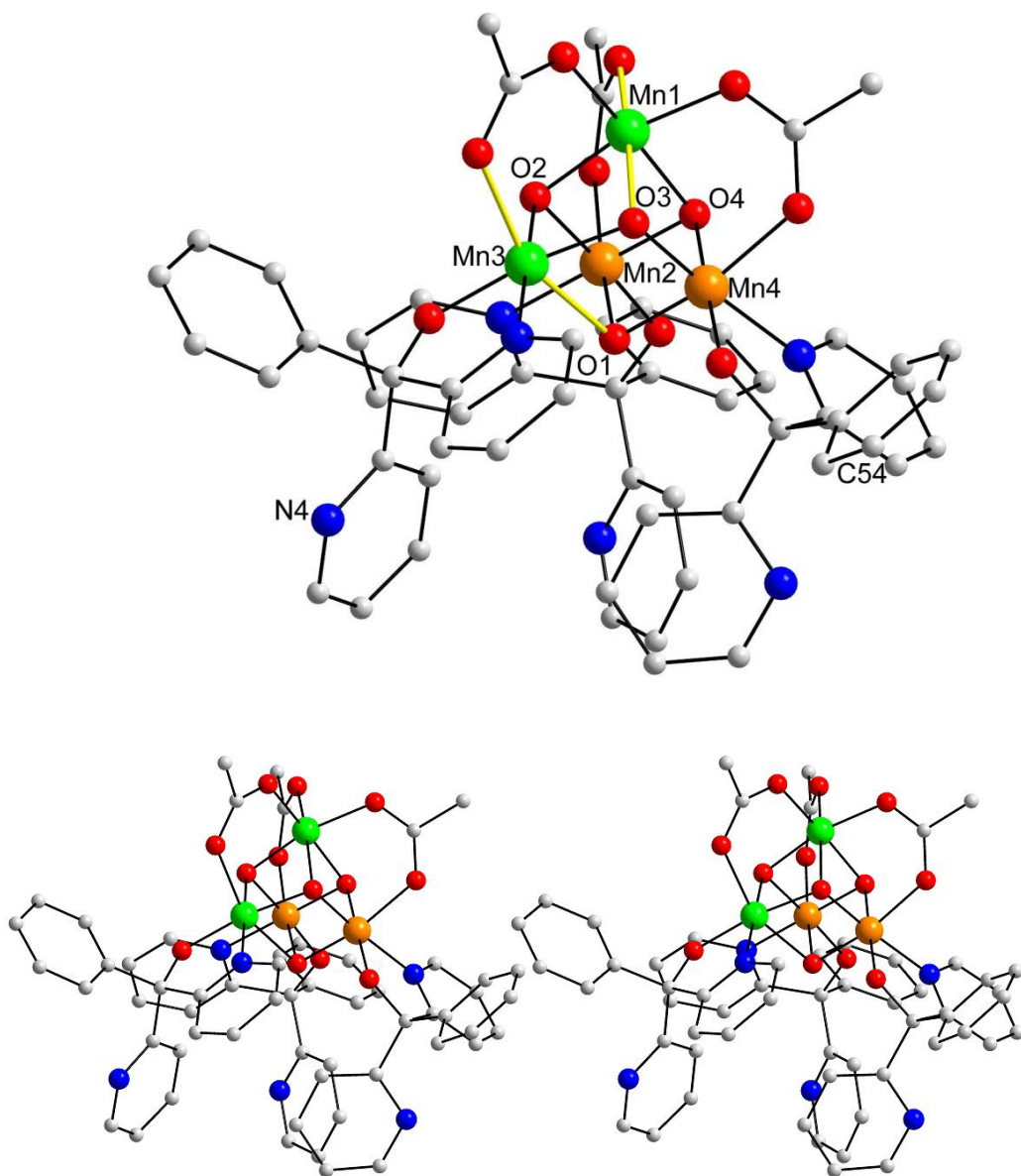


Figure 5-2. The structure of complex **5-1** (top), and a stereopair (bottom). The thicker yellow bonds indicate the positions of the  $\text{Mn}^{\text{III}}$  Jahn–Teller elongation axes. Hydrogen atoms have been omitted for clarity. Color code:  $\text{Mn}^{\text{III}}$  green;  $\text{Mn}^{\text{IV}}$  orange; O red; N blue; C grey.

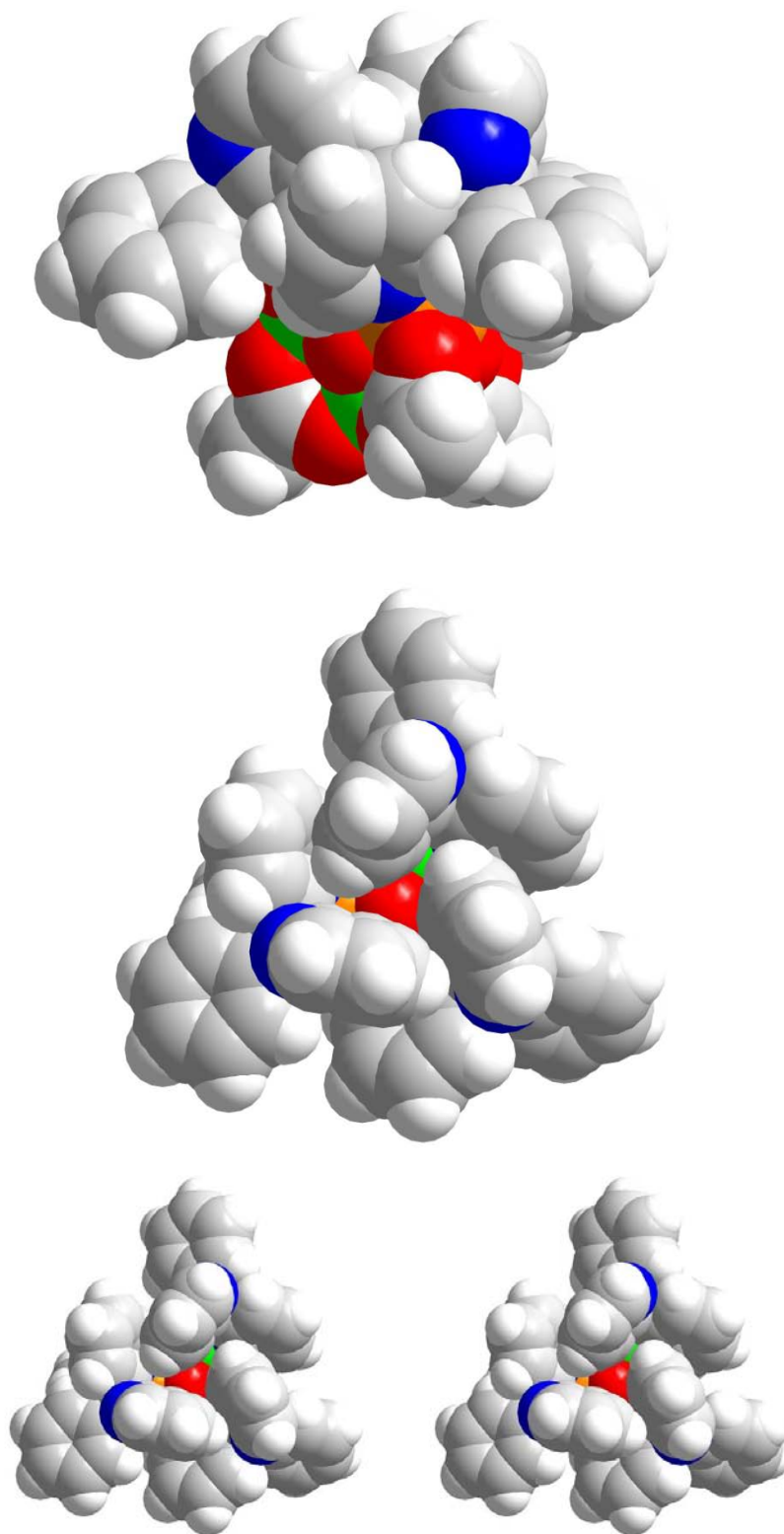


Figure 5-3. Space-filling diagram of **5-1**; sideview (top), topview (middle), and a stereoview (bottom), emphasizing the sterically hindered positioning of the unbound pyridine groups. Color code: Mn<sup>III</sup> green; Mn<sup>IV</sup> orange; O red; N blue; C grey.



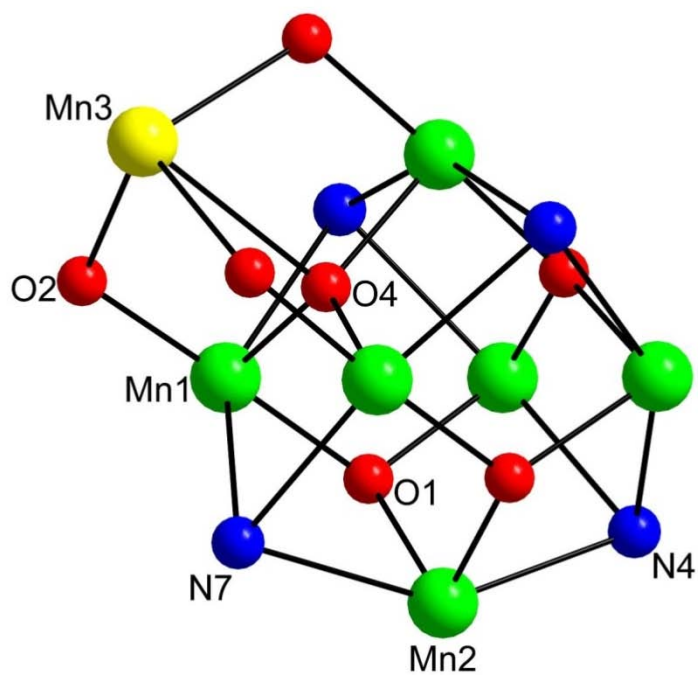


Figure 5-5. The labeled core of complex **5-2**. Color code: Mn<sup>II</sup> yellow; Mn<sup>III</sup> green; O red; C grey.

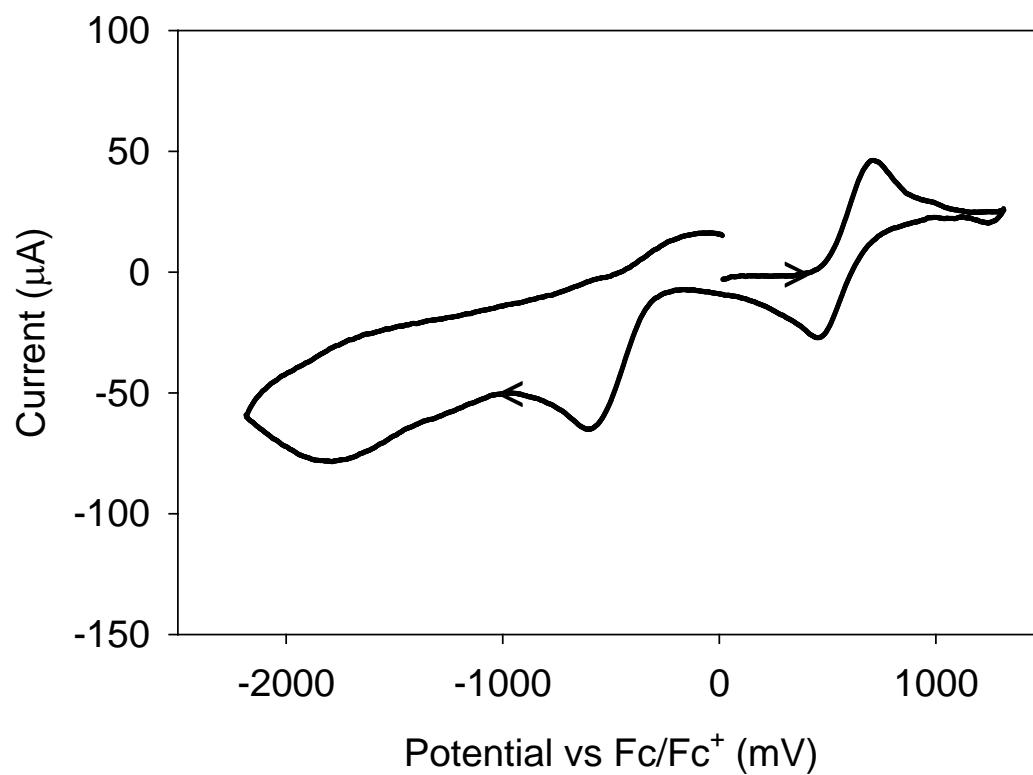


Figure 5-6. Cyclic voltammogram at glassy carbon electrode of complex **5-1** in CH<sub>2</sub>Cl<sub>2</sub> containing 0.1M NBu<sup>n</sup><sub>4</sub>PF<sub>6</sub> and ferrocene as an internal standard.

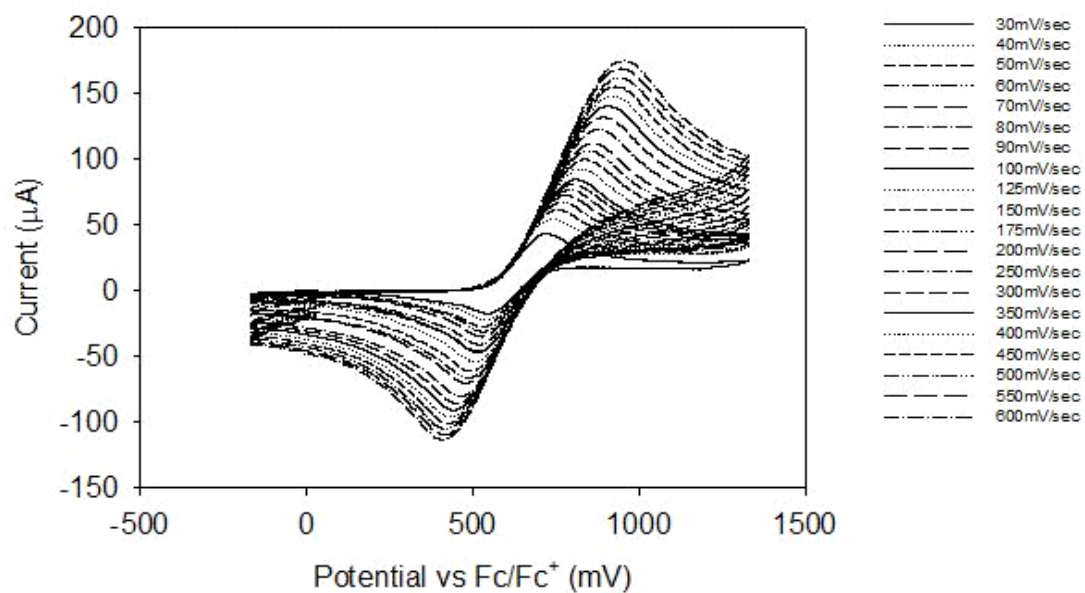


Figure 5-7. Cyclic voltammogram of **5-1** at different scan rates.

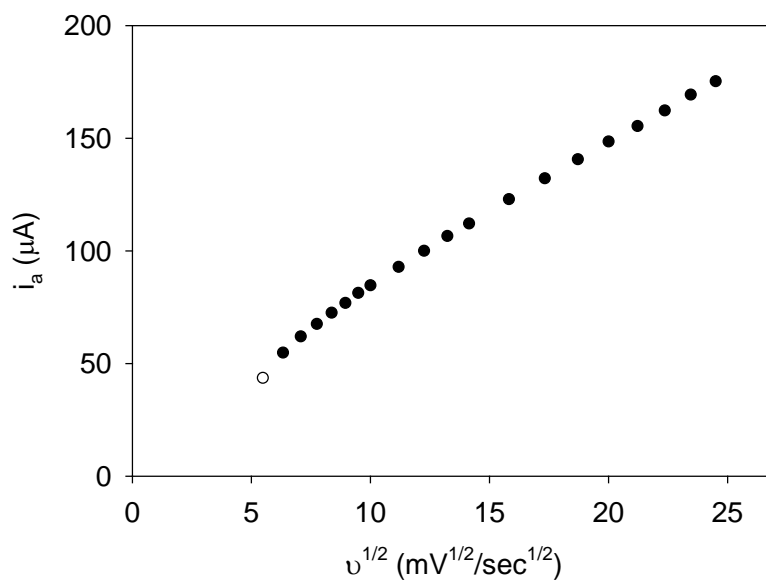


Figure 5-8. Plot of the square root of the scan rate,  $v^{1/2}$  vs the anodic peak current,  $i_a$  for the oxidation process in Figure **5-7**.

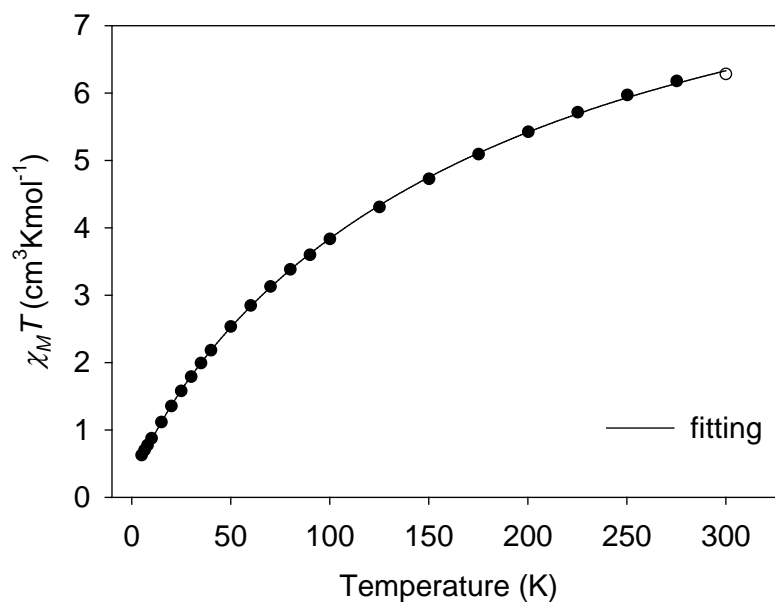


Figure 5-9. Plot of  $\chi_M T$  vs T for complex **5-1**. The solid line is the fit of the data; see the text for the fit parameters.

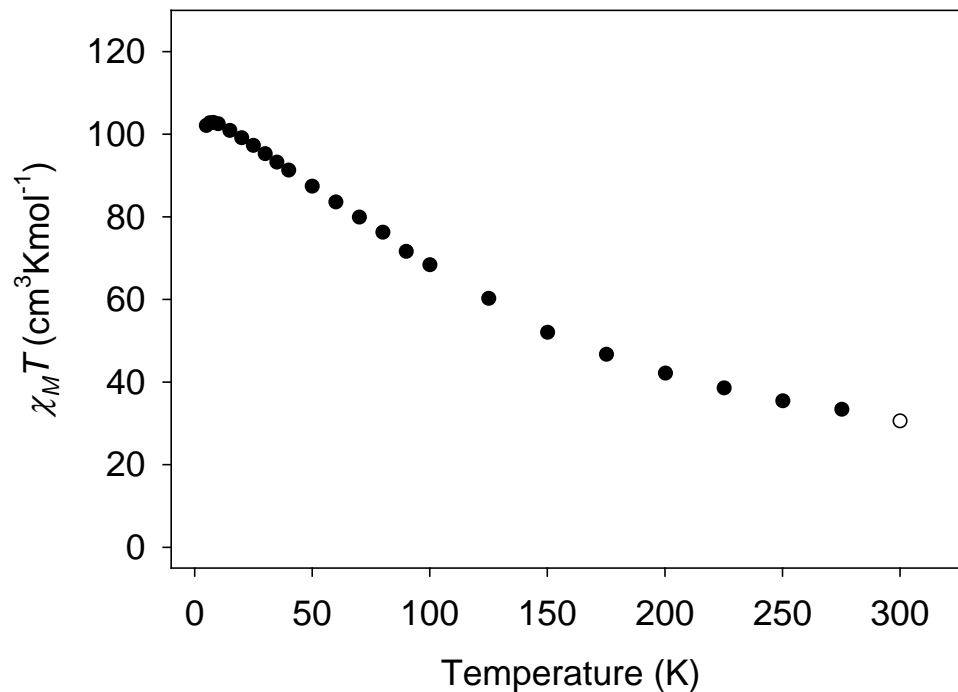


Figure 5-10. Plot of  $\chi_M T$  vs T for complex **5-2**.

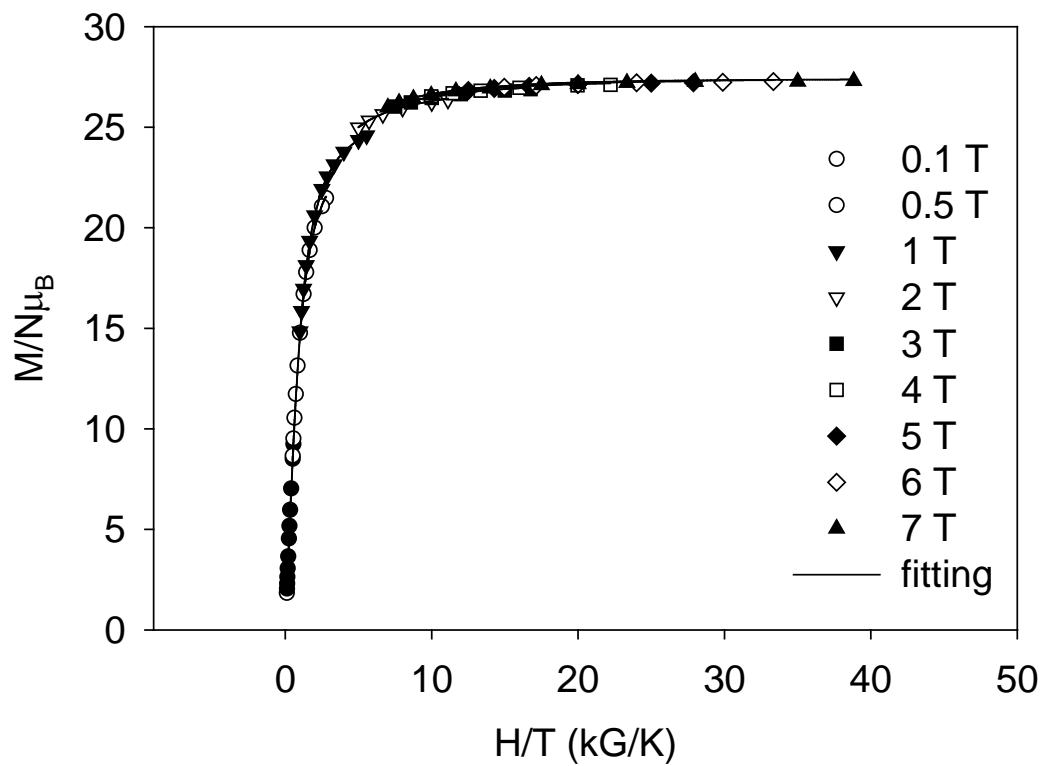


Figure 5-11. Plots of reduced magnetization ( $M/N\mu_B$ ) vs  $H/T$  for complex **5-2**. The solid lines are the fit of the data; see the text for the fit parameters

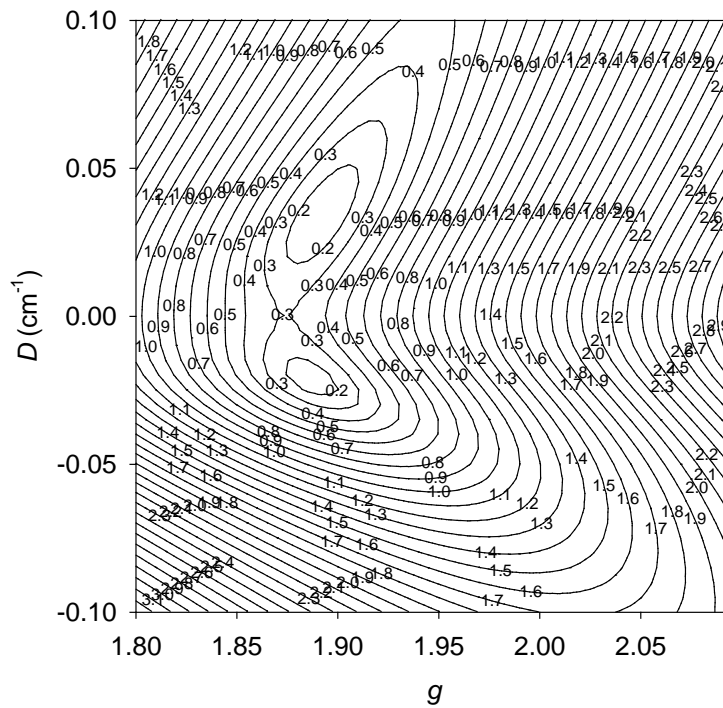


Figure 5-12. Two-dimensional contour plot of the root-mean-square error surface for the D vs g fit for complex **5-2**.

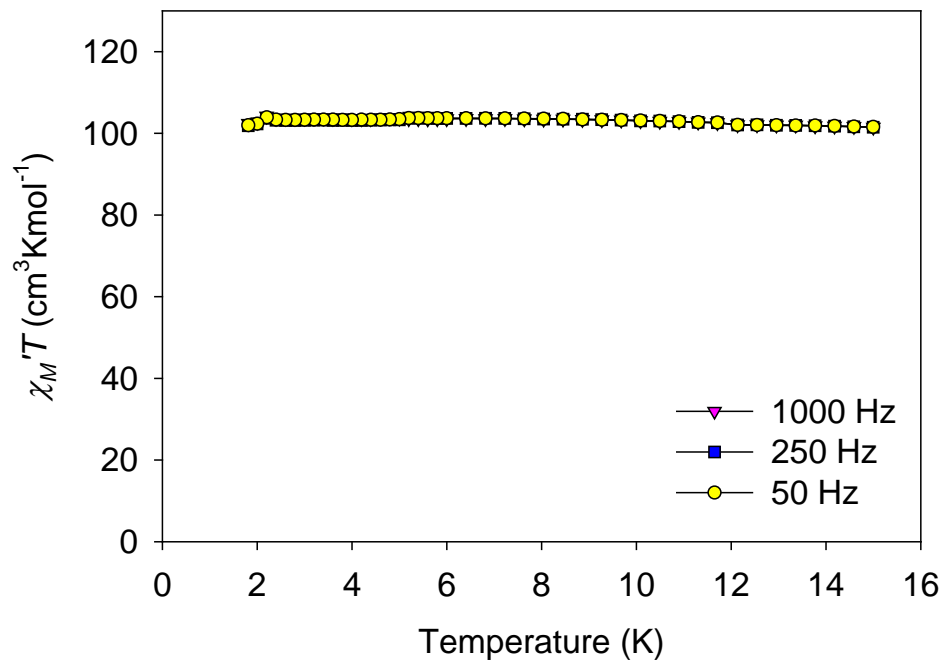


Figure 5-13. In-phase ac susceptibility ( $\chi_M'$ , plotted as  $\chi_M' T$  vs T) of complex **5-2** in a 3.5 Oe ac field oscillating at the indicated frequencies.

APPENDIX A  
BOND DISTANCES AND ANGLES

Table A-1. Selected interatomic distances (Å) and angles (°) for  
[Fe<sub>6</sub>O<sub>2</sub>(hmp)<sub>10</sub>(H<sub>2</sub>O)<sub>2</sub>](NO<sub>3</sub>)<sub>4</sub>·8MeCN (**2-1**·8MeCN)

atoms	distances(Å)	atoms	distances(Å)
Fe1-Fe2	3.671(1)	Fe2-O4	2.001(4)
Fe1-Fe3	3.604(3)	Fe2-O5	2.016(5)
Fe2-Fe3	3.030(3)	Fe2-N4	2.148(6)
Fe1-Fe2'	3.166(1)	Fe2-N3	2.151(5)
Fe1-O3	1.868(5)	Fe3-O6	1.886(5)
Fe1-O4'	1.993(4)	Fe3-O1	1.989(5)
Fe1-O2	2.004(4)	Fe3-O5	2.009(5)
Fe1-O1	2.027(4)	Fe3-O3	2.054(4)
Fe1-N2	2.158(5)	Fe3-O7	2.059(5)
Fe1-N1	2.186(6)	Fe3-N5	2.188(11)
Fe2-O3	1.880(5)	O2-Fe2'	1.980(4)
Fe2-O2'	1.980(4)	O4-Fe1'	1.993(4)
atoms	angles(°)	atoms	angles(°)
O3-Fe1-O4'	98.39(19)	O2'-Fe2-N3	149.35(19)
O3-Fe1-O2	111.63(19)	O4-Fe2-N3	76.54(19)
O4'-Fe1-O2	73.23(18)	O5-Fe2-N3	107.69(19)
O3-Fe1-O1	80.54(19)	N4-Fe2-N3	83.4(2)
O4'-Fe1-O1	103.51(17)	O6-Fe3-O1	97.8(2)
O2-Fe1-O1	167.6(2)	O6-Fe3-O5	96.3(2)
O3-Fe1-N2	93.2(2)	O1-Fe3-O5	153.5(2)
O4'-Fe1-N2	148.67(19)	O6-Fe3-O3	99.99(19)
O2-Fe1-N2	75.44(19)	O1-Fe3-O3	77.14(18)
O1-Fe1-N2	107.08(18)	O5-Fe3-O3	78.4(2)
O3-Fe1-N1	154.9(2)	O6-Fe3-O7	161.5(2)
O4'-Fe1-N1	94.7(2)	O1-Fe3-O7	87.9(2)
O2-Fe1-N1	92.6(2)	O5-Fe3-O7	85.7(2)
O1-Fe1-N1	75.7(2)	O3-Fe3-O7	98.38(18)
N2-Fe1-N1	86.4(2)	O6-Fe3-N5	76.6(3)
O3-Fe2-O2'	101.29(19)	O1-Fe3-N5	97.7(4)
O3-Fe2-O4	104.68(19)	O5-Fe3-N5	107.4(4)
O2'-Fe2-O4	73.54(18)	O3-Fe3-N5	173.5(4)
O3-Fe2-O5	82.4(2)	O7-Fe3-N5	85.3(3)
O2'-Fe2-O5	101.23(19)	Fe3-O1-Fe1	99.44(19)
O4-Fe2-O5	171.8(2)	Fe2'-O2-Fe1	105.3(2)
O3-Fe2-N4	155.5(2)	Fe1-O3-Fe2	156.7(3)
O2'-Fe2-N4	94.2(2)	Fe1-O3-Fe3	102.6(2)
O4-Fe2-N4	97.9(2)	Fe2-O3-Fe3	100.7(2)
O5-Fe2-N4	75.9(2)	Fe1'-O4-Fe2	104.9(2)
O3-Fe2-N3	92.5(2)	Fe3-O5-Fe2	97.7(2)

Table A-2. Selected interatomic distances (Å) and angles (°) for  
 $[\text{Fe}_6\text{O}_2(\text{hmp})_8(\text{NO}_3)_4(\text{H}_2\text{O})_2](\text{NO}_3)_2 \cdot 6\text{MeCN}$  (**2-2·6MeCN**)

atoms	distances(Å)	atoms	distances(Å)
Fe1-Fe2	3.648(3)	Fe2-O3'	1.9750(19)
Fe1-Fe3	3.127(5)	Fe2-O5	1.9958(19)
Fe2-Fe3	3.095(3)	Fe2-O4	2.0052(18)
Fe1-Fe2'	3.190(6)	Fe2-N3	2.151(2)
Fe1-O1	1.8903(17)	Fe2-N4	2.159(2)
Fe1-O2	1.9974(19)	Fe3-O5	1.9922(19)
Fe1-O4'	1.9989(19)	Fe3-O2	1.9959(19)
Fe1-O3	2.0099(18)	Fe3-O1	2.0184(18)
Fe1-N2	2.180(2)	Fe3-O6	2.034(2)
Fe1-N1	2.194(2)	Fe3-O7	2.044(4)
Fe2-O1	1.8939(18)	Fe3-O10	2.107(5)
atoms	angles(°)	atoms	angles(°)
O1-Fe1-O2	76.73(8)	O5-Fe2-N4	75.66(8)
O1-Fe1-O4'	99.13(8)	O4-Fe2-N4	100.49(8)
O2-Fe1-O4'	105.10(8)	N3-Fe2-N4	84.94(9)
O1-Fe1-O3	114.90(8)	O5-Fe3-O2	149.01(8)
O2-Fe1-O3	168.29(8)	O5-Fe3-O1	75.40(7)
O4'-Fe1-O3	72.64(8)	O2-Fe3-O1	73.94(7)
O1-Fe1-N2	94.88(8)	O5-Fe3-O6	90.02(9)
O2-Fe1-N2	106.58(9)	O2-Fe3-O6	90.92(9)
O4'-Fe1-N2	147.53(8)	O1-Fe3-O6	99.95(8)
O3-Fe1-N2	74.90(8)	O5-Fe3-O7	81.01(14)
O1-Fe1-N1	150.54(9)	O2-Fe3-O7	106.25(14)
O2-Fe1-N1	74.72(8)	O1-Fe3-O7	95.56(13)
O4'-Fe1-N1	95.14(8)	O6-Fe3-O7	159.52(13)
O3-Fe1-N1	93.91(8)	O5-Fe3-O10	127.70(13)
N2-Fe1-N1	86.44(9)	O2-Fe3-O10	83.27(13)
O1-Fe2-O3'	101.59(8)	O1-Fe3-O10	156.22(12)
O1-Fe2-O5	78.13(8)	O6-Fe3-O10	86.88(14)
O3'-Fe2-O5	101.30(8)	O7-Fe3-O10	84.22(18)
O1-Fe2-O4	106.60(8)	Fe1-O1-Fe2	149.13(11)
O3'-Fe2-O4	73.24(8)	Fe1-O1-Fe3	106.21(9)
O5-Fe2-O4	173.26(8)	Fe2-O1-Fe3	104.52(8)
O1-Fe2-N3	93.31(8)	Fe3-O2-Fe1	103.08(8)
O3'-Fe2-N3	148.93(9)	Fe2'-O3-Fe1	106.38(8)
O5-Fe2-N3	108.43(9)	Fe1'-O4-Fe2	105.65(8)
O4-Fe2-N3	76.43(8)	Fe3-O5-Fe2	101.80(8)
O1-Fe2-N4	151.65(9)	O5-Fe2-N4	75.66(8)
O3'-Fe2-N4	93.97(8)	O4-Fe2-N4	100.49(8)

Table A-3. Selected interatomic distances (Å) and angles (°) for [Fe<sub>4</sub>(N<sub>3</sub>)<sub>6</sub>(hmp)<sub>6</sub>].2MeOH (2-3·2MeOH)

atoms	distances(Å)	atoms	distances(Å)
Fe1-Fe2	3.170(1)	Fe1-N1	2.139(3)
Fe1-Fe1'	3.165(1)	Fe2-N7	1.988(3)
Fe1-Fe2'	5.735(2)	Fe2-N4	2.012(3)
Fe1-O1	1.954(2)	Fe2-N10	2.016(3)
Fe1-O2'	1.988(2)	Fe2-O1	2.058(2)
Fe1-O3	1.989(2)	Fe2-O3	2.072(2)
Fe1-O2	1.997(2)	Fe2-N3	2.191(3)
Fe1-N2	2.135(3)	O2-Fe1'	1.988(2)
atoms	angles(°)	atoms	angles(°)
O1-Fe1-O2'	108.25(10)	N4-Fe2-N10	92.06(13)
O1-Fe1-O3	78.37(9)	N7-Fe2-O1	90.96(11)
O2'-Fe1-O3	96.94(9)	N4-Fe2-O1	90.28(11)
O1-Fe1-O2	176.73(10)	N10-Fe2-O1	169.37(12)
O2'-Fe1-O2	74.85(11)	N7-Fe2-O3	160.78(11)
O3-Fe1-O2	102.46(9)	N4-Fe2-O3	93.15(11)
O1-Fe1-N2	100.53(10)	N10-Fe2-O3	95.31(11)
O2'-Fe1-N2	150.49(10)	O1-Fe2-O3	74.20(9)
O3-Fe1-N2	95.04(9)	N7-Fe2-N3	93.72(13)
O2-Fe1-N2	76.27(10)	N4-Fe2-N3	166.86(12)
O1-Fe1-N1	77.18(10)	N10-Fe2-N3	83.48(12)
O2'-Fe1-N1	88.65(10)	O1-Fe2-N3	91.95(10)
O3-Fe1-N1	155.44(10)	O3-Fe2-N3	75.04(10)
O2-Fe1-N1	102.08(10)	Fe1-O1-Fe2	104.34(10)
N2-Fe1-N1	91.54(11)	Fe1'-O2-Fe1	105.15(11)
N7-Fe2-N4	99.19(14)	Fe1-O3-Fe2	102.63(9)
N7-Fe2-N10	98.89(13)	Fe2-Fe1-Fe1'	129.73(2)

Table A-4. Selected interatomic distances (Å) and angles (°) for  
 $[\text{Fe}_8\text{O}_3(\text{OMe})(\text{pdm})_4(\text{pdmH})_4(\text{MeOH})_2](\text{ClO}_4)_5 \cdot 7\text{MeOH}$  (**3-1**·7MeOH)

atoms	distances(Å)	atoms	distances(Å)
Fe1-Fe2	3.133(23)	Fe3-O7	2.072(4)
Fe1-Fe8	3.101(4)	Fe3-N3	2.084(5)
Fe2-Fe3	3.499(2)	Fe4-O15	1.856(4)
Fe2-Fe7	3.246(14)	Fe4-O12	1.993(4)
Fe2-Fe8	3.529(14)	Fe4-O20	2.005(4)
Fe3-Fe4	3.425(27)	Fe4-O10	2.026(4)
Fe3-Fe5	3.645(9)	Fe4-N5	2.109(5)
Fe3-Fe6	3.365(33)	Fe4-O11	2.157(4)
Fe3-Fe7	3.562(5)	Fe5-O15	1.973(4)
Fe3-Fe8	3.091(10)	Fe5-O7	2.034(4)
Fe4-Fe5	3.129(15)	Fe5-O14	2.074(5)
Fe4-Fe6	3.541(4)	Fe5-O12	2.078(4)
Fe4-Fe7	3.484(3)	Fe5-O13	2.145(5)
Fe5-Fe6	3.094(8)	Fe5-O16	2.160(5)
Fe6-Fe7	3.072(3)	Fe5-N6	2.240(5)
Fe6-Fe8	3.160(7)	Fe6-O15	1.920(4)
Fe7-Fe8	3.366(35)	Fe6-O18	1.998(4)
Fe1-O22	1.978(4)	Fe6-O17	2.000(4)
Fe1-O21	2.009(4)	Fe6-O16	2.006(4)
Fe1-O3	2.072(4)	Fe6-N7	2.051(6)
Fe1-O1	2.090(4)	Fe6-O19	2.096(4)
Fe1-O9	2.177(4)	Fe7-O19	1.958(4)
Fe1-O2	2.177(4)	Fe7-O5	2.011(4)
Fe1-N1	2.220(5)	Fe7-O17	2.033(4)
Fe2-O22	1.865(4)	Fe7-O20	2.053(4)
Fe2-O5	2.005(4)	Fe7-N8	2.060(5)
Fe2-O3	2.010(4)	Fe7-O21	2.088(4)
Fe2-O6	2.020(4)	Fe8-O22	1.915(4)
Fe2-N2	2.106(6)	Fe8-O18	1.948(4)
Fe2-O4	2.147(5)	Fe8-O8	2.003(4)
Fe3-O19	1.952(4)	Fe8-O9	2.015(4)
Fe3-O10	1.992(4)	Fe8-N4	2.080(5)
Fe3-O6	2.059(4)	Fe8-O19	2.089(4)
Fe3-O8	2.068(4)		
atoms	angles(°)	atoms	angles(°)
Fe2-O3-Fe1	100.25(18)	Fe8-O18-Fe6	106.41(19)
Fe2-O5-Fe7	117.11(19)	Fe3-O19-Fe7	131.3(2)
Fe2-O6-Fe3	118.1(2)	Fe3-O19-Fe8	99.74(18)
Fe5-O7-Fe3	125.2(2)	Fe7-O19-Fe8	112.50(19)
Fe8-O8-Fe3	98.78(17)	Fe3-O19-Fe6	112.45(19)
Fe8-O9-Fe1	95.31(18)	Fe7-O19-Fe6	98.48(19)
Fe3-O10-Fe4	117.0(2)	Fe8-O19-Fe6	98.06(17)
Fe4-O12-Fe5	100.40(19)	Fe4-O20-Fe7	118.31(19)

Table A-4. Continued.

atoms	angles(°)	atoms	angles(°)
Fe4-O15-Fe6	139.4(2)	Fe1-O21-Fe7	126.3(2)
Fe4-O15-Fe5	109.5(2)	Fe2-O22-Fe8	138.1(2)
Fe6-O15-Fe5	105.3(2)	Fe2-O22-Fe1	109.2(2)
Fe6-O16-Fe5	95.85(18)	Fe8-O22-Fe1	105.6(2)
Fe6-O17-Fe7	99.25(19)		

Table A-5. Selected interatomic distances (Å) and angles (°) for  
[Fe<sub>18</sub>O<sub>6</sub>(OH)<sub>8</sub>(pdm)<sub>10</sub>(pdmH)<sub>4</sub>(H<sub>2</sub>O)<sub>4</sub>](ClO<sub>4</sub>)<sub>10</sub>·7MeCN·3H<sub>2</sub>O (**3-3**·7MeCN·3H<sub>2</sub>O)

atoms	distances(Å)	atoms	distances(Å)
Fe1-O3	1.921(7)	Fe5-N4	2.066(10)
Fe1-O10	1.994(7)	Fe5-O10	2.093(6)
Fe1-O13	2.000(7)	Fe6-O2	1.932(7)
Fe1-O17'	2.022(6)	Fe6-O19	1.960(7)
Fe1-O23	2.045(6)	Fe6-O11	1.967(7)
Fe1-O23'	2.117(6)	Fe6-O20	1.986(7)
Fe2-O3	1.906(6)	Fe6-O21	2.104(8)
Fe2-O6	1.947(6)	Fe6-O22	2.147(7)
Fe2-O12	1.994(7)	Fe7-O5	1.969(6)
Fe2-O1	2.073(6)	Fe7-O15	1.975(6)
Fe2-N5	2.074(10)	Fe7-O8	1.981(6)
Fe2-O13	2.130(6)	Fe7-O2	1.981(7)
Fe3-O3	1.857(6)	Fe7-N6	2.131(9)
Fe3-O4	1.987(7)	Fe7-O14	2.162(7)
Fe3-O16	1.998(7)	Fe8-O18	1.937(7)
Fe3-O17	2.068(6)	Fe8-O15	1.979(7)
Fe3-N7	2.072(8)	Fe8-O6	2.060(7)
Fe3-O23'	2.162(6)	Fe8-O7	2.126(6)
Fe4-O19	1.970(7)	Fe8-O2	2.170(6)
Fe4-O1	1.981(7)	Fe8-N2	2.175(8)
Fe4-O12	2.034(7)	Fe8-O1	2.254(6)
Fe4-O4	2.069(6)	Fe9-O7	1.908(6)
Fe4-O5	2.086(6)	Fe9-O20	1.918(7)
Fe4-N1	2.100(9)	Fe9-O8	1.985(8)
Fe5-O1	1.965(7)	Fe9-N3	2.111(8)
Fe5-O16	2.004(6)	Fe9-O2	2.169(6)

Table A-5. Continued.

Fe5-O18	2.013(6)	Fe9-O9	2.177(8)
Fe5-O11	2.054(7)		
atoms	angles(°)	atoms	angles(°)
Fe1-O3-Fe3	108.5(3)	Fe4-O1-Fe8	121.9(3)
Fe1-O3-Fe2	103.0(3)	Fe4-O5-Fe7	121.7(4)
Fe1-O10-Fe5	124.3(4)	Fe4-O19-Fe6	123.7(3)
Fe1-O13-Fe2	93.0(3)	Fe5-O1-Fe8	96.1(3)
Fe1-O23-Fe1'	105.4(3)	Fe5-O11-Fe6	119.1(4)
Fe1-O23-Fe3'	98.3(3)	Fe5-O18-Fe8	105.5(3)
Fe1'-O23-Fe3'	91.5(3)	Fe6-O2-Fe7	120.6(3)
Fe1'-O17-Fe3	102.2(3)	Fe6-O2-Fe9	97.0(3)
Fe2-O1-Fe5	110.5(3)	Fe6-O2-Fe8	132.8(3)
Fe2-O1-Fe4	96.9(3)	Fe6-O20-Fe9	103.9(3)
Fe2-O1-Fe8	99.2(3)	Fe7-O2-Fe8	99.8(3)
Fe2-O3-Fe3	141.7(3)	Fe7-O2-Fe9	98.8(3)
Fe2-O6-Fe8	110.8(3)	Fe7-O8-Fe9	105.3(3)
Fe2-O12-Fe4	97.7(4)	Fe7-O15-Fe8	106.9(3)
Fe3-O4-Fe4	119.9(3)	Fe8-O2-Fe9	100.0(2)
Fe3-O16-Fe5	115.7(3)	Fe8-O7-Fe9	110.9(3)
Fe4-O1-Fe5	128.7(3)		

Table A-6. Selected interatomic distances (Å) and angles (°) for  
 $[\text{Fe}_9\text{O}_4(\text{OH})_2(\text{O}_2\text{CMe})_{10}(\text{pdm})(\text{pdmH})_4](\text{NO}_3)\cdot 7\text{CH}_2\text{Cl}_2$  (**3-4**·7CH<sub>2</sub>Cl<sub>2</sub>)

atoms	distances(Å)	atoms	distances(Å)
Fe1-O3'	1.844(3)	Fe3-O4	2.041(3)
Fe1-O3	1.844(2)	Fe3-O9	2.077(3)
Fe1-O18'	2.051(3)	Fe4-O2	1.890(2)
Fe1-O18	2.051(3)	Fe4-O10	1.989(3)
Fe1-N3	2.084(5)	Fe4-O17	1.996(3)
Fe2-O2	1.866(3)	Fe4-O13	2.026(4)
Fe2-O3'	1.960(3)	Fe4-O8	2.053(3)
Fe2-O15'	2.034(3)	Fe4-N2	2.208(3)
Fe2-O11	2.065(3)	Fe5-O3	1.935(3)
Fe2-O6	2.074(3)	Fe5-O1	1.948(3)
Fe2-O12	2.086(3)	Fe5-O15	1.982(3)
Fe3-O2	1.942(3)	Fe5-O5	2.029(3)
Fe3-O1	1.962(3)	Fe5-O7'	2.051(3)
Fe3-O18	2.008(3)	Fe5-N1	2.253(3)
Fe3-O17	2.028(3)	Fe5-Fe2'	2.9796(7)
atoms	angles(°)	atoms	angles(°)
Fe5-O1-Fe3	125.13(14)	Fe1-O3-Fe2'	134.41(14)
Fe2-O2-Fe4	121.95(14)	Fe5-O3-Fe2'	99.79(11)
Fe2-O2-Fe3	134.18(13)	Fe5-O15-Fe2'	95.76(11)
Fe4-O2-Fe3	100.19(12)	Fe4-O17-Fe3	93.84(11)
Fe1-O3-Fe5	125.80(13)	Fe3-O18-Fe1	124.44(13)

Table A-7. Selected interatomic distances (Å) and angles (°) for  
 $[\text{Mn}_4\text{O}_2(\text{O}_2\text{CBu}^t)_5(\text{dphmp})_3]\cdot 2\text{MeCN}$  (**4-1**·2MeCN).

atoms	distances(Å)	atoms	distances(Å)
Mn1-O3	1.867(3)	Mn3-O2	1.883(3)
Mn1-O1	1.899(3)	Mn3-O5	1.887(3)
Mn1-O14	1.965(3)	Mn3-O1	1.904(3)
Mn1-N1	2.053(4)	Mn3-N3	2.021(4)
Mn1-O8	2.193(3)	Mn3-O9	2.101(3)
Mn1-O6	2.219(3)	Mn3...Mn4	2.7412(9)
Mn2-O4	1.861(3)	Mn4-O1	1.898(3)
Mn2-O2	1.887(3)	Mn4-O2	1.903(3)
Mn2-O13	1.974(3)	Mn4-O7	1.931(3)
Mn2-N2	2.049(4)	Mn4-O10	1.970(3)
Mn2-O11	2.151(3)	Mn4-O15	2.153(3)
Mn2-O5	2.505(3)	Mn4-O12	2.282(3)
Mn2...Mn3	3.1076(9)		
atoms	angles(°)	atoms	angles(°)
Mn4-O1-Mn1	120.15(16)	Mn3-O2-Mn4	92.79(13)
Mn4-O1-Mn3	92.25(13)	Mn2-O2-Mn4	125.40(17)
Mn1-O1-Mn3	130.31(17)	Mn3-O5-Mn2	88.93(12)
Mn3-O2-Mn2	111.06(15)		

Table A-8. Selected interatomic distances (Å) and angles (°) for  
 [Mn<sub>6</sub>O<sub>4</sub>(OMe)<sub>2</sub>(O<sub>2</sub>CPh)<sub>4</sub>(dphmp)<sub>4</sub>]·3MeCN (**4-2**·3MeCN).

atoms	distances(Å)	atoms	distances(Å)
Mn1-O1	1.918(6)	Mn2-O2'	1.945(6)
Mn1-O5'	1.924(6)	Mn2-N2	2.030(8)
Mn1-O2	1.935(6)	Mn2-O9	2.240(7)
Mn1-O8	1.945(7)	Mn2-O5	2.319(7)
Mn1-O7	2.101(7)	Mn2...Mn1'	3.084(2)
Mn1-O2'	2.390(7)	Mn3-O3	1.839(6)
Mn1...Mn3	2.803(2)	Mn3-O2	1.924(6)
Mn1...Mn2	2.934(2)	Mn3-O1	1.925(6)
Mn1...Mn2'	3.084(2)	Mn3-N1	2.037(8)
Mn1...Mn3'	3.208(2)	Mn3-O6	2.267(7)
Mn2-O4	1.851(6)	Mn3-O5	2.408(7)
Mn2-O1	1.938(6)	Mn3...Mn1'	3.208(2)
atoms	angles(°)	atoms	angles(°)
Mn3-O2-Mn1	93.1(3)	Mn2'-O2-Mn1'	84.5(2)
Mn3-O2-Mn2'	161.4(3)	Mn1'-O5-Mn2	92.7(3)
Mn1-O2-Mn2'	105.3(3)	Mn1'-O5-Mn3	94.9(3)
Mn3-O2-Mn1'	95.5(2)	Mn2-O5-Mn3	88.2(2)
Mn1-O2-Mn1'	98.7(2)		

Table A-9. Selected interatomic distances (Å) and angles (°) for  
 [Mn<sub>11</sub>O<sub>7</sub>(OMe)<sub>7</sub>(O<sub>2</sub>CPh)<sub>7</sub>(dphmp)<sub>4</sub>(MeOH)<sub>2</sub>]·4MeCN (**4-3**·4MeCN).

atoms	distances(Å)	atoms	distances(Å)
Mn1-O2	1.850(3)	Mn6-O13	1.996(3)
Mn1-O32	1.892(3)	Mn6-O33	2.160(3)
Mn1-O29	1.948(3)	Mn6-O26	2.279(3)
Mn1-N2	2.044(4)	Mn7-O21	1.881(3)
Mn1-O17	2.185(3)	Mn7-O31	1.903(3)
Mn1-O31	2.442(3)	Mn7-O8	1.993(3)
Mn2-O33	1.873(3)	Mn7-O30	2.010(3)
Mn2-O29	1.878(3)	Mn7-O9	2.082(3)
Mn2-O1	1.879(3)	Mn7-O19	2.268(3)
Mn2-N1	2.041(4)	Mn8-O32	1.900(3)
Mn2-O5	2.219(3)	Mn8-O30	1.925(3)
Mn2-O17	2.422(3)	Mn8-O22	1.944(3)
Mn3-O3	1.862(3)	Mn8-O31	1.964(3)
Mn3-O33	1.907(3)	Mn8-O34	2.191(3)
Mn3-O18	1.929(3)	Mn8-O10	2.242(3)
Mn3-N3	2.045(4)	Mn9-O34	1.874(3)
Mn3-O20	2.247(3)	Mn9-O25	1.893(3)
Mn3-O1	2.415(3)	Mn9-O14	1.962(3)
Mn4-O29	1.864(3)	Mn9-O30	1.965(3)
Mn4-O31	1.914(3)	Mn9-O19	2.217(3)
Mn4-O6	1.933(3)	Mn9-O27	2.266(3)
Mn4-O19	1.942(3)	Mn10-O4	1.862(3)
Mn4-O7	2.241(3)	Mn10-O28	1.872(3)
Mn4-O34	2.444(3)	Mn10-O22	1.938(3)
Mn5-O28	1.843(3)	Mn10-N4	2.041(3)
Mn5-O32	1.895(3)	Mn10-O12	2.219(3)
Mn5-O17	1.941(3)	Mn10-O26	2.308(3)
Mn5-O18	2.000(3)	Mn11-O25	2.121(3)
Mn5-O11	2.116(3)	Mn11-O16	2.128(4)
Mn5-O33	2.395(3)	Mn11-O21	2.131(3)
Mn6-O34	1.880(3)	Mn11-O23	2.174(4)
Mn6-O20	1.910(3)	Mn11-O24	2.241(4)
Mn6-O28	1.949(3)	Mn11-O30	2.293(3)

Table A-10. Selected interatomic distances (Å) and angles (°) for  
 $[\text{Mn}_7\text{O}_3(\text{OH})_3(\text{O}_2\text{CBu}^t)_7(\text{dmhmp})_4]\cdot 7\text{MeCN}$  (**4-4**·7MeCN)

atoms	distances(Å)	atoms	distances(Å)
Mn1-O1	1.866(2)	Mn5-O23	2.127(3)
Mn1-O7	1.887(2)	Mn5-O13	2.522(3)
Mn1-O2	1.895(2)	Mn6-O10	1.871(3)
Mn1-N1	2.015(3)	Mn6-O6	1.882(3)
Mn1-O15	2.263(3)	Mn6-O3	1.920(3)
Mn1-O13	2.303(3)	Mn6-N4	2.040(4)
Mn2-O5	1.867(2)	Mn6-O20	2.258(3)
Mn2-O8	1.899(3)	Mn6-O22	2.273(3)
Mn2-O2	1.910(3)	Mn7-O8	2.141(3)
Mn2-N2	2.031(3)	Mn7-O9	2.148(3)
Mn2-O24	2.110(3)	Mn7-O7	2.191(3)
Mn3-O3	1.889(3)	Mn7-O17	2.204(3)
Mn3-O1	1.916(2)	Mn7-O18	2.257(3)
Mn3-O21	1.946(3)	Mn7-O2	2.362(2)
Mn3-O16	1.973(3)	Mn7-C48	2.545(4)
Mn3-O5	2.206(3)	Mn1...Mn2	3.159(10)
Mn3-O11	2.254(3)	Mn1...Mn3	3.407(8)
Mn4-O1	1.893(3)	Mn1...Mn4	3.356(3)
Mn4-O3	1.899(3)	Mn1...Mn5	3.175(9)
Mn4-O19	1.941(3)	Mn1...Mn7	3.237(10)
Mn4-O14	2.004(3)	Mn2...Mn3	3.656(6)
Mn4-O4	2.224(3)	Mn2...Mn7	3.252(7)
Mn4-O12	2.236(3)	Mn3...Mn4	2.810(2)
Mn5-O4	1.859(3)	Mn3...Mn6	3.411(8)
Mn5-O2	1.897(3)	Mn4...Mn5	3.694(6)
Mn5-O9	1.905(3)	Mn4...Mn6	3.432(11)
Mn5-N3	2.021(3)	Mn5...Mn7	3.245(2)
atoms	angles(°)	atoms	angles(°)
Mn1-O1-Mn3	128.58(13)	Mn5-O2-Mn2	127.35(13)
Mn1-O1-Mn4	126.46(13)	Mn5-O2-Mn7	98.7(1)
Mn1-O2-Mn2	112.28(12)	Mn5-O4-Mn4	129.35(13)
Mn1-O2-Mn5	113.73(13)	Mn5-O9-Mn7	106.24(12)
Mn1-O2-Mn7	98.4(1)	Mn3-O3-Mn4	95.75(11)
Mn1-O7-Mn7	104.84(11)	Mn3-O3-Mn6	127.16(14)
Mn2-O2-Mn7	98.59(10)	Mn4-O3-Mn6	127.99(14)
Mn2-O5-Mn3	127.47(12)		
Mn2-O8-Mn7	107.07(12)		

Table A-11. Selected interatomic distances (Å) and angles (°) for  
 $[\text{Mn}_{12}\text{O}_7(\text{OH})(\text{OMe})_2(\text{O}_2\text{CPh})_{12}(\text{dmhmp})_4(\text{H}_2\text{O})] \cdot 3\text{CH}_2\text{Cl}_2$  (**4-5**·3CH<sub>2</sub>Cl<sub>2</sub>)

atoms	distances(Å)	atoms	distances(Å)
Mn1-O4	1.880(3)	Mn8-O10	1.894(3)
Mn1-O1	1.918(3)	Mn8-O7	1.896(3)
Mn1-O3	1.930(3)	Mn8-O14	1.943(3)
Mn1-O23	1.960(3)	Mn8-N2	2.041(3)
Mn1-O33	2.214(3)	Mn8-O27	2.120(3)
Mn1-O6	2.343(3)	Mn8-O9	2.264(3)
Mn2-O4	1.902(3)	Mn9-O5	1.844(3)
Mn2-O20	1.942(3)	Mn9-O11	1.908(3)
Mn2-O1	1.958(3)	Mn9-O8	1.908(3)
Mn2-O21	1.974(3)	Mn9-N3	2.034(4)
Mn2-O34	2.140(3)	Mn9-O18	2.118(3)
Mn2-O5	2.165(3)	Mn9-O22	2.447(3)
Mn3-O5	1.866(3)	Mn10-O12	1.879(3)
Mn3-O2	1.901(3)	Mn10-O4	1.895(3)
Mn3-O17	1.973(3)	Mn10-O8	1.909(3)
Mn3-O1	2.004(3)	Mn10-N4	2.022(4)
Mn3-O16	2.205(3)	Mn10-O24	2.217(3)
Mn3-O6	2.251(3)	Mn10-O22	2.321(3)
Mn4-O2	1.880(3)	Mn11-O6	1.857(3)
Mn4-O6	1.890(3)	Mn11-O39	1.891(3)
Mn4-O38	1.942(3)	Mn11-O8	1.925(3)
Mn4-O35	1.988(3)	Mn11-O36	2.003(3)
Mn4-O25	2.153(3)	Mn11-O26	2.093(3)
Mn4-O3	2.302(3)	Mn12-O39	2.085(3)
Mn5-O2	1.879(3)	Mn12-O11	2.143(3)
Mn5-O9	1.883(3)	Mn12-O12	2.160(4)
Mn5-O7	1.905(3)	Mn12-O32	2.225(10)
Mn5-N1	2.038(3)	Mn12-O31	2.227(11)
Mn5-O15	2.231(3)	Mn12-O8	2.326(3)
Mn5-O38	2.387(3)	Mn1...Mn2	2.8036(10)
Mn6-O29	2.129(3)	Mn1...Mn3	3.1568(9)
Mn6-O10	2.130(3)	Mn1...Mn4	3.1880(9)
Mn6-O3	2.170(3)	Mn2...Mn3	2.9905(9)

Table A-11. Continued.

Mn6-O37	2.226(3)	Mn3...Mn4	3.0396(9)
Mn6-O7	2.264(3)	Mn3...Mn9	3.2389(9)
Mn6-O38	2.284(3)	Mn4...Mn5	3.1034(9)
Mn7-O19	2.142(3)	Mn5...Mn8	2.9783(9)
Mn7-O7	2.155(3)	Mn6...Mn8	3.1335(9)
Mn7-O28	2.168(3)	Mn9...Mn10	3.1202(10)
Mn7-O13	2.209(3)	Mn9...Mn12	3.2111(10)
Mn7-O16	2.296(3)	Mn10...Mn12	3.2316(11)
Mn7-O1	2.314(3)		
atoms	angles(°)	atoms	angles(°)
Mn1-O1-Mn2	92.65(12)	Mn4-O2-Mn5	111.26(14)
Mn1-O1-Mn3	107.19(13)	Mn4-O6-Mn11	119.97(15)
Mn1-O1-Mn7	131.85(14)	Mn4-O38-Mn5	90.98(11)
Mn1-O3-Mn4	97.38(12)	Mn4-O38-Mn6	102.66(12)
Mn1-O3-Mn6	147.76(15)	Mn5-O7-Mn7	115.82(13)
Mn1-O4-Mn2	95.70(13)	Mn5-O7-Mn6	103.96(12)
Mn1-O4-Mn10	125.59(16)	Mn5-O7-Mn8	103.18(13)
Mn1-O6-Mn3	86.78(10)	Mn5-O9-Mn8	91.33(11)
Mn1-O6-Mn4	97.15(12)	Mn5-O38-Mn6	89.57(10)
Mn1-O6-Mn11	127.49(14)	Mn6-O7-Mn7	117.56(12)
Mn2-O1-Mn3	98.03(13)	Mn6-O7-Mn8	97.38(12)
Mn2-O1-Mn7	118.86(13)	Mn6-O10-Mn8	102.10(12)
Mn2-O4-Mn10	125.90(17)	Mn7-O7-Mn8	116.34(13)
Mn2-O5-Mn3	95.50(12)	Mn9-O8-Mn10	109.65(15)
Mn2-O5-Mn9	124.13(14)	Mn9-O8-Mn11	126.69(16)
Mn3-O1-Mn7	103.42(11)	Mn9-O8-Mn12	98.18(13)
Mn3-O2-Mn4	107.00(13)	Mn9-O11-Mn12	104.73(15)
Mn3-O2-Mn5	137.65(15)	Mn9-O22-Mn10	81.69(10)
Mn3-O5-Mn9	121.58(15)	Mn10-O8-Mn11	116.58(16)
Mn3-O6-Mn4	94.03(11)	Mn10-O8-Mn12	98.99(12)
Mn3-O6-Mn11	122.47(14)	Mn10-O12-Mn12	106.04(14)
Mn3-O16-Mn7	97.86(11)	Mn11-O8-Mn12	99.37(12)
Mn4-O3-Mn6	95.34(11)	Mn11-O39-Mn12	109.62(15)

Table A-12. Selected interatomic distances (Å) and angles (°) for  
(HNEt<sub>3</sub>)[NaMn<sub>6</sub>O<sub>4</sub>(dmhmp)<sub>4</sub>(N<sub>3</sub>)<sub>4</sub>](ClO<sub>4</sub>)<sub>2</sub>·Et<sub>2</sub>O (**4-6**·Et<sub>2</sub>O).

atoms	distances(Å)	atoms	distances(Å)
Mn1-O2	1.862(2)	Mn2-O1	1.897(2)
Mn1-O3	1.8797(9)	Mn2-O1'	1.915(2)
Mn1-O1	1.895(2)	Mn2-N8	2.028(3)
Mn1-N7	2.045(3)	Mn2-N1	2.354(3)
Mn1-N1'	2.394(3)	Mn2-N4	2.418(3)
Mn1-N1	2.423(3)	Mn2-Mn2'	3.2163(10)
Mn1-Mn2	3.1731(8)	Mn2-Mn1'	3.2310(7)
Mn1-Mn1'	3.1985(10)	Na1-O2	2.320(3)
Mn1-Mn2'	3.2310(7)	Na1-O3	2.386(4)
Mn1-Na1	3.302(2)	Na1-N6'	2.420(7)
Mn2-O4	1.861(2)		
atoms	angles(°)	atoms	angles(°)
Mn1-O1-Mn2	113.61(11)	Mn1-O3-Na1	100.76(11)
Mn1-O1-Mn2'	116.00(12)	Mn2-N1-Mn1'	85.78(10)
Mn2-O1-Mn2'	115.06(12)	Mn2-N1-Mn1	83.25(10)
Mn1-O2-Na1	103.73(12)	Mn1'-N1-Mn1	83.23(10)
Mn1'-O3-Mn1	116.60(7)	Mn2-N4-Mn2'	83.39(13)

Table A-13. Selected interatomic distances (Å) and angles (°) for [Mn<sub>4</sub>O<sub>4</sub>(O<sub>2</sub>CMe)<sub>3</sub>(pdpm)<sub>3</sub>·0.5MeCN (**5-1**·0.5MeCN)

atoms	distances (Å)	atoms	distances (Å)
Mn1-Mn2	2.7989(8)	Mn2-O2	1.916(2)
Mn1-Mn4	2.8548(7)	Mn2-O6	2.019(2)
Mn1-Mn3	2.8815(7)	Mn2-N1	2.034(2)
Mn2-Mn4	2.8543(7)	Mn3-O12	1.846(2)
Mn2-Mn3	3.0693(9)	Mn3-O3	1.882(2)
Mn3-Mn4	2.9579(7)	Mn3-O2	1.968(2)
Mn1-O2	1.913(2)	Mn3-N3	2.029(3)
Mn1-O9	1.966(2)	Mn3-O8	2.188(2)
Mn1-O4	1.976(2)	Mn3-O1	2.297(2)
Mn1-O7	1.982(2)	Mn4-O13	1.834(2)
Mn1-O5	2.103(2)	Mn4-O3	1.838(2)
Mn1-O3	2.107(2)	Mn4-O1	1.878(2)
Mn2-O11	1.851(2)	Mn4-O4	1.910(2)
Mn2-O4	1.857(2)	Mn4-O10	2.027(2)
Mn2-O1	1.912(2)	Mn4-N5	2.036(3)
atoms	angles (°)	atoms	angles (°)
Mn4-O1-Mn2	97.73(10)	Mn4-O3-Mn3	105.34(10)
Mn4-O1-Mn3	89.63(9)	Mn4-O3-Mn1	92.46(9)
Mn2-O1-Mn3	93.19(8)	Mn3-O3-Mn1	92.31(8)
Mn1-O2-Mn2	93.92(9)	Mn2-O4-Mn4	98.50(9)
Mn1-O2-Mn3	95.88(9)	Mn2-O4-Mn1	93.75(8)
Mn2-O2-Mn3	104.40(9)	Mn4-O4-Mn1	94.54(9)

Table A-14. Selected interatomic distances (Å) and angles (°) for  
 $[\text{Mn}_7\text{O}_4(\text{pdpm})_6(\text{N}_3)_4](\text{ClO}_4)_2 \cdot 2\text{MeCN}$  (5-2·2MeCN)

atoms	distances (Å)	atoms	distances (Å)
Mn1-O4	1.8667(15)	Mn2-O1	1.932(5)
Mn1-O1	1.880(4)	Mn2-O1'	1.934(4)
Mn1-O2	1.896(4)	Mn2-N3	2.035(6)
Mn1-N2	2.039(6)	Mn2-N4	2.329(6)
Mn1-N7'	2.328(6)	Mn2-N7	2.372(6)
Mn1-N7	2.469(6)	Mn2-Mn2'	3.2150(18)
Mn1-Mn1'	3.1911(17)	Mn3-O2	2.195(4)
Mn1-Mn2	3.2016(15)	Mn3-N1	2.329(6)
Mn1-Mn2'	3.2265(15)	Mn3-O4	2.579(7)
Mn2-O3	1.863(5)		
atoms	angles (°)	atoms	angles (°)
Mn2'-N4-Mn2	87.3(3)	Mn1-O1-Mn2'	115.6(2)
Mn1'-N7-Mn2	86.7(2)	Mn2-O1-Mn2'	112.6(2)
Mn1'-N7-Mn1	83.3(2)	Mn1-O2-Mn3	113.1(2)
Mn2-N7-Mn1	82.78(18)	Mn1-O4-Mn1'	117.46(12)
Mn1-O1-Mn2	114.2(2)		

APPENDIX B  
LIST OF COMPOUNDS

- [Mn<sub>12</sub>O<sub>12</sub>(O<sub>2</sub>CMe)<sub>16</sub>(H<sub>2</sub>O)<sub>4</sub>] (1-1)
- [Fe<sub>6</sub>O<sub>2</sub>(hmp)<sub>10</sub>(H<sub>2</sub>O)<sub>2</sub>](NO<sub>3</sub>)<sub>4</sub> (2-1).
- [Fe<sub>6</sub>O<sub>2</sub>(hmp)<sub>8</sub>(NO<sub>3</sub>)<sub>4</sub>(H<sub>2</sub>O)<sub>2</sub>](NO<sub>3</sub>)<sub>2</sub> (2-2)
- [Fe<sub>4</sub>(N<sub>3</sub>)<sub>6</sub>(hmp)<sub>6</sub>] (2-3).
- [Fe<sub>8</sub>O<sub>3</sub>(OMe)(pdm)<sub>4</sub>(pdmH)<sub>4</sub>(MeOH)<sub>2</sub>](ClO<sub>4</sub>)<sub>5</sub> (3-1).
- [Fe<sub>8</sub>O<sub>3</sub>(OEt)(pdm)<sub>4</sub>(pdmH)<sub>4</sub>(EtOH)<sub>2</sub>](ClO<sub>4</sub>)<sub>5</sub> (3-2).
- [Fe<sub>18</sub>O<sub>6</sub>(OH)<sub>8</sub>(pdm)<sub>10</sub>(pdmH)<sub>4</sub>(H<sub>2</sub>O)<sub>4</sub>](ClO<sub>4</sub>)<sub>10</sub> (3-3)
- [Fe<sub>9</sub>O<sub>4</sub>(OH)<sub>2</sub>(O<sub>2</sub>CMe)<sub>10</sub>(pdm)(pdmH)<sub>4</sub>](NO<sub>3</sub>) (3-4).
- [Mn<sub>4</sub>O<sub>2</sub>(O<sub>2</sub>CBu<sup>t</sup>)<sub>5</sub>(dphmp)<sub>3</sub>] (4-1).
- [Mn<sub>6</sub>O<sub>4</sub>(OMe)<sub>2</sub>(O<sub>2</sub>CPh)<sub>4</sub>(dphmp)<sub>4</sub>] (4-2).
- [Mn<sub>11</sub>O<sub>7</sub>(OMe)<sub>7</sub>(O<sub>2</sub>CPh)<sub>7</sub>(dphmp)<sub>4</sub>(MeOH)<sub>2</sub>] (4-3).
- [Mn<sub>7</sub>O<sub>3</sub>(OH)<sub>3</sub>(O<sub>2</sub>CBu<sup>t</sup>)<sub>7</sub>(dmhmp)<sub>4</sub>] (4-4).
- [Mn<sub>12</sub>O<sub>7</sub>(OH)(OMe)<sub>2</sub>(O<sub>2</sub>CPh)<sub>12</sub>(dmhmp)<sub>4</sub>(H<sub>2</sub>O)] (4-5).
- (HNEt<sub>3</sub>)[NaMn<sub>6</sub>O<sub>4</sub>(dmhmp)<sub>6</sub>(N<sub>3</sub>)<sub>4</sub>](ClO<sub>4</sub>)<sub>2</sub> (4-6).
- [Mn<sub>10</sub>O<sub>4</sub>(N<sub>3</sub>)<sub>4</sub>(hmp)<sub>12</sub>](ClO<sub>4</sub>)<sub>2</sub>·MeCN (4-7)
- NBu<sup>t</sup><sub>4</sub>[Mn<sub>4</sub>O<sub>2</sub>(O<sub>2</sub>CPh)<sub>7</sub>(hmp)<sub>2</sub>] (4-8)
- [Mn<sub>12</sub>O<sub>8</sub>Cl<sub>4</sub>(O<sub>2</sub>CPh)<sub>8</sub>(hmp)<sub>6</sub>] (4-9).
- [Mn<sub>4</sub>O<sub>4</sub>(O<sub>2</sub>CMe)<sub>3</sub>(pdpm)<sub>3</sub>] (5-1).
- [Mn<sub>7</sub>O<sub>4</sub>(pdpm)<sub>6</sub>(N<sub>3</sub>)<sub>4</sub>](ClO<sub>4</sub>)<sub>2</sub> (5-2).

APPENDIX C  
VAN VLECK EQUATIONS

p = paramagnetic impurity

$$c = N\mu_B^2/3k$$

N = Avogadro's number

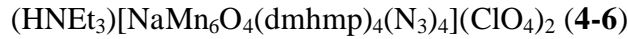
g = Lande's factor

k = Boltzmann constant

T = Temperature

TIP = Temperature independent paramagnetism

C-1



$$\chi_M = (c g^2)/T (\text{Num/Den}) + \text{TIP}$$

$$m = J_{\text{cis}}/k/T, n = J_{\text{trans}}/k/T$$

$$\begin{aligned} \text{Num} = & +0.0000*\exp(0.0000*m + 0.0000*n) + 18.0000*\exp(0.0000*m + 2.0000*n) \\ & + 150.0000*\exp(0.0000*m + 6.0000*n) + 504.0000*\exp(0.0000*m + 12.0000*n) \\ & + 3780.0000*\exp(0.0000*m + 20.0000*n) + 0.0000*\exp(-4.0000*m + 4.0000*n) + 18.0000*\exp(- \\ & 2.0000*m + 4.0000*n) + 90.0000*\exp(2.0000*m + 4.0000*n) + 36.0000*\exp(-6.0000*m \\ & + 8.0000*n) + 180.0000*\exp(-2.0000*m + 8.0000*n) + 504.0000*\exp(4.0000*m + 8.0000*n) \\ & + 450.0000*\exp(-8.0000*m + 14.0000*n) + 1260.0000*\exp(-2.0000*m + 14.0000*n) \\ & + 2160.0000*\exp(6.0000*m + 14.0000*n) + 504.0000*\exp(-10.0000*m + 22.0000*n) \\ & + 1080.0000*\exp(-2.0000*m + 22.0000*n) + 1980.0000*\exp(8.0000*m + 22.0000*n) \\ & + 0.0000*\exp(-12.0000*m + 12.0000*n) + 18.0000*\exp(-10.0000*m + 12.0000*n) \\ & + 90.0000*\exp(-6.0000*m + 12.0000*n) + 540.0000*\exp(8.0000*m + 12.0000*n) + 54.0000*\exp(- \end{aligned}$$

$$\begin{aligned}
&16.0000*m + 18.0000*n) + 330.0000*\exp(-12.0000*m + 18.0000*n) + 840.0000*\exp(-6.0000*m \\
&+ 18.0000*n) + 1620.0000*\exp(2.0000*m + 18.0000*n) + 2640.0000*\exp(12.0000*m \\
&+ 18.0000*n) + 450.0000*\exp(-20.0000*m + 26.0000*n) + 1260.0000*\exp(-14.0000*m \\
&+ 26.0000*n) + 2700.0000*\exp(-6.0000*m + 26.0000*n) + 4950.0000*\exp(4.0000*m \\
&+ 26.0000*n) + 6552.0000*\exp(16.0000*m + 26.0000*n) + 0.0000*\exp(-24.0000*m + 24.0000*n) \\
&+ 72.0000*\exp(-22.0000*m + 24.0000*n) + 540.0000*\exp(-18.0000*m + 24.0000*n) \\
&+ 2016.0000*\exp(-12.0000*m + 24.0000*n) + 4320.0000*\exp(-4.0000*m + 24.0000*n) \\
&+ 5940.0000*\exp(6.0000*m + 24.0000*n) + 6552.0000*\exp(18.0000*m + 24.0000*n) \\
&+ 72.0000*\exp(-30.0000*m + 32.0000*n) + 450.0000*\exp(-26.0000*m + 32.0000*n) \\
&+ 1512.0000*\exp(-20.0000*m + 32.0000*n) + 3780.0000*\exp(-12.0000*m + 32.0000*n) \\
&+ 5940.0000*\exp(-2.0000*m + 32.0000*n) + 8190.0000*\exp(10.0000*m + 32.0000*n) \\
&+ 10080.0000*\exp(24.0000*m + 32.0000*n) + 0.0000*\exp(-40.0000*m + 40.0000*n) \\
&+ 18.0000*\exp(-38.0000*m + 40.0000*n) + 90.0000*\exp(-34.0000*m + 40.0000*n) \\
&+ 252.0000*\exp(-28.0000*m + 40.0000*n) + 540.0000*\exp(-20.0000*m + 40.0000*n) \\
&+ 990.0000*\exp(-10.0000*m + 40.0000*n) + 1638.0000*\exp(2.0000*m + 40.0000*n) \\
&+ 2520.0000*\exp(16.0000*m + 40.0000*n) + 3672.0000*\exp(32.0000*m + 40.0000*n) \\
&+ 18.0000*\exp(-4.0000*m + 6.0000*n) + 270.0000*\exp(-4.0000*m + 10.0000*n) \\
&+ 756.0000*\exp(-4.0000*m + 16.0000*n) + 0.0000*\exp(-6.0000*m + 6.0000*n) + 36.0000*\exp(- \\
&8.0000*m + 10.0000*n) + 504.0000*\exp(2.0000*m + 10.0000*n) + 180.0000*\exp(-10.0000*m \\
&+ 16.0000*n) + 1080.0000*\exp(4.0000*m + 16.0000*n) + 84.0000*\exp(6.0000*m + 6.0000*n) \\
&+ 0.0000*\exp(-10.0000*m + 10.0000*n) + 540.0000*\exp(10.0000*m + 10.0000*n) \\
&+ 18.0000*\exp(-14.0000*m + 16.0000*n) + 990.0000*\exp(14.0000*m + 16.0000*n) \\
&+ 54.0000*\exp(-12.0000*m + 14.0000*n) + 540.0000*\exp(-14.0000*m + 20.0000*n)
\end{aligned}$$

$$\begin{aligned}
&+1512.0000*\exp(-8.0000*m +20.0000*n) +1512.0000*\exp(-16.0000*m +28.0000*n) \\
&+3240.0000*\exp(-8.0000*m +28.0000*n) +5940.0000*\exp(2.0000*m +28.0000*n) \\
&+0.0000*\exp(-14.0000*m +14.0000*n) +72.0000*\exp(-18.0000*m +20.0000*n) \\
&+3960.0000*\exp(10.0000*m +20.0000*n) +360.0000*\exp(-22.0000*m +28.0000*n) \\
&+6552.0000*\exp(14.0000*m +28.0000*n) +990.0000*\exp(16.0000*m +14.0000*n) \\
&+0.0000*\exp(-20.0000*m +20.0000*n) +3276.0000*\exp(22.0000*m +20.0000*n) \\
&+36.0000*\exp(-26.0000*m +28.0000*n) +5040.0000*\exp(28.0000*m +28.0000*n) \\
&+54.0000*\exp(-24.0000*m +26.0000*n) +540.0000*\exp(-28.0000*m +34.0000*n) \\
&+1512.0000*\exp(-22.0000*m +34.0000*n) +3240.0000*\exp(-14.0000*m +34.0000*n) \\
&+5940.0000*\exp(-4.0000*m +34.0000*n) +9828.0000*\exp(8.0000*m +34.0000*n) \\
&+0.0000*\exp(-26.0000*m +26.0000*n) +72.0000*\exp(-32.0000*m +34.0000*n) \\
&+10080.0000*\exp(22.0000*m +34.0000*n) +2520.0000*\exp(30.0000*m +26.0000*n) \\
&+0.0000*\exp(-34.0000*m +34.0000*n) +7344.0000*\exp(38.0000*m +34.0000*n) \\
&+54.0000*\exp(-40.0000*m +42.0000*n) +270.0000*\exp(-36.0000*m +42.0000*n) \\
&+756.0000*\exp(-30.0000*m +42.0000*n) +1620.0000*\exp(-22.0000*m +42.0000*n) \\
&+2970.0000*\exp(-12.0000*m +42.0000*n) +4914.0000*\exp(0.0000*m +42.0000*n) \\
&+7560.0000*\exp(14.0000*m +42.0000*n) +0.0000*\exp(-42.0000*m +42.0000*n) \\
&+7344.0000*\exp(30.0000*m +42.0000*n) +5130.0000*\exp(48.0000*m +42.0000*n) \\
&+0.0000*\exp(-18.0000*m +18.0000*n) +546.0000*\exp(24.0000*m +18.0000*n) \\
&+2520.0000*\exp(32.0000*m +24.0000*n) +0.0000*\exp(-32.0000*m +32.0000*n) \\
&+3672.0000*\exp(40.0000*m +32.0000*n) +450.0000*\exp(-24.0000*m +30.0000*n) \\
&+1260.0000*\exp(-18.0000*m +30.0000*n) +2700.0000*\exp(-10.0000*m +30.0000*n) \\
&+2520.0000*\exp(-26.0000*m +38.0000*n) +5400.0000*\exp(-18.0000*m +38.0000*n)
\end{aligned}$$

$$\begin{aligned}
&+9900.0000*\exp(-8.0000*m +38.0000*n) +54.0000*\exp(-28.0000*m +30.0000*n) \\
&+3960.0000*\exp(0.0000*m +30.0000*n) +720.0000*\exp(-32.0000*m +38.0000*n) \\
&+13104.0000*\exp(4.0000*m +38.0000*n) +0.0000*\exp(-30.0000*m +30.0000*n) \\
&+4914.0000*\exp(12.0000*m +30.0000*n) +108.0000*\exp(-36.0000*m +38.0000*n) \\
&+15120.0000*\exp(18.0000*m +38.0000*n) +5040.0000*\exp(26.0000*m +30.0000*n) \\
&+0.0000*\exp(-38.0000*m +38.0000*n) +14688.0000*\exp(34.0000*m +38.0000*n) \\
&+3672.0000*\exp(42.0000*m +30.0000*n) +10260.0000*\exp(52.0000*m +38.0000*n) \\
&+450.0000*\exp(-40.0000*m +46.0000*n) +1260.0000*\exp(-34.0000*m +46.0000*n) \\
&+2700.0000*\exp(-26.0000*m +46.0000*n) +4950.0000*\exp(-16.0000*m +46.0000*n) \\
&+8190.0000*\exp(-4.0000*m +46.0000*n) +54.0000*\exp(-44.0000*m +46.0000*n) \\
&+10080.0000*\exp(10.0000*m +46.0000*n) +0.0000*\exp(-46.0000*m +46.0000*n) \\
&+11016.0000*\exp(26.0000*m +46.0000*n) +10260.0000*\exp(44.0000*m +46.0000*n) \\
&+6930.0000*\exp(64.0000*m +46.0000*n) +588.0000*\exp(-24.0000*m +36.0000*n) \\
&+3780.0000*\exp(-24.0000*m +44.0000*n) +150.0000*\exp(-30.0000*m +36.0000*n) \\
&+1080.0000*\exp(-16.0000*m +36.0000*n) +1512.0000*\exp(-32.0000*m +44.0000*n) \\
&+5940.0000*\exp(-14.0000*m +44.0000*n) +18.0000*\exp(-34.0000*m +36.0000*n) \\
&+1650.0000*\exp(-6.0000*m +36.0000*n) +450.0000*\exp(-38.0000*m +44.0000*n) \\
&+8190.0000*\exp(-2.0000*m +44.0000*n) +0.0000*\exp(-36.0000*m +36.0000*n) \\
&+2184.0000*\exp(6.0000*m +36.0000*n) +54.0000*\exp(-42.0000*m +44.0000*n) \\
&+10080.0000*\exp(12.0000*m +44.0000*n) +2520.0000*\exp(20.0000*m +36.0000*n) \\
&+0.0000*\exp(-44.0000*m +44.0000*n) +11016.0000*\exp(28.0000*m +44.0000*n) \\
&+2448.0000*\exp(36.0000*m +36.0000*n) +10260.0000*\exp(46.0000*m +44.0000*n) \\
&+1710.0000*\exp(54.0000*m +36.0000*n) +6930.0000*\exp(66.0000*m +44.0000*n)
\end{aligned}$$

$$\begin{aligned}
&+1764.0000*\exp(-40.0000*m +52.0000*n) +3780.0000*\exp(-32.0000*m +52.0000*n) \\
&+6930.0000*\exp(-22.0000*m +52.0000*n) +450.0000*\exp(-46.0000*m +52.0000*n) \\
&+9828.0000*\exp(-10.0000*m +52.0000*n) +54.0000*\exp(-50.0000*m +52.0000*n) \\
&+12600.0000*\exp(4.0000*m +52.0000*n) +0.0000*\exp(-52.0000*m +52.0000*n) \\
&+14688.0000*\exp(20.0000*m +52.0000*n) +15390.0000*\exp(38.0000*m +52.0000*n) \\
&+13860.0000*\exp(58.0000*m +52.0000*n) +9108.0000*\exp(80.0000*m +52.0000*n) \\
&+1620.0000*\exp(-40.0000*m +60.0000*n) +588.0000*\exp(-48.0000*m +60.0000*n) \\
&+2640.0000*\exp(-30.0000*m +60.0000*n) +150.0000*\exp(-54.0000*m +60.0000*n) \\
&+3822.0000*\exp(-18.0000*m +60.0000*n) +18.0000*\exp(-58.0000*m +60.0000*n) \\
&+5040.0000*\exp(-4.0000*m +60.0000*n) +0.0000*\exp(-60.0000*m +60.0000*n) \\
&+6120.0000*\exp(12.0000*m +60.0000*n) +6840.0000*\exp(30.0000*m +60.0000*n) \\
&+6930.0000*\exp(50.0000*m +60.0000*n) +6072.0000*\exp(72.0000*m +60.0000*n) \\
&+3900.0000*\exp(96.0000*m +60.0000*n)
\end{aligned}$$

$$\begin{aligned}
\text{Den} = &+1.0000*\exp(0.0000*m +0.0000*n) +9.0000*\exp(0.0000*m +2.0000*n) \\
&+25.0000*\exp(0.0000*m +6.0000*n) +42.0000*\exp(0.0000*m +12.0000*n) \\
&+189.0000*\exp(0.0000*m +20.0000*n) +3.0000*\exp(-4.0000*m +4.0000*n) +9.0000*\exp(- \\
&2.0000*m +4.0000*n) +15.0000*\exp(2.0000*m +4.0000*n) +18.0000*\exp(-6.0000*m \\
&+8.0000*n) +30.0000*\exp(-2.0000*m +8.0000*n) +42.0000*\exp(4.0000*m +8.0000*n) \\
&+75.0000*\exp(-8.0000*m +14.0000*n) +105.0000*\exp(-2.0000*m +14.0000*n) \\
&+108.0000*\exp(6.0000*m +14.0000*n) +42.0000*\exp(-10.0000*m +22.0000*n) \\
&+54.0000*\exp(-2.0000*m +22.0000*n) +66.0000*\exp(8.0000*m +22.0000*n) +3.0000*\exp(- \\
&12.0000*m +12.0000*n) +9.0000*\exp(-10.0000*m +12.0000*n) +15.0000*\exp(-6.0000*m \\
&+12.0000*n) +27.0000*\exp(8.0000*m +12.0000*n) +27.0000*\exp(-16.0000*m +18.0000*n)
\end{aligned}$$

$$\begin{aligned}
&+55.0000*\exp(-12.0000*m +18.0000*n) +70.0000*\exp(-6.0000*m +18.0000*n) \\
&+81.0000*\exp(2.0000*m +18.0000*n) +88.0000*\exp(12.0000*m +18.0000*n) +75.0000*\exp(- \\
&20.0000*m +26.0000*n) +105.0000*\exp(-14.0000*m +26.0000*n) +135.0000*\exp(-6.0000*m \\
&+26.0000*n) +165.0000*\exp(4.0000*m +26.0000*n) +156.0000*\exp(16.0000*m +26.0000*n) \\
&+6.0000*\exp(-24.0000*m +24.0000*n) +36.0000*\exp(-22.0000*m +24.0000*n) \\
&+90.0000*\exp(-18.0000*m +24.0000*n) +168.0000*\exp(-12.0000*m +24.0000*n) \\
&+216.0000*\exp(-4.0000*m +24.0000*n) +198.0000*\exp(6.0000*m +24.0000*n) \\
&+156.0000*\exp(18.0000*m +24.0000*n) +36.0000*\exp(-30.0000*m +32.0000*n) \\
&+75.0000*\exp(-26.0000*m +32.0000*n) +126.0000*\exp(-20.0000*m +32.0000*n) \\
&+189.0000*\exp(-12.0000*m +32.0000*n) +198.0000*\exp(-2.0000*m +32.0000*n) \\
&+195.0000*\exp(10.0000*m +32.0000*n) +180.0000*\exp(24.0000*m +32.0000*n) \\
&+3.0000*\exp(-40.0000*m +40.0000*n) +9.0000*\exp(-38.0000*m +40.0000*n) +15.0000*\exp(- \\
&34.0000*m +40.0000*n) +21.0000*\exp(-28.0000*m +40.0000*n) +27.0000*\exp(-20.0000*m \\
&+40.0000*n) +33.0000*\exp(-10.0000*m +40.0000*n) +39.0000*\exp(2.0000*m +40.0000*n) \\
&+45.0000*\exp(16.0000*m +40.0000*n) +51.0000*\exp(32.0000*m +40.0000*n) +9.0000*\exp(- \\
&4.0000*m +6.0000*n) +45.0000*\exp(-4.0000*m +10.0000*n) +63.0000*\exp(-4.0000*m \\
&+16.0000*n) +1.0000*\exp(-6.0000*m +6.0000*n) +18.0000*\exp(-8.0000*m +10.0000*n) \\
&+42.0000*\exp(2.0000*m +10.0000*n) +30.0000*\exp(-10.0000*m +16.0000*n) \\
&+54.0000*\exp(4.0000*m +16.0000*n) +7.0000*\exp(6.0000*m +6.0000*n) +3.0000*\exp(- \\
&10.0000*m +10.0000*n) +27.0000*\exp(10.0000*m +10.0000*n) +9.0000*\exp(-14.0000*m \\
&+16.0000*n) +33.0000*\exp(14.0000*m +16.0000*n) +27.0000*\exp(-12.0000*m +14.0000*n) \\
&+90.0000*\exp(-14.0000*m +20.0000*n) +126.0000*\exp(-8.0000*m +20.0000*n) \\
&+126.0000*\exp(-16.0000*m +28.0000*n) +162.0000*\exp(-8.0000*m +28.0000*n)
\end{aligned}$$

$$\begin{aligned}
&+198.0000*\exp(2.0000*m + 28.0000*n) + 3.0000*\exp(-14.0000*m + 14.0000*n) + 36.0000*\exp(- \\
&18.0000*m + 20.0000*n) + 132.0000*\exp(10.0000*m + 20.0000*n) + 60.0000*\exp(-22.0000*m \\
&+ 28.0000*n) + 156.0000*\exp(14.0000*m + 28.0000*n) + 33.0000*\exp(16.0000*m + 14.0000*n) \\
&+ 6.0000*\exp(-20.0000*m + 20.0000*n) + 78.0000*\exp(22.0000*m + 20.0000*n) + 18.0000*\exp(- \\
&26.0000*m + 28.0000*n) + 90.0000*\exp(28.0000*m + 28.0000*n) + 27.0000*\exp(-24.0000*m \\
&+ 26.0000*n) + 90.0000*\exp(-28.0000*m + 34.0000*n) + 126.0000*\exp(-22.0000*m + 34.0000*n) \\
&+ 162.0000*\exp(-14.0000*m + 34.0000*n) + 198.0000*\exp(-4.0000*m + 34.0000*n) \\
&+ 234.0000*\exp(8.0000*m + 34.0000*n) + 3.0000*\exp(-26.0000*m + 26.0000*n) + 36.0000*\exp(- \\
&32.0000*m + 34.0000*n) + 180.0000*\exp(22.0000*m + 34.0000*n) + 45.0000*\exp(30.0000*m \\
&+ 26.0000*n) + 6.0000*\exp(-34.0000*m + 34.0000*n) + 102.0000*\exp(38.0000*m + 34.0000*n) \\
&+ 27.0000*\exp(-40.0000*m + 42.0000*n) + 45.0000*\exp(-36.0000*m + 42.0000*n) \\
&+ 63.0000*\exp(-30.0000*m + 42.0000*n) + 81.0000*\exp(-22.0000*m + 42.0000*n) \\
&+ 99.0000*\exp(-12.0000*m + 42.0000*n) + 117.0000*\exp(0.0000*m + 42.0000*n) \\
&+ 135.0000*\exp(14.0000*m + 42.0000*n) + 3.0000*\exp(-42.0000*m + 42.0000*n) \\
&+ 102.0000*\exp(30.0000*m + 42.0000*n) + 57.0000*\exp(48.0000*m + 42.0000*n) + 1.0000*\exp(- \\
&18.0000*m + 18.0000*n) + 13.0000*\exp(24.0000*m + 18.0000*n) + 45.0000*\exp(32.0000*m \\
&+ 24.0000*n) + 3.0000*\exp(-32.0000*m + 32.0000*n) + 51.0000*\exp(40.0000*m + 32.0000*n) \\
&+ 75.0000*\exp(-24.0000*m + 30.0000*n) + 105.0000*\exp(-18.0000*m + 30.0000*n) \\
&+ 135.0000*\exp(-10.0000*m + 30.0000*n) + 210.0000*\exp(-26.0000*m + 38.0000*n) \\
&+ 270.0000*\exp(-18.0000*m + 38.0000*n) + 330.0000*\exp(-8.0000*m + 38.0000*n) \\
&+ 27.0000*\exp(-28.0000*m + 30.0000*n) + 132.0000*\exp(0.0000*m + 30.0000*n) \\
&+ 120.0000*\exp(-32.0000*m + 38.0000*n) + 312.0000*\exp(4.0000*m + 38.0000*n) \\
&+ 3.0000*\exp(-30.0000*m + 30.0000*n) + 117.0000*\exp(12.0000*m + 30.0000*n)
\end{aligned}$$

$$\begin{aligned}
&+54.0000*\exp(-36.0000*m +38.0000*n) +270.0000*\exp(18.0000*m +38.0000*n) \\
&+90.0000*\exp(26.0000*m +30.0000*n) +6.0000*\exp(-38.0000*m +38.0000*n) \\
&+204.0000*\exp(34.0000*m +38.0000*n) +51.0000*\exp(42.0000*m +30.0000*n) \\
&+114.0000*\exp(52.0000*m +38.0000*n) +75.0000*\exp(-40.0000*m +46.0000*n) \\
&+105.0000*\exp(-34.0000*m +46.0000*n) +135.0000*\exp(-26.0000*m +46.0000*n) \\
&+165.0000*\exp(-16.0000*m +46.0000*n) +195.0000*\exp(-4.0000*m +46.0000*n) \\
&+27.0000*\exp(-44.0000*m +46.0000*n) +180.0000*\exp(10.0000*m +46.0000*n) \\
&+3.0000*\exp(-46.0000*m +46.0000*n) +153.0000*\exp(26.0000*m +46.0000*n) \\
&+114.0000*\exp(44.0000*m +46.0000*n) +63.0000*\exp(64.0000*m +46.0000*n) \\
&+49.0000*\exp(-24.0000*m +36.0000*n) +189.0000*\exp(-24.0000*m +44.0000*n) \\
&+25.0000*\exp(-30.0000*m +36.0000*n) +54.0000*\exp(-16.0000*m +36.0000*n) \\
&+126.0000*\exp(-32.0000*m +44.0000*n) +198.0000*\exp(-14.0000*m +44.0000*n) \\
&+9.0000*\exp(-34.0000*m +36.0000*n) +55.0000*\exp(-6.0000*m +36.0000*n) +75.0000*\exp(- \\
&38.0000*m +44.0000*n) +195.0000*\exp(-2.0000*m +44.0000*n) +1.0000*\exp(-36.0000*m \\
&+36.0000*n) +52.0000*\exp(6.0000*m +36.0000*n) +27.0000*\exp(-42.0000*m +44.0000*n) \\
&+180.0000*\exp(12.0000*m +44.0000*n) +45.0000*\exp(20.0000*m +36.0000*n) +3.0000*\exp(- \\
&44.0000*m +44.0000*n) +153.0000*\exp(28.0000*m +44.0000*n) +34.0000*\exp(36.0000*m \\
&+36.0000*n) +114.0000*\exp(46.0000*m +44.0000*n) +19.0000*\exp(54.0000*m +36.0000*n) \\
&+63.0000*\exp(66.0000*m +44.0000*n) +147.0000*\exp(-40.0000*m +52.0000*n) \\
&+189.0000*\exp(-32.0000*m +52.0000*n) +231.0000*\exp(-22.0000*m +52.0000*n) \\
&+75.0000*\exp(-46.0000*m +52.0000*n) +234.0000*\exp(-10.0000*m +52.0000*n) \\
&+27.0000*\exp(-50.0000*m +52.0000*n) +225.0000*\exp(4.0000*m +52.0000*n) +3.0000*\exp(- \\
&52.0000*m +52.0000*n) +204.0000*\exp(20.0000*m +52.0000*n) +171.0000*\exp(38.0000*m
\end{aligned}$$

$$\begin{aligned} &+52.0000*n) +126.0000*\exp(58.0000*m +52.0000*n) +69.0000*\exp(80.0000*m +52.0000*n) \\ &+81.0000*\exp(-40.0000*m +60.0000*n) +49.0000*\exp(-48.0000*m +60.0000*n) \\ &+88.0000*\exp(-30.0000*m +60.0000*n) +25.0000*\exp(-54.0000*m +60.0000*n) \\ &+91.0000*\exp(-18.0000*m +60.0000*n) +9.0000*\exp(-58.0000*m +60.0000*n) \\ &+90.0000*\exp(-4.0000*m +60.0000*n) +1.0000*\exp(-60.0000*m +60.0000*n) \\ &+85.0000*\exp(12.0000*m +60.0000*n) +76.0000*\exp(30.0000*m +60.0000*n) \\ &+63.0000*\exp(50.0000*m +60.0000*n) +46.0000*\exp(72.0000*m +60.0000*n) \\ &+25.0000*\exp(96.0000*m +60.0000*n) \end{aligned}$$

C-2

[Mn<sub>4</sub>O<sub>4</sub>(O<sub>2</sub>CMe)<sub>3</sub>(pdpm)] (5-1)

$$\chi_M = (c g^2)/T (\text{Num/Den}) + \text{TIP}$$

$$l=J_1/k/T, m=J_2/k/T, n=J_3/k/T$$

$$\begin{aligned} \text{Num} = & 300.0000 * \exp(0.0000 * l + 0.0000 * m + 0.0000 * n) \\ & + 6.0000 * \exp(2.0000 * l + 0.0000 * m + 0.0000 * n) + 0.0000 * \exp(2.0000 * l + -4.0000 * m + 2.0000 * n) \\ & + 300.0000 * \exp(2.0000 * l + -2.0000 * m + 2.0000 * n) + 30.0000 * \exp(2.0000 * l + 2.0000 * m + 2.0000 * n) \\ & + 6.0000 * \exp(2.0000 * l + -6.0000 * m + 6.0000 * n) + 84.0000 * \exp(2.0000 * l + 4.0000 * m + 6.0000 * n) \\ & + 30.0000 * \exp(2.0000 * l + -8.0000 * m + 12.0000 * n) \\ & + 180.0000 * \exp(2.0000 * l + 6.0000 * m + 12.0000 * n) + 84.0000 * \exp(2.0000 * l + - \\ & 10.0000 * m + 20.0000 * n) + 330.0000 * \exp(2.0000 * l + 8.0000 * m + 20.0000 * n) \\ & + 114.0000 * \exp(6.0000 * l + 0.0000 * m + 0.0000 * n) + 300.0000 * \exp(6.0000 * l + - \\ & 6.0000 * m + 2.0000 * n) + 30.0000 * \exp(6.0000 * l + -2.0000 * m + 2.0000 * n) \\ & + 414.0000 * \exp(6.0000 * l + 4.0000 * m + 2.0000 * n) + 30.0000 * \exp(6.0000 * l + - \\ & 12.0000 * m + 6.0000 * n) + 6.0000 * \exp(6.0000 * l + -10.0000 * m + 6.0000 * n) \\ & + 180.0000 * \exp(6.0000 * l + 8.0000 * m + 6.0000 * n) + 6.0000 * \exp(6.0000 * l + - \\ & 16.0000 * m + 12.0000 * n) + 180.0000 * \exp(6.0000 * l + 2.0000 * m + 12.0000 * n) \\ & + 330.0000 * \exp(6.0000 * l + 12.0000 * m + 12.0000 * n) + 30.0000 * \exp(6.0000 * l + - \\ & 20.0000 * m + 20.0000 * n) + 84.0000 * \exp(6.0000 * l + -14.0000 * m + 20.0000 * n) \\ & + 546.0000 * \exp(6.0000 * l + 16.0000 * m + 20.0000 * n) \\ & + 84.0000 * \exp(12.0000 * l + 0.0000 * m + 0.0000 * n) + 30.0000 * \exp(12.0000 * l + - \\ & 8.0000 * m + 2.0000 * n) + 414.0000 * \exp(12.0000 * l + -2.0000 * m + 2.0000 * n) \end{aligned}$$

$$\begin{aligned}
&+510.0000*\exp(12.0000*1+6.0000*m+2.0000*n) +6.0000*\exp(12.0000*1+- \\
&16.0000*m+6.0000*n) +294.0000*\exp(12.0000*1+-12.0000*m+6.0000*n) \\
&+84.0000*\exp(12.0000*1+-6.0000*m+6.0000*n) \\
&+180.0000*\exp(12.0000*1+2.0000*m+6.0000*n) \\
&+330.0000*\exp(12.0000*1+12.0000*m+6.0000*n) +0.0000*\exp(12.0000*1+- \\
&24.0000*m+12.0000*n) +6.0000*\exp(12.0000*1+-22.0000*m+12.0000*n) \\
&+30.0000*\exp(12.0000*1+-18.0000*m+12.0000*n) +180.0000*\exp(12.0000*1+- \\
&4.0000*m+12.0000*n) +546.0000*\exp(12.0000*1+18.0000*m+12.0000*n) \\
&+6.0000*\exp(12.0000*1+-30.0000*m+20.0000*n) +30.0000*\exp(12.0000*1+- \\
&26.0000*m+20.0000*n) +84.0000*\exp(12.0000*1+-20.0000*m+20.0000*n) \\
&+546.0000*\exp(12.0000*1+10.0000*m+20.0000*n) \\
&+840.0000*\exp(12.0000*1+24.0000*m+20.0000*n) \\
\\
&\text{Den}+=25.0000*\exp(0.0000*1+0.0000*m+0.0000*n) \\
&+3.0000*\exp(2.0000*1+0.0000*m+0.0000*n) +1.0000*\exp(2.0000*1+-4.0000*m+2.0000*n) \\
&+24.0000*\exp(2.0000*1+-2.0000*m+2.0000*n) +5.0000*\exp(2.0000*1+2.0000*m+2.0000*n) \\
&+3.0000*\exp(2.0000*1+-6.0000*m+6.0000*n) +7.0000*\exp(2.0000*1+4.0000*m+6.0000*n) \\
&+5.0000*\exp(2.0000*1+-8.0000*m+12.0000*n) +9.0000*\exp(2.0000*1+6.0000*m+12.0000*n) \\
&+7.0000*\exp(2.0000*1+-10.0000*m+20.0000*n) \\
&+11.0000*\exp(2.0000*1+8.0000*m+20.0000*n) +12.0000*\exp(6.0000*1+0.0000*m+0.0000*n) \\
&+24.0000*\exp(6.0000*1+-6.0000*m+2.0000*n) +5.0000*\exp(6.0000*1+-2.0000*m+2.0000*n) \\
&+18.0000*\exp(6.0000*1+4.0000*m+2.0000*n) +6.0000*\exp(6.0000*1+-12.0000*m+6.0000*n) \\
&+3.0000*\exp(6.0000*1+-10.0000*m+6.0000*n) +9.0000*\exp(6.0000*1+8.0000*m+6.0000*n) \\
&+3.0000*\exp(6.0000*1+-16.0000*m+12.0000*n) +9.0000*\exp(6.0000*1+2.0000*m+12.0000*n)
\end{aligned}$$

$$\begin{aligned}
&+11.0000*\exp(6.0000*1+12.0000*m+12.0000*n) +5.0000*\exp(6.0000*1+- \\
&20.0000*m+20.0000*n) +7.0000*\exp(6.0000*1+-14.0000*m+20.0000*n) \\
&+13.0000*\exp(6.0000*1+16.0000*m+20.0000*n) +7.0000*\exp(12.0000*1+0.0000*m+0.0000*n) \\
&+5.0000*\exp(12.0000*1+-8.0000*m+2.0000*n) +18.0000*\exp(12.0000*1+- \\
&2.0000*m+2.0000*n) +20.0000*\exp(12.0000*1+6.0000*m+2.0000*n) \\
&+3.0000*\exp(12.0000*1+-16.0000*m+6.0000*n) +21.0000*\exp(12.0000*1+- \\
&12.0000*m+6.0000*n) +7.0000*\exp(12.0000*1+-6.0000*m+6.0000*n) \\
&+9.0000*\exp(12.0000*1+2.0000*m+6.0000*n) +11.0000*\exp(12.0000*1+12.0000*m+6.0000*n) \\
&+1.0000*\exp(12.0000*1+-24.0000*m+12.0000*n) +3.0000*\exp(12.0000*1+- \\
&22.0000*m+12.0000*n) +5.0000*\exp(12.0000*1+-18.0000*m+12.0000*n) \\
&+9.0000*\exp(12.0000*1+-4.0000*m+12.0000*n) \\
&+13.0000*\exp(12.0000*1+18.0000*m+12.0000*n) +3.0000*\exp(12.0000*1+- \\
&30.0000*m+20.0000*n) +5.0000*\exp(12.0000*1+-26.0000*m+20.0000*n) \\
&+7.0000*\exp(12.0000*1+-20.0000*m+20.0000*n) \\
&+13.0000*\exp(12.0000*1+10.0000*m+20.0000*n) \\
&+15.0000*\exp(12.0000*1+24.0000*m+20.0000*n)
\end{aligned}$$

## LIST OF REFERENCES

- (1) Miller, J. S.; Epstein, A. J. *MRS Bulletin* **2000**, 25, 21.
- (2) Jiles, D. *Introduction to Magnetism and Magnetic Materials*; Chapman and Hall: New York, 1991, pp 1-344.
- (3) Huheey, J. E.; Keiter, E. A.; Keiter, R. L. *Inorganic Chemistry: Principles of Structure and Reactivity*; 4<sup>th</sup> ed.; HarperCollins College: New York, 1993; pp 459-468.
- (4) West, A. R. *Solid State Chemistry and Its Applications*; Wiley: New York, 1984; pp 553-582.
- (5) Smart, L.; Moore, E. *Solid State Chemistry: An Introduction*; Chapman and Hall: New York, 1992; pp 294-320.
- (6) West, A. R. *Basic Solid State Chemistry*; Wiley: New York, 1988; pp 342-375.
- (7) Kahn, O. *Molecular Magnetism*; VCH Publishers: New York, 1993; pp 287-328.
- (8) Miller, J. S. *Adv. Mater.* **1994**, 6, 4.
- (9) Wickman, H. H.; Trozzolo, A. M.; Williams, H. J.; Hull, G. W.; Merritt, F. R. *Phys. Rev.* **1967**, 155, 563.
- (10) Miller, J. S.; Calabrese, J. C.; Rommelmann, H.; Chittipeddi, S. R.; Zhang, J. H.; Reiff, W. M.; Epstein, A. J. *J. Am. Chem. Soc.* **1987**, 109, 769.
- (11) Miller, J. S.; Epstein, A. J.; Reiff, W. M. *Chem. Rev.* **1988**, 88, 201.
- (12) Bagai, R.; Christou, G. *Chem. Soc. Rev.*, **2009**, 38(4), 1011.
- (13) Christou, G.; Gatteschi, D.; Hendrickson, D. N., Sessoli, R. *MRS Bulletin* **2000**, 25, 66.
- (14) Lis, T. *Acta. Cryst.* **1980**, B36, 2042.
- (15) Sessoli, R.; Gatteschi, D.; Caneschi, A.; Novak, M. A. *Nature* **1993**, 365, 141.
- (16) Caneschi, A.; Gatteschi, D.; Sessoli, R.; Barra, A. L.; Brunel, L. C.; Guillot, M. *J. Am. Chem. Soc.* **1991**, 113, 5873.
- (17) Sessoli, R.; Tsai, H.-L.; Schake, A. R.; Wang, S.; Vincent, J. B.; Folting, K.; Gatteschi, D.; Christou, G.; Hendrickson, D. N. *J. Am. Chem. Soc.* **1993**, 115, 1804.
- (18) Thomas, L.; Lioni, F.; Ballou, R.; Gatteschi, D.; Sessoli, R.; Barbara, B. *Nature* **1996**, 383, 145.
- (19) Hendrickson, D. N.; Christou, G.; Ishimoto, H.; Yoo, J.; Brechin, E. K.; Yamaguchi, A.; Rumberger, E. M.; Aubin, S. M. J.; Sun, Z.; Aromí, G. *Polyhedron* **2001**, 20, 1479.

- (20) Ruiz, D.; Aubin, S. M. J.; Rumberger, E.; Incarvito, C. D.; Folting, K.; Rheingold, A. L.; Christou, G.; Hendrickson, D. N. *Mol. Cryst. Liq. Cryst.* **1999**, 335, 413.
- (21) Ruiz, D.; Sun, Z.; Albela, B.; Folting, K.; Ribas, J.; Christou, G.; Hendrickson, D. N. *Angew. Chem. Int. Ed.* **1998**, 37, 300.
- (22) Kurtz, D. M. *Chem. Rev.* **1990**, 90, 585.
- (23) Lippard, S. J. *Angew. Chem., Int. Ed. Engl.* **1988**, 27, 344.
- (24) Toftlund, H.; Murray, K. S.; Zwack, P. R.; Taylor, L. F.; Anderson, O. P. *J. Chem. Soc., Chem. Commun.* **1986**, 191.
- (25) Theil, E. C. *Annu. Rev. Biochem.* **1987**, 57, 289.
- (26) Xu, B.; Chasteen, N. D. *J. Biol. Chem.* **1991**, 266, 19965.
- (27) Bertini, I.; Gray, H. B.; Lippard, S. J.; Valentine, J. S. *Bioinorganic Chemistry*; University Science Books: Mill Valley, CA, 1994.
- (28) Powell, A. K. In *Comprehensive Coordination Chemistry II*; Mc Cleverty, J. A., Meyer, T. J., Eds.; Elsevier: Amsterdam, 2004; Vol. 8, pp 169–194.
- (29) Theil, E. C.; Matzapetakis, M.; Liu, X. *J. Biol. Inorg. Chem.* **2006**, 11, 803.
- (30) Taft, K. L.; Papaefthymiou, G. S.; Lippard, S. J. *Science* **1993**, 259, 1302.
- (31) Gorun, S. M.; Papaefthymiou, G. S.; Frankel, R. B.; Lippard, S. J. *J. Am. Chem. Soc.* **1987**, 109, 4244.
- (32) Powell, A. K. *Struct. Bonding (Berlin)* **1997**, 88, 1.
- (33) Gatteschi, D.; Sessoli, R. *Angew. Chem., Int. Ed.* **2003**, 42, 268.
- (34) Bircher, R.; Chaboussant, G.; Dobe, C.; Güdel, H. U.; Ochsenbein, S. I.; Sieber, A.; Waldmann, O. *Adv. Funct. Mater.* **2006**, 16, 209.
- (35) Christou, G. *Polyhedron* **2005**, 24, 2065.
- (36) Aromi, G.; Brechin, E. K. *Struct. Bonding (Berlin)* **2006**, 122, 1
- (37) McCusker, J. K.; Vincent, J. B.; Schmitt, E. A.; Mino, M. L.; Shin, K.; Coggin, D. K.; Hagen, P. M.; Huffman, J. C.; Christou, G.; Hendrickson, D. N. *J. Am. Chem. Soc.* **1991**, 113, 3012.
- (38) Libby, E.; McCusker, J. K.; Schmitt, E. A.; Folting, K.; Hendrickson, D. N.; Christou, G. *Inorg. Chem.* **1991**, 31, 3486.
- (39) Khan, O. *Chem. Phys. Lett.* **1997**, 265, 109.

- (40) Jones, L. F.; Brechin, E. K.; Collison, D.; Helliwell, M.; Mallah, T.; Piligkos, S.; Rajaraman, G.; Wernsdorfer, W. *Inorg. Chem.* **2003**, *42*, 6601.
- (41) Jones, L. F.; Batsanov, A.; Brechin, E. K.; Collison, D.; Helliwell, M.; Mallah, T.; McInnes, E. J. L.; Piligkos, S. *Angew. Chem., Int. Ed.* **2002**, *41*, 4318.
- (42) Saalfrank, R. W.; Bernt, I.; Uller, E.; Hampel, F. *Angew. Chem., Int. Ed.* **1997**, *36*, 2482.
- (43) Goodwin, J. C.; Sessoli, R.; Gatteschi, D.; Wernsdorfer, W.; Powell, A. K.; Heath, S. L. *Dalton Trans.* **2000**, *12*, 1835
- (44) Stamatatos, Th. C.; Abboud, K. A.; Wernsdorfer, W.; Christou, G. *Angew. Chem., Int. Ed.* **2006**, *45*, 4134.
- (45) Harden, N. C.; Bolcar, M. A.; Wernsdorfer, W.; Abboud, K. A.; Streib, W. E.; Christou, G. *Inorg. Chem.* **2003**, *42*, 7067.
- (46) Murugesu, M.; Habrych, M.; Wernsdorfer, W.; Abboud, K. A.; Christou, G. *J. Am. Chem. Soc.* **2004**, *126*, 4766.
- (47) Stamatatos, Th. C.; Abboud, K. A.; Wernsdorfer, W.; Christou, G. *Angew. Chem., Int. Ed.* **2007**, *46*, 884.
- (48) Yoo, J.; Brechin, E. K.; Yamaguchi, A.; Nakano, M.; Huffman, J. C.; Maniero, A. L.; Brunel, L.- C.; Awaga, K.; Ishimoto, H.; Christou, G.; Hendrickson, D. N. *Inorg. Chem.* **2000**, *39*, 3615.
- (49) Boskovic, C.; Wernsdorfer, W.; Folting, K.; Huffman, J. C.; Hendrickson, D. N.; Christou, G. *Inorg. Chem.* **2002**, *41*, 5107.
- (50) Murugesu, M.; Wernsdorfer, W.; Abboud, K. A.; Christou, G. *Polyhedron* **2005**, *24*, 2894.
- (51) Yang, E.- C.; Harden, N.; Wernsdorfer, W.; Zakharov, L.; Brechin, E. K.; Rheingold, A. L.; Christou, G.; Hendrickson, D. N. *Polyhedron* **2003**, *22*, 1857.
- (52) Yang, E.-C.; Wernsdorfer, W.; Hill, S.; Edwards, R. S.; Nakano, M.; Maccagnano, S.; Zakharov, L. N.; Rheingold, A. L.; Christou, G.; Hendrickson, D. N. *Polyhedron* **2003**, *22*, 1727.
- (53) Yang, E.- C.; Hendrickson, D. N.; Wernsdorfer, W.; Nakano, M.; Zakharov, L. N.; Sommer, R. D.; Rheingold, A. L.; Ledezma-Gairraud, M.; Christou, G. *J. Appl. Phys.* **2002**, *91*, 7382
- (54) Brechin, E. K.; Knapp, M. J.; Huffman, J. C.; Hendrickson, D. N.; Christou, G. *Inorg. Chim. Acta* **2000**, *297*, 389.

- (55) Christmas, C. A.; Tsai, H. L.; Pardi, L.; Kesselman, J. M.; Gantzel, P. K.; Chadha, R. K.; Gatteschi, D.; Harvey, D. F.; Hendrickson, D. N. *J. Am. Chem. Soc.* **1993**, *115*, 12483.
- (56) Ammala, P.; Cashion, J. D.; Kepert, C. M.; Moubaraki, M.; Murray, K. S.; Spiccia, L.; West, B. O. *Angew. Chem., Int. Ed.* **2000**, *39*, 1688..
- (57) Murugesu, M.; Abboud, K. A.; Christou, G. *Polyhedron* **2004**, *23*, 2779.
- (58) Taft, K. L.; Lippard, S. J. *J. Am. Chem. Soc.* **1990**, *112*, 9629.
- (59) Benelli, C.; Parsons, S.; Solan, G. A.; Winpenny, R. E. P. *Angew. Chem., Int. Ed.* **1996**, *35*, 1825.
- (60) Bagai, R.; Datta, S.; Betancur-Rodriguez, A.; Abboud, K. A.; Hill, S.; Christou, G. *Inorg. Chem.* **2007**, *46*, 4535.
- (61) Bagai, R.; Abboud, K. A.; Christou, G. *Inorg. Chem.* **2007**, *46*, 5567
- (62) Brechin, E. K. *Chem. Commun.* **2005**, 5141.
- (63) Papaefstathiou, G. S.; Perlepes, S. P. *Comments Inorg. Chem.* **2002**, *23*, 249.
- (64) *SHELXTL6*; Bruker-AXS, Madison, Wisconsin, **2000**.
- (65) Van der Sluis, P.; Spek, A. L. *Acta Crystallogr., Sect. A: Found. Crystallogr.* **1990**, *A46*, 194.
- (66) Davidson, E. R. *MAGNET*; Indiana University, Bloomington, IN, 1999.
- (67) Cañada-Vilalta, C.; O'Brien, T. A.; Brechin, E. K.; Pink, M.; Davidson, E. R.; Christou, G. *Inorg. Chem.* **2004**, *43*, 5505.
- (68) O'Brien, T. A.; Davidson, E. R. *Int. J. Quantum Chem.* **2003**, *92*, 294.
- (69) Zerner, M. C.; Loew, G. H.; Kirchner, R. F.; Mueller-Westerhoff, U. T. *J. Am. Chem. Soc.* **1980**, *102*, 589.
- (70) Zerner, M. C. *Semiempirical Molecular Orbital Methods*; Lipkowitz, K. B.; Boyd, D. B., Ed. VCH, **1991**; vol.2, pp313-363.
- (71) Clark, A. E.; Davidson, E. R. *J. Chem. Phys.* **2001**, *115*, 7382.
- (72) Davidson, E. R.; Clark, A. E. *Mol. Phys.* **2002**, *100*, 373.
- (73) Cañada-Vilalta, C.; O'Brien, T. A.; Pink, M.; Davidson, E. R.; Christou, G. *Inorg. Chem.* **2003**, *42*, 7819.
- (74) O'Brien, T. A.; O'Callaghan, B. J. *J. Chem. Theory Comput.* **2007**, *3*, 1275.

- (75) Escuer, A.; Aromi, G. *Eur. J. Inorg. Chem.* **2006**, 4721.
- (76) Jones, L. F.; Jensen, P.; Moubaraki, B.; Cashion, J. D.; Berry, K. J.; Murray, K. S. *Dalton Trans.* **2005**, 3344.
- (77) Cañada-Vilalta, C.; Rumberger, E.; Brechin, E. K.; Wernsdorfer, W.; Folting, K.; Davidson, E. R.; Hendrickson, D. N.; Christou, G. *J. Chem. Soc., Dalton Trans.* **2002**, 4005.
- (78) Yoon, S.; Lippard, S. J. *J. Am. Chem. Soc.* **2005**, *127*, 8386.
- (79) McCusker, J. K.; Christmas, C. A.; Hagen, P. M.; Chadha, R. K.; Harvey, D. F.; Hendrickson, D. N. *J. Am. Chem. Soc.* **1991**, *113*, 6114
- (80) Smith, A. A.; Coxall, R. A.; Harrison, A.; Helliwell, M.; Parsons, S.; Winpenny, R. E. P. *Polyhedron.* **2004**, *23*, 1557.
- (81) Ammala, P. S.; Cashion, J. D.; Kepert, C. M.; Murray, K. S.; Moubaraki, B.; Spiccia, L.; West, B. O. *J. Chem. Soc., Dalton Trans.* **2001**, 2032.
- (82) Micklitz, W.; Lippard, S. J. *J. Am. Chem. Soc.* **1988**, *27*, 3067.
- (83) Micklitz, W.; Bott, S. G.; Bentsen, J. G.; Lippard, S. J. *J. Am. Chem. Soc.* **1989**, *111*, 372.
- (84) Çelenligil-Çetin, R.; Staples, R. J.; Stavropoulos, P. *Inorg. Chem.* **2000**, *39*, 5838
- (85) Schnepfensieper, T.; Liehr, G.; van Eldik, R.; Enslin, J.; Gütllich, P. *Inorg. Chem.* **2000**, *39*, 5565.
- (86) Shweky, I.; Pence, L. E.; Papaefthymiou, G. C.; Sessoli, R.; Yun, J. W.; Bino, A.; Lippard, S. J. *J. Am. Chem. Soc.* **1997**, *119*, 1037.
- (87) Saalfrank, R. W.; Glaser, H.; Demleitner, B.; Hampel, F.; Chowdhry, M. M.; Schünemann, V.; Trautwein, A. X.; Vaughan, G. B. M.; Yeh, R.; Davis, A. V.; Raymond, K. N. *Chem. Eur. J.* **2002**, *8*, 493.
- (88) Harding, C. J.; Henderson, R. K.; Powell, A. K. *Angew. Chem., Int. Ed.* **1993**, *32*, 570
- (89) Hegetschweiler, K.; Schmalle, H. W.; Streit, H. M.; Gramlich, V.; Hund, H.-U.; Erni, I. *Inorg. Chem.* **1992**, *31*, 1299.
- (90) Hegetschweiler, K.; Schmalle, H. W.; Streit, H. M.; Schneider, W. *Inorg. Chem.* **1990**, *29*, 3625.
- (91) Cornia, A.; Gatteschi, D.; Hegetschweiler, K.; Hausherr-Primo, L.; Gramlich, V. *Inorg. Chem.* **1996**, *35*, 4414.
- (92) Spandl, J.; Kusserow, M.; Brüdgam, I. *Z. Anorg. Allg. Chem.* **2003**, 629, 968.

- (93) Ammala, P. S.; Batten, S. R.; Cashion, J. D.; Keppert, C. M.; Moubaraki, B.; Murray, K. S.; Spiccia, L.; West, B. O. *Inorg. Chim. Acta.* **2002**, *331*, 90.
- (94) Carson, E. C.; Lippard, S. J. *Inorg. Chem.* **2006**, *45*, 837.
- (95) Burkill, H. A.; Robertson, N.; Vilar, R.; White, A. J. P.; Williams, D. J. *Inorg. Chem.* **2005**, *44*, 3337.
- (96) Seddon, E. J.; Huffman, J. C.; Christou, G. J. *Chem. Soc., Dalton Trans.* **2000**, 4446.
- (97) Nair, V. S.; Hagen, K. S. *Inorg. Chem.* **1992**, *31*, 4048.
- (98) Seddon, E. J.; Yoo, J.; Folting, K.; Huffman, J. C.; Hendrickson, D. N.; Christou, G. J. *Chem. Soc., Dalton Trans.* **2000**, 3640.
- (99) Grant, C. M.; Knapp, M. J.; Huffman, J. C.; Hendrickson, D. N.; Christou, G. *Chem. Commun.* **1998**, 1753.
- (100) Trettenhahn, G.; Nagl, M.; Neuwirth, N.; Arion, V. B.; Jary, W.; Pöchlauer, P.; Schmid, W. *Angew. Chem., Int. Ed.* **2006**, *45*, 2794.
- (101) Tokii, T.; Ide, K.; Nakashima, M.; Koikawa, M. *Chem. Lett.* 1994, 441.
- (102) Saalfrank, R. W.; Bernt, I.; Chowdhry, M. M.; Hampel, F.; Vaughan, G. B. M. *Chem. Eur. J.* **2001**, *7*, 2765
- (103) Lin, S.; Liu, S.-X.; Lin, B.-Z. *Inorg. Chim. Acta.* **2002**, *328*, 69.
- (104) Murugesu, M.; Abboud, K. A.; Christou, G. *Dalton Trans.* **2003**, 4552.
- (105) Saalfrank, R. W.; Deutscher, C.; Sperner, S.; Nakajima, T.; Ako, A. M.; Uller, E.; Hampel, F.; Heinemann, F. W. *Inorg. Chem.* **2004**, *43*, 4372.
- (106) Koizumi, S.; Nihei, M.; Nakano, M.; Oshio, H. *Inorg. Chem.* **2005**, *44*, 1208.
- (107) Saalfrank, R. W.; Reimann, U.; Göritz, M.; Hampel, F.; Scheurer, A.; Heinemann, F. W.; Büschel, M.; Daub, J.; Schünemann, V.; Trautwein, A. X. *Chem. Eur. J.* **2002**, *8*, 3614.
- (108) Tolis, E. I.; Helliwell, M.; Langley, S.; Raftery, J.; Winpenney, R. E. P. *Angew. Chem., Int. Ed.* **2003**, *42*, 3804.
- (109) Raptopoulou, C. P.; Boudalis, A. K.; Sanakis, Y.; Psycharis, V.; Clemente-Juan, J. M.; Fardis, M.; Diamantopoulos, G.; Papavassiliou, G. *Inorg. Chem.* **2006**, *45*, 2317.
- (110) Wemple, M. W.; Coggin, D. K.; Vincent, J. B.; McCusker, J. K.; Streib, W. E.; Huffman, J. C.; Hendrickson, D. N.; Christou, G. *Chem. Soc., Dalton Trans.* **1998**, 719.
- (111) Grant, C. M.; Knapp, M. J.; Huffman, J. C.; Hendrickson, D. N.; Christou, G. *Inorg. Chem.* **1998**, *37*, 6065.

- (112) Stamatatos, Th. C.; Christou, A. G.; Jones, C. M.; O'Callaghan, B. J.; Abboud, K. A.; O'Brien, T. A.; Christou, G. *J. Am. Chem. Soc.* **2007**, *129*, 9840
- (113) Stamatatos, Th. C.; Boudalis, A. K.; Sanakis, Y.; Raptopoulou, C. P. *Inorg. Chem.* **2006**, *45*, 7372.
- (114) Boudalis, A. K.; Dahan, F.; Bousseksou, A.; Tuchagues, J.-P.; Perlepes, S. P. *Dalton Trans.* **2003**, 3411.
- (115) Burger, J.; Klüfers, P. *Z. Anorg. Allg. Chem.* **1997**, *623*, 1547.
- (116) Davidson, E. R. *GRID*, Indiana University, Bloomington, IN, 1999.
- (117) Powell, A. K.; Heath, S. L.; Gatteschi, D.; Pardi, L.; Sessoli, R.; Spina, G.; Del Giallo, F.; Pieralli, F. *J. Am. Chem. Soc.* **1995**, *117*, 2491.
- (118) Barra, A. L.; Caneschi, A.; Cornia, A.; de Biani, F. F.; Gatteschi, D.; Sangregorio, C.; Sessoli, R.; Sorace, L. *J. Am. Chem. Soc.* **1999**, *121*, 5302.
- (119) Powell, G. W.; Lancashire, H. N.; Brechin, E. K.; Collison, D.; Heath, S. L.; Malluh, T.; Wernsdorfer, W. *Angew. Chem., Int. Ed.* **2004**, *43*, 5772.
- (120) Schmitt, W.; Anson, C. E.; Wernsdorfer, W.; Powell, A. K. *Chem. Commun.* **2005**, 2098.
- (121) Moragues-Canovas, M.; Riviere, P.; Ricard, L.; Paulsen, C.; Wernsdorfer, W.; Rajaraman, G.; Brechin, E. K.; Mallah, T. *Adv. Mater.* **2004**, *16*, 1101.
- (122) Kajiwarra, T.; Ito, T. *Angew. Chem., Int. Ed.* **2000**, *39*, 230.
- (123) Delfs, C.; Gatteschi, D.; Pardi, L.; Sessoli, R.; Wieghardt, K.; Hanke, D. *Inorg. Chem.* **1993**, *32*, 3099.
- (124) Gatteschi, D.; Sessoli, R.; Cornia, A. *Chem. Commun.*, **2000**, *9*, 725.
- (125) Barra, A. L.; Debrunner, P.; Gatteschi, D.; Schulz, Ch. E.; Sessoli, R. *Europhys. Lett.* **1996**, *35*, 133.
- (126) Caciuffo, R.; Amoretti, G.; Murani, A.; Sessoli, R.; Caneschi, A.; Gatteschi, D. *Phys. Rev. Lett.* **1998**, *81*, 4744.
- (127) Wieghardt, K.; Pohl, K.; Jibril, I.; Huttner, G. *Angew. Chem.* **1984**, *23*, 77.
- (128) Frey, M.; Harris, S.; Holmes, J.; Nation, D.; Parsons, S.; Tasker, P.; Teat, S.; Winpenny, R. *Angew. Chem.* **1998**, *37*, 3245
- (129) Benelli, C.; Cano, J.; Journaux, Y.; Sessoli, R.; Solan, G. A.; Winpenny, R. E. P. *Inorg. Chem.* **2001**, *40*, 188.
- (130) Liu, T.; Zhang, Y.-J.; Wang, Z.-M.; Gao, S. *J. Am. Chem. Soc.* **2008**, *130*, 10500.

- (131) Zhang, Z.-M.; Li, Y.-G.; Yao, S.; Wang, E.-B.; Wang, Y.-H.; Clérac, R.; *Angew. Chem., Int. Ed.* **2009**, *48*, 1581.
- (132) Gorun, S.M.; Lippard, S. J. *Nature*, **1986**, *319*, 666.
- (133) Gorun, S. M.; Papaefthymiou, G. C.; Frankel, R. B.; Lippard, S. J. *J. Am. Chem. Soc.* **1987**, *109*, 3337
- (134) Micklitz, W.; McKee, V.; Rardin, R. L.; Pence, L. E.; Papaefthymiou, G. C.; Bott, S. G.; Lippard, S. J. *J. Am. Chem. Soc.* **1994**, *116*, 8061.
- (135) Raptopoulou, C. P.; Tangoulis, V.; Devlin, E. *Angew. Chem., Int. Ed.* **2002**, *41*, 2386.
- (136) Jones, L. F.; Low, D. M.; Helliwell, M.; Raftery, J.; Collison, D.; Aromi, G.; Cano, J.; Mallah, T.; Wernsdorfer, W.; Brechin, E. K.; McInnes, E. J. L. *Polyhedron*, **2006**, *25*, 325.
- (137) Heath, S. L.; Powell, A. K. *Angew. Chem., Int. Ed.* **1992**, *31*, 191.
- (138) Foguet-Albiol, D.; Abboud, K. A.; Christou, G. *Chem. Commun.* **2005**, 4282.
- (139) Frey, M.; Harris, S. G.; Holmes, J. M.; Nation, D. A.; Parsons, S.; Tasker, P. A.; Teat, S. J.; Winpenny, R. E. P. *Angew. Chem., Int. Ed.* **1998**, *37*, 3246.
- (140) Parsons, S.; Solan, G.A.; Winpenny, R.E.P. *Chem. Commun.* **1995**, 1987.
- (141) Bino, A.; Ardon, M.; Lee, D.; Spingler, B.; Lippard, S. J. *J. Am. Chem. Soc.* **2002**, *124*, 4578.
- (142) Caneschi, A.; Cornia, A.; Fabretti, A.C.; Gatteschi, D. *Angew. Chem., Int. Ed.* **1999**, *38*, 1295.
- (143) Evangelisti, M.; Candini, A.; Ghirri, A.; Affronte, M.; Powell, G. W.; Gass, I. A.; Wood, P. A.; Parsons, S.; Brechin, E. K.; Collison, D.; Heath, S. L. *Phys. Rev. Lett.* **2006**, *97*, 167202.
- (144) Grapperhaus, C. A.; O'Toole, M. G.; Mashuta, M. S. *Inorg. Chem. Commun.*, **2006**, *9*, 1204.
- (145) Asirvatham, S.; Khan, M. A.; Nicholas, K. M. *Inorg. Chem.* **2000**, *39*, 2006.
- (146) O'Keefe, B. J.; Monnier, S. M.; Hillmyer, M. A.; Tolman, W. B. *J. Am. Chem. Soc.* **2001**, *123*, 339.
- (147) Bolcar, M. A. Aubin, S. M. J.; Foltling, K.; Hendrickson, D. N. *Chem. Commun.* **1997**, 1485.
- (148) Yoo, J.; Yamaguchi, A.; Nakano, M.; Krzystek, J.; Streib, W. E.; Brunel, L.-C.; Ishimoto, H.; Christou, G.; Hendrickson, D. N. *Inorg. Chem.* **2001**, *40*, 4604.

- (149) Lecren, L.; Roubeau, O.; Li, Y-G.; Le Goff, X. F.; Miyasaka, H.; Richard, F.; Wernsdorfer, W.; Coulon, C.; Clérac, R. *Dalton Trans.*, **2008**, 755.
- (150) Miyasaka, H.; Nakata, K.; Lecren, L.; Coulon, C.; Nakazawa, Y.; Fujisaki, T.; Sugiura, K.; Yamashita, M.; Clérac, R. *J. Am. Chem. Soc.* **2006**, *128*, 3770.
- (151) Boskovic, C.; Brechin, E.; Streib, W. E.; Folting, K.; Bollinger, J. C.; Hendrickson, D. N.; Christou, G. *J. Am. Chem. Soc.* **2002**, *124*, 3725.
- (152) Sanudo, E. C.; Wernsdorfer, W.; Abboud, K. A.; Christou, G. *Inorg. Chem.* **2004**, *43*, 4137.
- (153) Taguchi, T.; Stamatatos, T. C.; Abboud, K. A.; Jones, C. M.; Poole, K. M.; O'Brien, T. A.; Christou, G. *Inorg. Chem.* **2008**, *47*, 4095.
- (154) Murugesu, M.; Mishra, A.; Wernsdorfer, W.; Abboud, K. A.; Christou, G. *Polyhedron* **2006**, *25*, 613.
- (155) Duncan, J. F.; Kanekar, C. R.; Mok, K. F. *J. Chem. Soc. A* **1969**, *3*, 480.
- (156) Earnshaw, A.; Figgis, B. N.; Lewis, J. J. *J. Chem. Soc. A* **1966**, *12*, 1656.
- (157) Bond, A. M.; Clark, R. J. H.; Humphrey, D. G.; Panayiotopoulos, P.; Skelton, B. W.; White, A. H. *J. Chem. Soc., Dalton Trans.* **1998**, *11*, 1845.
- (158) Sheldrick, G. M. *SHELXL-97*; University of Göttingham: Germany, **1997**.
- (159) Spek, A. L. *Acta Crystallogr., Sect. A* **1990**, *46*, C34.
- (160) Mola, M.; Hill, S.; Goy, P.; Gross, M., *Rev. Sci. Instrum.*, **2000**, *71*, 186.
- (161) Takahashi, S.; Hill, S. *Rev. Sci. Instrum.*, **2005**, *76*, 023114.
- (162) Boudalis, A. K.; Donnadiou, B.; Nastopoulos, V.; Clemente-Juan, J. M.; Alain, M.; Sanakis, Y.; Tuchagues, J. P.; Perlepes, S. P. *Angew. Chem., Int. Ed.* **2004**, *43*, 2266.
- (163) Papaefstathiou, G. S.; Escuer, A.; Vicente, R.; Font-Bardia, M.; Solans, X.; Perlepes, S. P. *Chem. Commun.* **2001**, 2414.
- (164) Cotton, F. A.; Wilkinson, G. *Advanced Inorganic Chemistry*; Wiley: New York, 1980; pp 154-155
- (165) Cannon, R. D.; White, R. P. *Prog. Inorg. Chem.* **1988**, *36*, 195.
- (166) Raptis, R. G.; Georgakaki, I. P.; Hockless, D. C. R. *Angew. Chem., Int. Ed.* **1999**, *38*, 1632.
- (167) Gass, I. A.; Milios, C. J.; Whittaker, A. G.; Fabiani, F. P. A.; Parsons, S.; Murrie, M.; Perlepes, S. P.; Brechin, E. K. *Inorg. Chem.* **2006**, *45*, 5281.

- (168) Hahn, F. E.; Jocher, C.; Lugger, T. *Z. Naturforsch. B.* **2004**, *59*, 855.
- (169) Nair, V. S.; Hagen, K. S. *Inorg. Chem.* **1994**, *33*, 185.
- (170) Schmitt, W.; Murugesu, M.; Goodwin, J. C.; Hill, J. P.; Mandel, A.; Bhalla, R.; Anson, C. E.; Heath, S. L.; Powell, A. K. *Polyhedron* **2001**, *20*, 1687.
- (171) Satcher, J. H., Jr.; Olmstead, M. M.; Droege, M. W.; Parkin, S. R.; Noll, B. C.; May, L.; Balch, A. L. *Inorg. Chem.* **1998**, *37*, 6751.
- (172) Gautier-Luneau, I.; Fouquard, C.; Merle, C.; Pierre, J.-L.; Luneau, D. *Dalton Trans.* **2001**, 2127.
- (173) Ako, A. M.; Waldmann, O.; Mereacre, V.; Klöwer, F.; Hewitt, I. J.; Anson, C. E.; Güdel, H. U.; Powell, A. K. *Inorg. Chem.* **2007**, *46*, 756.
- (174) Watton, S. P.; Fuhrmann, P.; Pence, L. E.; Caneschi, A.; Cornia, A.; Abbati, G. L.; Lippard, S. J. *Angew. Chem., Int. Ed. Engl.*, **1997**, *36*, 2774.
- (175) King, P.; Stamatatos, T. C.; Abboud, K. A.; Christou, G. *Angew. Chem., Int. Ed.*, **2006**, *45*, 7379.
- (176) Bagai, R.; Abboud, K. A.; Christou, G. *Chem. Commun.*, **2007**, 3359.
- (177) Waldmann, O.; Stamatatos, T. C.; Christou, G.; Güdel, H. U.; Sheikin, I.; Mutka, H. *Phys. Rev. Lett.* **2009**, *102*, 157202(1-4).
- (178) Prakash, R.; Saalfrank, R. W.; Maid, H.; Scheurer, A.; Heinemann, F. W.; Trautwein, A. X.; Böttger, L. H. *Angew. Chem., Int. Ed.* **2006**, *45*, 5885.
- (179) Yao, H.-C.; Wang, J.-J.; Ma, Y.-S.; Waldmann, O.; Du, W.-X.; Song, Y.; Li, Y.-Z.; Zheng, L.-M.; Decurtins, S.; Xina, X.-Q. *Chem. Commun.*, **2006**, 1745.
- (180) Konar, S.; Bhuvanesh, N.; Clearfield, A. *J. Am. Chem. Soc.* **2006**, *128*, 9064.
- (181) Bino, A.; Shweky, I.; Cohen, S.; Bauminger, E. R.; Lippard, S. J. *Inorg. Chem.* **1998**, *37*, 5168.
- (182) Veith, M.; Grätz, F.; Huch, V. *Eur. J. Inorg. Chem.* **2001**, 367.
- (183) Soler, M.; Wernsdorfer, W.; Foltz, K.; Pink, M.; Christou, G. *J. Am. Chem. Soc.* **2004**, *126*, 2156.
- (184) Brechin, E. K.; Sanudo, E. C.; Wernsdorfer, W.; Boskovic, C.; Yoo, J.; Hendrickson, D. N.; Yamaguchi, A.; Ishimoto, H.; Concolino, T. E.; Rheingold, A. L.; Christou, G. *Inorg. Chem.* **2005**, *44*, 502.
- (185) Murugesu, M.; Raftery, J.; Wernsdorfer, W.; Christou, G.; Brechin, E. K. *Inorg. Chem.* **2004**, *43*, 4203.

- (186) Scott, R. T. W.; Parsons, S.; Murugesu, M.; Wernsdorfer, W.; Christou, G.; Brechin, E. K. *Angew. Chem., Int. Ed.* **2005**, *44*, 6540.
- (187) Gorun, S. M.; Lippard, S. J. *Inorg. Chem.* **1991**, *30*, 1625.
- (188) Rumberger, E. M.; Hill, S.; Edwards, R. S.; Wernsdorfer, W.; Zakharov, L. N.; Rheingold, A. L.; Christou, G.; Hendrickson, D. N. *Polyhedron*, **2003**, *22*, 1865.
- (189) Lee, S.-C.; Stamatatos, T. C.; Hill, S.; Perlepes, S. P.; Christou, G. *Polyhedron*, **2007**, *26*, 2225.
- (190) Stamatatos, Th. C.; Foguet-Albiol, D.; Stoumpos, C. C.; Lee, S.-C.; Hill, S. O.; Raptopoulou, C. P.; Terzis, A.; Wernsdorfer, W.; Perlepes, S. P.; Christou, G. *J. Am. Chem. Soc.* **2007**, *129*, 9484.
- (191) Hill, S.; Edwards, R. S.; Jones, S. I.; North, J. M.; Dalal, N. S. *Phys. Rev. Lett.* **2003**, *90*, 217204.
- (192) del Barco, E.; Kent, A. D.; Hill, S.; North, J. M.; Dalal, N. S.; Rumberger, E. M.; Hendrickson, D. N.; Chakov, N.; Christou, G. *J. Low Temp. Phys.* **2005**, *140*, 119.
- (193) Park, K.; Novotny, M. A.; Dalal, N. S.; Hill, S.; Rikvold, P. A. *Phys. Rev. B*, **2002**, *65*, 014426.
- (194) S. Hill, S. Maccagnano, K. Park, R. M. Achey, J. M. North and N. S. Dalal, *Phys. Rev. B.* **2002**, *65*, 224410.
- (195) Lawrence, J.; Yang, E.-C.; Edwards, R.; Olmstead, M. M.; Ramsey, C.; Dalal, N. S.; Gantzel, P. K.; Hill, S.; Hendrickson, D. N. *Inorg. Chem.*, **2008**, *47*, 1965.
- (196) Wang, X. J.; Langetepe, T.; Persau, C.; Kang, B.-S.; Sheldrick, G. M.; Fenske, D. *Angew. Chem., Int. Ed.* **2002**, *41*, 3818.
- (197) Oshio, H.; Nakano, M. *Chem. Eur. J.* **2005**, *11*, 5178.
- (198) Friedman, J. R. ; Sarachik, M. P.; Tejada, J.; Ziolo, R. *Phys. Rev. Lett.* **1996**, *76*, 3830.
- (199) Wernsdorfer, W.; Sessoli, R. *Science*, **1999**, *284*, 133.
- (200) Wernsdorfer, W.; Soler, M.; Christou, G. ; Hendrickson, D. N. *J. Appl. Phys.* **2002**, *91*, 7164.
- (201) Wernsdorfer, W.; Chakov, N. E.; Christou, G. *Phys. Rev. Lett.* **2005**, *95*, 037203.
- (202) Sun, Z. M.; Grant, C. M.; Castro, S. L.; Hendrickson, D. N.; Christou, G. *Chem. Commun.* **1998**, 721.

- (203) Andres, H.; Basler, R.; Blake, A. J.; Cadiou, C.; Chaboussant, G.; Grant, C. M.; Gudel, H. U.; Murrie, M.; Parsons, S.; Paulsen, C.; Semadini, F.; Villar, V.; Wernsdorfer, W.; Winpenny, R. E. P. *Chem. Eur. J.* **2002**, *8*, 4867.
- (204) Tasiopoulos, A. J.; Vinslava, A.; Wernsdorfer, W.; Abboud, K. A.; Christou, G. *Angew. Chem., Int. Ed.* **2004**, *43*, 2117.
- (205) Price, D. J.; Batten, S. R.; Moubaraki, B.; Murray, K. S. *Chem. Comm.* **2002**, 762.
- (206) Milios, C. J.; Raptopoulou, C. P.; Terzis, A.; Lloret, F.; Vicente, R.; Perlepes, S. P.; Escuer, A. *Angew. Chem., Int. Ed.* **2003**, *43*, 210.
- (207) Tasiopoulos, A. J.; Wernsdorfer, W.; Abboud, K. A.; Christou, G. *Angew. Chem., Int. Ed.* **2004**, *43*, 6338.
- (208) King, P.; Wernsdorfer, W.; Abboud, K. A.; Christou, G. *Inorg. Chem.* **2004**, *43*, 7315.
- (209) Tasiopoulos, A. J.; Wernsdorfer, W.; Abboud, K. A.; Christou, G. *Inorg. Chem.*, **2005**, *44*, 6324.
- (210) Maheswaran, S.; Chastanet, G.; Teat, S. J.; Mallah, T.; Sessoli, R.; Wernsdorfer, W.; Winpenny, R. E. P. *Angew. Chem., Int. Ed.* **2005**, *44*, 5044.
- (211) Wu, Q.; Li, Y-G.; Wang, Y-H.; Wang, E-B.; Zhang, Z-M.; Clerac, R.; *Inorg. Chem.*, **2009**, *48*, 1606.
- (212) Manoli, M.; Prescimone, A.; Mishra, A.; Parsons, S.; Christou, G. Brechin, E. K. *Dalton Trans.*, **2007**, 532.
- (213) Bhaduri, S.; Tasiopoulos, A.; Pink, M.; Abboud, K. A.; Christou, G. *Chem. Commun.* **2002**, 2352.
- (214) Aliaga-Alcalde, N.; Edwards, R. S.; Hill, S. O.; Wernsdorfer, W.; Folting, K.; Christou, G. *J. Am. Chem. Soc.* **2004**, *126*, 12503.
- (215) Wang, S.; Wemple, M. S.; Tsai, H.-L.; Folting, K.; Huffman, J. C.; Hagen, K. S.; Hendrickson, D. N.; Christou, G. *Inorg. Chem.* **2000**, *39*, 1501.
- (216) Wang, S.; Tsai, H.-L.; Hagen, K. S.; Hendrickson, D. N.; Christou, G. *J. Am. Chem. Soc.* **1994**, *116*, 8376.
- (217) Eppley, H. J.; Tsai, H.-L.; de Vries, N.; Folting, K.; Christou, G.; Hendrickson, D. N. *J. Am. Chem. Soc.* **1995**, *117*, 301.
- (218) Eppley, H. J.; Christou, G.; Law, N. A.; Pecoraro, V. L. *Inorg. Synth.* **2002**, *33*, 61.
- (219) Chakov, N. E.; Zakharov, L. N.; Rheingold, A. L.; Abboud, K. A.; Christou, G. *Inorg. Chem.*, **2005**, *44*, 4555.

- (220) Brechin, E. K.; Soler, M.; Christou, G. Helliwell, M.; Teat, S. J.; Wernsdorfer, W. *Chem. Commun.*, **2003**, 1276.
- (221) Rajaraman, G.; Murugesu, M. Soler, M.; Wernsdorfer, W.; Helliwell, M.; Teat, S. J.; Christou, G.; Brechin, E. K. *J. Am. Chem. Soc.*, **2004**, *126*, 15445.
- (222) Piligkos, S.; Rajaraman, G.; Soler, M.; Kirchner, N.; van Slageren, J.; Bircher, R.; Parsons, S.; Güdel, H.-U.; Kortus, J.; Wernsdorfer, W.; Christou, G.; Brechin, E. K. *J. Am. Chem. Soc.*, **2005**, *127*, 5572.
- (223) Milios, C. J.; Vinslava, A.; Wernsdorfer, W.; Moggach, S.; Parsons, S.; Perlepes, S. P.; Christou, G.; Brechin, E. K.; *J. Am. Chem. Soc.*, **2007**, *129*, 2754
- (224) Milios, C. J.; Vinslava, A.; Wernsdorfer.; Prescimone, A.; Wood, P. A.; Parsons, S.; Perlepes, S. P.; Christou, G.; Brechin, E. K. *J. Am. Chem. Soc.*, **2007**, *129*, 6547.
- (225) Milios, C. J.; Inglis, R.; Vinslava, A.; Bagai, R.; Wernsdorfer, W.; Parsons, S.; Perlepes, S. P.; Christou, G.; Brechin, E. K. *J. Am. Chem. Soc.*, **2007**, *129*, 12505
- (226) Foguet-Albiol, D.; O'Brien, T. A.; Wernsdorfer, W.; Moulton, B.; Zaworotko, M. J.; Abboud, K. A.; Christou, G. *Angew. Chem. Int. Ed.*, **2005**, *44*, 897.
- (227) Saalfrank, R.W.; Nakajima, T.; Mooren, N.; Scheurer, A.; Maid, H.; Hampel, F.; Trieflinger, C.; Daub. J. *Eur. J. Inorg. Chem.* **2005**, 1149.
- (228) Rumberger, E.M.; Shah, S.J.; Beedle, C.C.; Zakharov, L.N.; Rheingold, A.L.; Hendrickson, D.N. *Inorg. Chem.*, **2005**, *44*, 2742.
- (229) Murugesu, M. Wernsdorfer, W.; Abboud, K. A.; Christou, G. *Angew. Chem. Int. Ed.*, **2005**, *44*, 892
- (230) Wittick, L.M.; Jones, L.F.; Jensen, P.; Moubaraki, B.; Spiccia, L.; Berry, K.J.; Murray, K.S. *Dalton Trans.*, **2006**, 1534
- (231) Wittick, L.M.; Murray, K.S.; Moubaraki, B.; Batten, S.R. Spiccia, L.; Berry, K.J. *Dalton Trans.*, **2004**, 1003.
- (232) Ako, A. M.; Hewitt, I. J; Mereacre, V.; Clérac, R., Wernsdorfer, W.; Anson, C. E.; Powell, A. K. *Angew. Chem. Int. Ed.*, **2006**, *45*, 4926.
- (233) Moushi, E. E.; Stamatatos, Th. C.; Wernsdorfer, W.; Nastopoulos, V.; Christou, G.; Tasiopoulos, A. J. *Inorg. Chem.*, **2009**, *48*, 5049.
- (234) Nayak, S.; Lan, Y.; Clérac, R.; Ansona, C. E.; Powell, A. K. *Chem. Commun.*, **2008**, 5698.
- (235) Stamatatos, Th. C.; Foguet-Albiol, D.; Stoumpos, C. C.; Raptopoulou, C. P.; Terzis, A.; Wernsdorfer, W.; Perlepes, S. P.; Christou, G. *J. Am. Chem. Soc.* **2005**, *127*, 15380.

- (236) Milios, C. J.; Kefalloniti, E.; Raptopoulou, C. P.; Terzis, A.; Vicente, R.; Lalioti, N.; Escuer, A.; Perlepes, S. P. *Chem. Commun.* **2003**, 819.
- (237) Zaleski, C. M.; Depperman, E. C.; Dendrinou-Samara, C.; Alexiou, M.; Kampf, J. W.; Kessissoglou, D. P.; Kirk, M. L.; Pecoraro, V. L. *J. Am. Chem. Soc.* **2005**, *127*, 12862.
- (238) Stamatatos, Th. C.; Abboud, K. A.; Wernsdorfer, W.; Christou, G. *Angew. Chem., Int. Ed.* **2008**, *47*, 6694.
- (239) Doherty, S.; Errington, R. J.; Jarvis, A. P.; Collins, S.; Clegg, W.; Elsegood, M. R. J. *Organometallics*, **1998**, *17*, 3408
- (240) Schlitz, B. E.; Gheller, S. F.; Muetterties, M. C.; Scott, M. J.; Holm, R. H. *J. Am. Chem. Soc.*, **1993**, *115*, 2714.
- (241) Wong, Y-L.; Yang, Q.; Zhou, Z-Y.; Lee, H. K.; Mak, T. C. W.; Ng, D. K. P. *New J. Chem.*, **2001**, *25*, 353
- (242) Hagen, H.; Bezemer, C.; Boersma, J.; Kooijman, H.; Lutz, M.; Spek, A. L.; Van Koten, G. *Inorg. Chem.*, **2000**, *39*, 3970.
- (243) Tsukahara, T.; Swenson, D. C.; Jordan, R. F. *Organometallics*, **1997**, *16*, 3303.
- (244) Brandts, J. A. M.; Boersma, J.; Spek, A. L.; van Koten, G. *Eur. J. Inorg. Chem.* **1999**, 1727.
- (245) Herrmann, W. A.; Fridgen, J.; Lobmaier, G. M.; Spiegler, M. *New J. Chem.* **1999**, *23*, 5.
- (246) Hayton, T. W.; Boncella, J. M.; Scott, B. L.; Abboud, K. A.; Mills, R. C. *Inorg. Chem.*, **2005**, *44*, 9506.
- (247) Speiser, F.; Braunstein, P.; Saussine, L. *Inorg. Chem.* **2004**, *43*, 4234
- (248) Coutelier, O.; Gauvin, R. M.; Nowogrocki, G.; Trebosc, J.; Delevoye, L.; Mortreux, A. *Eur. J. Inorg. Chem.*, **2007**, 5541
- (249) Ridd, M. J.; Gakowski, D. J.; Sneddon, G. E.; Keene, F. R. *J. Chem. Soc., Dalton Trans.* **1992**, 1949.
- (250) Tzerpos, N. I.; Zarkadis, A. K.; Kreher, R. P.; Repas, L.; Lehnig, M. *J. Chem. Soc., Perkin Trans. 2*, **1995**, *4*, 755.
- (251) Weast, R. C. *CRC Handbook of Chemistry and Physics*, Ed. **1984**, CRC Press, Inc. Boca Raton, Florida.
- (252) Lecren, L.; Wernsdorfer, W.; Li, Y-G.; Roubeau, O.; Miyasaka, H.; Clerac, R. *J. Am. Chem. Soc.* **2005**, *127*, 11311.
- (253) Lecren, L.; Li, Y-G.; Wernsdorfer, W.; Roubeau, O.; Miyasaka, H.; Clerac, R. *Inorg. Chem. Commun.* **2005**, *8*, 626.

- (254) Lecren, L.; Roubeau, O.; Coulon, C. Li, Y-G.; Le Goff, X. F.; Wernsdorfer, W.; Miyasaka, H.; Clerac, R. *J. Am. Chem. Soc.* **2005**, *127*, 17353.
- (255) Vincent, J. B.; Christmas, C.; Chang, H.-R.; Li, Q.; Boyd, P. D. W.; Huffman, J. C.; Hendrickson, D. N.; Christou, G. *J. Am. Chem. Soc.* **1989**, *111*, 2086
- (256) Christou, G. *Acc. Chem. Res.* **1989**, *22*, 328.
- (257) Bouwman, E.; Bolcar, M. A.; Libby, E.; Huffman, J. C.; Folting, K.; Christou, G. *Inorg. Chem.*, **1992**, *31*, 5185
- (258) Brown, I. D.; Altermatt, D. *Acta Crystallogr.* **1985**, *B41*, 244.
- (259) Liu, W.; Thorp, H. H. *Inorg. Chem.* **1993**, *32*, 4102.
- (260) Godbole, M. D.; Roubeau, O.; Mills, A. M.; Kooijman, H.; Spek, A. L.; Bouwman, E. *Inorg. Chem.* **2006**, *45*, 6713.
- (261) S. P. Perlepes, J. C. Huffman and G. Christou, *J. Chem. Soc., Chem. Commun.*, **1991**, 1657.
- (262) Aromi, G.; Knapp, M.J.; Claude, J.-P.; Huffman, J. C.; Hendrickson, D. N.; Christou, G. *J. Am. Chem. Soc.* **1999**, *121*, 5489.
- (263) Kambe, K. *J. Phys. Soc. Jpn.* **1950**, *5*, 48.
- (264) VanVleck, J. H. *The Theory of Electrical and Magnetic Susceptibilities*; Oxford Press, London, 1932.
- (265) King, P.; Wernsdorfer, W.; Abboud, K. A.; Christou, G. *Inorg. Chem.* **2005**, *44*, 8659.
- (266) Chakov, N. E.; Lawrence, J.; Harter, A. G.; Hill, S. O.; Dalal, N. S.; Wernsdorfer, W.; Abboud, K. A.; Christou, G. *J. Am. Chem. Soc.* **2006**, *128*, 6975.
- (267) Wernsdorfer, W. *Adv. Chem. Phys.* **2001**, *118*, 99.
- (268) Sanudo, E. C.; Brechin, E. K.; Boskovic, C.; Wernsdorfer, W.; Yoo, J.; Yamaguchi, A.; Concolino, T. R.; Abboud, K. A.; Rheingold, A. L.; Ishimoto, H.; Hendrickson, D. N.; Christou, G. *Polyhedron*, **2003**, *22*, 2267.
- (269) Ferreira, K. N.; Iverson, T. M.; Maghlaoui, K.; Barber, J.; Iwata, S. *Science* **2004**, *303*, 1831.
- (270) Carrell, T. G.; Tyryshkin, A. M.; Dismukes, G. C. *J. Biol. Inorg. Chem.* **2002**, *7*, 2.
- (271) Cinco, R. M.; Rompel, A.; Visser, H.; Aromi, G.; Christou, G.; Sauer, K.; Klein, M. P.; Yachandra, V. K. *Inorg. Chem.* **1999**, *38*, 5988.

- (272) Yachandra, V. K.; Sauer, K.; Klein, M. P. *Chem. Rev.* **1996**, *96*, 2927.
- (273) Law, N. A.; Caudle, M. T.; Pecoraro, V. L. In *Advances in Inorganic Chemistry*; Sykes, A. G., Ed.; Academic Press: London, 1998; Vol. 46, p 305.
- (274) Yocum, C. F.; Pecoraro, V. L. *Curr. Opin. Chem. Biol.* **1999**, *3*, 182.
- (275) Milios, C. J.; Manoli, M.; Rajaraman, G.; Mishra, A.; Budd, L. E.; White, F.; Parsons, S.; Wernsdorfer, W.; Christou, G.; Brechin, E. K. *Inorg.Chem.* **2006**, *45*, 6782.
- (276) Manoli, M.; Prescimone, A.; Bagai, R.; Mishra, A.; Murugesu, M.; Parsons, S.; Wernsdorfer, W.; Christou, G. Brechin, E. K. *Inorg.Chem.* **2007**, *46*, 6968.
- (277) Murugesu, M.; Wernsdorfer, W.; Abboud, K. A.; Brechin, E. K.; Christou, G. *Dalton Trans.* **2006**, 2285.
- (278) Manoli, M.; Milios, C. J.; Mishra, A.; Christou, G.; Brechin, E. K. *Polyhedron* **2007**, *26*,1923.
- (279) Brechin, E. K.; Soler, M.; Davidson, J.; Hendrickson, D. N.; Parsons, S.; Christou, G. *Chem.Commun.* **2002**, 2252.
- (280) Brechin, E. K.; Soler, M.; Christou, G.; Davidson, J.; Hendrickson, D. N.; Parsons, S.; Wernsdorfer, W. *Polyhedron* **2003**, *22*, 1771.
- (281) Murugesu, M.; Wernsdorfer, W.; Christou, G.; Brechin, E. K. *Polyhedron* **2007**, *26*, 1845.
- (282) Milios, C. J.; Fabbiani, F. P. A.; Parsons, S.; Murugesu, M.; Christou, G.; Brechin, E. K. *Dalton Trans.* **2006**, 351.
- (283) Scott, R. T. W.; Milios, C. J.; Vinslava, A.; Lifford, D.; Parsons, S.; Wernsdorfer, W.; Christou, G.; Brechin, E. K. *Dalton Trans.* **2006**, 3161
- (284) Moushi, E. E.; Lampropoulos, C.; Wernsdorfer, W.; Nastopoulos, V.; Christou, G.; Tasiopoulos, A. J. *Inorg.Chem.* **2007**, *46*, 3795.
- (285) Moushi, E. E.; Stamatatos, T. C.; Wernsdorfer, W.; Nastopoulos, V.; Christou, G.; Tasiopoulos, A. J. *Angew.Chem.,Int.Ed.* **2006**, *45*, 7722.
- (286) Aromi, G.; Gamez, P.; Roubeau, O.; Berzal, P. C.; Kooijman, H.; Spek, A. L.; Driessen, W. L.; Reedijk, J. *Inorg.Chem.* **2002**, *41*, 3673.
- (287) Yang, C.-I.; Lee, G.-H.; Wur, C.-S. Lin, J. G.; Tsai, H.-L. *Polyhedron* **2005**, *24*, 2215.
- (288) Rumberger, E. M.; Zakharov, L. N.; Rheingold, A. L.; Hendrickson, D. N. *Inorg.Chem.* **2004**, *43*, 6531.
- (289) Saalfrank, R. W.; Prakash, R.; Maid, H.; Hampel, F.; Heinemann, F. W.; Trautwein, A. X.; Bottger, L. H. *Chem.-Eur.J.* **2006**, *12*, 2428.

- (290) Saalfrank, R.W.; Scheurer, A.; Prakash, R.; Heinemann, F.W.; Nakajima, T.; Hampel, F.; Leppin, R.; Pilawa, B.; Rupp, H.; Muller, P. *Inorg.Chem.* **2007**, *46*, 1586.
- (291) Ako, A. M.; Mereacre, V.; Hewitt, I. J.; Clerac, R.; Lecren, L.; Anson, C. E.; Powell, A. K. *J.Mater.Chem.* **2006**, *16*, 2579.
- (292) Liu, T.; Wang, B.-W. Chen, Y.-H.; Wang, Z.-M.; Gao, S. *Z.Anorg.Allg.Chem.* **2008**, *634*, 778.
- (293) Beedle, C. C.; Heroux, K. J.; Nakano, M.; DiPasquale, A. G.; Rheingold, A. L.; Hendrickson, D. N. *Polyhedron* **2007**, *26*, 2200.
- (294) Milios, C. J.; Kyritsis, P.; Raptopoulou, C. P.; Terzis, A.; Vicente, R.; Escuer, A.; Perlepes, S. P. *Dalton Trans.* **2005**, 501.
- (295) Milios, C. J.; Raptopoulou, C. P.; Terzis, A.; Vicente, R.; Escuer, A.; Perlepes, S. P. *Inorg.Chem.Commun.* **2003**, *6*, 1056.
- (296) Papaefstathiou, G. S.; Escuer, A.; Raptopoulou, C. P.; Terzis, A.; Perlepes, S. P.; Vicente, R. *Eur.J.Inorg.Chem.* **2001**, 1567.
- (297) Papaefstathiou, G. S.; Escuer, A.; Mautner, F. A.; Raptopoulou, C.; Terzis, A.; Perlepes, S. P.; Vicente, R. *Eur.J.Inorg.Chem.* **2005**, 879.
- (298) Stoumpos, C. C.; Gass, I. A.; Milios, C. J.; Kefalloniti, E.; Raptopoulou, C. P.; Terzis, A.; Lalioti, N.; Brechin, E. K.; Perlepes, S. P. *Inorg.Chem.Commun.* **2008**, *11*, 196.
- (299) Dendrinou-Samara, C.; Alexiou, M.; Zaleski, C. M.; Kampf, J. W.; Kirk, M. L.; Kessissoglou, D.P.; Pecoraro, V. L. *Angew.Chem.,Int.Ed.*, **2003**, *42*, 3763.
- (300) Tong, M.-L.; Lee, H. K.; Zheng, S.-L.; Chen, X.-M. *Chem.Lett.* **1999**, 1087.
- (301) Tong, M.-L.; Zheng, S.-L.; Shi, J.-X. Tong, Y.-X.; Lee, H. K.; Chen, X.-M. *J.Chem.Soc.,Dalton Trans.* **2002**, 1727.
- (302) Brechin, E. K.; Yoo, J.; Huffman, J. C.; Hendrickson, D. N.; Christou, G. *Chem. Commun.* **1999**, 783.
- (303) Stamatatos, T. C.; Luisi, B. S.; Moulton, B.; Christou, G. *Inorg.Chem.* **2008**, *47*, 1134.
- (304) Milios, C. J.; Kefalloniti, E.; Raptopoulou, C. P.; Terzis, A.; Escuer, A.; Vicente, R.; Perlepes, S. P. *Polyhedron* **2004**, *23*, 83.
- (305) Milios, C. J.; Stamatatos, T. C.; Kyritsis, P.; Terzis, A.; Raptopoulou, C. P.; Vicente, R.; Escuer, A.; Perlepes, S. P. *Eur.J.Inorg.Chem.* **2004**, 2885.
- (306) Milios, C. J.; Piligkos, S.; Bell, A. R.; Laye, R. H.; Teat, S. J.; Vicente, R.; McInnes, E.; Escuer, A.; Perlepes, S. P.; Winpenny, R. E. P. *Inorg.Chem.Commun.* **2006**, *9*, 638.

- (307) Dendrinou-Samara, C.; Zaleski, C. M.; Evagorou, A.; Kampf, J. W.; Pecoraro, V. L.; Kessissoglou, D. P. *Chem. Commun.* **2003**, 2668.
- (308) Alexiou, M.; Zaleski, C. M.; Dendrinou-Samara, C.; Kampf, J.; Kessissoglou, D. P.; Pecoraro, V. L. *Z.Anorg.Allg.Chem.* **2003**, 629, 2348.
- (309) Alexiou, M.; Dendrinou-Samara, C.; Karagianni, A.; Biswas, S.; Zaleski, C. M.; Kampf, J.; Yoder, D.; Penner-Hahn, J. E.; Pecoraro, V. L.; Kessissoglou, D. P. *Inorg.Chem.* **2003**, 42, 2185.
- (310) Psomas, G.; Stemmler, A. J.; Dendrinou-Samara, C.; Bodwin, J. J.; Schneider, M.; Alexiou, M.; Kampf, J. W.; Kessissoglou, D. P.; Pecoraro, V. L. *Inorg.Chem.* **2001**, 40, 1562.
- (311) Roubeau, O.; Lecren, L.; Li, Y.-G.; Le Goff, X.F.; Clerac, R. *Inorg.Chem.Communic.* **2005**, 8, 314.
- (312) Dimitrakopoulou, A.; Dendrinou-Samara, C.; Pantazaki, A. A.; Alexiou, M.; Nordlander, E.; Kessissoglou, D. P. *J.Inorg.Biochem.* **2008**, 102, 618.
- (313) Papatriantafyllopoulou, C.; Raptopoulou, C. P.; Escuer, A.; Milios, C. J. *Inorg.Chim.Acta* **2007**, 360, 61.
- (314) Prescimone, A.; Milios, C. J.; Moggach, S.; Warren, J. E.; Lennie, A. R.; Sanchez-Benitez, J.; Kamenev, K.; Bircher, R.; Murrie, M.; Parsons, S.; Brechin, E. K. *Angew.Chem.,Int.Ed.* **2008**, 47, 2828
- (315) Milios, C. J.; Inglis, R.; Vinslava, A.; Prescimone, A.; Parsons, S.; Perlepes, S. P.; Christou, G.; Brechin, E. K. *Chem. Commun.* **2007**, 2738.
- (316) Milios, C. J.; Gass, I. A.; Vinslava, A.; Budd, L.; Parsons, S.; Wernsdorfer, W.; Perlepes, S. P.; Christou, G.; Brechin, E. K. *Inorg.Chem.* **2007**, 46, 6215.
- (317) Milios, C. J.; Vinslava, A.; Wood, P. A.; Parsons, S.; Wernsdorfer, W.; Christou, G.; Perlepes, S. P.; Brechin, E. K. *J.Am.Chem.Soc.* **2007**, 129, 8.
- (318) Milios, C. J.; Inglis, R.; Bagai, R.; Wernsdorfer, W.; Collins, A.; Moggach, S.; Parsons, S.; Perlepes, S. P.; Christou, G.; Brechin, E. K. *Chem. Commun.* **2007**, 3476.
- (319) Milios, C. J.; Wood, P. A.; Parsons, S.; Foguet-Albiol, D.; Lambropoulos, C.; Christou, G.; Perlepes, S. P.; Brechin, E. K. *Inorg.Chim.Acta* **2007**, 360, 3932.
- (320) Milios, C. J.; Prescimone, A.; Mishra, A.; Parsons, S.; Wernsdorfer, W.; Christou, G.; Perlepes, S. P.; Brechin, E.K. *Chem. Commun.* **2007**, 153.
- (321) Milios, C. J.; Vinslava, A.; Whittaker, A. G.; Parsons, S.; Wernsdorfer, W.; Christou, G.; Perlepes, S. P.; Brechin, E. K. *Inorg.Chem.* **2006**, 45, 5272.

- (322) Chaudhuri, P.; Birkelbach, F.; Winter, M.; Staemmler, V.; Fleischhauer, P.; Haase, W.; Florke, U.; Haupt, H.-J. *J.Chem.Soc.,Dalton Trans.* **1994**, 2313
- (323) Chaudhuri, P.; Rentschler, E.; Birkelbach, F.; Krebs, C.; Bill, E.; Weyhermuller, T.; Florke, U. *Eur.J.Inorg.Chem.* **2003**, 541.
- (324) Xu, H.-B.; Wang, B.-W.; Pan, F.; Wang, Z.-M.; Gao, S. *Angew.Chem.,Int.Ed.* **2007**, 46, 7388.
- (325) Yang, C.-I.; Wernsdorfer, W.; Lee, G.-H.; Tsai, H.-L. *J.Am.Chem.Soc.* **2007**, 129, 456.
- (326) Zhou, A.-J.; Qin, L.-J.; Beedle, C. C.; Ding, S.; Nakano, M.; Leng, J.-D.; Tong, M.-L.; Hendrickson, D. N. *Inorg.Chem.* **2007**, 46, 8111.
- (327) Bagai, R.; Abboud, K. A.; Christou, G. *Inorg.Chem.* **2008**, 47, 621.
- (328) Koizumi, S.; Nihei, M.; Shiga, T.; Nakano, M.; Nojiri, H.; Bircher, R.; Waldmann, O.; Ochsenein, S. T.; Gudel, H. U.; Fernandez-Alonso, F.; Oshio, H. *Chem.-Eur.J.* **2007**, 13, 8445.
- (329) Xia, X.; Verelst, M. Daran, J.-C.; Tuchagues, J.-P. *Chem. Commun.* **1995**, 2155.
- (330) Lah, M. S.; Pecoraro, V.L. *J.Am.Chem.Soc.* **1989**,111, 7258
- (331) Gibney, B. R.; Wang, H.; Kampf, J. W.; Pecoraro, V. L. *Inorg.Chem.* **1996**, 35, 6184.
- (332) Kessissoglou, D. P.; Bodwin, J. J.; Kampf, J.; Dendrinou-Samara, C.; Pecoraro, V. L. *Inorg.Chim.Acta* **2002**, 331,73.
- (333) Kessissoglou, D. P.; Kampf, J.; Pecoraro, V. L. *Polyhedron* **1994**, 13, 1379
- (334) Aromi, G.; Bell, A.; Teat, S. J.; Whittaker, A. G.; Winpenny, R. E. P. *Chem. Commun.* **2002**, 1896.
- (335) Taguchi, T; Daniels, M. R.; Abboud, K. A.; Christou, G. *Inorg.Chem.*, **2009**, 48, 9325.
- (336) Canty, A. J.; Titcombe, L. A.; Skelton, B. W.; White, A. H. *J.Chem.Soc.,Dalton Trans.* ,**1988**, 35
- (337) Wibaut, J. P., De Jonge, A. P., van der Voort, H. Q. P., and Otto, P. Ph. H. L., *Red Trav.Chim. Pays-Bas*, **1951**, 70, 1054.
- (338) Sala, T.; Sargent, M. V. *Chem. Commun.* **1978**, 253.
- (339) Vincent, J. B.; Chang H. R.; Folting, K.; Huffman, J. C.; Christou, G.; Hendrickson, D. N. *J. Am. Chem. Soc.* **1987**, 109, 5703.
- (340) Bashkin, J. S.; Chang, H.-R.; Streib, W. E.; Huffman, J. C.; Hendrickson, D. N.; Christou, G. *J. Am. Chem. Soc.* **1987**, 109, 6502

- (341) Li, Q.; Vincent, J. B.; Libby, E.; Chang, H.-R.; Huffman, J. C.; Boyd, P. D. W.; Christou, G.; Hendrickson, D. N. *Angew. Chem., Int. Ed. Engl.* **1988**, *27*, 1721.
- (342) Wang, S.; Tsai, H.-L.; Folting, K.; Streib, W. E.; Hendrickson, D. N.; Christou, G. *Inorg. Chem.* **1996**, *35*, 7578.
- (343) Ruettinger, W. F.; Campana, C.; Dismukes, G. C. *J.Am.Chem.Soc.*, **1997**, *119*, 6670.
- (344) Ruettinger, W. F.; Ho, D.M.; Dismukes, G. C. *Inorg.Chem.*, **1999**, *38*, 1036.
- (345) Wu, J.-Z.; Sellitto, E.; Yap, G. P. A.; Sheats, J.; Dismukes, G. C. *Inorg.Chem.*, **2004**, *43*, 5795.

## BIOGRAPHICAL SKETCH

Taketo Taguchi was born in Shiga, Japan in 1978. He entered Osaka University, Japan in 1998 and received Bachelor of Science. He did undergraduate research in the research group of Professor Michio Matsumura. Title of his bachelor's thesis is "Chemical Etching of TiO<sub>2</sub> Photocatalyst Particles". In 2002, he joined the research group of Professor Akira Fujishima at the University of Tokyo, and obtained his master's degree in engineering in 2004. Title of his master's thesis is "Solid-State Dye-Sensitized Solar Cells". He then decided to pursue a doctoral degree in the United States, and joined the research group of Professor George Christou in 2004. His doctoral research primarily involves in new ligand design for the preparation and magnetic characterization of polynuclear Mn and Fe clusters of unprecedented structural types.